RADIO-EMITTING COMPACT BINARIES IN MILKY WAY GLOBULAR CLUSTERS

By

Laura Katharine Shishkovsky

A DISSERTATION

Submitted to
Michigan State University
in partial fulfillment of the requirements
for the degree of

Astronomy & Astrophysics—Doctor of Philosophy

2022

ABSTRACT

RADIO-EMITTING COMPACT BINARIES IN MILKY WAY GLOBULAR CLUSTERS

By

Laura Katharine Shishkovsky

Globular clusters are dense populations of hundreds of thousands to millions of stars, and were expected to at one point also contain a population of around 1000 stellar-mass black holes. However, theory predicted that as the clusters evolved, these black holes would be ejected from the cluster through gravitational interactions with other black holes, leaving only ∼1-2of globular clusters with a stellar-mass black hole. Recent research suggests though, that stellar-mass black holes could be far more common in globular clusters. This project aims to investigate the frequency of black holes in globular clusters using radio observations of Milky Way globular clusters from the Very Large Array (VLA), and has the potential to increase the number of known black holes in the Milky Way significantly.

This project focuses the search for stellar-mass black holes on cores of globular clusters, where, through dynamical mass-segregation, these black holes are expected to be. Radio observations are increasingly sensitive to low-luminosity accretion onto compact objects, which makes the deep VLA observations ideal for this search. Stellar-mass black hole candidates are identified by their flat spectrum radio emission, and followed up with observations at different wavelengths to confirm that candidates are not accreting neutron stars, white dwarfs, or background galaxies. If stellar-mass black holes are indeed common in globular clusters, this would have significant implications, such as that more accurate study of stellar-mass black holes could be done, and there would be increased chance of the formation of black hole-black hole binaries, which would be important sources of gravitational waves.

I dedicate this to me and only me.

ACKNOWLEDGMENTS

I acknowledge Liller.

TABLE OF CONTENTS

LIST OF TABLES

LIST OF FIGURES

KEY TO ABBREVIATIONS

- ACIS - The Advanced CCD Imaging Spectrometer
- AGN - Active Galactic Nuclei
- AIPS - Astronomical Image Processing System
- ATCA - Australia Telescope Compact Array
- BH - Black Hole
- CASA - Common Astronomy Software Application
- CCD - Charge-Coupled Device
- CIAO - Chandra Interactive Analysis of Observations
- CMD - Color-Magnitude Diagram
- CV - Cataclysmic Variable
- DEC - Declination
- FWHM - Full Width at Half Maximum
- GC - Globular Cluster
- HST - Hubble Space Telescope
- IRAF - Image Reduction and Analysis Facility
- LMXB - Low Mass X-Ray Binary
- MAVERIC - Milky-way ATCA and VLA Exploration of Radio-sources In Clusters
- NRAO - National Radio Astronomy Observatory
- NS - Neutron Star
- PSF - Point Spread Function
- RA - Right Ascension
- RFI - Radio frequency interference
- RMS - Root Mean Square
- RS CVn - RS Canum Venaticorum
- SNR - Signal-to-noise ratio

- SOAR - Southern Astrophysical Research Telescope
- UV - Ultraviolet
- UVOT Ultraviolet/Optical Telescope on board Swift
- VLA - Very Large Array
- VLBA - Very Long Baseline Array
- WFC - Wide Field Camera
- WD - White Dwarf
- XMM - X-ray Multi-Mirror Mission
- XSPEC - X-Ray Spectral Fitting Package

Chapter 1

Introduction

1.1 Compact Objects

Compact objects represent the end of life for most of the stars in the universe. Very low-mass stars ($M \lesssim 0.5$ M$_\odot$) evolve too slowly to experience stellar death, but most stars with initial masses above 0.8 will eventually become a white dwarf, neutron star, or black hole. Stars in the mass range 0.5–8 M$_\odot$ shed their outer layers after becoming red giants, eventually leaving behind only their dense core, a white dwarf. Neutron stars are created when a more massive star, 8 – 20M$_\odot$, evolves to the point where its degenerate iron core cannot be supported against the bulk of the star. This creates a core-collapse supernova when the core eventually collapses inward, leaving behind a compact neutron star, with the explosion expelling the envelope. Black holes are also typically formed this way when the progenitor star is above ≥ 20 M$_\odot$, but when the core collapse is not energetic enough to expel the envelope, leading to a core mass too high to be supported against degeneracy pressure.

These compact object remnants have the highest densities of any celestial objects. White dwarfs (WDs) have an average density of $\rho \lesssim 10^7$ g cm^{-3}, and are supported only by electron degeneracy pressure, which limits their mass at $M \lesssim 1.4$ M$_\odot$. Neutron stars (NSs) are held up by neutron degeneracy pressure with mean densities estimated as $\rho \lesssim 10^{15}$ g cm^{-3}. The complex structure and physical properties of NSs prevents their mass from being firmly constrained from first principles, with broad theoretical limits placing NS masses in the range

$1M_\odot \lesssim M \lesssim 3M_\odot$. Black holes (BHs) are practically infinitely dense, with gravitational forces so extreme even light cannot escape. They are categorized by their estimated masses, the greatest being the supermassive black holes that reside in the center of most massive galaxies, having masses $M > 10^6$ $M_\odot$. The least massive stellar-mass BHs are categorized by estimated masses in the range $3M_\odot \lesssim M \lesssim 100M_\odot$. Intermediate mass BHs ($\approx 10^2$ – 10^4 $M_\odot$) are proposed to be the evolutionary link from stellar-mass BHs to supermassive BHs, but no definitive evidence of their existence has been found as yet.

The high densities of compact objects make them unique testbeds for physical theories, including how neutrons and potentially other exotic particles behave at above nuclear densities (for NSs) and of detailed tests of general relativity (for BHs). In the cases of both NSs and BHs, gravitational waves created by the collision of binary compact objects allows for the detection of compact object binaries at large distances from the Earth through gravitational wave detectors like the Laser Interferometer Gravitational-Wave Observatory (LIGO).

On their own, compact objects are somewhat difficult to find. White dwarfs are often able to be detected in optical imaging, but neutron stars and black holes don't show any bright intrinsic optical emission. However, if a neutron star is in a pulsar state they often show detectable radio emission, and sometimes X-ray emission. The bright X-ray emission that is commonly observed in binaries with compact objects is a consequence of the interaction between the compact object and the other star in the system. It is typically caused by mass transfer from the donor star to the compact object, a process called accretion.

1.2 Accretion

Accretion occurs when some sort of matter falls toward an object due to its gravitational field. As the infall of matter occurs, it experiences a change in its gravitational potential energy, which is converted other forms of energy such as kinetic energy as well as electromagnetic radiation. The radiation can be emitted suddently if the infalling matter collides with the surface of the accreting object, or more slowly if it is due to the viscous interaction of material in the accretion flow. The characteristics of this emission can give valuable insight to the properties of the accreting system.

Accretion is ubiquitous in our universe, occurring in a variety of circumstances and at all time and mass scales. It is the process driving the accumulation of material into protoplanetary discs, as well as the process that feeds the supermassive black holes at the centers of galaxies. When white dwarfs, neutron stars, and stellar-mass black holes accrete material from a stellar companion, it allows for the study of accretion on relatively short timescales, as well as study of the compact objects themselves.

In the case of compact binaries accretion primarily occurs in two different scenarios: stellar wind accretion or Roche-lobe overflow. If the stellar companion is of high mass (≥ 10 $M_\odot$) it will blow off material via stellar winds which gets captured by the compact object. These binaries are typically very bright at X-ray and optical wavelengths, and short-lived due to the relatively short lives of the massive stars that drive strong stellar winds.

Roche-lobe overflow occurs in compact binaries with lower mass companions ($\lesssim 1$ $M_\odot$) when the companion is close to the compact object so that it fills its Roche-lobe: the potential boundary in which material is bound to the star. It defines the edge of equilibrium between the star and other objects. If some portion of the stellar material crosses it, either driven

by to stellar evolution of the donor star, or via loss of angular momentum that drives the components into closer contact, the star will transfer mass to the compact object through the inner Lagrangian point of the binary system. The matter in the accretion stream will typically not directly impact the compact object (due to its residual angular momentum) but instead form an accretion disk that spreads through viscous friction with other infalling matter (See Figure 1.1). The matter in the accretion disk will then slowly spiral inward until it eventually has shed enough angular momentum to be accreted onto the compact object (Misner et al., 1973; Steiner et al., 2010).

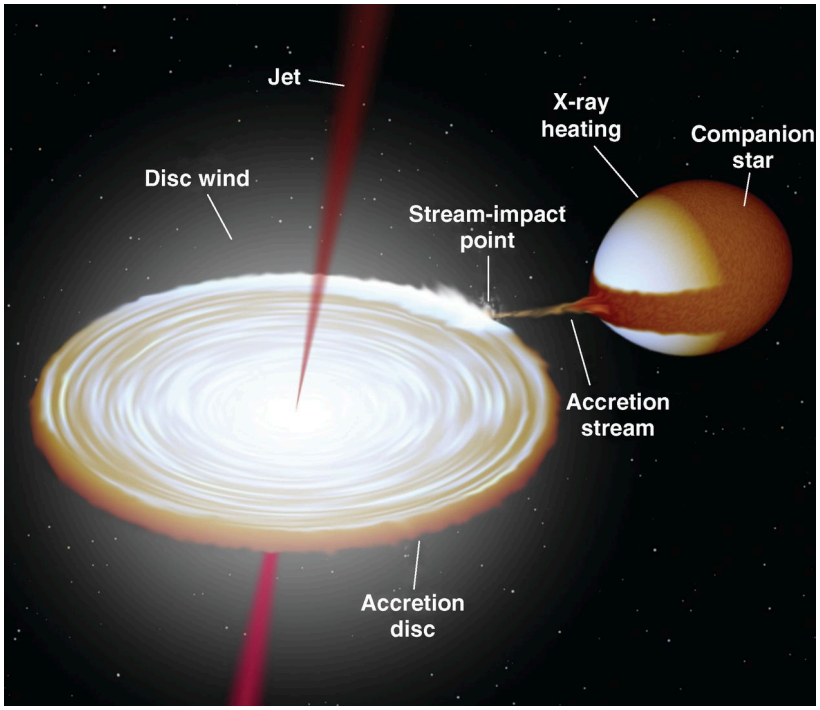

Figure 1.1 An artist's depiction of a compact object accreting through Roche-Lobe overflow. Credit: Rob Hynes

1.3 X-ray Binaries

X-ray binaries are accreting systems with either a central neutron star or black hole accreting from a less massive companion star. They are often very bright at X-ray wavelengths and differentiated into two categories according to the mass of the companion star. X-ray binaries hosting donors stars with masses $M \leq 3M_{\odot}$ are called low mass X-ray binaries (LMXBs) while high mass X-ray binaries (HMXBs) host companion stars with masses $M \geq 10M_{\odot}$ (due to evolutionary reasons, donor masses between these values are relatively rare).

HMXBs are driven by wind-fed accretion and are typically found in young stellar populations with an available host of massive stars. LMXBs are generally powered by the Roche-Lobe overflow of their companion, and are expected to be far more common than HMXBs in typical galaxies. LMXBs are typically found in older stellar populations such as the galactic bulge and globular clusters. The companion star in LMXBs is usually an older and faint main-sequence or slightly evolved star (i.e. G, K and M) with a mass rarely exceeding $\approx 1\mathrm{M}_{\odot}$(*Lewinet al.*, 1997).

LMXBs are often classified according to their accretion rate. Persistent systems (e.g, GRS 1915+105) typically have high accretion rates ($\sim 10^{-8}$ $\mathrm{M}_{\odot}$/year), and X-ray luminosities close to Eddington limit:

$$L_{Edd} = \frac{4\pi MGm_pc}{\sigma_\tau} = 1.26 \times 10^{38}(\frac{M}{M_{\odot}})erg\ s^{-1}$$

These systems are more easily detectable due to their high luminosities, but are not expected to be typical of LMXBs. Sources with lower accretion rates ($\leq 10^{-9}$ $\mathrm{M}_{\odot}$/year) show more transient behavior, and likely are more representative of the overall LMXB population. These systems spend most of their life in a quiescent states where they are challenging

to detect, but can undergo sporadic outbursts during which their brightness can rise by orders of magnitude, reaching luminosities similar to persistent sources (Tanaka & Shibazaki, 1996). It is during these X-ray outbursts that most transient LMXBs have been found. During outbursts, the X-ray spectrum is dominated by a "thermal" component that is well-represented by a multi-temperature blackbody and is thought to arise from the hot accretion disk.

After the peak of the outburst, the accretion rate drops and the X-ray spectrum hardens, signaling that the LMXB has entered the low-hard state. During the hard state, the source's X-ray spectrum is dominated by a hard non-thermal power law (power law photon index $1.4 < \Gamma < 2$), which is though to be the result of inverse-Compton scattering by hot electrons in a "corona" close to the compact object (Zdziarski & Gierliński, 2004; Poutanen & Veledina, 2014). During this time, radio emission is also present, resulting from self-absorbed synchrotron radiation created by outflowing compact jets (Corbel et al., 2000; Fender, 2001). Close observation of quiescent LMXBs has shown that the emission of outflowing compact radio jets seems to be strongly coupled to the accretion flow, i.e., the observed X-ray emission.

A correlation between the radio and the X-ray luminosity during the hard spectral state has been observed in many LMXB systems (Corbel et al., 2000, 2003; Gallo et al., 2012, 2014). This disk-jet coupling between the radio and X-ray luminosities of LMXBs generally differs for neutron star vs. black hole accretors, with neutron stars being generally less radio bright than black holes. This can be seen in Figure 1.2, which shows the radio-X-ray correlation for accreting compact objects.

In addition to its usefulness in understanding accretion dynamics, the radio-X-ray correlation for accreting compact objects has also been shown to be a useful tool in the practice of

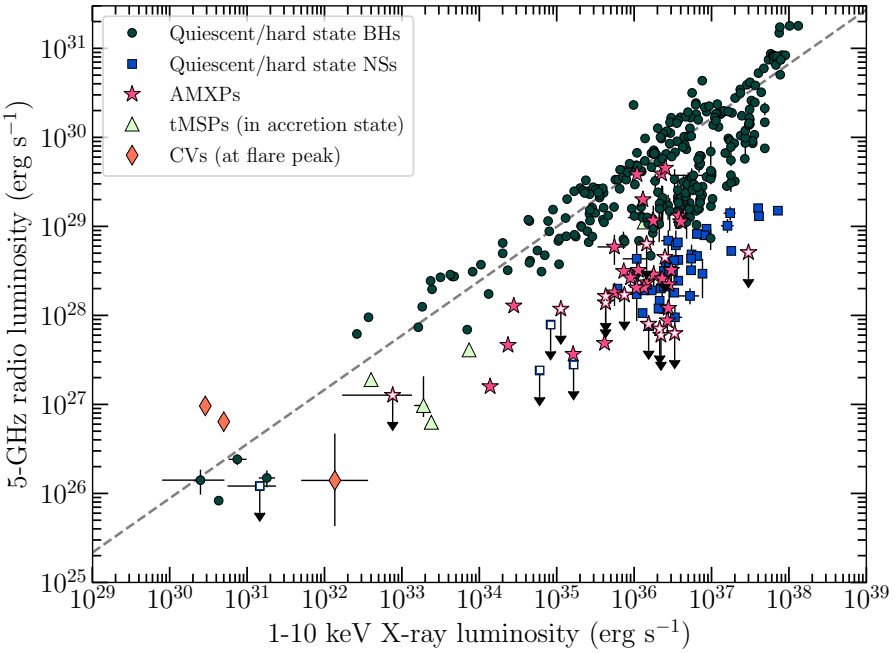

Figure 1.2 The radio/X-ray correlation for accreting compact objects. The black circles show known quiescent black holes in the field (Miller-Jones et al., 2011; Gallo et al., 2012; Ratti et al., 2012; Corbel et al., 2013; Rushton et al., 2016; Plotkin et al., 2017). The dotted black line shows the best-fitting L_R–L_X correlation for black holes from Gallo et al. (2014). The green triangles are transitional millisecond pulsars (Hill et al., 2011; Papitto et al., 2013; Deller et al., 2015; Bogdanov et al., 2018a). Blue squares are NSs in the hard state, and pink stars are accretion-powered millisecond X-ray pulsars (Migliari & Fender, 2006; Tudor et al., 2017). The orange diamonds are the bright CVs AE Aqr ($L_X = 5.0 \times 10^{30}$ erg s^{-1}), SS Cyg (in outburst; $L_X = 1.4 \times 10^{32}$ erg s^{-1}; Russell et al. (2016)), and white dwarf "pulsar" AR Sco ($L_X = 2.9 \times 10^{30}$ erg s^{-1}; Marsh et al. (2016)). Figure adapted from Bahramian et al. (2018)).

identifying the nature of different compact object binaries. At the higher luminosity end of the source population, quiescient BH and NS systems mostly occupy different regions of the parameter space, with BHs being brighter. Neutron star systems can be further differentiated based on whether they have shown X-ray pulsations (accreting milliecond pulsars; AMXPs), or have been observed to transition between a radio pulsar state and accreting neutron star state (transitional millisecond pulsars; tMSPs). Bright accreting white dwarf systems (cataclysmic variables; CVs) are also included as they have some overlapping characteristics with LMXBs.

In the case of black hole binaries, the radio and X-ray properties can be a strong indicator of the presence of a black hole accretor, but the most definitive way to determine a BH candidate's true nature is through stringent constraints placed on its mass. With the established upper limits on white dwarf mass ($M < 1.4\ M_{\odot}$) and neutron stars ($M < 3\ M_{\odot}$), one can say to high certainty that a central compact object is a black hole if justified by accurate and precise measurements of the binary orbital parameters. The period (P) and velocity semi-amplitude (K_2), in addition to the mass of the companion donor, place constraints on the candidate's mass via the mass-function:

$$f(M) = \frac{P\ {K_2}^3}{2\pi G} = \frac{(m_1 \sin i)^3}{(m_1+m_2)^2}$$

where i is the binary inclination. Measurement of the period and velocity semi-amplitude requires measurements of spectral Doppler shifts in the companions spectrum over multiple spectrographic observations. This often requires satisfactory justification for repeated optical telescope observations, and this equation also shows that if a binary system happens to have a more face-on orientation (low i) then it may have a low mass function even if the compact object is a BH. These points underscore the utility of radio and X-ray observations

in identifying new black hole candidates.

1.4 Globular Clusters

Figure 1.3 HST optical image of Galactic GC M15. Credit: ESA/HST/NASA.

Globular clusters are dense spherical systems of stars with masses M $\approx 10^5$—10^6 $M_\odot$. The Milky Way GC M15 is shown in 1.3. Most GC populations are very old ($\geq$ 10 Gyr), with primarily late-type stars, and are particularly abundant in stellar remnants. Rapidly rotating neutron stars (millisecond pulsars) are frequently detected at low-frequency radio wavelengths in GCs (e.g., Camilo & Rasio 2005; Ransom 2008), and CVs are suspected in many GCs to account for low-luminosity X-ray sources. NS LMXBs are at least an order of magnitude more common in GCs that isolated field systems, and are expected to account for

nearly all of the brightest ($L_X \sim 10^{36}$ erg s^{-1}) GC X-ray sources (Verbunt & Lewin 2006).

The efficient formation of binary compact object systems in GCs is attributed to their evolved stellar populations in hand with their high stellar densities. Field binaries outside of star clusters likely co-evolved in isolation, but GC binaries are expected to form through one or more close encounters in the dense environment. The physical nature of these formation encounters are likely tidal capture, three-body exchange, and direct collision with another cluster object (e.g., Fabian, Pringle & Rees 1975; Hills 1976; Verbunt & Hut 1983; Bailyn & Grindlay 1990; Davies & Hansen 1998; Ivanova et al. 2008; Ivanova et al. 2010). Being fundamentally gravitational encounters, they ensure that most massive cluster members — NSs and potentially BHs — capture companions at an enhanced rate. Massive compact objects also sink towards the cluster center over time due to dynamical friction, which further increases the capture rate.

1.4.1 Black Holes in Globular Clusters

Though rates of NS LMXBs in GCs are elevated, there is only one dynamically confirmed BH in a GC, and it is not in an X-ray binary (Giesers et al. 2018). This in contrast to the rates of BH and NS LMXBs in the field, where BH LMXBs account for approximately one-third of the LMXB systems (vlad cites liu 2007). For a typical GC with a present day mass of M $\approx 10^5$—10^6 $M_\odot$, 100—1000 stellar-mass BHs, each of mass M $\approx$ 5-20 $M_\odot$, should be born in the first 10 Myr of the GC. Assuming the BHs receive small natal kicks, they will rapidly mass segregate to the cluster center and form a subcluster that is dynamically segregated from the rest of the GC. Many BH–BH binaries will then be formed through three-body interactions. These binaries halt the collapse of the subcluster through interactions with one another. This process will tend to harden the binaries and lead to interactions with large

recoil velocities, ejecting the BHs from the GC.

Analytical arguments once held that the ejection process would continue until all of the BHs were ejected from the cluster, and that only perhap 1 in 100 GCs would still have a BH (Sigurdsson & Hernquist 1993; Kulkarni et al. 1993). But subsequent observational and theoretical results have suggested that the BH ejection process is less efficient that previously believed, and that GCs may be able to retain many BHs. Extragalactic GCs have produced several prime ultra-luminous BH binary candidates (e.g., Sarazin et al. 2001; Maccarone et al. 2007; Zepf et al., Zepf et al.; Irwin et al. 2010; Peacock et al. 2012), and several Milky Way GCs host low-luminosity candidates identified with multi-wavelength observations (Strader et al. 2012; Chomiuk et al. 2013; Miller-Jones et al. 2015; Bahramian et al. 2017; Shishkovsky et al. 2018). Numerous theoretical studies have also shown that a BH subcluster will dynamically re-couple with the GC as it loses mass, halting the ejection process (Mackey et al. 2008; Moody & Sigurdsson 2009; Sippel & Hurley 2013; Morscher et al. 2013; Breen & Heggie 2013; Heggie & Giersz 2014; Morscher et al. 2015a).

1.5 Motivation

This thesis outlines our ongoing work to discover new LMXBs in globular clusters by searching for radio emission. Most LMXB systems that have been discovered were found due to a spontaneous X-ray outburst. But it is believed that most LMXBs may never go into a bright X-ray outburst, which makes our collective knowledge of LMXB behavior biased toward a minority of X-ray bright systems. By selecting LMXB candidates because of their radio emission, we are more likely to find systems that are typical rather than uncommonly bright X-ray sources. Any LMXBs we find are also likely to have formed via a dynami-

cal exchange rather than co-evolving with its companion. This would allow comparison of physical properties with those of primordial LMXBs. Chapter 2 discusses a new black hole candidate in M10, and was published as a peer-reviewed article in the Astrophysical Journal as Shishkovsky et al. (2018). Chapter 3 describes our radio survey and gives a broad interpretation of the sample as a whole, and this chapter was published as a peer-reviewed article in the Astrophysical Journal as Shishkovsky et al. (2020). Chapter 4 introduces black hole candidates selected from the radio survey sample. We then summarize in Chapter 5 our interpretation of the current results and outline plans for further work on this project.

Chapter 2

The MAVERIC Survey: A Red Straggler Binary with an Invisible Companion in the Galactic Globular Cluster M10

2.1 Introduction

Due to their high stellar densities and large populations of stellar remnants, globular clusters are unique environments for the efficient formation of binaries with compact objects. The pathways to forming these low-mass X-ray binaries in globular clusters include tidal capture, three-body binary exchange, and direct stellar collisions with compact objects (e.g., Fabian, Pringle & Rees 1975; Hills 1976; Verbunt & Hut 1983; Bailyn & Grindlay 1990; Davies & Hansen 1998; Ivanova et al. 2008; Ivanova et al. 2010)—in contrast with field X-ray binaries, which likely evolved as isolated systems. The formation of low-mass X-ray binaries through close encounters accounts for the high specific abundance of X-ray binaries in globular clusters in both the Milky Way and in other galaxies (e.g., Pooley et al. 2003; Kundu et al. 2002).

While a substantial fraction of field low-mass X-ray binaries in the Milky Way host black holes (e.g., Tetarenko et al. 2016a; Remillard & McClintock 2006), the overwhelming majority of low-mass X-ray binaries in globular clusters—at least those which are bright and well-studied—host neutron stars rather than black holes (Verbunt & Lewin 2006; Bahramian et al. 2014), typically identified through Type I X-ray bursts (Lewin et al. 1993).

Many authors have argued that the relative paucity of black holes was real, beginning with analytic arguments about the fate of black holes in the dense cluster environment. After formation, any black holes that do not receive strong natal kicks will sink to center of the cluster and become segregated from less massive stars. In these close quarters, the black holes will form tight binaries that are largely ejected, through interactions with other black holes or black hole–black hole binaries. This process was argued to continue until all (or nearly all) black holes were depleted from the cluster (Sigurdsson & Hernquist 1993; Kulkarni et al. 1993).

Parallel observational and theoretical tracks have led to a reconsideration of this conclusion. Several globular clusters in external galaxies may contain black holes accreting near the Eddington luminosity, with the quality of the evidence ranging from suggestive to compelling (e.g., Sarazin, Irwin & Bregman 2001; Maccarone et al. 2007; Zepf et al. 2008; Irwin et al. 2010; Peacock et al. 2012). In the Milky Way, low-luminosity black hole candidates have been identified by a combination of radio continuum, X-ray, and optical data in the globular clusters M22 (Strader et al. 2012), M62 (Chomiuk et al. 2013), and 47 Tuc (Miller-Jones et al. 2015; Bahramian et al. 2017). A number of theoretical papers have concluded that black hole ejection is less efficient than originally thought, since a putative subcluster of black holes cannot remain dynamically isolated from the rest of the cluster as its mass declines (Mackey et al. 2008; Moody & Sigurdsson 2009; Sippel & Hurley 2013; Morscher et

al. 2013; Breen & Heggie 2013; Heggie & Giersz 2014; Morscher et al. 2015). This work has accelerated since the discovery of merging black hole–black hole binaries by Advanced LIGO (Abbott et al. 2016), and the dynamical formation of black hole–black hole binaries in globular clusters may be an important or even dominant channel for such systems (Rodriguez et al. 2016; Chatterjee et al. 2017).

No bright ($> 10^{36}$ erg s^{-1}) X-ray binary in a Galactic globular cluster has ever been identified to host a black hole; the candidates identified thus far are all in quiescence. Given the limited number of bright X-ray binaries in clusters, this could be due to small number statistics or could reflect unusual formation channels for cluster X-ray binaries compared to field systems. For example, short-period black hole X-ray binaries could undergo shorter, less-luminous outbursts that would not be detected by all-sky X-ray monitors (Maccarone & Patruno 2013; Knevitt et al. 2014).

In any case, black hole low-mass X-ray binaries are expected to spend most of their lives in a low-luminosity state with $L_X \sim 10^{30}$–10^{33} erg s^{-1} (Corbel et al. 2006) In this state it is typically not possible to separate them from other X-ray sources, such as compact binaries containing white dwarfs or neutron stars, or even active binaries, on the basis of X-ray observations alone. However, in quiescence, black holes are observed to emit steady flat-spectrum radio continuum emission, thought to originate via partially self-absorbed synchrotron radiation from compact jets (Blandford & Königl 1979).

The possibility of identifying quiescent black hole low-mass X-ray binaries through radio continuum emission motivated our group to conduct a systematic survey of 50 Galactic globular clusters using radio continuum observations from the upgraded Karl G. Jansky Very Large Array (VLA) and the Australia Telescope Compact Array (ATCA). We name this survey MAVERIC (Milky-way ATCA and VLA Exploration of Radio-sources In Clusters).

Here we present a multi-wavelength study of a radio-selected black hole candidate in the Galactic globular cluster M10 (NGC 6254; D = 4.4 kpc; Hurley et al. 1989; Harris 1996 (2010 edition)). M10 has a [Fe/H] ~ -1.5, and its mass is about 1.5 $\times 10^5$ $M_\odot$ (McLaughlin & van der Marel 2005; Haynes et al. 2008). In Section 2, we discuss our VLA observations, *Chandra* X-ray data, *Hubble Space Telescope* optical photometry, and ground-based SOAR spectroscopy of the system. In Section 3 we discuss the properties of the binary: identity of the binary companion, orbital parameters, and mass constraints. In Section 4 we discuss the interpretation of the system, and summarize our findings and discuss future work in Section 5.

2.2 Observations and Analysis

2.2.1 Radio

We observed M10 using the VLA in early 2014 in five 2-hr blocks (10 hr total, about 7 hr on source). The observations were done in A configuration and with C band receivers, with two 1-GHz basebands centered at 5.0 GHz and 7.4 GHz. Each baseband consisted of eight spectral windows, each 128 MHz wide, sampled with 64 channels of width 2 MHz. We used 8-bit samplers and obtained full polarization products.

3C286 was used as a flux density and bandpass calibrator, while J1651+0129 was used as a phase calibrator. The radio data from each epoch were reduced using *Common Astronomy Software Application* (CASA) (McMullin et al. 2007) version 4.2.2 with version 1.3.1 of the VLA calibration pipeline.[1] The pipeline imports raw data, applies preliminary flags, and then iteratively calibrates the data while running automatic flagging algorithms for radio

[1] https://science.nrao.edu/facilities/vla/data-processing/pipeline

frequency interference. We manually flagged any remaining corrupt data and then re-ran the pipeline. Once the target was properly calibrated and flagged, we imaged each baseband separately.

The field of view was selected to match the FWHM size of the primary beam: $11'$ at 5.0 GHz and $7.5'$ at 7.4 GHz. We used Briggs weighting with a robust parameter of 1, and nterms = 2 to account for the non-zero spectral indices of the various sources in the field. The synthesized beams for the 5.0 and 7.4 GHz images are $0.75'' \times 0.36''$ and $0.53'' \times 0.26''$, respectively.

In a future paper we will discuss the details of all radio continuum sources detected within the VLA's primary beam. This paper focuses on the only source within the $48''$ (1.0 pc; Dalessandro et al. 2011) cluster core radius detected in both the upper and lower basebands. This source, which we term M10-VLA1, is located at a J2000 position of (R.A., Dec.) = (16:57:08.478 $\pm$ 0.013s, $-$04:05:55.72 $\pm$ $0.19''$), only $10''$ (0.2 pc) in projection from the photometric center of the cluster (Goldsbury et al. 2010). The source was clearly detected in both basebands during the first 2-hr observing block (on 2014 Feb 20; Table 1) and marginally detected at 5 GHz on 2014 Apr 29; it was not detected in the other three blocks in either baseband. The images of the source from the first block are shown in Figure 1.

We determined the flux densities of M10-VLA1 by fitting a point source in the image plane using the task `imfit` in CASA, constraining the source size to the dimensions of the synthesized beam. On 2014 Feb 20, the flux density was 16.2 ± 5.4 μJy (5.0 GHz) and 27.2 ± 4.2 μJy (7.4 GHz, giving a luminosity spectral density of 6×10^{26} erg s^{-1} GHz^{-1}). Assuming a power-law frequency dependence ($S_\nu \propto \nu^\alpha$) the source has evidence for a flat to inverted spectrum, with $\alpha = 1.3 \pm 0.9$. There was no clear detection of M10-VLA1

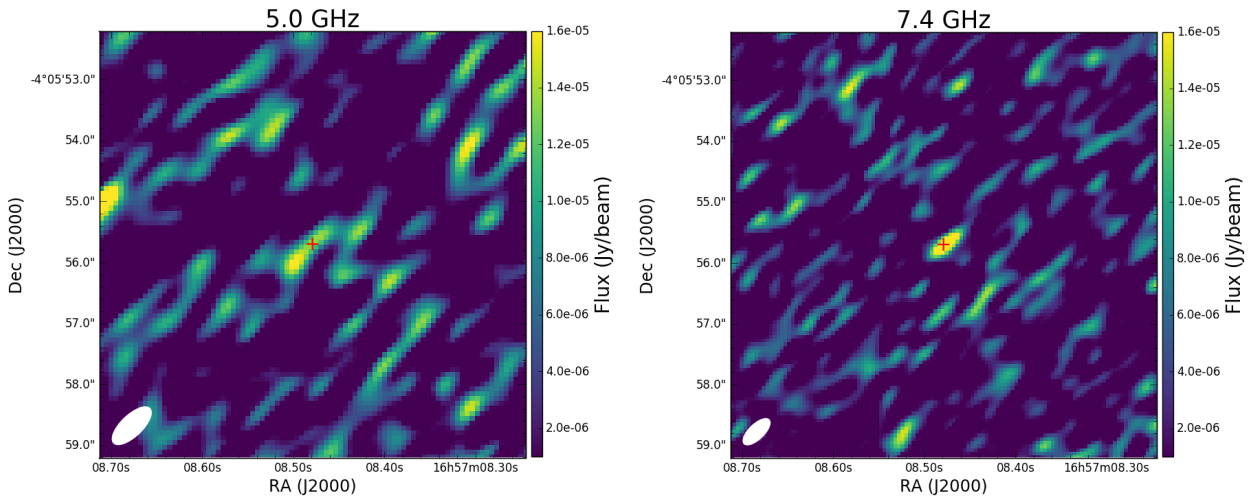

Figure 2.1 VLA 5.0 GHz (top) and 7.4 GHz (bottom) radio images of the 2014 Feb 20 detection of M10-VLA1. The red cross marks the location of the source center given by `imfit` from the combined 6.0 GHz image of the 2014 Feb 20 observation. We note that the source position is dominated by the 7.4 GHz flux — at 5.0 GHz the detection is just 3σ. The image synthesized beam is denoted as a white ellipse in the bottom left corner of each image.

in either baseband for the subsequent epochs, taken 36 to 68 days after the initial data. There is a marginal 5 GHz detection of the source on 2014 Apr 29 ($14.7 \pm 4.5 \mu$Jy beam^{-1}), accompanied by a non-detection at 7.4 GHz at this epoch (3σ upper limit of $< 10.8 \mu$Jy beam^{-1}). This suggests a spectral index of $\alpha < -0.8$, which is much steeper than the 2014 Feb 20 epoch. However, given the large uncertainties in the flux densities, an inverted spectral slope consistent with the earlier epoch ($\alpha = 1.3 \pm 0.9$) cannot be ruled out at even the 2σ level. The flux densities and 3σ upper limits from the initial detection and the other epochs are listed in Table 1. The individual epochs with non-detections were also combined and imaged, yielding no detections and 3σ upper limits of 7.7μJy beam^{-1} (5.0 GHz) and 5.8μJy beam^{-1} (7.4 GHz).

To check for short-term variability, we re-imaged the 2014 Feb 20 epoch on timescales of about 10 min (averaging 9 target scans, each of 62.8 s duration) in each frequency band.

Table 2.1. VLA Radio Flux Densities of M10-VLA1

Epoch Date	Epoch Date (MJD)	Time (UTC)	5.0 GHz Peak Flux (μJy)	RMS (μJy/beam)	7.4 GHz Peak Flux (μJy)	RMS (μJy/beam)
Feb 20, 2014	56708.4	09:19:32 − 11:19:12	16.2	5.4	27.2	4.2
Mar 28, 2014	56744.3	07:32:59 − 09:32:36	< 13.8	4.6	< 11.4	3.8
Apr 7, 2014	56754.3	06:49:09 − 08:48:46	< 14.7	4.9	< 11.4	3.8
Apr 10, 2014	56757.4	09:07:49 − 08:06:32	< 15.9	5.3	< 12.3	4.1
Apr 29, 2014	56776.2	04:56:49 − 06:56:29	14.7	4.5	< 10.8	3.6

Note. — The flux density upper limits represent 3σ limits.

For both basebands, the flux densities were constant within the uncertainties across the observation. Therefore, there is no evidence that M10-VLA1 was variable over the 2 hr observation on 2014 Feb 20.

2.2.2 X-ray

2.2.2.1 Chandra

Subsequent to the detection of the radio continuum source, we observed M10 in X-rays with *Chandra*/ACIS-S for 32.6 ksec on 2015 May 08. The *Chandra* image is shown in Figure 2. We used `CIAO` 4.7 and `CalDB` 4.6.9 to complete the *Chandra* data analysis (Fruscione et al. 2006). Using the `CIAO wavdetect` task for source detection, a faint X-ray source with ~ 12 net counts is clearly present at the position of the radio source to within the *Chandra* absolute astrometric accuracy of $0.6''$. There is no evidence for variability, however the low number of counts prevents us from concluding this definitively. The field is not crowded in the X-rays: only 10 X-ray sources are detected by `wavdetect` within the $1.95'$ half-light radius of M10 (equivalent to a source density of $\sim 2 \times 10^{-4}$ arcsec^{-2}). There are less than ten 5σ radio sources (at 6.0 GHz) within the half-light radius, suggesting extremely low odds of a chance match between an X-ray source and the radio source. Therefore the X-ray source

is almost certainly associated with the radio source.

Using a circular source region of $2''$ radius and a source-free annulus background around the source (inner/outer radii: $10''/20''$), we extracted the X-ray spectrum with `specextract`. The spectral analysis was performed using XSPEC (version 12.9.0; Arnaud 1996), assuming Anders & Grevesse (1989) abundances and Verner et al. (1996) absorption cross-sections. Given the limited number of photons, we analyzed the spectrum by binning the data with at least one count per bin and using the XSPEC operation cstat, a modified version of the Cash statistic (Cash 1979) for studying low-count spectra.[2] Assuming an absorbed power-law with an X-ray absorption of

$N_h = 2.44 \times 10^{21}$ (frozen to this value, derived from $E(B-V) = 0.25$–0.28; Schlafly & Finkbeiner 2011; Harris 1996; Bahramian et al. 2015; Foight et al. 2016), the best-fit photon index is $\Gamma = 2.8^{+1.1}_{-1.0}$ and the absorption-corrected 0.5–10 keV flux is

$4.5^{+2.5}_{-1.8} \times 10^{-15}$ (all uncertainties represent 90% confidence intervals). This flux is equivalent to $L_X \sim 1.0^{+0.6}_{-0.4} \times 10^{31}$ erg s^{-1} at the distance of M10. The spectrum was also fit using a MEKAL model (Mewe, Gronenschild & van den Oord 1985; Mewe, Lemen & van den Oord 1986; Kaastra 1992; Liedahl, Osterheld & Goldstein 1995), also with the cstat operation. Again we assume $N_H = 2.44 \times 10^{21}$ and that the metallicity is 0.03 solar. The best-fit temperature from the MEKAL model is $1.1^{+2.1}_{-0.5}$ keV, and the unabsorbed flux from 0.5 - 10 keV is $3.6^{+2.1}_{-1.4} \times 10^{-15}$ at 90% confidence. This flux corresponds to $L_X \sim 8.4^{+4.9}_{-3.2} \times 10^{30}$ erg s^{-1} at the distance of M10.

[2] https://heasarc.gsfc.nasa.gov/xanadu/xspec/manual/~XSappendixStatistics.html

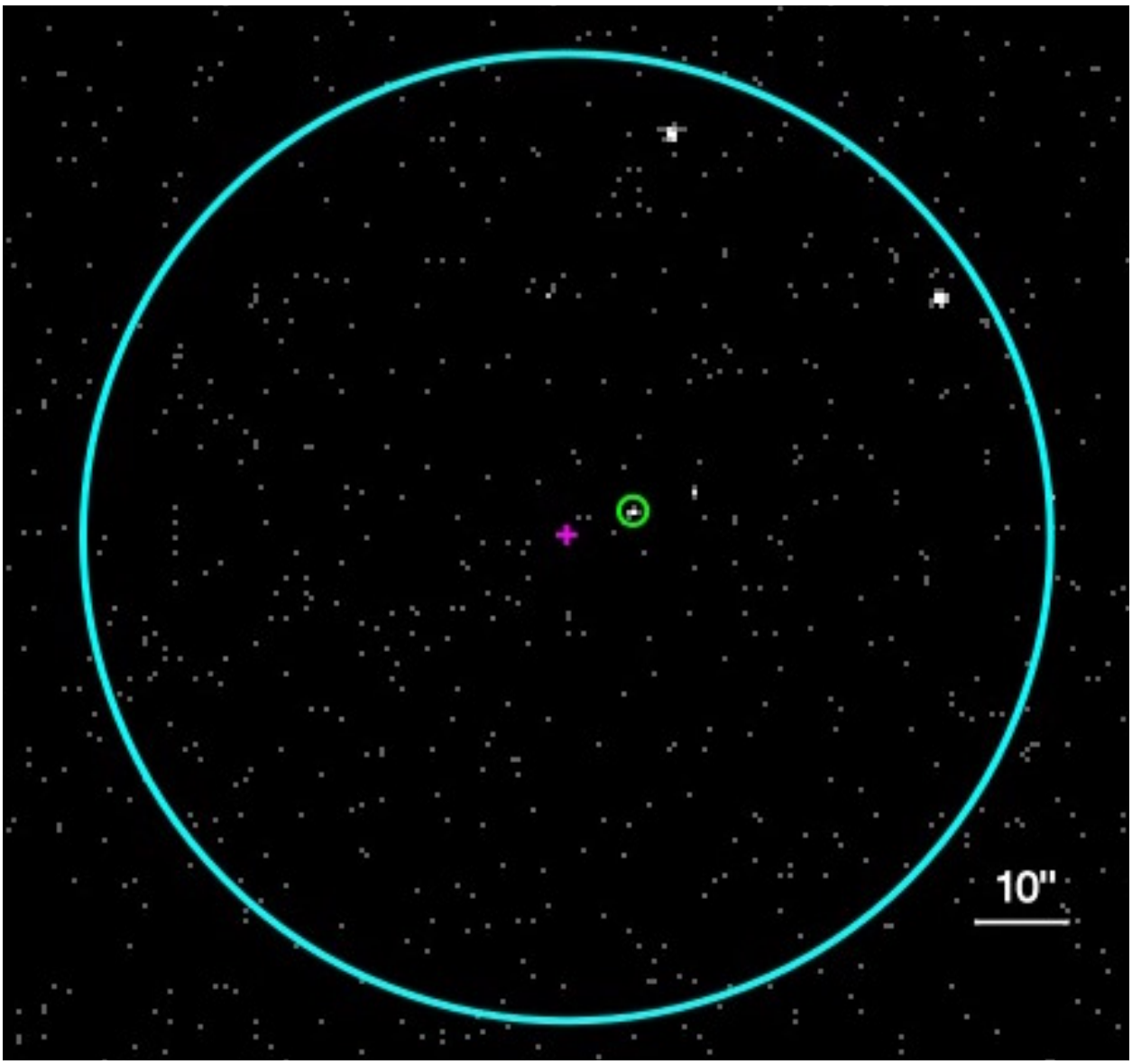

Figure 2.2 *Chandra*/ACIS-S X-ray image of the core of M10 (blue circle; radius $46.2'' \sim 1.0$ pc) in the 0.3 - 7.0 keV energy band. The magenta cross marks the cluster photometric center (Goldsbury et al. 2010). The X-ray source associated with M10-VLA1 is circled in green.

Table 2.2. Swift X-ray Constraints

Epoch Date	Epoch Date (MJD)	Effective time (s)	Luminosity limit (erg s^{-1})
Oct 30, 2009	55117.81375	1928	$< 4.7 \times 10^{31}$
Feb 21, 2014	56709.72004	1071	$< 5.3 \times 10^{31}$
Oct 21, 2014	56951.26891	402	$< 1.6 \times 10^{32}$
Jan 20, 2015	57042.62936	465	$< 1.3 \times 10^{32}$
Oct 20, 2015	57315.31564	787	$< 7.7 \times 10^{31}$
Jan 20, 2016	57407.33950	1631	$< 5.6 \times 10^{31}$
Jan 21, 2016	57408.13957	989	$< 1.3 \times 10^{32}$
Combined		7272	$< 2.2 \times 10^{31}$

Note. — All limits are at the 95% level and over the energy range 0.5–10 keV. Luminosities assume a distance of 4.4 kpc.

2.2.2.2 Swift

There are several *Swift*/XRT observations of M10, including one taken essentially simultaneously (within one day) of the initial radio observations reported in §2.1. These X-ray observations are detailed in Table 2. M10-VLA1 is not detected in any of these observations. To determine flux upper limits, we assumed the best-fit parameters from the *Chandra* observations, using an extraction radius of $25''$ to reduce the chance of contamination from the nearby X-ray sources. These background-subtracted upper limits are at the 95% confidence level and assume an energy range of 0.5–10 keV. Table 2 also contains a stacked upper limit from a combination of all the *Swift* observations.

The individual epoch upper limits are all in the range of $<$ (5–16) $\times 10^{31}$ erg s^{-1}, and the stacked upper limit is $< 2.2 \times 10^{31}$ erg s^{-1}, hence consistent with the *Chandra* flux value.

2.2.3 Optical Photometry

Hubble Space Telescope/Advanced Camera for Surveys (ACS) photometry for M10 in $F606W$ and $F814W$ has already been published as part of the ACS survey of Galactic globular clusters (Sarajedini et al. 2007; Anderson et al. 2008). We corrected the astrometry of these images using a large number of *Gaia* stars (Gaia collaboration et al. 2016), finding an rms of about $0.02''$ per coordinate. The closest optical source to M10-VLA1 is located $0.116''$ from the radio source, consistent within the combined positional uncertainties of the radio and optical sources. The unusual optical properties of this source (see below) confirm its identity as the optical counterpart to M10-VLA1.

Figure 4 shows the position of the source in a color-magnitude diagram (CMD) of M10. Here the plotted stars are restricted to a radius of $15''$ around M10-VLA1 to reduce the effects of differential reddening on the distribution of stars in the CMD (we note all photometry listed is as observed, not corrected for the substantial foreground reddening ($E(B-V) =$ 0.25–0.28)). The optical counterpart to M10-VLA1 has $F606W = 17.238 \pm 0.005$ and $F606W$-$F814W = 1.036 \pm 0.009$ mag on the VEGAMAG system. It sits ~ 0.19 mag redward in $F606W - F814W$ of the lower giant branch members of M10 of the same $F606W$ mag. The unusual color would normally lead to the conclusion that the star is not a cluster member. However, the spectroscopic observations (Section 2.2.4) show the star has a radial velocity consistent with the cluster systemic velocity, and it is located only 0.2 pc in projection from the center of M10. Hence we conclude that the star is indeed a member of the cluster but with an unexpectedly low effective temperature for its luminosity. The nomenclature of these stars is somewhat confusing, and we follow the recent suggestion of Geller et al. (2017) that such stars, when brighter than the subgiant branch, be referred to

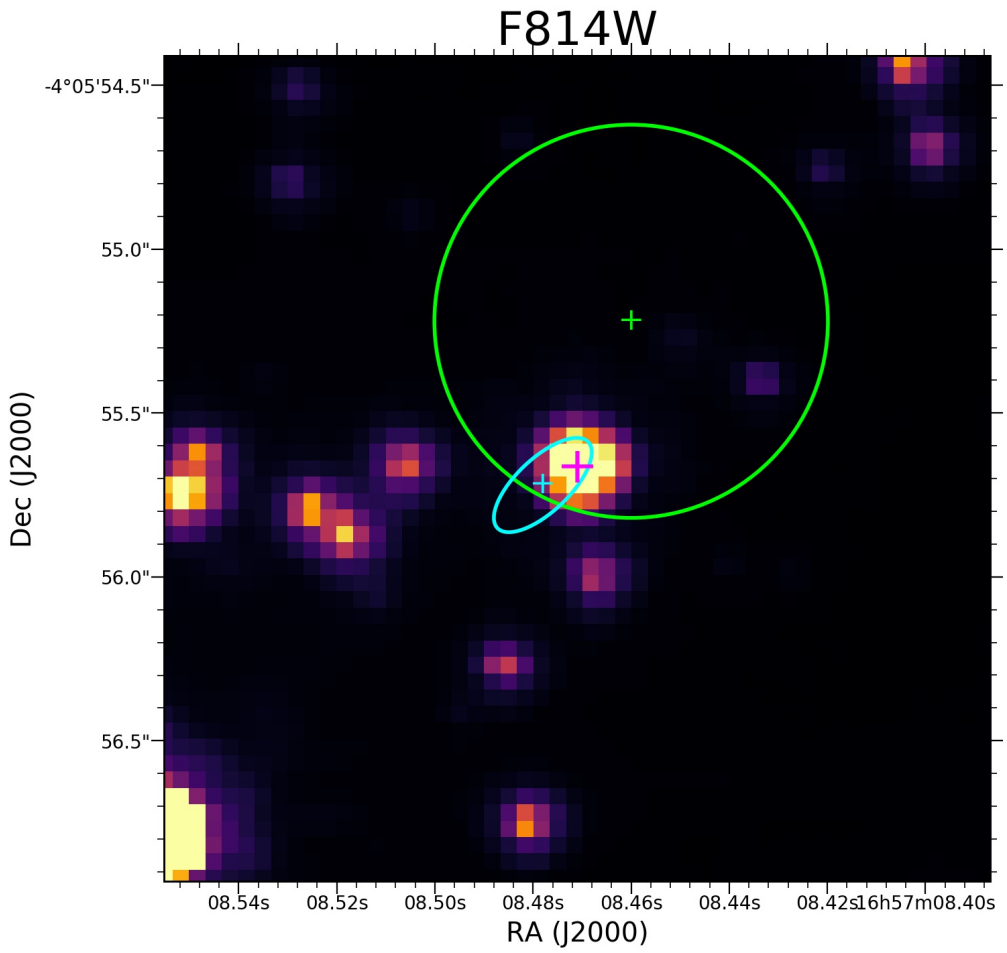

Figure 2.3 *HST F*814*W* image of the optical counterpart to M10-VLA1 with the detection positions of the *Chandra* observation and 20 Feb 2014 VLA observation overlaid. The optical counterpart is marked by the magenta cross. The VLA position and associated positional error is shown by the blue cross and blue ellipse. The *Chandra* position is shown by the green cross, with the green circle representing the *Chandra* astrometric accuracy.

as "red stragglers"; the term "sub-subgiants" is reserved for systems fainter than normal subgiants.

Using the solar-scaled MIST isochrones (Dotter 2016; Choi et al. 2016) for $[Z/\mathrm{H}] = -1.2$, an age of 12 Gyr, and assumed $E(B-V) = 0.28$, giants with $F606W - F814W$ matching that observed for M10-VLA1 have $T_{eff} \sim 4800$ K (of course, these giants are much more luminous than M10-VLA1). The bolometric luminosity inferred from the temperature and the $F814W$ magnitude is about $4.4 L_{\odot}$. While these ACS data were obtained on 2006 Mar 5, the ground-based SOAR telescope photometry of Salinas et al. (2016), taken in July 2015, show a qualitatively similar location of the star in a $g-i$ vs. i CMD (Figure 5). This implies the location of M10-VLA1 in the ACS CMD is not a fluke, but is persistent over timescales of years. The star's short-term variability is poorly constrained: the SOAR photometry covered about 6.7 hr, over which the star became ~ 0.01 mag fainter in i, but these data cover only a tiny fraction of the 80 hr orbital period (see §2.2.4).

Additional HST/WFC3 imaging in $F275W$, $F336W$, and $F438W$ was obtained on 2013 Aug 16 and 2014 May 27 with Wide Field Camera 3 (WFC3). The time-averaged photometry at these bands is available from the catalogs of Soto et al. (2017), which represent preliminary measurements from the *HST* Treasury program of Piotto et al. (2015). These values are $F275W = 20.80 \pm 0.18$, $F336W = 19.09 \pm 0.14$, and $F438W = 18.80 \pm 0.09$. As the uncertainties in these measurements are substantially larger than for other stars of this brightness, we individually photometered the two epochs to search for variability. We found that the source brightened by -0.21 ± 0.03 mag in $F275W$, -0.16 ± 0.03 mag in $F336W$, and -0.23 ± 0.02 mag in $F438W$ between the two epochs.

Given this evidence for variability, we cannot combine the data for these bluer bands with the $F606W$ and $F814W$ data to model the spectral energy distribution. CMDs made

with the bluer filters confirm that the star is an outlier, sitting far redward of the main locus of stars in any pair of filters, consistent with the unusual $F606W$-$F814W$ color. If we use the same MIST isochrones discussed above to infer the T_{eff} from $F275W$–$F438W$ or $F336W$–$F438W$, we find $T_{eff} \sim 5100$ K for both, warmer than found for the $F606W$-$F814W$ color. This difference could be due to a real change in the disk-averaged T_{eff} (e.g., from starspots) or due to a varying contribution from a warmer component, such as an accretion disk. Future simultaneous photometry over a broad baseline could allow one to better constrain the presence of a hot companion or a disk.

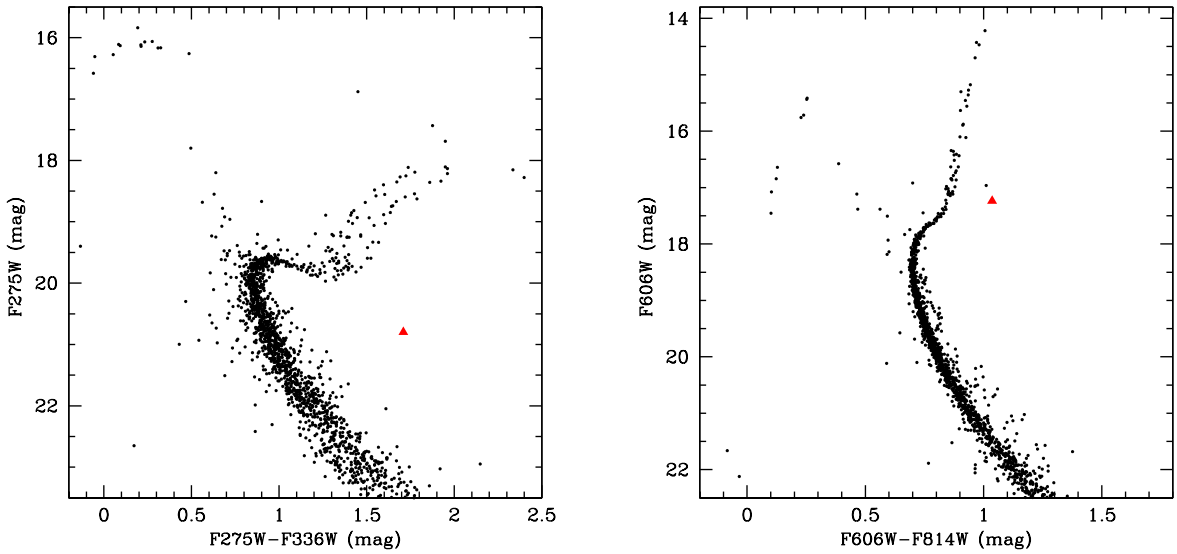

Figure 2.4 *HST* color-magnitude diagrams in $F275W$ vs. $F275W - F336W$ (top) and $F606W$ vs. $F606W - F814W$ (bottom) of the stars within $15''$ of M10-VLA1. The optical counterpart to M10-VLA1 is shown with the red triangle.

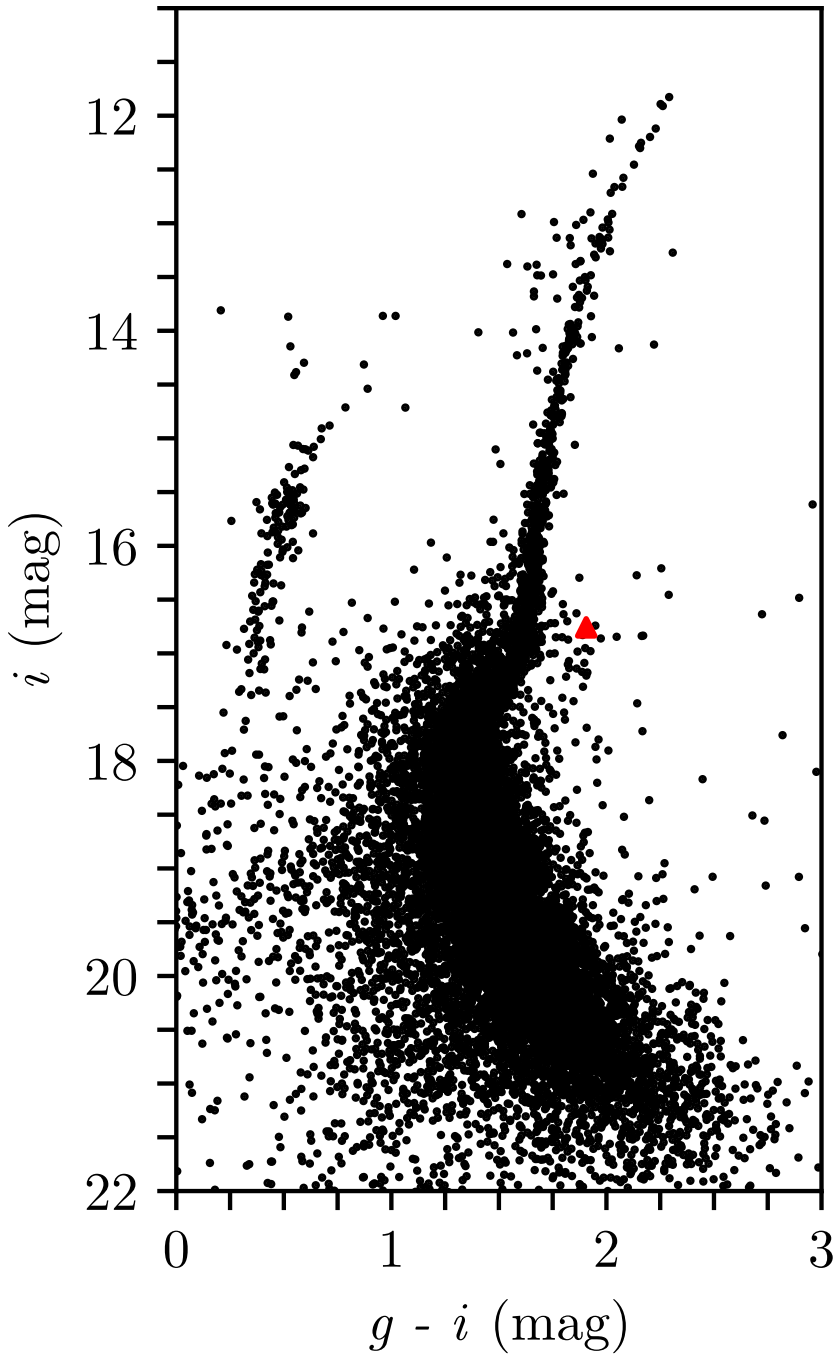

Figure 2.5 *SOAR* color-magnitude diagram in i vs. $g-i$ of M10, observed ∼9 years after the *HST* photometry presented in Figure 3. The optical counterpart to M10-VLA1 is shown with the red triangle. The similarity to its location in the Figure 3 CMD shows that its unusual color is persistent over long timescales and is not due to variability.

2.2.4 Optical Spectroscopy

We initiated spectroscopy of the optical counterpart to M10-VLA1 in 2015, using the Goodman spectrograph on the SOAR 4.1-m telescope (Clemens et al. 2004). All observations were made with a $0.95''$ slit, but used several different gratings: some with a 1200 l mm^{-1} grating (resolution 1.7 Å; range 5380–6640 Å, for studying Hα), and radial velocity measurements with a 2100 l mm^{-1} grating (resolution 0.9 Å; range 5020–5660 Å) or a 2400 l mm^{-1} grating (resolution 0.7 Å; range 5080–5610 Å). Typical individual exposure times were 900 sec each, with two spectra generally taken back-to-back on a particular night. Spectra were reduced and wavelength calibrated with a FeAr arc lamp using standard routines in IRAF. The spectra covering Hα show clear Hα emission (Figure 7), indicative of binary interaction, providing additional evidence that this object is the counterpart to the radio source.

We determined radial velocities through cross-correlation over the region 5150–5300 Å with spectral templates of similar spectral type taken with the same setup. Given the long period of the system (see below), we used a weighted average of the radial velocities for the consecutive 900-sec spectra to represent each epoch of data. The barycentric radial velocities are listed in Table 3. The corresponding observation times are given as Barycentric Julian Dates on the TDB system (Eastman et al. 2010).

2.3 Binary Properties and Analysis

2.3.1 Orbital Parameters

Using the custom Keplerian sampler *TheJoker*[3] (Price-Whelan et al. 2017), we initially fit a circular model to the 20 radial velocity epochs. The posterior distributions for the fitted parameters were all unimodal and close to Gaussian, with median values: period $P = 3.3391 \pm 0.0010$ d, systemic velocity $v_{sys} = 86.3 \pm 1.1$ km s^{-1}, semi-amplitude $K_2 = 12.5 \pm 1.5$ km s^{-1}, and the ascending node of the compact object $T_0 = 2457169.1292 \pm 0.0846$ d. A fit with these values is plotted in Figure 6. The residuals around the best orbital fit have an rms dispersion of 3.9 km s^{-1}.

For an eccentric model, the posterior distribution of the eccentricity is very broad, strongly disfavoring only high eccentricities > 0.4. As expected, allowing an eccentric fit slightly improves the model, with a small reduction of the rms from 3.9 to 3.7 km s^{-1} for eccentricities in the range ~ 0.1–0.2. These fits still yield periods and semi-amplitudes very similar to the circular case and hence do not affect any of our scientific conclusions. A modest eccentricity is possible, but given the long period and low semi-amplitude, it is not well-constrained with the current set of observations, and we restrict our discussion to the circular case.

The systemic velocity is somewhat surprising: the velocity of M10 itself is 74 km s^{-1}, with a central velocity dispersion of about 5 km s^{-1} (Bellazzini et al. 2012; Carretta et al. 2009). Hence M10-VLA1 has a relative velocity close to escape velocity for the cluster. To investigate this possible velocity discrepancy, we used a Besançon Galactic model (Robin et al. 2003) to simulate the field star population in a square degree around M10. Of field

[3] https://github.com/adrn/thejoker/

stars with colors and magnitudes comparable to M10-VLA1, only about 1.3% had radial velocities as high as that inferred for the systematic velocity of M10-VLA1. Hence, given the radial velocity of this binary and its position very close to the center of M10, we conclude that it is much more likely to be a cluster member than an interloping field star. A future proper motion measurement with the *Hubble Space Telescope* or *Gaia* can confirm this definitively. It is possible that the binary had a recent encounter with another system and received a kick.

If mass transfer is occurring (§3.3), the multi-day period implies a low-density, evolved donor, as expected on the basis of the location of the star in the color-magnitude diagram (Figure 4).

2.3.2 Masses

The semi-amplitude and period together give the mass function $f(M)$

$$f(M) = \frac{PK_2^3}{2\pi G} = \frac{M_1 \left(\sin i\right)^3}{(1+q)^2} \tag{2.1}$$

where i is the inclination and q the mass ratio M_2/M_1. We find $f(M) = 6.7^{+2.7}_{-2.1} \times 10^{-4} M_\odot$ using the posterior samples from §3.1. There are two possible cases: first, if the visible star is indeed the donor, then the low $f(M)$ immediately implies that the system must be close to face-on.

To quantify this, we note that the donor mass M_2 must be in the range $0.3 M_\odot \lesssim M_2 \lesssim 0.8 M_\odot$. The upper limit of $0.8 M_\odot$ corresponds to the main sequence turnoff mass and $0.3 M_\odot$ corresponds to the mass of a heavily-stripped star that still appears to be a red giant in the color-magnitude diagram. As a comparison, the stripped optical companion to a millisecond

pulsar in NGC 6397 (COM J1740-5340) has a dynamical mass of $0.22M_\odot$ – $0.32M_\odot$ and a red color, but is fainter than the main sequence turnoff of the cluster (Ferraro et al. 2003; Mucciarelli et al. 2013). The red giant optical companion of M10-VLA1 is more luminous than this star, consistent with a comparable or higher mass than COM J1740-5340.

Given the value of $f(M)$, an assumed value of M_2 then gives a relationship between the primary mass M_1 and the inclination i. For the case where the visible star is the secondary, the maximum inclination would be at the extreme case where the primary is a low-mass He white dwarf or a main sequence star with a mass slightly above $\sim 0.3M_\odot$; in this case $i \sim 12^\circ$. For any less extreme set of assumptions, the inclination would be even lower. If the red straggler is the secondary, *M10-VLA1 must be essentially face-on.*

The alternative case is if the red straggler is the source of the X-ray and radio emission. It might still be the donor if accretion is occurring onto a $\sim 0.2M_\odot$ He white dwarf (see §4.4), or it could be the sole source of the X-ray and radio emission, due to chromospheric activity rather than mass transfer. Depending on the red straggler mass, in the former case we find $i = 16 - 26^\circ$, which is still relatively face-on. If no accretion is occurring and the secondary is not a compact object, a wide range of inclinations are allowed. For for a typical case with $M_1 = 0.8M_\odot$ and an inclination of $i = 60^\circ$, $M_2 \sim 0.09M_\odot$, near the border between brown dwarfs and the lowest-mass main sequence stars.

If the red straggler is the donor in the binary, an independent estimate of the mass is possible by assuming the star fills its Roche Lobe and using the optical photometry. From the orbital period, the density of the red straggler is ~ 0.017 g cm^{-3} (Eggleton 1983). Using the temperature and bolometric luminosity determined above, we find a donor mass of $0.34M_\odot$, which would be consistent with a scenario in the star was substantially stripped. However, we emphasize this mass estimate is strongly dependent on the assumptions that

Table 2.3. Barycentric Radial Velocities of M10-VLA1

BJD (d)	RV (km s^{-1})	Error (km s^{-1})
2457166.6664853	83.2	3.3
2457166.8171978	92.3	3.4
2457166.8458049	92.3	3.6
2457170.6829383	99.3	3.5
2457170.7138864	97.6	4.4
2457186.6184706	88.3	3.4
2457186.7838743	84.9	3.0
2457196.7163945	94.0	5.1
2457252.5998639	72.0	3.6
2457257.5697872	97.9	4.9
2457473.8156011	94.5	3.6
2457476.8085067	79.6	5.3
2457484.8487222	95.3	3.1
2457508.8464624	90.9	3.1
2457598.6466511	93.1	4.6
2457602.6214264	84.6	4.4
2457603.5856243	70.6	3.3
2457509.8408503	76.1	7.1

the red straggler is Roche lobe-filling and on the temperature and luminosity used.

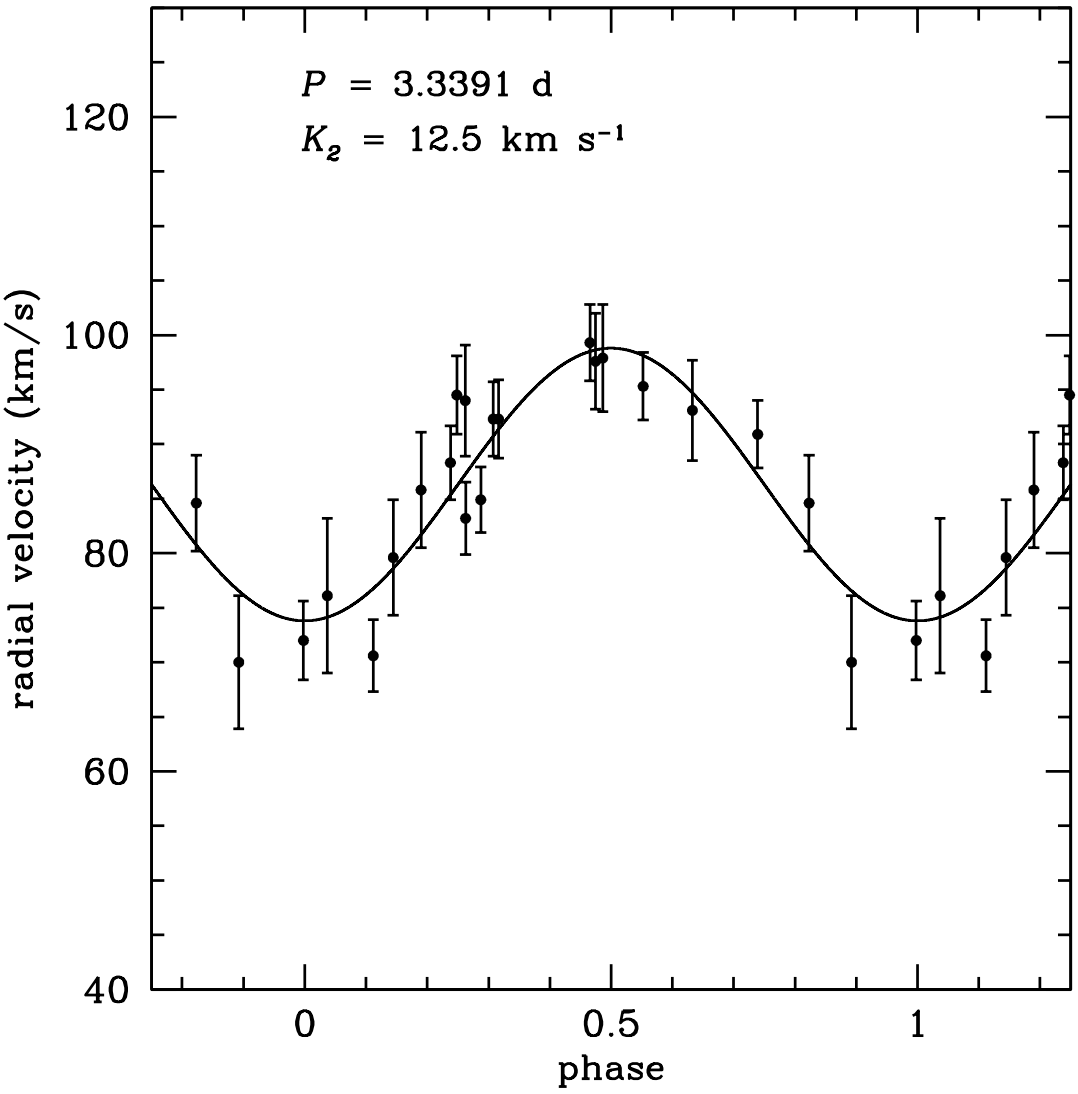

Figure 2.6 Radial velocity curve of the red straggler in M10-VLA1, with the best-fit circular Keplerian model overplotted.

Table 2.3 (cont'd)

BJD (d)	RV (km s^{-1})	Error (km s^{-1})
2457629.5657976	70.0	6.1
2457630.5586368	85.8	5.3

2.3.3 Optical Spectrum and Emission

The optical spectra of M10-VLA1 are consistent with a G-type star, with relatively modest metal lines, as would be expected for a star in M10 (with [Fe/H] ~ -1.5, Haynes et al. 2008). The most notable feature of the spectra is the presence of Hα in emission, which is observed at all six epochs (spanning 16 months) for which spectra covering this region were obtained. By fitting a Gaussian convolved with the instrumental resolution (79 km s^{-1}) to rectified spectra in this region, we find that the mean full-width at half-maximum (FWHM) of the Hα line is 180 ± 25 km s^{-1} (with the uncertainty representing the standard error of the mean).

In some of the Hα spectra, the line appears double-peaked rather than simply broadened, though this is challenging to confirm in individual exposures given the modest width of the line. In Figure 7 we show an average spectrum of six 15-min exposures taken on 2015 May 15, which represents the highest signal-to-noise spectrum of the region. Here the double-peaked nature of the line is obvious. Fitting a single Gaussian model as above yields a FWHM wider than the mean value (243 ± 19 km s^{-1}). We also fit a double-Gaussian model, yielding a velocity difference of the two emission peaks of 147 ± 11 km s^{-1}.

Given the modest Hα velocities and that these values are not orbital averages, we do not wish to over-interpret them. Instead we simply remark that the ratio of the peak separation

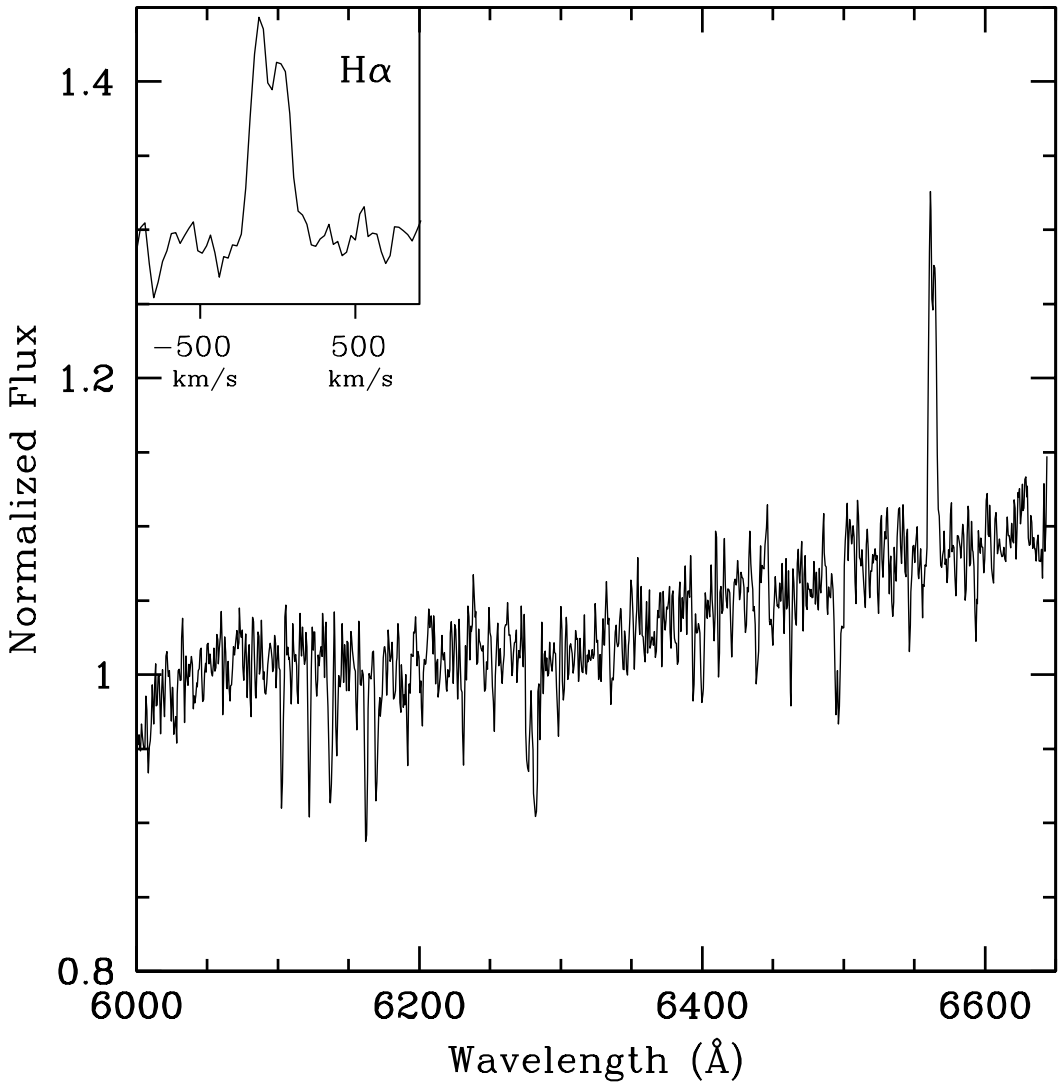

Figure 2.7 Radial velocity curve of the red straggler in M10-VLA1, taken on 2015 May 15, over the wavelength range 6000 to 6650 Å. The inset panel shows a zoom-in on Hα, where the double-peaked nature of the line is obvious.

to the FWHM is 0.60 ± 0.06, exactly the value observed for typical accretion disks around compact objects (e.g., Casares 2015; Casares 2016). Therefore these observations provide evidence that an accretion disk could be present in M10-VLA1.

2.4 Discussion

The X-ray and radio emission and optical photometry and spectroscopy all point to the identification of M10-VLA1 as an interacting binary in the globular cluster M10. While we have observed a red straggler star as one member of this system, the nature of its companion is not clear. We discuss the options in turn.

2.4.1 Black Hole

There are several pieces of observational evidence that suggest a black hole origin for M10-VLA1. First, its ratio of radio to X-ray luminosity puts M10-VLA1 within the scatter of the L_X–L_R correlation for quiescent black hole systems (Figure 8; Gallo et al. 2014). The radio continuum spectral index is $\alpha = 1.3 \pm 0.9$, poorly constrained but consistent with the flat-to-inverted value expected for self-absorbed synchrotron emission from a compact jet, as observed for low-luminosity accreting black holes (e.g., Gallo et al. 2005). We must add that the radio and X-ray observations of M10-VLA1 were not obtained simultaneously, and interpret its position on the L_X–L_R diagram cautiously. The Feb 20 2014 VLA observed radio luminosity is shown with both the *Chandra* X-ray detection from May 08 2015 as well as the almost simultaneous Feb 21 2014 *Swift* observation upper limit in Figure 8. Both points lie above the L_X–L_R relation, with the Feb 2014 datapoint somewhat closer the the parameter space occupied by accreting neutron star systems. We also remind the reader that

the source is variable in the radio, and multiple simultaneous X-ray and radio observations are needed in the future to determine its relationship with the L_X–L_R relation with more certainty.

Another line of argument uses the X-ray luminosity and orbital period of the system. M10-VLA1 has a low X-ray luminosity of $\sim 10^{31}$ erg s^{-1}. In the context of an X-ray binary, the X-ray luminosity is determined by the accretion rate and radiative efficiency of the accretion flow. For an evolved Roche lobe-filling donor, the mass loss rate is thought to be set by the nuclear evolution of the star. The physical mechanism that determines the quiescent radiative efficiency is not well-understood, but it has been argued that black hole binaries typically have lower X-ray luminosities than neutron star X-ray binaries at the same orbital periods (and thus accretion rates), perhaps because accretion luminosity can be advected across the event horizon in a black hole (Garcia et al. 2001). It has also been suggested that black holes simply transfer more energy to jets rather than into the area of the hot accretion disk as hard X-rays (Fender et al. 2003).

Using the Reynolds & Miller (2011) relation for X-ray luminosity vs. orbital period for quiescent black holes and neutron stars, M10-VLA1, with an orbital period of 3.339 d, has properties much more consistent with a black hole than a neutron star: a typical neutron star with this period should have $L_X \gtrsim 5\times10^{32}$ erg s^{-1}. It is worth noting that some sources "disobey" this relation: e.g., GS 1354-64, which is much more X-ray luminous than other black holes with comparable orbital periods (Reynolds & Miller 2011). This is unsurprising given the tenuous physical basis for understanding the radiative efficiency in these systems. Nonetheless, it is still true that the X-ray luminosity of M10-VLA1 would be remarkably low for an accreting neutron star.

Circumstantial evidence for a black hole primary is the possible presence of an accre-

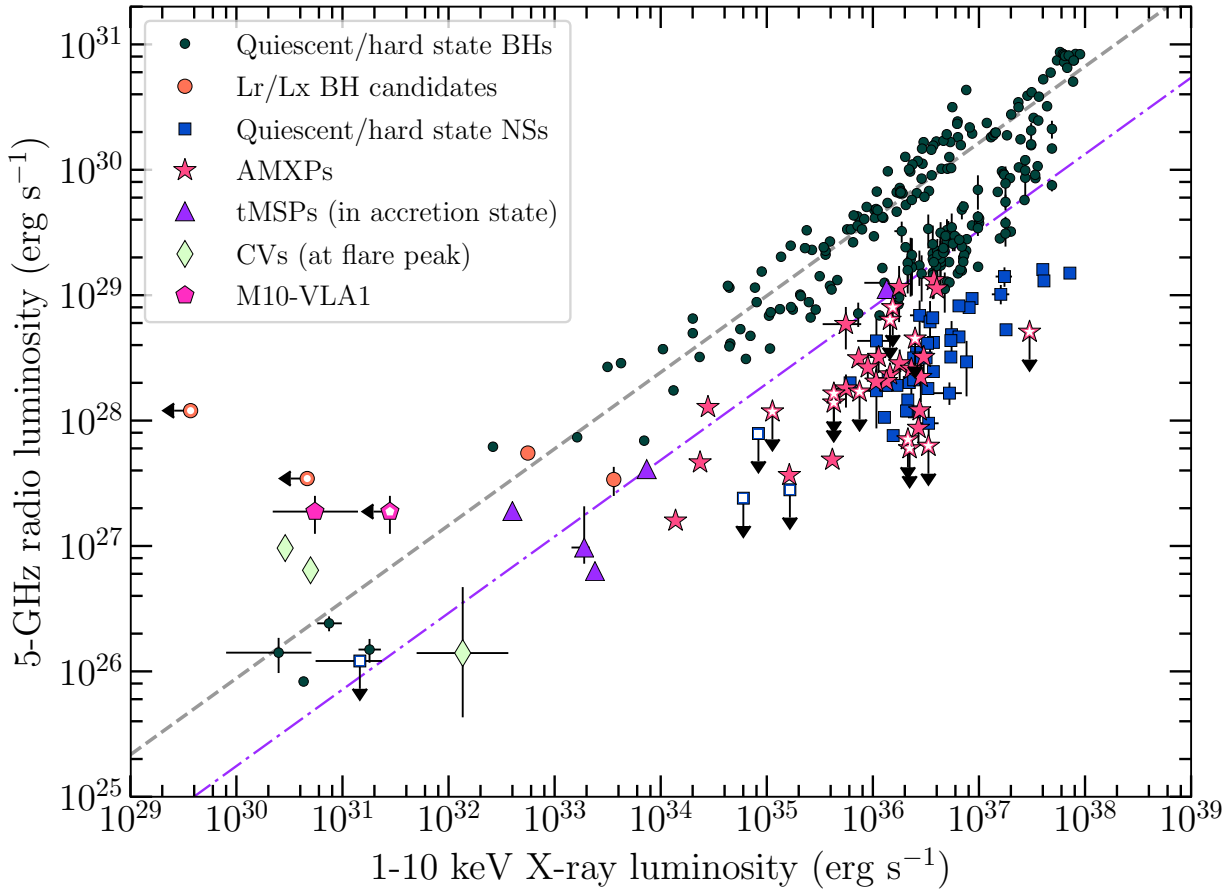

Figure 2.8 The radio/X-ray correlation for accreting compact objects, showing that M10-VLA1 has properties consistent with a quiescent stellar-mass black hole. Hollow points indicate an upper limit. Two magenta pentagons are shown for M10-VLA1, both using the radio luminosity of the 20 Feb 2014 VLA observation with the *Chandra* X-ray detection on 08 May 2015 and *Swift* upper limit of 21 Feb 2014.The dark green circles show known quiescent black holes in the field (Miller-Jones et al. 2011; Gallo, Miller & Fender 2012; Ratti et al. 2012; Corbel et al. 2013; Rushton et al. 2016; Plotkin et al. 2017). The dotted black line shows the best-fitting L_R–L_X correlation for black holes from Gallo et al. (2014). Orange circles are radio-selected black hole candidates, (Strader et al. 2012; Chomiuk et al. 2013; Miller-Jones et al. 2015; Tetarenko et al. 2016b; Bahramian et al. 2017). The purple triangles are transitional millisecond pulsars (Hill et al. 2011; Papitto et al. 2013; Deller et al. 2015; Bogdanov et al. 2017) and the dotted purple line shows their proposed L_R–L_X track. Blue squares are NSs in the hard state, and pink stars are accretion-powered millisecond X-ray pulsars (Migliari & Fender 2006; Tudor et al. 2017). The light green diamonds are the bright CVs AE Aqr ($L_X = 5.0 \times 10^{30}$ erg s^{-1}), SS Cyg (in outburst; $L_X = 1.4 \times 10^{32}$ erg s^{-1}; Russell et al. 2016), and white dwarf "pulsar" AR Sco ($L_X = 2.9 \times 10^{30}$ erg s^{-1}; Marsh et al. 2016). Figure adapted from Bahramian et al (2017).

tion disk in the system, as suggested by the unusual donor (consistent with mass transfer), double-peaked Hα emission and UV/optical variability. An accretion disk suggests a compact primary, and as this and the other subsections show, in this case the radio and X-ray emission strongly favor a black hole.

The counterargument is straightforward: if the primary is a black hole, the inclination must be very low. Even in the extreme case of a $3M_\odot$ black hole, $i = 3.9 \pm 0.5^\circ$. If we instead assume a uniform distribution of black hole masses between 3 and 15 $M_\odot$, we find $i = (2.5^{+0.7}_{-0.4})^\circ$. Such a low inclination is unlikely to occur by chance (~ 0.1 % chance), and in Sec. 4.5 we discuss the possibility that face-on systems would be preferentially observed.

One fact not strongly on either side is the variability of the radio source. There is substantial evidence that the flat-spectrum radio emission from compact jets from neutron stars and black holes is variable on a range of timescales (we discuss white dwarfs below in Sec. 3.3). For example, Miller-Jones et al. (2008) show that the stellar-mass black hole V404 Cyg has factor of ~ 3 variations in its quiescent 8.4 GHz radio continuum flux density on timescales of < 1 hr, an observation borne out by a much larger sample of VLA data obtained over decades (R. Plotkin et al. 2018, in preparation). Similar variability persists on longer timescales; the low-luminosity black hole X-ray binary A0620-00 has been seen to vary by a factor of $\sim$2.5 between 2005 and 2013 in quiescence (Dinçer et al. 2017).

Finally, we note that Ivanova et al. (2017) have recently proposed that red straggler companions (like that of M10-VLA1) are expected for some stellar-mass BHs in globular clusters. The binary is formed in a glancing tidal capture between a BH and a subgiant star, and the interaction strips a few $\times 0.1 M_\odot$ off the subgiant. As the donor evolves, it may spend 0.5–1 Gyr in the red straggler portion of the color-magnitude diagram. The long timespan that stars spend as subgiants and their enhanced cross-sections as they swell favor

such interactions for subgiants above that of main sequence stars or normal giants (Ivanova et al. 2017). This scenario is consistent with the location of M10-VLA1 near the cluster center, at a projected radius of only 0.2 core radii.

2.4.2 RS CVn

RS CVn systems are detached binary systems with an evolved primary (typically a F/G subgiant or a K giant) and a non-degenerate secondary. Generally the secondary is of similar mass (Gunn 1996), though here we also consider systems with a wider range of mass ratios. The evolved star shows enhanced chromospheric activity, resulting in variability at a wide range of wavelengths. Relevant for M10-VLA1, RS CVn stars show increased radio and X-ray luminosity compared to similar stars without binary companions (Montesinos et al. 1988; Gunn 1996). The orbital periods of RS CVn systems are typically between 2 and 14 days, and shorter period systems are more active due to enhanced tidal synchronization. Activity in RS CVn stars is manifested in flares, lasting minutes to hours, with order-of-magnitude increases in the X-ray, UV, and radio luminosities (Osten et al. 2000).

RS CVns show non-thermal radio emission associated with the enhanced magnetic field of the rapidly rotating evolved star (Osten et al. 2000; García-Sánchez et al. 2003). At cm wavelengths, the spectral luminosity typically ranges from 10^{23}–10^{26} erg s^{-1} GHz^{-1} (Morris & Mutel 1988; Drake, Simon & Linsky 1989, 1992), and extreme flaring events may reach 10^{27} erg s^{-1} GHz^{-1} (Mutel et al. 1987). The spectral indices of these systems are typically between –1 and 1, with quiescent radio emission flat to steep ($\alpha \lesssim 0$), tending toward inverted ($\alpha \sim 1$) during luminous flares (Gibson et al. 1975; Owen & Gibson 1978; Mutel et al. 1987). Quiescent radio emission from RS CVn systems shows moderate circular polarization at frequencies above 5 GHz, but less than 3% during flares. Flares also produce

X-ray emission, with typical luminosities of $L_X \sim 10^{29}$–10^{32} erg s^{-1}. The X-ray and radio emission during flares is correlated (Osten et al. 2000). Standard chromospheric emission lines (Ca H+K; Balmer lines) are commonly observed.

These systems have several overlapping characteristics with those of M10-VLA1. The X-ray luminosity of M10-VLA1 is well within the range of known X-ray luminosities of RS CVn binaries, and the optical counterpart is evolved, as expected for an RS CVn system. The radio spectral luminosity of M10-VLA is at the upper edge of those observed for RS CVn systems in flares, though the low flux density means that any polarization constraints are not useful.

The aspects of the system less consistent with standard RS CVn binaries are the low mass of the secondary for reasonable inclinations and the tentative evidence for an accretion disk (double-peaked Hα). Double-peaked Hα has been exceptionally observed in RS CVn systems, e.g., in SZ Pis (Bopp 1981), where it was attributed to circumstellar material ejected in transient mass transfer events. Unusually for RS CVn stars, the subgiant in SZ Pis nearly fills its Roche lobe. This suggests that if the origin of the Hα is similar in M10-VLA1, then it is also likely to be close to Roche lobe-filling. The analysis in §3.2 would then imply that the subgiant in M10-VLA1 is likely to be a stripped, low-mass star.

We note that the X-ray luminosity and orbital period of M10-VLA1 are consistent with those of some binaries containing sub-subgiant or red straggler primaries (Geller et al. 2017), though such systems do not typically have evidence for accretion, and their radio continuum properties are unknown. At least some sub-subgiants are found in compact binaries (e.g., Mucciarelli et al. 2013).

2.4.3 Neutron Star

Compact binaries with neutron star primaries are frequently identified in globular clusters. Many of these neutron stars are millisecond radio pulsars spun up by accretion in a dynamically-formed binary, but for which the accretion has temporarily or permanently ceased. The flat to inverted spectrum radio continuum emission and evidence for an accretion disk from M10-VLA1 are unlike the steep spectrum radio emission and lack of accretion observed for normal millisecond pulsars (e.g., Kramer et al. 1999).

As mentioned above in Sec. 4.1, M10-VLA1 does not have properties consistent with being an actively accreting neutron star X-ray binary: its X-ray luminosity is at least a factor of ~ 40 lower than expected for an accreting neutron star at its orbital period, and it is much more radio bright than would be expected (Figure 8). Indeed, the only class of neutron stars with detected flat-spectrum radio emission at X-ray luminosities $< 10^{34}$ erg s^{-1} are the transitional millisecond pulsars that switch between accretion-powered disk states and rotation-powered pulsar states on timescales of days to years (Archibald et al. 2009; Bond et al. 2002; Hill et al. 2011; Papitto et al. 2013; Bassa et al. 2014; Deller et al. 2015). During their disk state, transitional millisecond pulsars emit flat spectrum radio emission, which is typically interpreted as compact radio jets. They may also show double peaked Hα emission originating from an accretion disk.

While our radio detection was not simultaneous with the *Chandra* X-ray detection, we can constrain this scenario through the quasi-simultaneous *Swift* observations, which limit an X-ray source at this position to $< 5.2 \times 10^{31}$ erg s^{-1} (0.5–10 keV). This is a factor of 10 below the X-ray luminosities observed for transitional millisecond pulsars in even their "low mode" disk states (de Martino et al. 2013; Patruno et al. 2014; Bogdanov et al. 2017). In

fact, the seven *Swift* observations all have flux limits at least a factor of 5 below the typical 2×10^{33} erg s^{-1} X-ray luminosity observed for accreting transitional millisecond pulsars (a mixture of the "low" and "high" modes), and some *Swift* observations are much deeper.

The ratio of radio to X-ray flux of M10-VLA1 is also dissimilar to the average values for known transitional millisecond pulsars. Bogdanov et al. (2017) show that the transitional PSR J1023+0023 shows anti-correlated radio and X-ray variability in the disk state, including periods in which the system can enter the parameter space in L_X–L_R occupied by accreting black holes. However, the *Swift* upper limit for M10-VLA1 is still about a magnitude fainter than would be expected for a transitional millisecond pulsar in the low mode disk state at the observed radio luminosity. M10-VLA1 also lacks the short-term (< 2 hours) radio variability observed in the PSR J1023+0023 disk state.

Overall, the radio and X-ray evidence suggests that M10-VLA1 does not have properties similar to known transitional millisecond pulsars in their disk states, though we cannot definitely rule out the possibility that we are observing such a system in an "sub-subluminous" disk state not yet observed among the confirmed transitional millisecond pulsars.

Considering the dynamical evidence, if we assume a neutron star in the mass range 1.4–2.0 $M_\odot$, the inclination inferred is $i = 5.1 \pm 0.7^\circ$. Hence this scenario has the same drawback as the black hole case (an unlikely face-on inclination) and the additional issue that the properties of M10-VLA1 are inconsistent with those of known low-mass X-ray binaries containing neutron stars. Hence a neutron star primary is disfavored, though not ruled out.

2.4.4 White Dwarf

Here we discuss a number of possibilities in which the red straggler is in a binary with a white dwarf.

2.4.4.1 Flare from Accreting White Dwarf

Miller-Jones et al. (2015) have exhaustively catalogued evidence for bright radio flares among accreting white dwarfs in the context of interpreting the stellar-mass black hole candidate X9 in the globular cluster 47 Tuc, and we do not repeat their discussion here. In brief, while accreting white dwarfs do emit variable radio continuum emission, this emission is generally 1–4 orders of magnitude fainter than observed for M10-VLA1 (e.g., Coppejans et al. 2015, 2016). A few well-studied intermediate polars (AE Aqr, DQ Her) occasionally emit bright flares, but these are still typically less luminous than M10-VLA1 or decay on short ($<$ hr) timescales (Bastian et al. 1988; Abada-Simon et al. 1993; Pavelin et al. 1994). A bright, very brief ($<$ 20 min) 15 GHz flare was observed from the dwarf nova SS Cyg (Mooley et al. 2017), which would have a scaled flux density of 10–13 μJy at the distance of M10.

As discussed in §3.2, a white dwarf accretor also does not easily explain the low semi-amplitude of the binary. The most favorable case would be if the white dwarf is a low-mass $\sim 0.2 M_{\odot}$ He white dwarf formed through mass transfer during the evolution of the initially more massive star, and we are now witnessing the evolution of the initially less massive (but now more massive) star. The evolving red straggler would likely be more massive than the white dwarf, so by standard criteria stable mass transfer is unlikely. Some recent theoretical work suggests a wider range of mass ratios might allow stable mass transfer from giants (Pavlovskii & Ivanova 2015), which could allow accretion onto a low-mass white dwarf.

Nonetheless, even if we take their most extreme case of a donor to accretor mass ratio

of 2.2, a relatively face-on inclination of $i \lesssim 19^\circ$ is still required, and this source would still be the most radio-loud accreting white dwarf known. In addition, while we do observe optical/UV variability from the system, there is no strong evidence for a substantial UV excess indicative of a hot disk, though the *Swift*/UVOT absolute UV limit on an outburst at the time of the radio detection ($UVW2_0 > 2.9$) is not strong. As a comparison, the variable, long-period accreting white dwarf AKO 9 in the globular cluster 47 Tuc has an inferred $UVW2_0 \sim 3.8$–4.3 (Edmonds et al. 2003; Knigge et al. 2003).

2.4.4.2 A White Dwarf "Pulsar"

The white dwarf binary AR Sco was previously classified as an intermediate polar, but has has recently been shown to emit bright, pulsed radio continuum radiation, and it may represent the first member of a separate class of "white dwarf pulsars". The radio emission appears to originate in an interaction between a close magnetic white dwarf–M dwarf binary rather than primarily from accretion. AR Sco has a 0.15 d period (Marsh et al. 2016; Buckley et al. 2016), quite unlike the long 3.339 d period of M10-VLA1. If the radio emission in M10-VLA1 is not associated with accretion, the double-peaked Hα line is difficult to explain, and this scenario has the same requirement of a face-on inclination as a normal accreting white dwarf. Therefore, it seems reasonable to argue that this scenario is disfavored, but a stronger statement would require a better understanding of the white dwarf pulsar mechanism. It is worth pointing out that AR Sco is very nearby (116 pc; Marsh et al. 2016) and so white dwarf pulsars might well be common.

2.4.4.3 An Ionized Red Straggler Wind

A third scenario posits an enhanced wind from the red straggler, such as for a symbiotic system, with the X-rays produced by accretion and the radio emission due to thermal radiation from the ionized wind. The X-ray luminosity suggests an accretion rate of $\sim 10^{-10} - 10^{-11} M_{\odot}$ yr^{-1} (assuming a boundary layer on a 0.2 M$_{\odot}$ white dwarf; Kuulkers et al. 2006). Assuming the radio emission is from an ionized wind with a velocity of 100 km s^{-1}, this mass loss rate would be undetectable in the radio (Panagia & Felli 1975); a much higher mass loss rate of $\sim 10^{-8} M_{\odot}$ yr^{-1} would be necessary to produce a thermal radio source with $\sim 10\mu$Jy. Such a mass loss rate is much higher than observed for metal-poor giants of this luminosity (Dupree et al. 2009). The natural expectation is that this thermal emission would also not be variable; significant variation in the ionizing source would be necessary to produce the time-variable radio emission observed. Hence we believe this scenario is unlikely.

2.4.4.4 The Red Straggler Alone

A final option is that, if the white dwarf is *not* accreting, the X-ray and radio emission could be associated entirely with the rapidly rotating red straggler, as for the RS CVn scenario. As discussed in §3.2, the inclination requirements for this scenario are less extreme than for more massive white dwarfs, neutron stars, or black holes, but a face-on inclination with $i \lesssim 26^{\circ}$ is still necessary.

2.4.5 A Face-On Binary: Relativistic Beaming?

If the faint companion in M10-VLA1 is a compact object, the binary's radial velocity curve implies that it must be relatively face-on. Face-on inclinations are a priori unlikely. For example, given a random distribution of orientations in $\cos(i)$, the value $i < 11.1^\circ$ (as implied for a compact object primary) would occur by chance only 1.9% of the time. This leads us to consider whether any selection biases might exist for radio or X-ray emission in favor of face-on systems. Tentative evidence for a similar bias toward face-on low-mass X-ray binaries has been observed at γ-ray wavelengths in systems with lower X-ray luminosities (Britt et al. 2017), including the candidate transitional millisecond pulsar 3FGL J1544.6–1125, which has an inferred inclination of 5–8°.

There are a limited number of physical mechanisms that would lead to a bias for face-on systems. Perhaps the most promising candidate is relativistic beaming of the radio emission. The X-ray emission might also be beamed depending on its origin.

For $\beta = v/c$, the jet Lorentz factor is $\Gamma = (1 - \beta^2)^{-1/2}$. Assuming a flat radio spectral index $\alpha = 0$ and a continuous jet, the observed flux density is boosted by a factor $[\Gamma(1 - \beta\, cos\, i)]^{-2} + [\Gamma(1 + \beta\, cos\, i)]^{-2}$, where the second term is negligible for face-on inclinations.

As a proof of concept, we consider the case where the X-ray flux is not beamed and the radio flux of M10-VLA1 is consistent with the black hole L_X–L_R relation in the rest frame. This would require a beaming factor of ~ 5. For any inclination allowed by the dynamical analysis (§3.2), this beaming would require $\Gamma \sim 1.32$–1.36, corresponding to $\beta \sim 2/3$, for the inferred flux boost. Beaming factors of 10 or even 20 are easily reached with $\beta \lesssim 0.9$, still in the mildly relativistic regime. The beaming required to move a source from the (admittedly poorly-defined) L_X–L_R relation for transitional millisecond pulsars to the

location of M10-VLA1 is a factor of ~ 4–10 higher than the black hole case.

For relativistic beaming to be a likely explanation for M10-VLA1, there are two requirements for the source class. First, it requires a significant population of sources with flux densities below our detection limit but which become detectable if the orientation is favorable. Second, it requires that these sources regularly produce at least mildly relativistic jets in the quiescent regime.

Both requirements would tend to favor neutron star or black hole binaries: while accreting white dwarfs might well be common in globular clusters, those that emit bright radio flares are unusual, and to our knowledge relativistic jets have not been proposed to exist for dwarf nova systems outside of outburst.

Very little is known definitively about the Lorentz factors of jets in X-ray binaries, especially for low-luminosity sources with $L_X < 10^{34}$ erg s^{-1}. Heinz & Merloni (2004) show that the moderate scatter in the L_X–L_R correlation for black holes in the low/hard state implies that the width of the Lorentz factor distribution should be relatively small, but also that no upper limit on Γ can be derived from this correlation.

In a study of the stellar-mass black hole GX 339-4 undertaken in the hard state (with $L_X \gtrsim 10^{36}$ erg s^{-1}), Casella et al. (2010) show that $\Gamma \gtrsim 2$ near the jet base. Gallo et al. (2014) considered whether the different normalizations of L_X–L_R for different stellar-mass black holes could be explained by beaming, with no compelling evidence that this is the case. Russell et al. (2015) argue that the steep L_X–L_R relation of the radio-bright face-on ($i = 4$–15°; Russell et al. 2014) candidate stellar-mass black hole MAXI J1836-194 could potentially be explained by a decreasing Lorentz factor as the luminosity decayed to below 10^{36} erg s^{-1} after a failed outburst, but such an argument cannot be universally applied for stellar-mass black holes (Heinz & Merloni 2004; Soleri & Fender 2011).

Overall, we conclude that there is no strong evidence for or against the presence of relativistic jets among low-luminosity X-ray binaries. If such binaries *do* generally host mildly relativistic jets that could result in flux boosts from beaming, then we would expect the discovery of other face-on systems, an idea readily testable with future observations.

2.5 Summary and Future Work

The central result of the paper is the discovery of a interacting binary star with an evolved red straggler companion in the globular cluster M10. The identity of this star's companion is uncertain.

As discussed in §4.1, the observed properties of the system are all consistent with a black hole primary, with the exception of the low mass function, which could be explained if M10-VLA1 is face-on and there is a selection effect favoring radio detection of face-on systems. §4.2 discussed the alternative possibility that M10-VLA1 is an extreme flaring RS CVn binary, which would better explain the dynamical data, but is in tension with the long-term evidence for accretion in the binary.

There are a number of avenues for future work that could help distinguish between these possibilities. For a nominal $10M_{\odot}$ black hole primary, the semi-major axis would be $\sim 20\mu$as, which might be marginally detectable with *Gaia* astrometry given the brightness of the red straggler (Barstow et al. 2014). Perhaps more attainable, a simultaneous UV to near-IR spectral energy distribution, well-sampled in orbital phase, would allow improved modeling of the system. Simultaneous deep radio and X-ray observations, taken over multiple epochs, would help distinguish among classes of accreting compact objects. Theoretical modeling of the evolution of the system, as done for some specific sub-subgiant systems by Leiner et

al. (2017), would also be desirable.

In any case, it is clear that radio continuum imaging offers unique insights on the close binary populations in Galactic globular clusters.

Chapter 3

The MAVERIC Survey: Radio catalogs and source counts from deep Very Large Array imaging of 25 Galactic globular clusters

3.1 Introduction

Radio observations of globular clusters (GCs) have been central to studies of compact binaries in GCs for decades. The first radio surveys of GCs were motivated by detection of variable X-ray sources in GCs by *Uhuru* and *OSO-7* (Clark et al., 1975). There was immediate speculation that these cluster sources were formed dynamically rather than through the evolution of primordial binaries as for field X-ray sources (Clark 1975; Fabian et al. 1975; Sutantyo 1975). These radio surveys (e.g., Johnson 1976; Johnson et al. 1977; Rood et al. 1978; Gopal-Krishna & Steppe 1980) were limited to relatively bright sources (typically > 1 mJy) and in many cases the sources were found to be more likely associated with the background than with the cluster (Birkinshaw & Downes, 1982).

While pulsars are expected to be abundant in deep low-frequency radio continuum imag-

ing of GCs (e.g., Camilo & Rasio 2005; Ransom 2008), other classes of binaries readily observed at other wavelengths (such as in the X-ray) should also be detectable in the radio. Low-mass X-ray binaries (LMXBs), in which a neutron star or black hole accretes from a Roche lobe-filling companion, are abundant within GCs. In field neutron star LMXBs, radio emission associated with non-thermal jets has been observed at X-ray luminosities of $L_X \gtrsim 10^{34}$ erg s^{-1} (e.g., Tudor et al. 2017), and down to even lower luminosities of $L_X \sim 10^{33}$ erg s^{-1} for a few "transitional" millisecond pulsars (e.g., Deller et al. 2015), though the origin of the radio emission in this state is less clear (Bogdanov et al., 2018b). Black hole LMXBs have been observed in the radio even down to quiescent luminosities of $L_X \sim 10^{30}$ erg s^{-1} (e.g., Gallo et al. 2014), with the emission thought to come from partially self-absorbed synchrotron radiation from a compact jet (Blandford & Königl 1979, Hjellming & Johnston 1988). Other binaries with lower typical X-ray luminosities, such as cataclysmic variables, active binaries, and even exotic systems such as "white dwarf pulsars" are also detectable with sufficiently sensitive imaging (e.g., Drake et al. 1992; Abada-Simon et al. 1993; Coppejans et al. 2015; Marsh et al. 2016).

Given the depth of modern X-ray images (from *Chandra* or *XMM*) it is worthwhile to consider the utility of new radio imaging observations of GCs. One motivation is the search for radio emission from putative accreting intermediate-mass black holes (e.g., Maccarone 2004; Tremou et al. 2018). Another is the possibility of distinguishing between neutron star and black hole primaries in LMXBs: on average, accreting black holes show more luminous radio emission than neutron stars at a fixed L_X (e.g., Gallo et al. 2014, 2018), even though the X-ray spectra look very similar. Nearly all X-ray bright LMXBs in GCs are confirmed to host neutron stars, but for many of the fainter sources, the identity of the accretor is unknown, except in those cases where thermal emission from the surface of the neutron star

is detectable or multi-wavelength information is available (e.g., Heinke et al. 2003).

For many years it was thought unlikely that GCs hosted stellar-mass black holes in any substantial quantity, with their ejection the natural outcome of mass segregation and violent interactions in the cluster core (Sigurdsson & Hernquist, 1993; Kulkarni et al., 1993). This view was revisited starting about a decade ago with the discovery of a compelling stellar-mass black hole candidate in an extragalactic GC (e.g., Maccarone et al. 2007; Zepf et al., Zepf et al.).

The subsequent upgrade of the Karl G. Jansky Very Large Array (VLA), yielding a great increase in its radio continuum sensitivity, enabled the possibility of a wide-scale search for radio emission from quiescent black hole LMXBs in GCs. Our pilot surveys with the VLA and the Australia Telescope Compact Array (ATCA) successfully uncovered stellar-mass black hole candidates in the GCs M22 (Strader et al., 2012), M62 (Chomiuk et al., 2013), and 47 Tuc (Miller-Jones et al., 2015). We then initiated MAVERIC (Milky Way ATCA VLA Exploration of Radio Sources in Clusters) as a systematic survey for radio sources in 50 GCs with VLA and ATCA. The broader scientific implications of this project have accelerated in the last few years with the discovery that close black hole–black hole binaries are common in the local universe (Abbott et al., 2016), with dynamical formation in GCs a possibility to account for some or many of these systems (Rodriguez et al., 2016; Chatterjee et al., 2017). There has been a similar salvo of theoretical work on the presence of stellar-mass black holes in GCs, now arguing that some clusters could host tens to hundreds of black holes at the present day (e.g., Mackey et al. 2008; Sippel & Hurley 2013; Morscher et al. 2015b; Kremer et al. 2018; Weatherford et al. 2018)

While the ultimate goal of the survey is to identify, follow-up, and classify a wide variety of binaries, including perhaps accreting stellar-mass black holes, it will not be possible in

every case to definitively assess a source's classification. Even if a given source is associated with a compact object, a binary could have a sufficiently faint donor star that dynamical confirmation of the nature of the accretor is beyond the capability of present-day instrumentation. Therefore, in addition to these detailed investigations, it is useful to take a *global* view of the radio source populations in our radio images.

Here, as an intermediate product of our overall scientific goal to assess the population of radio sources, especially black hole candidates, in Galactic GCs, we present a radio source catalog compiled from our deep VLA observations of 25 Milky Way globular clusters (the GCs with ATCA observations are presented in a companion paper by Tudor et al., in preparation). We use these catalogs to do a source count and spectral index analysis of the radio continuum sources in our images, and show evidence for a significant population of individual radio sources in both our combined sample and in some individual GCs.

This paper is arranged as follows. In Section 2 we describe our data reduction procedures. Section 3 outlines our source finding method and spectral index analysis. Section 4 contains our main source count and spectral index results. We summarize and conclude in Section 5.

3.2 Radio Observations & Data Reduction

3.2.1 Sample and Observations

The initial MAVERIC cluster sample was selected to include all Galactic GCs with masses $> 10^5$ $M_\odot$ and distances < 9 kpc (Figure 3.1). These limits were designed to include massive clusters more likely to host a black hole population, and clusters close enough that we had sufficient sensitivity to detect radio emission akin to the candidate quiescent stellar-mass black holes in M22 (Strader et al., 2012). We also added a few more massive GCs at larger

distances, since these GCs are potential hosts for intermediate-mass black holes. More recent mass and distance determinations have moved a subset of the sample beyond these nominal mass and distance limits (see Figure 1), but the spirit of the selection is intact.

Owing to its higher sensitivity, we observed as much of the sample as possible with the VLA, reserving ATCA for the more southerly clusters not accessible to the VLA. There are 50 clusters in the final sample. The 25 clusters for which reasonably homogeneous VLA datasets have been completed are presented in this paper; we expect to add about 7 additional objects in future papers.

Pilot observations for the survey were made as part of National Radio Astronomy Observatory (NRAO) programs 10C-109 (P.I. Chomiuk) in 2011 and 12B-073 (P.I. Strader) in 2012. The main survey was approved as an NRAO Large Program (project codes 13B-014 and 15A-100), with observations made in 2014 and 2015, respectively. Table 3.1 lists the observation blocks for each cluster. The observations were primarily made in the most-extended A configuration, though a subset of southern clusters were observed in BnA or BnA to A "move time". The goal and median observing time per cluster was 10 hr, though a few clusters had a total observation time shorter or longer than this goal. Of this 10 hr of total observing time, the median time on source was 7.4 hr. Most of the off source time was allocated to the observation of phase calibrators, with a median cycle time of about 10 min. The observing efficiency was determined primarily by the length of the observed blocks. Table 3.2 lists the total and on source time for each cluster.

We made a few observations that are not used in this paper: these were all taken in move time between A and D configurations. In the course of verifying the catalogs in this paper, we found that the flux densities of apparent point sources were lower in these data compared to non-move time VLA data or ATCA data for the same clusters. We tried many

experiments to account for these discrepancies and were unable to do so, other than to say they are consistent with substantial decorrelation (up to a factor of 2) in the A to D move time data. These data are excluded from this paper. The main effect of this is to remove Liller 1 and NGC 6522 from our present sample.[1]

For all clusters we observed with the C band receiver, including full polarization products. Data taken in 2014 or earlier used an 8-bit setup with two 1-GHz basebands centered at 5.0 and 7.4 GHz, while the 2015 data used 3-bit receivers with two 2-GHz basebands centered at 5.0 and 7.0 GHz. However, the final central wavelengths depend on the details of the flagging of radio frequency interference, which varies among the sample (see Table 3.2). For simplicity, for the remainder of the paper we refer to the lower baseband as 5.0 GHz and the upper baseband as 7.2 GHz, even if the central frequencies differ slightly from these values.

3.2.2 Data Reduction

The data for both cluster frequency bands were separately flagged and calibrated according to standard procedures with either *Common Astronomy Software Application* (CASA; McMullin et al. 2007) version 4.2.2, or *Astronomical Image Processing System* (AIPS; Greisen 2003). Before imaging, the reduced visibilities from each observational epoch were stacked to maximize the sensitivity in each baseband. The combined bands were then imaged separately, with minimum fields of view (diameters) of 11′ at 5.0 GHz and 7.5′ at 7.2 GHz. These were chosen to match the full width at half-maximum (FWHM) of the primary beam at the lowest frequency of each baseband (4.0 or 6.0 GHz, respectively). Pixel sizes were set

[1] We also note that the VLA intermediate-mass black hole upper limits from Tremou et al. (2018) for only these two clusters should be increased by about 30%. While this has no effect on the overall conclusions of that paper—and indeed ATCA data for these clusters show no evidence of a central source that could be an intermediate-mass black hole—these clusters should be revisited when higher-quality data are available.

to $0.08''$ at 5.0 GHz and $0.06''$ at 7.2 GHz to adequately sample the synthesized beams of each frequency range. In AIPS, the data were imaged using IMAGR, Briggs weighting with a robust parameter of 1, frequency-independent deconvolution, and facets to account for wide-field effects. With data imaged in CASA/clean, nterms=2 was used to account for non-zero spectral indices of sources in the field. A primary beam response correction was applied to each subband image assuming the average frequency in that subband. The synthesized beam size for each image, as well as the image rms flux density values in μJy per beam, are listed in Table 3.2. The median rms values for the low and high frequency basebands across all clusters were 2.3 and 2.1 μJy per beam, respectively. We used self-calibration on the few clusters for which there was sufficient flux ($\gtrsim$ 5 mJy), typically with a single pass of phase self-calibration with a solution interval of 10 min.

The final reduced images for each cluster are hosted as science-ready data products at NRAO[2].

3.3 Source Finding Procedure & Analysis

We do source finding on the individual baseband images using Aegean (Hancock et al. 2012; Hancock et al. 2018) and the associated program BANE. This latter routine creates local background and rms images which are used as input to Aegean. Aegean searches for individual pixels above a threshold to seed a potential source, then grows this source using pixels above a lower threshold. With a goal of having a final catalog of sources of 5σ significance, after experimentation, we settled on a seed threshold of 4.5σ and a grow ("flood") threshold of 3σ. The final significance cut was made after final flux density fitting

[2]http://archive-new.nrao.edu/

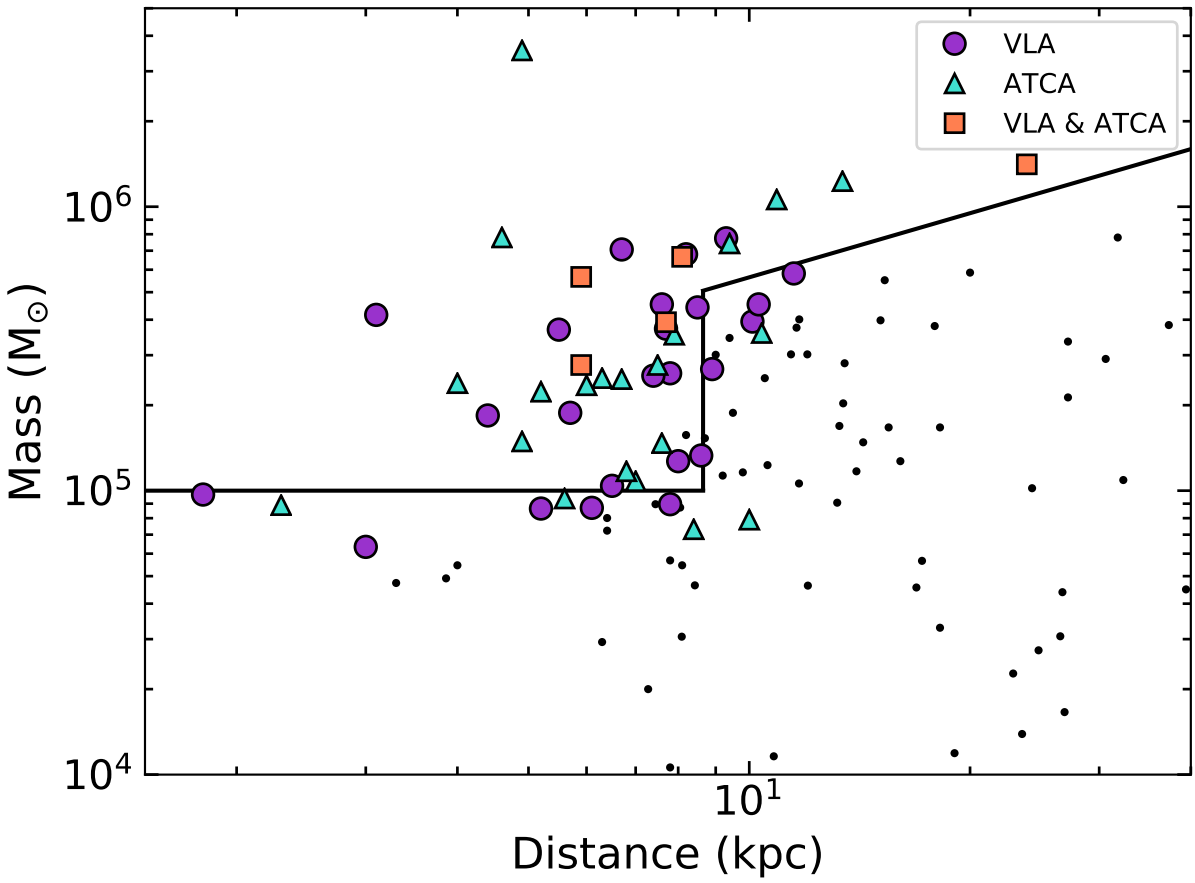

Figure 3.1 GC mass vs. distance for Galactic GCs, showing the selection of the MAVERIC (VLA and ATCA) GC sample with masses $> 10^5 M_\odot$ and distance < 9 kpc, with an extension to massive distant GCs for intermediate mass black hole searches. The VLA sample is shown by the purple circles and the ATCA sample (Tudor et al., in preparation) by the turquoise triangles. Orange squares are the five clusters observed by both the VLA and ATCA. Black points are other Galactic GCs (Baumgardt & Hilker, 2018). For the VLA sample, the cluster distances are listed in Table 3.2 (see Tremou et al. 2018 for a full set of references) and the masses are taken from (Baumgardt & Hilker, 2018).

(see below).

Given the modest extent of most of the GCs (median half-light radius $1.3'$) and the desire to have spectral information for source classification, in both basebands we restrict our source finding to a radius of $3.7'$ around the cluster center. This value is the typical half-width at half maximum of the upper baseband, and is sufficiently large to cover the area

within the half-light radii of all but one of the sample GCs (M4: $r_h = 4.33'$).

All detections were visually inspected. The main changes made after this inspection were to remove a few instances of obvious artifacts and to note any extended sources that had been split into multiple detections. These were replaced by a single source positioned at the most central or compact location of the emission.

Given the high resolution of our images and the expectation that all cluster sources of interest will be unresolved, we performed the final source fitting in a different manner. The detection catalogs were fed as input to the AIPS task `JMFIT`, which fits a model of the beam to a small 20 pixel box ($1.6''$ for lower baseband; $1.2''$ for upper baseband) around each detection. This fitting gave a flux density and uncertainty and position and uncertainty for each source. Sources were removed if $< 5\sigma$ after this process. After experimentation, we also removed any sources whose position changed by more than 4 pixels from the initial detection. We then matched the baseband source lists. The final catalog for each GC contains all sources detected at 5σ at either frequency.

The formal astrometric uncertainties in source positions are related to the beam FWHM and the signal-to-noise (SNR) of the detection as $\sim$ FWHM/(2 SNR), where the approximation is due to the typically correlated nature of noise in radio images, among other factors (Condon, 1997). However, calibration uncertainties typically limit the astrometric precision of the VLA to $\sim 10\%$ of the beam FWHM.[3] In the absence of additional external tests of the astrometric precision, espescially at the level of $\lesssim 0.1''$, we adopt this value as a floor. Future tests of the quality of our absolute astrometry would be valuable.

[3] https://science.nrao.edu/facilities/vla/docs/manuals/oss/ performance/positional-accuracy

3.3.1 Spectral Index Analysis

The radio spectral indices contain important information about the nature of the sources, and some information is available even for those sources without 5σ detections at both frequencies. For such sources, we force fit the location of the significant source at the other frequency using `JMFIT`. If the resulting fit yields a 3σ detection at a location within 4 pixels of the original location, this is retained as a valid detection of the same source at the other frequency. If these conditions are not met, the 3σ upper limit is given instead. For these cases with limits, we also report the exact flux density at the corresponding pixel (in case a reader is interested), but we only use the upper limits for the subsequent analysis in this paper.

We modeled spectral indices assuming a power law with the flux density $S_\nu \sim \nu^\alpha$. We used a Bayesian Markov Chain Monte Carlo code to fit these values, which self-consistently includes both the uncertainties on the flux densities and the 3σ upper limits, if present. We assumed a flat prior over the range $\alpha = -3.5$ to $+1.5$. This prior has little effect for brighter sources with measurements at both flux densities but a larger effect for very fainter sources, or those with a single detection. In the individual source tables, if there are detections in both bands, we report the median of the posterior as the best point estimate of the spectral index, equivalent 1σ limits (containing 68.3% of the posterior density around the median). If there is only a detection in a single band, we report a 3σ lower or upper limit on the spectral index.

3.3.2 Final Catalogs

Our final catalogs are available in machine-readable format. Table 3.3 shows a sample of the catalog for M2, and the final 5.0 GHz and 7.2 GHz images of M2 are shown in Figure 3.2 with the source detection regions overlaid.

A small fraction of the sources in this catalog are known previously, such as bright millisecond pulsars or luminous X-ray binaries. A comprehensive cross-matching with other catalogs and existing data at other wavelengths is a substantial undertaking that we defer to a future paper.

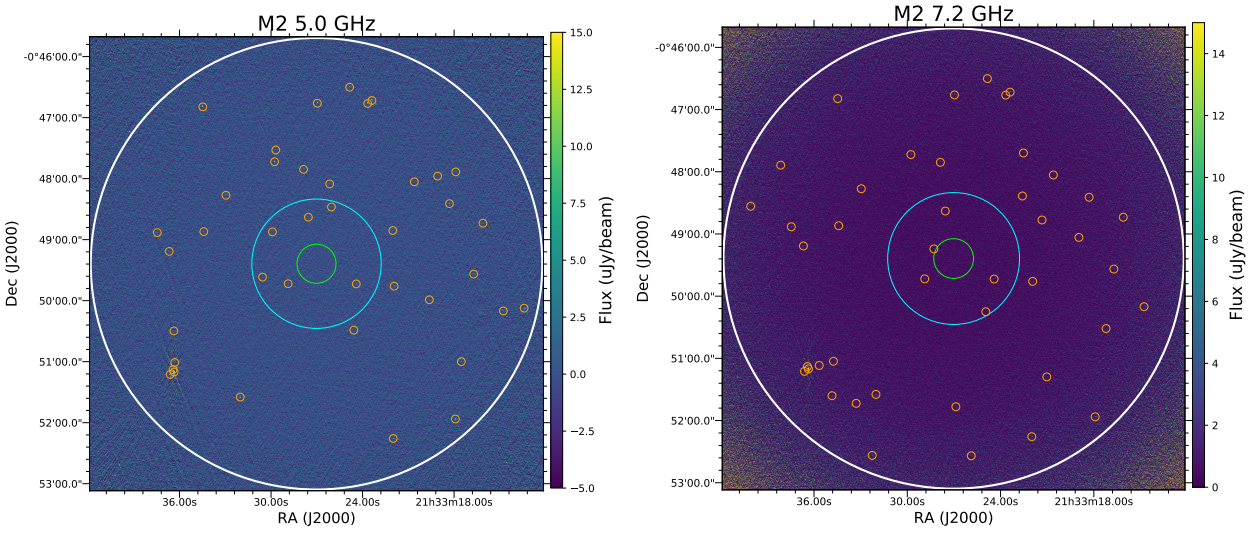

Figure 3.2 Final images of M2 at 5.0 GHz (a) and 7.2 GHz (b). The white circle represents the area within our 3.7 $'$ total search radius, and the green and blue circles show the areas enclosed by the cluster core radius and half-light radius of M2. The detected sources at each frequency are indicated in the corresponding image by the orange circles.

3.3.3 Potential Sources of Bias

There are several sources of bias that can affect the interpretation of our catalogs.

First, the faintest sources in our catalog could potentially be affected by "flux boosting": sources pushed above their true flux densities by rare positive noise spikes at the source

position. We discuss the effects of flux boosting on our source count analysis in §4, but in general, flux boosting is unlikely to significantly affect 5σ catalogs like the ones in this paper.

A related, but separate issue is that of entirely spurious sources. In the highest resolution images at 7.2 GHz there are of order 2×10^6 beams within the central $3.7'$, which would imply about 0.5 false detections per cluster if the noise were perfectly Gaussian (the false detection rate at 5.0 GHz is about half this size). Since real noise is correlated it is reasonable to expect a somewhat higher false detection rate, and indeed in some of the clusters there are 5σ sources detected at 7.2 GHz without even a 3σ detection at 5.0 GHz. Sources with such inverted spectra ($\alpha \sim 1.4$) are expected to be rare and hence many or most of these 7.2 GHz-only sources may indeed be spurious. All 5σ sources are retained in the catalogs but they should be interpreted with this caveat. We expect few spurious sources within the smaller cluster cores, especially at 5.0 GHz.

A separate source of bias is "resolution bias": the loss of diffuse flux from sources more extended than the synthesized beam. This can result in non-detection of sources whose total flux would place them above the nominal flux density detection limit, or a bias to a lower flux even if detected. While we expect most of the cluster sources to be unresolved, this is not the case for field or background sources. Previous work on radio source counts have estimated the effects of resolution bias, which has the strongest impact on sources below 100 μJy, but with a substantial uncertainty both in the size of the effect and how it depends on frequency (Windhorst et al., 1990, 1993; Huynh et al., 2020). This bias may affect the number counts around these flux densities by up to $\sim 25\%$, depending on the assumptions made about the source size distribution (Windhorst et al., 1984, 1993; Fomalont et al., 1991). We also note that we did not attempt to measure the diffuse flux from a small number of extended bright (mostly $>>$ 1 mJy) sources. The listed flux densities for these sources solely reflect a point

source fit to the core. All sources that appeared to be extended in our imaging, whether bright or not, are marked as such in the catalog.

3.4 Source Counts

A number of radio continuum sources discovered in our survey have already been confirmed as cluster members through optical spectroscopy (e.g., Shishkovsky et al. 2018), with compelling multi-wavelength evidence for others (e.g., Chomiuk et al. 2013). Such work will eventually be extended to our entire survey in a systematic manner. In the meantime, we consider the radio source counts in the clusters by themselves.

Historically, studies of radio source counts were undertaken with the goal of understanding the evolution of the universe, as their distribution was among the earliest evidence against the existence of uniform cosmic evolution (Ryle & Scheuer, 1955; Scheuer, 1957; Ryle & Neville, 1962). The suggested sources that dominate the differential counts are radio-loud AGN, galaxies with active star formation, and radio-quiet AGN (e.g., Condon 1984), with each class contributing more or less as a function of flux density. Bright sources are mostly AGN, but below ~ 1 mJy extragalactic source counts exhibit some flattening in the the slope of the Euclidian-normalized differential counts. The origin of this flattening is uncertain, and may be due to radio-quiet AGN, star forming galaxies, or a combination thereof (Padovani et al., 2007; Huynh et al., 2008; Smolčić et al., 2008).

Known Galactic radio sources are primarily composed of regions and nominally confined to Galactic latitudes $|b| < 5^\circ$ (e.g., Becker et al. 1990; Griffith & Wright 1993; Giveon et al. 2005). In a 5.0 GHz VLA survey of the Galactic plane radio source population, Purcell et al. (2013) found that bright resolved regions overwhelmingly accounted for the excess of radio

sources around $|b| = 0°$, yet only comprised $\approx 25\%$ of their 7σ sample (see also Hoare et al. 2012). The regions were distributed very close to the Galactic plane with a scale height of 0.47°. Their unresolved sources dominated the fainter population, and were distributed evenly over their Galactic latitude coverage ($|b| < 1°$), suggesting that the faint compact sources in their sample were predominantly background sources. However, the flux density limits of the Purcell et al. (2013) study were a factor of ~ 100 brighter than the VLA GCs in MAVERIC, so it is quite possible our data are probing a new, fainter regime where the density of Galactic radio continuum sources is yet unknown.

We can make a separate argument that Galactic sources are unlikely to substantially affect our study: none of our sample GCs are within 1.5° of the Galactic plane, and only four (NGC 6440, NGC 6544, NGC 6712, NGC 6760) are within 5° of the plane. These four GCs have an average of 18 sources detected at 5σ at 5.0 GHz in the radial range 2.5–3.7′ that we take as the "background" region. The other VLA GCs with imaging of comparable sensitivity have an average of 18.6 sources per GC in this region. Hence, from our data themselves there is no evidence of a population of sources that is more common at low Galactic latitude, as would be expected for essentially any Galactic population except for one within tens of pc of the Sun. The serendipitous discovery of a 0.2–0.3 mJy Galactic radio continuum source in the foreground (distance ~ 2.2 kpc) of the GC M15 ($b = -27$) with Very Long Baseline Array (Tetarenko et al., 2016a) shows that such sources do exist at some density, but evidently not a level sufficient to measurably affect our results.

The main goal of the source counts in this paper is to allow an estimate, on a cluster-by-cluster basis, the evidence for a population of radio source associated with the GC itself. However, we also check our source counts against previous work and models of the faint extragalactic population.

3.4.1 Calculation of Radio Source Counts

We present our radio source counts in the typical differential form normalized to a static Euclidean universe, given by: $S_\nu{}^{2.5}\frac{dN}{dS}(\mathrm{Jy}^{1.5}\ \Omega^{-1})$. Since each image has a different depth, and within each image the sensitivity falls off with radius, the catalogs cannot be directly used to calculate source counts. Instead, for each cluster, we sort the sources by flux density and radius, and use the aforementioned background and rms images from `BANE` to create sensitivity maps. We use these to calculate the area of the image in which a source could have been detected at 5σ. These corrected counts, added together for all clusters, make up the full differential source counts for the survey. The total survey area is ~ 0.4 deg^2, with a median 5σ depth of $\sim 11\mu$Jy per beam, making it among the deepest C band surveys with this angular coverage.

These radio source counts are shown in Table 3.4 and plotted in Figure 3.3. As expected, we observe a modest flattening in the Euclidian-normalized differential source counts below 1 mJy, and perhaps an upturn in the faintest flux bins. Fainter sources dominate the total counts: 1254 of the total 1267 5σ sources are below 700μJy.

For comparison, we also plot the source counts from several other deep surveys. At the lower frequency, Huynh et al. (2015) present source counts from a deep ATCA survey, reaching 43μJy (5σ) over ~ 0.34 deg^2 in the *Chandra* Deep Field South. We scale these 5.5 GHz counts to 5.0 GHz using the median spectral index of their sample ($\alpha = -0.58$). Heywood et al. (2013) describe their radio catalog derived from deep VLA observations of the William Herschel Deep Field, reaching a sensitivity of 2.5μJy. Their 8.4 GHz source counts are included with the upper band counts, and were scaled to 7.2 GHz using the typical extragalactic spectral index $\alpha = -0.7$. We also include the older literature compilation by de

Zotti et al. (2010), scaled from 4.8 GHz to 5.0 GHz and 8.4 GHz to 7.2 GHz assuming α = –0.7. Finally, we include the simulations of Wilman et al. (2008), which were derived semi-empirically using existing radio luminosity functions extrapolated down to nanoJy levels. These values, presented at 4.86 GHz, are scaled to both 5.0 GHz and 7.2 GHz, again using α = –0.7.

Overall, given the uncertainties in our new measurements and the scatter among previous source count estimates, our differential source counts are generally consistent with previous work, at least down to $\sim 100\mu$Jy. We note that somewhat lower counts for brighter sources might be expected from our survey, given our high resolution and limited treatment of extended emission.

Fainter than 100μJy, our source counts have much smaller Poissonian uncertainties than the comparison studies. The differential source counts are flat down to the $\sim 11\mu$Jy 5σ survey limit at 5.0 GHz and show a small upturn at 7.2 GHz. Since most sources are not expected to have inverted radio spectra, we attribute this 7.2 GHz upturn primarily to spurious sources rather than real sources, but this point should be revisited in the context of future follow-up and other deep surveys.

3.4.2 Cluster Radio Source Excess

To determine whether individual GCs show an excess of radio sources, we choose a somewhat conservative approach with a minimum set of assumptions. Since most sources have higher flux densities at 5.0 GHz than 7.2 GHz, we only carry out the following analysis at 5.0 GHz.

Because of cosmic variance, it is better to use a local estimate of the background, rather than the global source counts discussed above. After examination of the radial distribution of sources in each cluster, we found that radii beyond $2.5'$ are strongly dominated by non-cluster

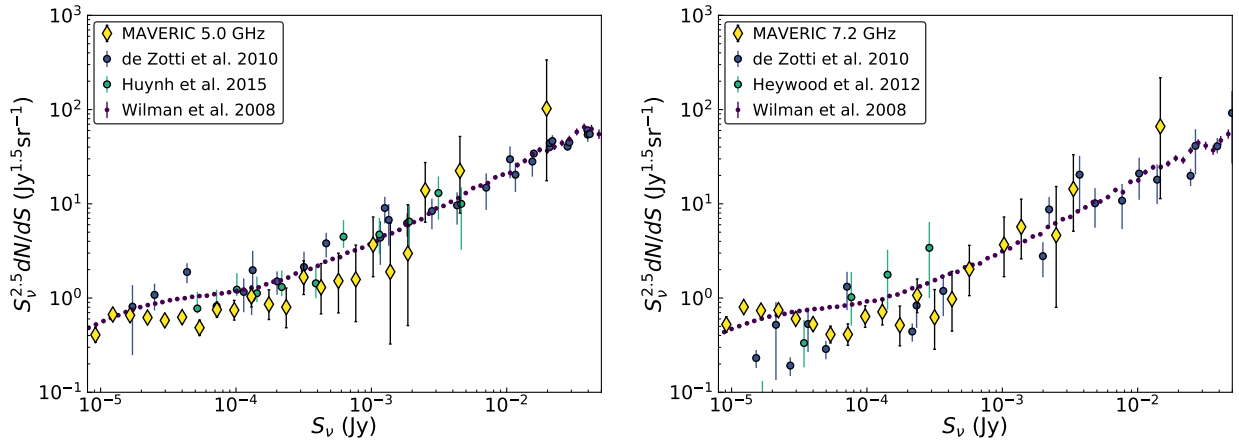

Figure 3.3 Differential radio source counts for our sample at 5.0 GHz (a) and 7.2 GHz (b), normalized for the standard $S^{2.5}$ Euclidian term (yellow diamonds). The other points represent different literature measurements, as described in the text. Our measurements are in general agreement with published values but slightly lower in the flux density range $\sim 50 - 200$ μJy, likely due to us resolving out diffuse flux at our higher resolution.

sources in most or all GCs. Hence we chose an annulus of 2.5–3.7′ as a clean, relatively large area in which a local background can be estimated. For each cluster, we estimated the areal density of background sources using a sensitivity analysis similar to that as for the source counts.

We took two bracketing approaches for defining a likely set of radio sources that could be associated with the GC: the sources within the core radius or within the half-light radius. The former is guided by the observed central mass segregation of X-ray populations within GCs (e.g., Grindlay et al. 1984; Verbunt & Hut 1987; Grindlay et al. 2002; Verbunt & Lewin 2006). Cluster X-ray sources are mostly binary stars or their progeny: the relatively massive (and hence centrally concentrated) objects one would expect to be observable as radio continuum sources. If the radio sources instead follow the cluster stars—an unlikely limiting case since nearly all single cluster stars are undetectable in the radio with current facilities (e.g., Maccarone et al. 2012)—then half would be expected to be contained within

the half-light radius.

To determine the "excess" number of sources within the core or half-light radius of each GC, we first calculated the expected number of background sources by scaling the sensitivity-corrected background density to the comparison GC area. We then subtracted this from the sensitivity-corrected observed number of sources in the core or half-light radius. This latter correction had little effect on the results, with two exceptions discussed below. Uncertainties in all quantities were determined by bootstrapping.

For the few GCs with half-light radii larger than $2.5'$ (M4, M22, and M55), we use $2.5'$ as the boundary between the background and the inner area we take to be associated with the GC. While we cannot be entirely sure that there are zero sources associated with the GC outside $2.5'$ in these GCs, they have an average background source density comparable to that of the other clusters, suggesting this assumption is reasonable for our first-order analysis. In our final catalog, there are 54 sources detected at 5.0 GHz within the core radius of a cluster, 201 within the half-light radius (this includes the 54 sources with the core radius), and 435 in the 2.5–$3.7'$ background region.

These core and half-light excesses are shown in Figure 3.4 and listed in Table 3.5. The points represent median values of the boostrapped samples and the error bars standard 1σ uncertainties.

The behaviors differ somewhat between the core and half-light samples. About 1/3 of the GCs show some evidence for an excess within a core radius, including four clusters that show excesses of at least 2 sources. One of these is M22, the first cluster in which our collaboration found candidate quiescent stellar-mass black holes (Strader et al., 2012). Three of these four GCs also have relatively large core radii. About half the clusters show no apparent excess (see Figure 3.4), in many cases due to their very small core radii. The combined overall

significance of the core radius excess in this conservative bootstrapped analysis is about 4σ.

The half-light radius excesses generally track those of the core radius, though in some cases with larger uncertainties or more extreme values. The two GCs with the largest half-light excesses are M4 and NGC 6544. The values for both of these GCs are boosted by the sensitivity correction, since there are a significant number of sources just above 5σ within the half-light radius. Each cluster would have a noticeable (but less extreme) excess were no correction applied.

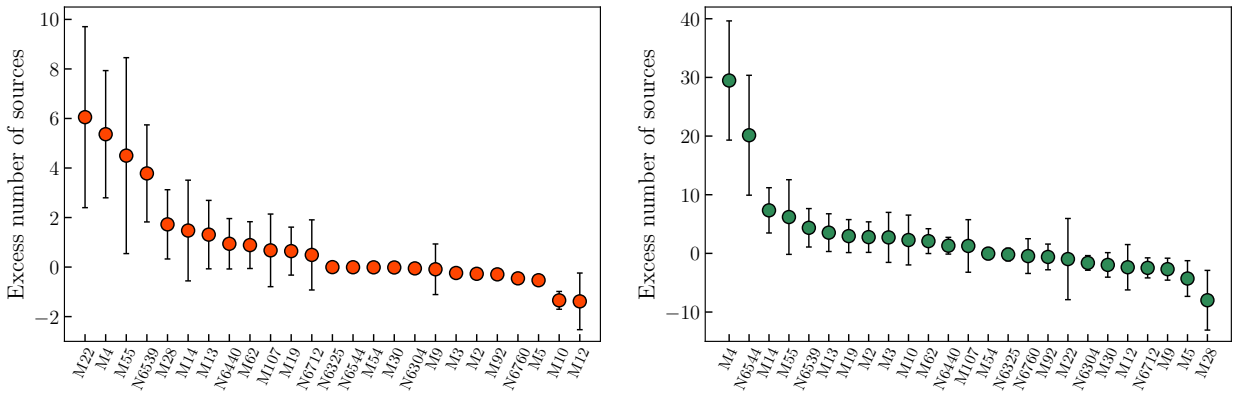

Figure 3.4 "Excess" of 5.0 GHz radio sources within the core radius (top panel) or half-light radius (bottom panel) of each GC in our sample, compared to the local density of background sources. In each panel, the GCs are sorted in descending order from greatest to least excess. 1σ uncertainties inferred from bootstrapping are also plotted. Excess values of 0, without apparent uncertainties, are GCs with very small core or half-light radii.

3.4.3 Interpreting the Radio Counts

It is worth emphasizing that some radio sources have been individually established as cluster members, even in clusters where there is not a statistically significant excess of sources. For example, M10 contains a radio continuum source (M10-VLA1) which is slightly too faint to appear in a 5σ catalog for this cluster, but which optical spectroscopy of the counterpart proves is a cluster member (Shishkovsky et al., 2018). Other clusters in the sample host radio

pulsars, which are certainly radio continuum sources, but mostly too faint to be detectable at 5.0 GHz. The two clusters with the largest core excesses are M4 and M22, two of the nearest objects in our sample. It is clear that our survey is sensitivity limited and that even the VLA can only reveal the brighter part of the luminosity distribution of radio continuum sources in GCs. Hence our excess measurements represent conservative lower limits to the radio source population. A complete analysis of the luminosity function of radio sources in the MAVERIC sample, including both VLA and ATCA data, will occur in a future paper.

We compared the excess values to a variety of cluster parameters to search for correlations with some possibly relevant parameters: core and half-light radius, mass, distance, central interaction rate (Bahramian et al., 2013), metallicity (Harris, 2010), and the number of known pulsars[4]. The plots for the core excess are show in Figure 3.11. Both formally (using a Spearman's rank correlation test) and by eye, no significant correlations are present, except perhaps a weak anti-correlation with distance. This is consistent with the conclusion that our survey is strongly limited by sensitivity.

Since one of the central goals of MAVERIC is to constrain the population of stellar-mass black holes in GCs, we note that twelve of our sample GCs also appear in the study of Weatherford et al. (2019), who combine models of how black hole populations affect cluster structure and mass segregation with observed data for a sample of Galactic GCs, theoretically predicting the number of black holes in each cluster. Of the twelve overlapping GCs, the two with the largest core excesses of radio sources, M22 and M55, are both in the top quartile of predicted black hole numbers. On the other hand, we see only mild evidence for a core radio source excess in M13, which has the largest predicted black hole population in the Weatherford et al. (2019) sample. Since most black holes are unlikely to be in mass-

[4]http://www.naic.edu/ pfreire/GCpsr.html

transferring binaries and hence observable as radio continuum sources, these comparisons are not straightforward to interpret. It would be valuable to obtain new, deep radio data for some of the GCs not in our current VLA sample that are suggested to host large black hole populations.

3.4.4 Spectral Index Distribution

An independent comparison of GC vs. background sources is possible by considering the radio continuum spectral indices of the sources. Background AGN can have a range of spectral indices, depending on their orientation, size, and accretion state; those with large-scale jets typically show steeper $\alpha < -0.5$ spectra, while emission from the compact core of the AGN has a flatter spectrum ($\alpha \sim 0$) due to partially self-absorbed synchrotron radiation. Star forming galaxies typically have steeper spectra around $\alpha \sim -0.8$ arising from optically thin synchrotron radiation associated with supernovae (Condon, 1992; de Zotti et al., 2010; Huynh et al., 2015; Tisanić et al., 2019). The median spectral index observed in different surveys varies depending on the depth, selection method, and precise frequencies used, but is typically around $\alpha \sim$ –0.6 to –0.7, with a standard deviation of $\sim$ 0.4–0.5 (e.g., Huynh et al. 2015; Smolčić et al. 2017).

In Figure 3.12 we compare the spectral index distributions of sources within 1 core radius and outside 2.5′, representing "clean" GC and background populations, respectively. Only those sources with spectral index uncertainties < 0.5 are plotted, and the distributions are normalized for comparison.

We find that the 120 background sources that meet these criteria have a broad distribution, as expected, with a median around $\alpha =$–0.9. By contrast, the 13 sources within the core radius have a bimodal distribution, with a very steep population with α mostly in the

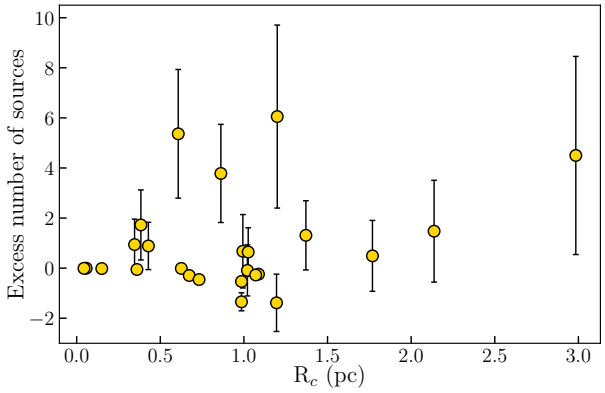

Figure 3.5 Core radius

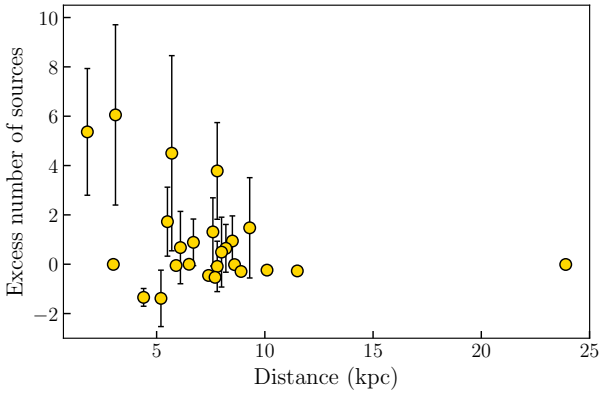

Figure 3.6 Distance

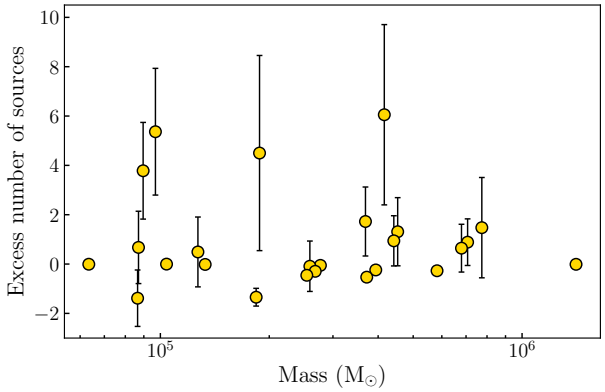

Figure 3.7 Cluster mass

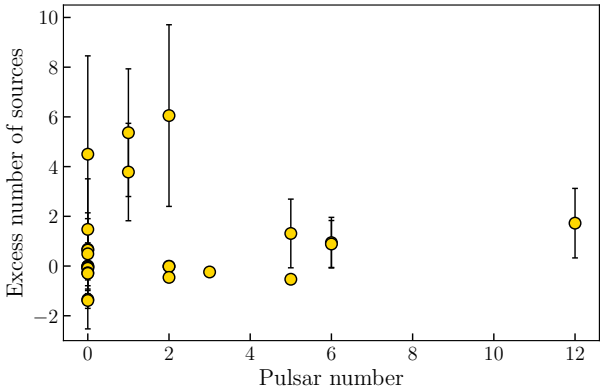

Figure 3.8 Number of known pulsars

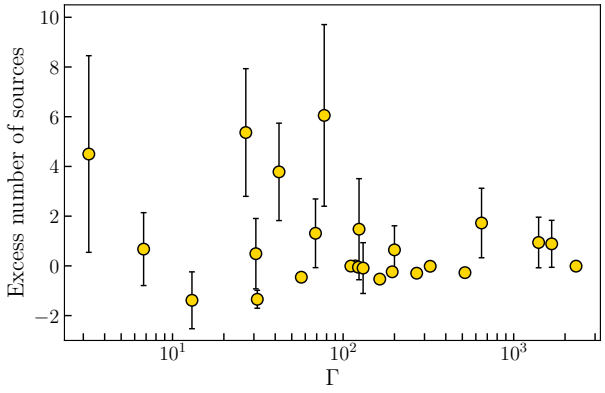

Figure 3.9 Stellar interaction rate

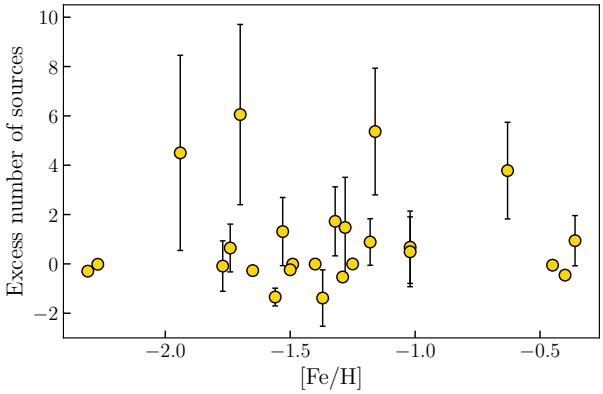

Figure 3.10 Cluster metallicity

Figure 3.11 A comparison of the cluster core radio source excesses to potentially relevant cluster parameters.

range –1 to –2, and a narrower peak centered around $\alpha \sim 0$ where there are few background sources. We tentatively identify the first population as millisecond pulsars, which show steep spectra (e.g., Bates et al. 2013; Zhao et al. 2020). The second, narrower peak is consistent with a population of binaries that show flat spectra, such as quiescent stellar-mass black holes, transitional millisecond pulsars, or even active binaries (see discussion in Shishkovsky et al. 2018; Bahramian et al. 2018; Miller-Jones et al. 2015; Chomiuk et al. 2013; Strader et al. 2012). For example, one of these sources is M62-VLA1, which has been established as a low-mass X-ray binary in M62 (Chomiuk et al., 2013), though the nature of the accretor has yet to be definitely determined.

The formal statistical support for a difference between the core and background populations is not well-established with these samples: an Anderson-Darling test finds $p = 0.11$, which is not surprising given that the the number of sources within the core radii with well-measured spectral indices is relatively small. Hence the visually suggestive difference between the distribution of spectral indices for GC and background sources needs to be bolstered by additional future work.

The spectral index distribution of the 61 sources within the half-light radius (but outside the core) is more similar to the distribution of background sources (Figure 3.12b), suggesting that many (or even most) of the sources outside the core but within the half-light radius are indeed background sources. A similar Anderson-Darling test between the half-light radius and background samples gives $p = 0.68$. Follow-up observations will be necessary to identify and classify the subset of these sources associated with the cluster rather than the background.

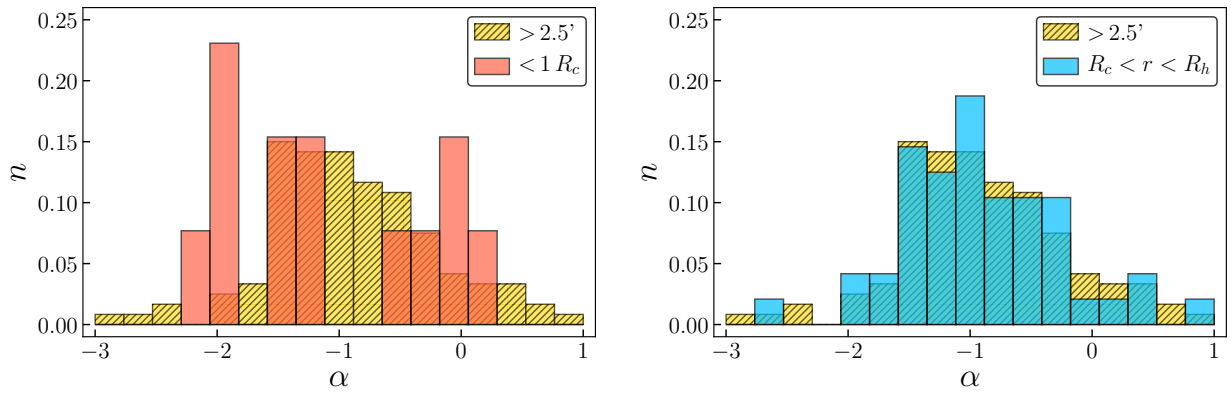

Figure 3.12 Normalized distribution of spectral indices for sources inside the core (a: orange) or between the half-light radius and the core (b: blue) vs. sources outside of 2.5′, our estimated background (yellow).

3.5 Conclusions

Here we have presented the initial results of our VLA radio continuum survey of Milky Way GCs. We observed 25 relatively nearby and massive clusters for $\sim$ 10 hrs each with the VLA at typical frequencies of 5.0 GHz and 7.2 GHz. These data represent the first deep high-resolution radio continuum survey of GCs as well as a sensitive C band $\sim$ 0.4 deg^2 extragalactic survey. This paper presents radio source catalogs for each GC; in most cases these catalogs will represent a mixture of cluster and background sources.

Through both source counts and spectral indices we found strong evidence for a population of radio sources associated with GCs. It is likely that a subset of these sources are steep-spectrum millisecond pulsars, while others represent compact or other kinds of binaries whose classification is not yet clear.

These catalogs represent an important but incomplete step in our efforts to understand the radio continuum source populations in GCs. Future papers from our group will use the full range of multi-wavelength information, including X-ray observations and optical photometry and spectroscopy, to determine and refine classifications of individual sources.

Table 3.1. Epochs of VLA Data

ID	Date	Obs. Time (hr)	Project Code
M2	2015 Jun 28	5	15A-100
	2015 Jul 3	5	15A-100
M3	2015 Jun 30	1	15A-100
	2015 Jul 26	1	15A-100
	2015 Aug 1	2	15A-100
	2015 Aug 4	1	15A-100
	2015 Aug 16	1	15A-100
	2015 Aug 28	1	15A-100
	2015 Aug 30	1	15A-100
	2015 Sep 2	1	15A-100
	2015 Sep 4	1	15A-100
M4	2014 Feb 11	1	13B-014
	2014 Feb 12	2	13B-014
	2014 Feb 15	2	13B-014
	2015 May 20	1	15A-100
	2015 May 25	1	15A-100

Table 3.1 (cont'd)

ID	Date	Obs. Time (hr)	Project Code
	2015 Jun 1	1	15A-100
	2015 Jun 7	2	15A-100
M5	2015 Jun 25	4	15A-100
	2015 Jun 26	4	15A-100
M9	2015 Jul 16	5	15A-100
	2015 Jul 20	5	15A-100
M10	2014 Feb 20	2	13B-014
	2014 Mar 28	2	13B-014
	2014 Apr 7	2	13B-014
	2014 Apr 10	2	13B-014
	2014 Apr 29	2	13B-014
M12	2015 Jun 27	4	15A-100
	2015 Jul 3	4	15A-100
M13	2014 Feb 25	1	13B-014
	2014 Mar 1	1	13B-014
	2014 Mar 7	1	13B-014

Table 3.1 (cont'd)

ID	Date	Obs. Time (hr)	Project Code
	2014 Apr 12	1	13B-014
	2014 May 1	1	13B-014
	2014 May 20	1	13B-014
	2015 Jun 18	2.5	15A-100
	2015 Jul 1	2.5	15A-100
M14	2015 Jul 10	5	15A-100
	2015 Jul 12	5	15A-100
M19	2011 May 19	5	10C-109
	2011 May 20	2.5	10C-109
	2011 May 21	2.5	10C-109
M22	2011 May 22	2.5	10C-109
	2011 May 23	2.5	10C-109
	2011 May 25	2.5	10C-109
	2011 May 29	2.5	10C-109
M28	2014 May 2	1	13B-014
	2014 May 4	2	13B-014

Table 3.1 (cont'd)

ID	Date	Obs. Time (hr)	Project Code
	2014 May 19	2	13B-014
	2014 May 23	1	13B-014
	2014 May 29	1	13B-014
	2014 May 30	2	13B-014
M30	2015 Jun 23	3.3	15A-100
	2015 Jul 4	3.3	15A-100
	2015 Jul 5	3.3	15A-100
M54	2015 Jun 9	2	15A-100
	2015 Jun 10	1	15A-100
	2015 Jun 12	2	15A-100
	2015 Jun 17	1	15A-100
M55	2015 May 20	1	15A-100
	2015 May 22	1	15A-100
	2015 Jun 1	1	15A-100
	2015 Jun 2	1	15A-100
	2015 Jun 4	1	15A-100

Table 3.1 (cont'd)

ID	Date	Obs. Time (hr)	Project Code
	2015 Jun 5	1	15A-100
	2015 Jun 6	2	15A-100
M62	2012 Sep 10	1	12B-073
	2012 Sep 11	3.75	12B-073
	2012 Sep 14	1.75	12B-073
	2012 Sep 15	1.75	12B-073
	2012 Sep 16	1.75	12B-073
M92	2015 Jun 19	3.3	15A-100
	2015 Jun 24	3.3	15A-100
	2015 Jul 4	3.3	15A-100
M107	2015 Jul 8	5	15A-100
	2015 Jul 9	5	15A-100
NGC 6304	2015 Jun 9	3	15A-100
	2015 Jun 12	1	15A-100
	2015 Jun 17	1	15A-100
NGC 6325	2015 Jul 23	2	15A-100

Table 3.1 (cont'd)

ID	Date	Obs. Time (hr)	Project Code
	2015 Jul 29	4	15A-100
	2015 Aug 1	2	15A-100
	2015 Aug 3	4	15A-100
NGC 6440	2014 May 5	1	13B-014
	2014 May 12	1	13B-014
	2014 May 16	1	13B-014
	2014 Jun 1	2	13B-014
	2015 Jul 6	5	15A-100
NGC 6539	2015 Jul 2	5	15A-100
	2015 Jul 4	5	15A-100
NGC 6544	2014 May 3	1	13B-014
	2014 May 5	1	13B-014
	2014 May 6	1	13B-014
	2014 May 10	1	13B-014
	2014 May 13	1	13B-014
	2014 May 22	1	13B-014

Table 3.1 (cont'd)

ID	Date	Obs. Time (hr)	Project Code
	2014 May 31	2	13B-014
	2014 Jun 2	1	13B-014
	2015 Jul 11	1	15A-100
NGC 6712	2014 Apr 5	2	13B-014
	2014 May 5	1	13B-014
	2014 May 8	2	13B-014
	2014 May 9	1	13B-014
	2014 May 13	2	13B-014
	2014 May 18	1	13B-014
	2014 May 20	1	13B-014
NGC 6760	2015 Jul 1	5	15A-100
	2015 Jul 7	5	15A-100

Table 3.2. Information for our cluster sample and images

ID	R.A. (J2000) (h:m:s)	Dec. (J2000) (° : ′ : ″)	Distance (kpc)	Core radius (″)	Half-light radius (″)	time (hr)	on src (hr)	$\nu_{\rm low}$ (GHz)	$\rm beam_{low}$	$\rm rms_{low}$ μJy beam^{-1}	$\nu_{\rm high}$ (GHz)	$\rm beam_{high}$	$\rm rms_{high}$ μJy beam^{-1}
M2	21:33:26.96	–00:49:22.90	11.5	19.2	63.6	10	8.3	5.2	$0.46'' \times 0.38''$	1.8	7.2	$0.31'' \times 0.26''$	1.7
M3	13:42:11.38	+28:22:39.10	10.1	22.2	138.6	10	7.1	5.0	$0.58'' \times 0.46''$	2.8	7.0	$0.37'' \times 0.29''$	2.1
M4	16:23:35.03	–26:31:33.80	1.8	69.6	259.8	10	6.9	5.0	$1.18'' \times 0.88''$	2.3	7.2	$0.84'' \times 0.63''$	2.1
M5	15:18:33.21	+02:04:51.80	7.7	26.4	106.2	8	6.6	5.2	$0.47'' \times 0.39''$	1.8	7.2	$0.33'' \times 0.28''$	1.8
M9	17:19:11.78	–18:30:58.50	7.8	27.0	57.6	10	8.2	5.0	$0.63'' \times 0.41''$	1.7	7.0	$0.44'' \times 0.31''$	1.7
M10	16:57:08.92	–04:05:58.00	4.4	46.2	117.0	10	7.9	5.0	$0.75'' \times 0.36''$	2.5	7.4	$0.53'' \times 0.26''$	1.9
M12	16:47:14.18	–01:56:54.70	5.2	47.4	106.2	8	6.6	5.2	$0.49'' \times 0.40''$	2.0	7.2	$0.39'' \times 0.27''$	1.8
M13	16:41:41.21	+36:27:35.60	7.6	37.2	101.4	11	7.6	5.0	$0.54'' \times 0.45''$	2.0	7.2	$0.35'' \times 0.28''$	2.1
M14	17:37:36.10	–03:14:45.30	9.3	47.4	78.0	10	8.4	5.3	$0.46'' \times 0.40''$	1.8	7.2	$0.35'' \times 0.29''$	1.7
M19	17:02:37.80	–26:16:04.70	8.2	25.8	79.2	10	7.4	5.0	$1.28'' \times 0.96''$	2.3	6.8	$0.95'' \times 0.72''$	2.0
M22	18:36:23.94	–23:54:17.10	3.1	79.8	201.6	10	7.3	5.0	$1.54'' \times 0.81''$	2.4	6.8	$1.14'' \times 0.59''$	2.0
M28	18:24:32.73	–24:52:13.00	5.5	14.4	118.2	9	6.0	5.0	$0.94'' \times 0.40''$	2.5	7.4	$0.66'' \times 0.27''$	2.1
M30	21:40:22.12	–23:10:47.50	8.6	3.6	61.8	10	8.0	4.9	$0.74'' \times 0.39''$	1.7	7.0	$0.52'' \times 0.28''$	1.6
M54	18:55:03.33	–30:28:47.50	23.9	5.4	49.2	6	3.8	5.1	$1.09'' \times 0.44''$	3.4	7.1	$0.74'' \times 0.30''$	2.8
M55	19:39:59.71	–30:57:53.10	5.7	108.0	169.8	8	5.1	5.1	$1.15'' \times 0.75''$	2.3	7.1	$0.83'' \times 0.62''$	2.2
M62	17:01:12.98	–30:06:49.00	6.7	13.2	55.2	10	7.0	5.0	$1.53'' \times 1.16''$	3.2	7.4	$0.95'' \times 0.71''$	2.2
M92	17:17:07.43	+43:08:09.30	8.9	15.6	61.2	10	7.9	5.0	$0.35'' \times 0.38''$	1.7	7.1	$0.33'' \times 0.27''$	1.6
M107	16:32:31.86	–13:03:13.60	6.1	33.6	103.8	10	8.2	5.0	$0.63'' \times 0.42''$	2.3	7.2	$0.41'' \times 0.29''$	2.2

Table 3.2 (cont'd)

ID	R.A. (J2000) (h:m:s)	Dec. (J2000) (° : ′ : ″)	Distance (kpc)	Core radius (″)	Half-light radius (″)	time (hr)	on src (hr)	$\nu_{\rm low}$ (GHz)	$\rm beam_{low}$	$\rm rms_{low}$ μJy beam^{-1}	$\nu_{\rm high}$ (GHz)	$\rm beam_{high}$	$\rm rms_{high}$ μJy beam^{-1}
N6304	17:14:32.25	–29:27:43.30	5.9	12.6	85.2	5	3.2	5.0	$0.91'' \times 0.56''$	3.8	7.1	$0.65'' \times 0.44''$	3.9
N6325	17:17:59.21	–23:45:57.60	6.5	1.8	37.8	12	9.0	5.0	$0.68'' \times 0.41''$	1.9	7.1	$0.52'' \times 0.31''$	2.0
N6440	17:48:52.70	–20:21:36.90	8.5	8.4	28.8	10	7.7	5.0	$0.90'' \times 0.60''$	2.7	7.1	$0.65'' \times 0.40''$	2.6
N6539	18:04:49.68	–07:35:09.10	7.8	22.8	102.0	10	8.2	5.2	$0.51'' \times 0.39''$	1.7	7.2	$0.39'' \times 0.28''$	2.2
N6544	18:07:20.12	–24:59:53.60	3.0	3.0	72.6	10	6.2	5.0	$1.02'' \times 0.39''$	2.5	7.4	$0.69'' \times 0.26''$	2.1
N6712	18:53:04.30	–08:42:22.00	8.0	45.6	79.8	10	7.2	5.0	$0.66'' \times 0.39''$	2.3	7.4	$0.46'' \times 0.26''$	2.1
N6760	19:11:12.01	+01:01:49.70	7.4	20.4	76.2	10	8.2	5.1	$0.52'' \times 0.42''$	2.2	7.2	$0.37'' \times 0.29''$	2.0

Note. — The sources for the photometric centers, distances, and structural parameters are as in Tremou et al. (2018).

Table 3.3. Radio Continuum Sources

ID	R.A.[a] (h:m:s)	Dec.[a] (°:′:″)	R.A. unc. (″)	Dec. unc. (″)	S_5[b] (μJy)	S_5 unc. (μJy)	S_7[c] (μJy)	S_7 unc. (μJy)	note[d]	radius[e] (′)	loc.[f]	α[g]
M2-VLA1	21:33:36.358	–00:51:10.14	···	···	19013.3	5.6	12724.0	4.8	ext.	2.95	···	$-1.23^{+0.01}_{-0.01}$
M2-VLA2	21:33:23.668	–00:46:46.08	0.03	0.03	190.7	2.2	156.4	2.7	···	2.74	···	$-0.61^{+0.06}_{-0.06}$
M2-VLA3	21:33:32.016	–00:51:34.79	0.03	0.03	134.4	2.1	119.4	2.7	···	2.54	···	$-0.36^{+0.08}_{-0.09}$
M2-VLA4	21:33:29.770	–00:47:43.41	0.03	0.03	97.6	2.0	104.1	2.1	···	1.80	···	$+0.20^{+0.09}_{-0.09}$
M2-VLA5	21:33:26.964	–00:46:45.88	0.03	0.03	90.9	2.2	70.1	2.7	···	2.62	···	$-0.80^{+0.14}_{-0.14}$
M2-VLA6	21:33:17.915	–00:51:56.40	0.03	0.03	86.2	2.7	141.0	3.9	···	3.41	···	$+1.42^{+0.06}_{-0.09}$
M2-VLA7	21:33:34.476	–00:46:49.45	0.03	0.03	76.7	2.4	83.3	3.4	···	3.17	···	$+0.25^{+0.16}_{-0.16}$
M2-VLA8	21:33:23.387	–00:46:43.19	0.03	0.03	52.7	2.2	40.8	2.8	···	2.81	···	$-0.80^{+0.24}_{-0.25}$
M2-VLA9	21:33:36.614	–00:51:12.55	0.03	0.03	43.8	5.4	50.1	4.4	···	3.03	···	$+0.43^{+0.47}_{-0.46}$
M2-VLA10	21:33:28.879	–00:49:43.34	0.03	0.03	41.5	1.9	30.4	1.8	···	0.59	r_h	$-0.95^{+0.23}_{-0.24}$
M2-VLA11	21:33:21.993	–00:52:15.52	0.03	0.03	34.3	2.5	27.9	3.5	···	3.13	···	$-0.66^{+0.44}_{-0.48}$
M2-VLA12	21:33:18.304	–00:48:24.60	0.03	0.03	33.9	2.1	53.9	2.4	···	2.37	···	$+1.31^{+0.13}_{-0.18}$
M2-VLA13	21:33:24.849	–00:46:30.12	0.03	0.03	27.1	2.3	25.8	3.0	···	2.93	···	$-0.17^{+0.44}_{-0.46}$
M2-VLA14	21:33:21.935	–00:49:45.76	0.03	0.03	27.0	1.9	25.0	1.9	···	1.31	···	$-0.24^{+0.32}_{-0.32}$
M2-VLA15	21:33:36.424	–00:51:07.87	0.03	0.03	24.4	5.7	33.2	4.6	art.?	2.94	···	$+0.70^{+0.53}_{-0.67}$
M2-VLA16	21:33:36.316	–00:51:00.79	0.04	0.05	23.3	3.7	< 11.7	-1.2	art.?	2.85	···	< 0.5
M2-VLA17	21:33:36.680	–00:49:11.56	0.03	0.03	22.0	2.4	15.3	2.6	···	2.44	···	$-1.18^{+0.62}_{-0.68}$
M2-VLA18	21:33:24.414	–00:49:43.52	0.03	0.03	20.2	1.9	11.8	1.8	···	0.72	r_h	$-1.71^{+0.55}_{-0.59}$

Table 3.3 (cont'd)

ID	R.A.[a] (h:m:s)	Dec.[a] (°:′:″)	R.A. unc. (″)	Dec. unc. (″)	S_5[b] (μJy)	S_5 unc. (μJy)	S_7[c] (μJy)	S_7 unc. (μJy)	note[d]	radius[e] (′)	loc.[f]	α[g]
M2-VLA19	21:33:32.957	–00:48:16.40	0.03	0.03	18.2	2.0	10.9	2.0	···	1.86	···	$-1.64^{+0.66}_{-0.71}$
M2-VLA20	21:33:36.371	–00:50:29.77	0.04	0.05	17.9	2.8	< 8.4	0.3	···	2.60	···	< 0.2
M2-VLA21	21:33:13.408	–00:50:07.37	0.04	0.05	17.1	2.7	< 12.0	-0.1	···	3.47	···	< 1.1
M2-VLA22	21:33:16.108	–00:48:43.84	0.03	0.03	16.4	2.2	11.5	2.9	···	2.79	···	$-1.23^{+0.88}_{-1.00}$
M2-VLA23	21:33:37.458	–00:48:53.07	0.03	0.03	16.3	2.4	15.6	2.7	···	2.67	···	$-0.19^{+0.70}_{-0.75}$
M2-VLA24	21:33:14.770	–00:50:10.13	0.03	0.03	16.0	2.5	15.0	3.5	···	3.15	···	$-0.32^{+0.84}_{-0.99}$
M2-VLA25	21:33:34.411	–00:48:52.10	0.03	0.03	15.1	2.1	9.4	2.1	···	1.93	···	$-1.54^{+0.81}_{-0.87}$
M2-VLA26	21:33:17.525	–00:50:59.97	0.04	0.05	14.9	2.4	< 9.0	3.5	···	2.86	···	< 0.8
M2-VLA27	21:33:27.870	–00:47:50.93	0.03	0.03	14.7	1.9	10.1	1.9	···	1.55	···	$-1.21^{+0.70}_{-0.77}$
M2-VLA28	21:33:16.714	–00:49:33.90	···	···	14.5	2.2	16.6	2.6	ext.	2.57	···	$+0.36^{+0.61}_{-0.68}$
M2-VLA29	21:33:20.605	–00:48:03.13	0.03	0.03	12.3	2.0	9.6	2.2	···	2.07	···	$-0.85^{+0.88}_{-0.96}$
M2-VLA30	21:33:29.690	–00:47:31.84	0.04	0.05	11.9	2.0	< 6.4	1.2	···	1.97	···	< 0.6
M2-VLA31	21:33:26.042	–00:48:27.87	0.04	0.05	11.8	1.9	< 5.3	0.9	···	0.95	r_h	< 0.2
M2-VLA32	21:33:17.892	–00:47:53.39	0.04	0.05	11.3	2.1	< 8.2	-2.2	···	2.71	···	< 1.1
M2-VLA33	21:33:19.078	–00:47:57.54	0.04	0.05	11.1	2.1	< 7.3	-1.1	···	2.43	···	< 1.0
M2-VLA34	21:33:29.909	–00:48:52.38	0.04	0.05	11.1	1.9	< 5.1	4.5	···	0.90	r_h	< 0.4
M2-VLA35	21:33:19.622	–00:49:59.10	0.04	0.05	10.7	2.1	< 6.4	0.7	···	1.93	···	< 0.9
M2-VLA36	21:33:27.555	–00:48:37.90	0.03	0.04	10.7	1.8	6.2	1.7	···	0.77	r_h	$-1.73^{+0.94}_{-0.96}$

Table 3.3 (cont'd)

ID	R.A.[a] (h:m:s)	Dec.[a] (°:′:″)	R.A. unc. (″)	Dec. unc. (″)	S_5[b] (μJy)	S_5 unc. (μJy)	S_7[c] (μJy)	S_7 unc. (μJy)	note[d]	radius[e] (′)	loc.[f]	α[g]
M2-VLA37	21:33:22.021	–00:48:51.05	0.04	0.05	10.5	1.9	< 5.6	1.6	···	1.34	···	< 0.7
M2-VLA38	21:33:26.157	–00:48:05.20	0.04	0.05	10.0	1.9	< 5.5	1.3	···	1.31	···	< 0.8
M2-VLA39	21:33:24.576	–00:50:28.96	0.04	0.05	9.4	1.9	< 5.6	-1.0	···	1.25	···	< 0.9
M2-VLA40	21:33:30.561	–00:49:36.84	0.04	0.05	9.4	1.8	< 5.3	1.3	···	0.93	r_h	< 0.8
M2-VLA41	21:33:32.254	–00:52:33.62	0.03	0.03	< 7.8	1.6	20.6	4.1	···	3.44	···	> -2.8
M2-VLA42	21:33:40.073	–00:48:33.28	0.03	0.03	< 7.7	-0.6	19.0	3.7	···	3.38	···	> -2.6
M2-VLA43	21:33:25.886	–00:52:33.99	0.03	0.03	< 7.4	5.8	18.4	3.6	···	3.20	···	> -2.6
M2-VLA44	21:33:38.141	–00:47:53.68	0.03	0.03	< 7.3	-1.9	17.8	3.2	···	3.17	···	> -1.8
M2-VLA45	21:33:34.839	–00:51:36.04	0.03	0.03	< 7.3	1.9	16.4	3.2	···	2.97	···	> -2.6
M2-VLA46	21:33:35.665	–00:51:06.89	0.03	0.03	< 8.6	0.9	15.7	2.9	···	2.78	···	> -2.0
M2-VLA47	21:33:17.216	–00:50:31.26	0.03	0.03	< 6.6	-2.3	14.9	2.8	···	2.69	···	> -2.3
M2-VLA48	21:33:33.288	–00:51:43.43	0.03	0.03	< 7.2	1.4	14.3	2.9	···	2.83	···	> -2.9
M2-VLA49	21:33:34.750	–00:51:02.81	0.03	0.03	< 6.6	1.6	13.1	2.6	···	2.56	···	> -2.7
M2-VLA50	21:33:26.873	–00:51:46.69	0.03	0.03	< 6.3	-0.7	13.1	2.5	···	2.40	···	> -2.4
M2-VLA51	21:33:18.961	–00:49:03.33	0.03	0.03	< 6.0	-1.9	12.6	2.2	···	2.03	···	> -1.7
M2-VLA52	21:33:21.025	–00:51:17.87	0.03	0.03	< 6.5	-4.0	12.4	2.5	···	2.42	···	> -2.9
M2-VLA53	21:33:21.335	–00:48:46.50	0.03	0.03	< 5.7	2.8	11.9	1.9	···	1.53	···	> -1.3
M2-VLA54	21:33:22.528	–00:47:41.89	0.03	0.03	< 5.9	-0.8	10.6	2.1	···	2.02	···	> -2.7

Table 3.3 (cont'd)

ID	R.A.[a] (h:m:s)	Dec.[a] (°:′:″)	R.A. unc. (″)	Dec. unc. (″)	S_5[b] (μJy)	S_5 unc. (μJy)	S_7[c] (μJy)	S_7 unc. (μJy)	note[d]	radius[e] (′)	loc.[f]	α[g]
M2-VLA55	21:33:22.595	–00:48:23.36	0.03	0.03	< 5.7	0.5	9.7	1.9	···	1.47	···	> -2.6
M2-VLA56	21:33:24.948	–00:50:15.03	0.03	0.03	< 5.6	2.6	9.5	1.8	···	1.00	r_h	> -2.3
M2-VLA57	21:33:28.288	–00:49:14.42	0.03	0.03	< 5.3	-0.3	9.1	1.7	···	0.36	r_h	> -2.4
M3-VLA1	13:42:03.265	+28:23:20.06	0.04	0.03	409.2	3.0	285.0	2.9	···	1.91	r_h	$-1.08^{+0.04}_{-0.04}$
M3-VLA2	13:42:14.904	+28:24:17.23	0.04	0.03	322.4	3.0	227.0	2.7	···	1.81	r_h	$-1.04^{+0.04}_{-0.05}$
M3-VLA3	13:42:24.692	+28:24:54.10	0.04	0.03	171.9	3.9	92.5	6.2	···	3.69	···	$-1.85^{+0.20}_{-0.21}$
M3-VLA4	13:42:16.589	+28:19:33.78	0.04	0.03	168.5	3.7	119.9	4.9	···	3.30	···	$-1.01^{+0.14}_{-0.14}$
M3-VLA5	13:42:04.465	+28:20:16.79	0.04	0.03	94.5	3.3	58.1	3.9	···	2.82	···	$-1.45^{+0.22}_{-0.24}$
M3-VLA6	13:42:01.162	+28:20:59.75	0.04	0.03	84.7	3.3	73.1	3.7	···	2.79	···	$-0.44^{+0.19}_{-0.19}$
M3-VLA7	13:42:09.796	+28:20:17.23	0.04	0.03	72.6	3.1	60.1	3.1	···	2.39	···	$-0.56^{+0.20}_{-0.20}$
M3-VLA8	13:42:10.997	+28:21:03.57	0.04	0.03	42.6	3.0	24.6	2.4	···	1.59	r_h	$-1.65^{+0.36}_{-0.37}$
M3-VLA9	13:42:22.173	+28:22:47.59	0.04	0.03	39.0	3.0	20.0	3.0	···	2.38	···	$-2.04^{+0.49}_{-0.53}$
M3-VLA10	13:42:10.327	+28:20:28.16	0.04	0.03	35.5	3.0	23.1	2.9	···	2.19	r_h	$-1.31^{+0.45}_{-0.48}$
M3-VLA11	13:42:23.916	+28:23:03.13	0.06	0.05	30.5	3.2	20.5	3.7	···	2.79	···	$-1.25^{+0.62}_{-0.69}$
M3-VLA12	13:42:13.937	+28:25:07.59	0.04	0.03	28.9	3.1	21.2	3.3	···	2.54	···	$-0.97^{+0.56}_{-0.61}$
M3-VLA13	13:42:25.636	+28:21:31.45	0.06	0.05	28.1	3.6	24.2	5.0	···	3.33	···	$-0.53^{+0.73}_{-0.83}$
M3-VLA14	13:42:07.293	+28:19:28.03	0.06	0.05	27.9	3.6	25.3	4.9	···	3.31	···	$-0.36^{+0.70}_{-0.78}$
M3-VLA15	13:42:08.707	+28:19:36.93	0.06	0.05	27.3	3.4	14.7	4.1	···	3.09	···	$-1.92^{+0.83}_{-0.87}$

Table 3.3 (cont'd)

ID	R.A.[a] (h:m:s)	Dec.[a] (°:′:″)	R.A. unc. (″)	Dec. unc. (″)	S_5[b] (μJy)	S_5 unc. (μJy)	S_7[c] (μJy)	S_7 unc. (μJy)	note[d]	radius[e] (′)	loc.[f]	α[g]
M3-VLA16	13:42:08.791	+28:23:06.06	0.04	0.03	25.0	2.9	16.9	2.2	···	0.72	r_h	$-1.17^{+0.53}_{-0.54}$
M3-VLA17	13:42:18.915	+28:19:23.75	0.04	0.03	22.1	3.6	34.1	5.8	···	3.65	···	$+0.91^{+0.41}_{-0.61}$
M3-VLA18	13:42:12.755	+28:21:15.14	0.04	0.03	21.9	2.8	16.2	2.4	···	1.43	r_h	$-0.92^{+0.60}_{-0.61}$
M3-VLA19	13:41:58.744	+28:24:38.32	0.06	0.05	21.4	3.8	26.9	5.4	···	3.42	···	$+0.48^{+0.63}_{-0.81}$
M3-VLA20	13:42:05.144	+28:20:49.02	0.06	0.05	20.5	3.1	< 9.3	2.4	···	2.29	r_h	< 0.1
M3-VLA21	13:42:09.015	+28:23:48.62	0.06	0.05	19.8	3.0	8.7	2.4	···	1.27	r_h	$-2.35^{+0.81}_{-0.72}$
M3-VLA22	13:42:23.952	+28:20:36.39	0.06	0.05	19.7	3.6	< 15.4	6.0	···	3.44	···	< 1.3
M3-VLA23	13:42:08.949	+28:19:33.36	0.06	0.05	19.7	3.4	12.8	4.2	···	3.14	···	$-1.40^{+1.06}_{-1.13}$
M3-VLA24	13:42:09.969	+28:21:30.95	0.06	0.05	18.2	2.8	10.5	2.3	···	1.18	r_h	$-1.69^{+0.80}_{-0.83}$
M3-VLA25	13:42:05.159	+28:22:26.91	0.06	0.05	16.3	2.8	< 7.2	5.7	···	1.38	r_h	< 0.3
M3-VLA26	13:42:14.550	+28:20:46.62	0.04	0.03	15.6	3.1	15.6	2.8	···	2.00	r_h	$-0.03^{+0.77}_{-0.82}$
M3-VLA27	13:42:10.560	+28:22:15.72	0.06	0.05	15.1	2.8	< 6.5	4.3	···	0.43	r_h	< 0.4
M3-VLA28	13:42:14.158	+28:23:08.49	0.06	0.05	14.4	2.9	< 6.6	2.9	···	0.78	r_h	< 0.7
M3-VLA29	13:42:15.463	+28:24:17.29	0.04	0.03	12.9	3.0	14.3	2.7	···	1.87	r_h	$+0.18^{+0.73}_{-0.86}$
M3-VLA30	13:42:02.224	+28:21:30.55	0.04	0.03	10.8	3.1	17.0	3.1	···	2.32	···	$+0.74^{+0.48}_{-0.74}$
M3-VLA31	13:42:10.298	+28:26:09.88	0.04	0.03	< 10.8	-6.7	31.4	5.8	···	3.52	···	> -2.0
M3-VLA32	13:41:58.413	+28:23:48.00	0.04	0.03	< 10.4	4.1	23.7	4.4	···	3.07	···	> -1.8
M3-VLA33	13:41:57.609	+28:21:34.15	0.04	0.03	< 10.5	-1.2	23.3	4.7	···	3.22	···	> -2.6

Table 3.3 (cont'd)

ID	R.A.[a] (h:m:s)	Dec.[a] (°:′:″)	R.A. unc. (″)	Dec. unc. (″)	S_5[b] (μJy)	S_5 unc. (μJy)	S_7[c] (μJy)	S_7 unc. (μJy)	note[d]	radius[e] (′)	loc.[f]	α[g]
M3-VLA34	13:42:00.726	+28:20:52.11	0.04	0.03	< 10.2	-4.1	21.6	4.1	···	2.95	···	> -2.1
M3-VLA35	13:42:16.025	+28:19:54.01	0.04	0.03	< 10.0	-2.9	19.7	3.9	···	2.94	···	> -2.3
M3-VLA36	13:42:11.131	+28:25:17.57	0.04	0.03	< 9.6	5.4	19.1	3.4	···	2.64	···	> -1.6
M3-VLA37	13:42:23.631	+28:22:55.87	0.04	0.03	< 9.6	3.2	18.5	3.6	···	2.71	···	> -2.2
M3-VLA38	13:42:18.325	+28:21:17.44	0.04	0.03	< 8.9	0.0	17.0	2.7	···	2.05	r_h	> -1.2
M3-VLA39	13:42:19.006	+28:24:30.06	0.04	0.03	< 9.3	0.5	16.5	3.3	···	2.50	···	> -2.5
M3-VLA40	13:42:16.460	+28:20:24.84	0.04	0.03	< 9.4	-2.0	16.3	3.3	···	2.50	···	> -2.6
M3-VLA41	13:42:08.963	+28:20:25.43	0.04	0.03	< 9.4	4.9	16.1	2.9	···	2.29	r_h	> -1.8
M3-VLA42	13:42:17.478	+28:21:31.20	0.04	0.03	< 8.8	-3.0	13.7	2.5	···	1.76	r_h	> -2.1
M3-VLA43	13:42:18.274	+28:23:30.87	0.04	0.03	< 8.7	4.1	13.4	2.6	···	1.74	r_h	> -2.4
M3-VLA44	13:42:15.663	+28:23:32.09	0.04	0.03	< 8.5	2.9	12.6	2.4	···	1.29	r_h	> -2.4
M3-VLA45	13:42:11.839	+28:22:08.93	0.04	0.03	< 8.5	-6.3	11.1	2.2	···	0.51	r_h	> -2.7
M4-VLA1	16:23:29.180	–26:29:49.16	0.08	0.07	1289.4	2.9	995.5	3.5	···	2.18	r_h	$-0.71^{+0.01}_{-0.01}$
M4-VLA2	16:23:32.259	–26:34:34.25	0.08	0.07	558.7	3.1	515.0	5.2	···	3.07	r_h	$-0.22^{+0.03}_{-0.03}$
M4-VLA3	16:23:29.117	–26:33:41.78	0.08	0.07	122.0	2.8	106.8	3.8	···	2.51	r_h	$-0.37^{+0.12}_{-0.12}$
M4-VLA4	16:23:28.455	–26:30:51.82	0.08	0.07	106.2	2.5	90.5	2.5	···	1.63	r_h	$-0.44^{+0.10}_{-0.10}$
M4-VLA5	16:23:37.166	–26:32:23.51	0.08	0.07	82.7	2.2	49.2	2.1	···	0.96	r_c	$-1.43^{+0.14}_{-0.14}$
M4-VLA6	16:23:35.983	–26:32:16.62	0.08	0.07	64.8	2.4	39.4	2.2	···	0.74	r_c	$-1.37^{+0.18}_{-0.19}$

Table 3.3 (cont'd)

ID	R.A.[a] (h:m:s)	Dec.[a] (°:′:″)	R.A. unc. (″)	Dec. unc. (″)	S_5[b] (μJy)	S_5 unc. (μJy)	S_7[c] (μJy)	S_7 unc. (μJy)	note[d]	radius[e] (′)	loc.[f]	α[g]
M4-VLA7	16:23:33.635	–26:29:53.70	0.08	0.07	59.4	2.5	28.8	2.5	···	1.70	r_h	$-2.00^{+0.26}_{-0.28}$
M4-VLA8	16:23:44.955	–26:29:19.94	0.08	0.07	45.1	2.9	32.1	4.5	···	3.15	r_h	$-0.98^{+0.42}_{-0.46}$
M4-VLA9	16:23:38.201	–26:31:54.24	0.10	0.10	40.5	2.4	< 6.5	2.4	···	0.79	r_c	< -2.6
M4-VLA10	16:23:22.551	–26:32:20.77	0.10	0.10	29.3	3.1	18.8	4.3	···	2.90	r_h	$-1.33^{+0.68}_{-0.80}$
M4-VLA11	16:23:45.569	–26:29:19.22	0.10	0.10	27.9	3.2	15.3	4.8	···	3.25	r_h	$-1.78^{+0.85}_{-0.94}$
M4-VLA12	16:23:34.128	–26:33:27.26	0.10	0.10	27.3	2.8	< 9.3	11.7	···	1.90	r_h	< -1.0
M4-VLA13	16:23:41.611	–26:29:38.11	0.08	0.07	26.1	2.8	16.9	2.9	···	2.43	r_h	$-1.24^{+0.55}_{-0.61}$
M4-VLA14	16:23:30.635	–26:33:51.64	0.10	0.10	23.5	3.0	15.2	4.3	···	2.50	r_h	$-1.35^{+0.84}_{-0.98}$
M4-VLA15	16:23:27.998	–26:32:33.78	0.08	0.07	23.1	2.7	18.1	2.9	···	1.86	r_h	$-0.71^{+0.55}_{-0.59}$
M4-VLA16	16:23:38.879	–26:28:10.69	0.10	0.10	22.1	3.3	< 16.2	4.4	···	3.49	r_h	< 1.1
M4-VLA17	16:23:32.883	–26:33:53.89	0.08	0.07	21.0	3.1	22.5	3.4	ext.?	2.38	r_h	$+0.17^{+0.58}_{-0.60}$
M4-VLA18	16:23:21.935	–26:32:33.96	0.10	0.10	20.6	3.0	20.6	5.2	···	3.10	r_h	$-0.16^{+0.78}_{-0.96}$
M4-VLA19	16:23:25.999	–26:33:54.77	0.10	0.10	19.1	3.7	< 14.7	8.1	···	3.10	r_h	< 1.3
M4-VLA20	16:23:38.936	–26:32:00.14	0.10	0.10	18.8	2.6	< 7.3	4.3	···	0.98	r_c	< -0.4
M4-VLA21	16:23:32.388	–26:28:26.37	0.10	0.10	18.5	3.1	< 13.9	11.9	···	3.18	r_h	< 1.2
M4-VLA22	16:23:29.112	–26:29:58.59	0.10	0.10	18.3	2.9	< 9.1	4.1	···	2.07	r_h	< 0.3
M4-VLA23	16:23:36.625	–26:29:21.27	0.10	0.10	17.8	2.6	< 9.1	2.7	···	2.24	r_h	< 0.3
M4-VLA24	16:23:37.532	–26:32:25.06	0.10	0.10	15.7	2.3	8.8	2.3	···	1.02	r_c	$-1.68^{+0.80}_{-0.88}$

Table 3.3 (cont'd)

ID	R.A.[a] (h:m:s)	Dec.[a] (°:′:″)	R.A. unc. (″)	Dec. unc. (″)	S_5[b] (μJy)	S_5 unc. (μJy)	S_7[c] (μJy)	S_7 unc. (μJy)	note[d]	radius[e] (′)	loc.[f]	α[g]
M4-VLA25	16:23:41.489	–26:30:11.61	0.10	0.10	14.7	2.5	< 8.3	3.7	···	1.99	r_h	< 0.7
M4-VLA26	16:23:32.795	–26:31:18.59	0.10	0.10	14.3	2.2	9.8	2.2	···	0.56	r_c	$-1.11^{+0.76}_{-0.84}$
M4-VLA27	16:23:30.645	–26:32:46.59	0.10	0.10	13.9	2.7	10.7	2.8	···	1.56	r_h	$-0.82^{+0.91}_{-1.04}$
M4-VLA28	16:23:40.762	–26:30:09.14	0.10	0.10	12.9	2.4	< 7.7	3.5	···	1.91	r_h	< 0.9
M4-VLA29	16:23:35.070	–26:31:13.85	0.10	0.10	12.7	2.1	8.7	2.0	···	0.33	r_c	$-1.11^{+0.80}_{-0.88}$
M4-VLA30	16:23:30.219	–26:30:45.07	0.10	0.10	11.1	2.1	10.6	2.2	···	1.35	r_h	$-0.20^{+0.75}_{-0.82}$
M4-VLA31	16:23:31.448	–26:30:57.90	0.08	0.07	9.7	2.7	12.2	2.2	···	1.00	r_c	$+0.37^{+0.59}_{-0.77}$
M4-VLA32	16:23:43.619	–26:33:42.70	0.08	0.07	< 9.6	4.8	28.0	4.3	···	2.88	r_h	> -0.4
M4-VLA33	16:23:44.837	–26:28:56.90	0.08	0.07	< 9.3	-1.0	28.2	5.3	···	3.41	r_h	> -2.2
M4-VLA34	16:23:29.634	–26:29:36.49	0.08	0.07	< 9.0	5.4	22.7	3.3	···	2.30	r_h	> -0.4
M4-VLA35	16:23:47.311	–26:32:10.09	0.08	0.07	< 8.4	1.8	21.3	4.1	···	2.81	r_h	> -2.1
M4-VLA36	16:23:28.574	–26:33:24.56	0.08	0.07	< 8.3	-3.2	21.7	3.2	···	2.34	r_h	> -0.4
M4-VLA37	16:23:36.309	–26:29:31.21	0.08	0.07	< 7.6	-2.2	13.4	2.6	···	2.06	r_h	> -2.1
M4-VLA38	16:23:36.372	–26:30:26.23	0.08	0.07	< 6.5	0.9	10.5	2.1	···	1.17	r_h	> -2.5
M5-VLA1	15:18:36.065	+02:03:05.19	0.03	0.03	129.8	2.1	106.3	2.3	···	1.91	···	$-0.61^{+0.08}_{-0.08}$
M5-VLA2	15:18:47.968	+02:04:34.54	0.04	0.05	34.1	3.1	23.7	5.0	···	3.70	···	$-1.23^{+0.69}_{-0.81}$
M5-VLA3	15:18:27.727	+02:07:51.86	0.03	0.03	33.1	2.7	24.7	3.9	···	3.30	···	$-0.96^{+0.54}_{-0.60}$
M5-VLA4	15:18:28.868	+02:04:26.39	0.03	0.03	29.8	1.9	18.4	2.0	···	1.16	r_h	$-1.51^{+0.39}_{-0.41}$

Table 3.3 (cont'd)

ID	R.A.[a] (h:m:s)	Dec.[a] (°:′:″)	R.A. unc. (″)	Dec. unc. (″)	S_5[b] (μJy)	S_5 unc. (μJy)	S_7[c] (μJy)	S_7 unc. (μJy)	note[d]	radius[e] (′)	loc.[f]	α[g]
M5-VLA5	15:18:32.237	+02:02:47.31	0.03	0.03	28.4	2.2	17.3	2.5	···	2.09	···	$-1.57^{+0.49}_{-0.55}$
M5-VLA6	15:18:19.018	+02:03:49.66	0.04	0.05	27.4	3.0	23.7	4.8	···	3.69	···	$-0.54^{+0.70}_{-0.81}$
M5-VLA7	15:18:38.704	+02:03:21.73	0.04	0.05	27.0	2.1	11.1	2.4	···	2.03	···	$-2.66^{+0.58}_{-0.52}$
M5-VLA8	15:18:42.000	+02:05:23.74	0.03	0.03	26.6	2.1	13.5	2.5	···	2.26	···	$-2.14^{+0.59}_{-0.64}$
M5-VLA9	15:18:40.940	+02:03:13.27	0.04	0.05	24.3	2.2	14.5	2.7	···	2.54	···	$-1.66^{+0.62}_{-0.70}$
M5-VLA10	15:18:29.835	+02:01:35.46	0.04	0.05	22.1	2.7	14.9	4.0	···	3.38	···	$-1.36^{+0.87}_{-1.01}$
M5-VLA11	15:18:19.822	+02:03:44.75	0.04	0.05	20.5	2.9	17.2	4.5	···	3.53	···	$-0.70^{+0.90}_{-1.08}$
M5-VLA12	15:18:32.329	+02:07:32.62	0.04	0.05	19.4	2.3	< 8.8	6.1	···	2.69	···	< -0.2
M5-VLA13	15:18:33.325	+02:05:27.35	0.04	0.05	18.8	1.9	< 5.5	2.3	···	0.59	r_h	< -1.4
M5-VLA14	15:18:20.864	+02:06:45.70	0.04	0.05	18.0	2.9	< 13.8	-6.5	···	3.62	···	< 1.3
M5-VLA15	15:18:30.030	+02:01:47.57	0.04	0.05	16.8	2.6	< 11.2	0.4	···	3.17	···	< 1.0
M5-VLA16	15:18:42.262	+02:05:26.04	0.03	0.03	15.1	2.1	13.7	2.5	···	2.33	···	$-0.36^{+0.71}_{-0.77}$
M5-VLA17	15:18:31.189	+02:01:57.40	0.04	0.05	14.2	2.5	< 9.7	4.9	···	2.95	···	< 1.1
M5-VLA18	15:18:24.103	+02:07:34.06	0.04	0.05	14.1	2.8	< 13.0	-0.5	···	3.53	···	< 1.4
M5-VLA19	15:18:28.172	+02:07:12.82	0.04	0.05	13.6	2.3	8.7	2.8	···	2.67	···	$-1.48^{+1.05}_{-1.11}$
M5-VLA20	15:18:39.040	+02:02:15.09	0.04	0.05	13.2	2.5	< 10.0	3.2	···	2.99	···	< 1.2
M5-VLA21	15:18:32.061	+02:07:28.29	0.04	0.05	12.6	2.3	< 8.4	4.5	···	2.62	···	< 1.0
M5-VLA22	15:18:29.899	+02:02:24.63	0.04	0.05	11.7	2.2	< 8.3	6.7	···	2.59	···	< 1.1

Table 3.3 (cont'd)

ID	R.A.[a] (h:m:s)	Dec.[a] (°:′:″)	R.A. unc. (″)	Dec. unc. (″)	S_5[b] (μJy)	S_5 unc. (μJy)	S_7[c] (μJy)	S_7 unc. (μJy)	note[d]	radius[e] (′)	loc.[f]	α[g]
M5-VLA23	15:18:27.209	+02:03:30.30	0.04	0.05	11.1	2.0	< 6.9	-2.0	···	2.02	···	< 0.9
M5-VLA24	15:18:34.158	+02:03:44.79	0.04	0.05	10.7	1.9	< 5.9	0.3	···	1.14	r_h	< 0.7
M5-VLA25	15:18:32.670	+02:05:23.74	0.04	0.05	9.7	1.9	< 5.5	1.9	···	0.55	r_h	< 0.8
M5-VLA26	15:18:27.569	+02:04:51.06	0.03	0.03	7.0	1.9	10.4	2.0	···	1.41	r_h	$+0.50^{+0.47}_{-0.75}$
M5-VLA27	15:18:47.266	+02:05:05.09	0.03	0.03	< 8.5	0.2	22.5	4.3	···	3.52	···	> -2.4
M5-VLA28	15:18:46.208	+02:05:45.16	0.03	0.03	< 7.9	1.3	21.5	4.0	···	3.37	···	> -2.2
M5-VLA29	15:18:28.590	+02:07:55.50	0.03	0.03	< 7.8	-0.2	20.2	3.7	···	3.27	···	> -2.0
M5-VLA30	15:18:20.041	+02:05:42.54	0.03	0.03	< 8.1	2.8	20.2	3.9	···	3.40	···	> -2.5
M5-VLA31	15:18:24.623	+02:07:18.28	0.03	0.03	< 7.7	-3.5	20.0	3.6	···	3.25	···	> -1.7
M5-VLA32	15:18:22.483	+02:03:09.83	0.03	0.03	< 7.7	-0.8	18.8	3.7	···	3.17	···	> -2.7
M5-VLA33	15:18:22.219	+02:05:54.37	0.03	0.03	< 7.2	1.5	18.3	3.2	···	2.94	···	> -1.6
M5-VLA34	15:18:21.652	+02:06:19.16	0.03	0.03	< 7.8	-2.0	18.0	3.6	···	3.23	···	> -2.8
M5-VLA35	15:18:21.422	+02:04:47.94	0.03	0.03	< 7.3	2.3	17.7	3.2	···	2.95	···	> -1.8
M5-VLA36	15:18:26.540	+02:07:25.64	0.03	0.03	< 7.5	-1.7	17.1	3.3	···	3.06	···	> -2.4
M5-VLA37	15:18:32.269	+02:07:34.66	0.03	0.03	< 7.1	1.7	16.1	3.0	···	2.72	···	> -2.1
M5-VLA38	15:18:44.491	+02:04:38.66	0.03	0.03	< 7.3	-1.8	14.9	3.0	···	2.83	···	> -2.7
M5-VLA39	15:18:31.095	+02:02:28.91	0.03	0.03	< 6.7	-0.3	14.7	2.7	···	2.44	···	> -1.9
M5-VLA40	15:18:31.595	+02:07:24.39	0.03	0.03	< 6.7	-0.6	14.6	2.8	···	2.57	···	> -2.4

Table 3.3 (cont'd)

ID	R.A.[a] (h:m:s)	Dec.[a] (°:′:″)	R.A. unc. (″)	Dec. unc. (″)	S_5[b] (μJy)	S_5 unc. (μJy)	S_7[c] (μJy)	S_7 unc. (μJy)	note[d]	radius[e] (′)	loc.[f]	α[g]
M5-VLA41	15:18:23.930	+02:04:48.90	0.03	0.03	< 6.5	-2.0	13.7	2.5	···	2.32	···	> -1.9
M5-VLA42	15:18:25.483	+02:05:48.08	0.03	0.03	< 6.2	-0.2	12.7	2.4	···	2.15	···	> -2.3
M5-VLA43	15:18:42.001	+02:04:52.83	0.03	0.03	< 6.2	-5.5	12.6	2.4	···	2.20	···	> -2.3
M5-VLA44	15:18:39.131	+02:05:49.43	0.03	0.03	< 5.9	3.6	11.4	2.2	···	1.76	r_h	> -2.5
M5-VLA45	15:18:26.771	+02:05:49.79	0.03	0.03	< 6.1	-0.1	11.3	2.1	···	1.88	···	> -2.2
M5-VLA46	15:18:36.255	+02:03:39.31	0.03	0.03	< 5.7	-0.1	10.7	2.1	···	1.43	r_h	> -2.6
M5-VLA47	15:18:37.723	+02:05:58.54	0.03	0.03	< 5.9	-1.1	10.6	2.1	···	1.58	r_h	> -2.7
M5-VLA48	15:18:33.863	+02:05:41.82	0.03	0.03	< 5.7	-1.3	10.1	1.9	···	0.85	r_h	> -2.3
M9-VLA1	17:19:19.694	–18:31:44.25	0.03	0.03	598.5	2.0	492.9	2.4	···	2.02	···	$-0.58^{+0.02}_{-0.02}$
M9-VLA2	17:19:21.480	–18:28:44.37	0.03	0.03	328.0	2.4	270.4	3.8	···	3.21	···	$-0.57^{+0.05}_{-0.05}$
M9-VLA3	17:18:58.682	–18:30:12.98	0.03	0.03	165.9	2.3	115.5	3.3	···	3.20	···	$-1.08^{+0.09}_{-0.10}$
M9-VLA4	17:19:23.666	–18:30:30.21	0.03	0.03	57.3	2.2	54.8	3.4	···	2.86	···	$-0.14^{+0.22}_{-0.22}$
M9-VLA5	17:19:24.696	–18:32:26.08	0.03	0.03	47.4	2.6	37.3	4.3	···	3.39	···	$-0.75^{+0.37}_{-0.40}$
M9-VLA6	17:19:02.365	–18:29:09.00	0.03	0.03	44.5	2.0	28.5	2.9	···	2.88	···	$-1.35^{+0.32}_{-0.35}$
M9-VLA7	17:18:59.519	–18:32:10.31	0.03	0.03	41.7	2.3	26.6	3.3	···	3.14	···	$-1.37^{+0.39}_{-0.43}$
M9-VLA8	17:19:14.536	–18:33:58.16	0.03	0.03	36.6	2.5	25.4	3.6	···	3.06	···	$-1.13^{+0.46}_{-0.51}$
M9-VLA9	17:19:03.072	–18:33:00.72	0.03	0.03	33.0	2.1	19.7	3.1	···	2.90	···	$-1.60^{+0.49}_{-0.56}$
M9-VLA10	17:19:16.857	–18:33:40.64	0.03	0.03	30.5	2.3	25.8	3.5	···	2.96	···	$-0.54^{+0.46}_{-0.50}$

Table 3.3 (cont'd)

ID	R.A.[a] (h:m:s)	Dec.[a] (°:′:″)	R.A. unc. (″)	Dec. unc. (″)	S_5[b] (μJy)	S_5 unc. (μJy)	S_7[c] (μJy)	S_7 unc. (μJy)	note[d]	radius[e] (′)	loc.[f]	α[g]
M9-VLA11	17:19:05.645	–18:30:14.18	0.03	0.03	26.6	1.8	21.6	1.9	···	1.63	···	$-0.63^{+0.33}_{-0.34}$
M9-VLA12	17:19:19.856	–18:30:42.03	0.03	0.03	24.8	1.9	23.1	2.2	···	1.93	···	$-0.22^{+0.36}_{-0.37}$
M9-VLA13	17:19:04.853	–18:27:48.09	0.04	0.05	23.6	2.3	18.3	4.1	···	3.57	···	$-0.90^{+0.72}_{-0.86}$
M9-VLA14	17:19:22.615	–18:33:16.12	0.04	0.05	22.2	3.0	20.9	4.9	···	3.44	···	$-0.31^{+0.80}_{-0.95}$
M9-VLA15	17:19:11.555	–18:28:00.40	0.04	0.05	19.6	2.2	< 9.1	7.3	···	2.97	···	< -0.2
M9-VLA16	17:19:04.691	–18:29:18.18	···	···	18.7	1.9	21.3	2.3	ext.	2.37	···	$+0.38^{+0.44}_{-0.45}$
M9-VLA17	17:19:00.890	–18:32:32.89	0.03	0.03	17.7	2.1	18.9	3.2	ext.?	3.02	···	$+0.13^{+0.61}_{-0.67}$
M9-VLA18	17:19:13.757	–18:28:00.63	0.04	0.05	17.1	2.1	18.1	3.2	···	3.00	···	$+0.10^{+0.63}_{-0.69}$
M9-VLA19	17:19:15.059	–18:28:40.83	0.04	0.05	16.9	2.0	13.1	2.5	···	2.42	···	$-0.83^{+0.67}_{-0.75}$
M9-VLA20	17:19:09.380	–18:29:12.91	0.04	0.05	16.4	1.8	10.3	2.1	···	1.85	···	$-1.47^{+0.68}_{-0.77}$
M9-VLA21	17:18:58.508	–18:31:05.14	···	···	16.4	2.3	12.7	3.1	ext.	3.15	···	$-0.89^{+0.83}_{-0.97}$
M9-VLA22	17:19:06.791	–18:27:44.85	0.04	0.05	15.4	2.4	11.5	3.8	···	3.44	···	$-1.06^{+1.04}_{-1.22}$
M9-VLA24	17:19:11.256	–18:31:18.65	0.03	0.03	14.7	1.7	11.0	1.7	···	0.36	r_c	$-0.90^{+0.58}_{-0.62}$
M9-VLA25	17:19:17.605	–18:33:38.82	0.04	0.05	14.6	2.3	< 10.7	2.8	···	3.01	···	< 1.2
M9-VLA26	17:19:05.321	–18:33:34.67	0.04	0.05	13.7	2.3	15.1	3.4	···	3.02	···	$+0.13^{+0.75}_{-0.93}$
M9-VLA27	17:19:00.353	–18:30:41.13	0.04	0.05	13.4	2.0	< 7.9	1.1	···	2.72	···	< 0.7
M9-VLA28	17:19:25.877	–18:31:00.72	0.04	0.05	13.2	2.5	14.2	4.2	···	3.34	···	$-0.11^{+0.92}_{-1.26}$
M9-VLA29	17:19:07.037	–18:33:01.47	0.03	0.03	13.0	2.0	12.5	2.5	···	2.34	···	$-0.19^{+0.74}_{-0.83}$

Table 3.3 (cont'd)

ID	R.A.[a] (h:m:s)	Dec.[a] (°:′:″)	R.A. unc. (″)	Dec. unc. (″)	S_5[b] (μJy)	S_5 unc. (μJy)	S_7[c] (μJy)	S_7 unc. (μJy)	note[d]	radius[e] (′)	loc.[f]	α[g]
M9-VLA30	17:19:06.534	–18:27:56.02	0.04	0.05	12.8	2.3	< 10.3	-0.6	···	3.29	···	< 1.2
M9-VLA31	17:19:07.177	–18:31:22.06	0.03	0.03	12.7	1.7	11.7	1.8	···	1.16	···	$-0.27^{+0.61}_{-0.64}$
M9-VLA32	17:19:20.963	–18:33:30.24	0.04	0.05	12.4	2.4	< 12.7	1.9	···	3.34	···	< 1.4
M9-VLA33	17:19:17.161	–18:29:08.00	0.04	0.05	12.3	1.9	9.8	2.4	···	2.24	···	$-0.79^{+0.86}_{-0.99}$
M9-VLA34	17:19:03.489	–18:32:41.70	0.04	0.05	12.1	2.1	< 8.0	1.9	···	2.61	···	< 1.0
M9-VLA35	17:19:08.488	–18:27:57.09	0.04	0.05	12.0	2.2	< 9.8	-1.2	···	3.12	···	< 1.2
M9-VLA36	17:19:19.307	–18:33:27.46	0.04	0.05	11.5	2.2	< 10.8	3.1	···	3.06	···	< 1.3
M9-VLA37	17:19:08.697	–18:32:02.69	0.04	0.05	11.4	1.8	8.4	1.9	···	1.30	···	$-0.99^{+0.83}_{-0.92}$
M9-VLA38	17:19:05.942	–18:32:11.62	0.04	0.05	11.2	1.9	< 6.1	3.0	···	1.84	···	< 0.6
M9-VLA39	17:19:02.209	–18:29:07.55	0.04	0.05	11.2	2.1	< 9.0	2.3	···	2.93	···	< 1.2
M9-VLA40	17:19:20.544	–18:29:52.17	0.04	0.05	10.9	2.0	< 7.4	-1.1	···	2.35	···	< 1.0
M9-VLA41	17:19:05.377	–18:28:14.19	0.04	0.05	10.8	2.2	< 9.8	1.2	···	3.13	···	< 1.3
M9-VLA42	17:19:09.447	–18:32:08.80	0.03	0.03	10.7	1.8	9.5	1.9	···	1.29	···	$-0.42^{+0.78}_{-0.85}$
M9-VLA43	17:19:18.314	–18:30:51.94	0.04	0.05	10.5	1.8	< 6.0	3.0	···	1.55	···	< 0.8
M9-VLA44	17:19:02.861	–18:29:12.70	0.04	0.05	10.2	2.0	< 8.1	1.7	···	2.75	···	< 1.1
M9-VLA45	17:19:05.093	–18:31:56.10	0.04	0.05	9.9	1.8	< 6.1	2.1	···	1.85	···	< 0.9
M9-VLA46	17:19:13.980	–18:29:03.06	0.04	0.05	9.7	1.9	< 6.6	0.1	···	1.99	···	< 1.0
M9-VLA47	17:19:13.375	–18:29:20.62	0.04	0.05	9.6	1.8	6.8	2.0	···	1.67	···	$-1.16^{+1.02}_{-1.13}$

Table 3.3 (cont'd)

ID	R.A.[a] (h:m:s)	Dec.[a] (°:′:″)	R.A. unc. (″)	Dec. unc. (″)	S_5[b] (μJy)	S_5 unc. (μJy)	S_7[c] (μJy)	S_7 unc. (μJy)	note[d]	radius[e] (′)	loc.[f]	α[g]
M9-VLA48	17:19:06.221	–18:30:55.76	0.03	0.03	9.3	1.7	11.8	1.8	···	1.32	···	$+0.52^{+0.50}_{-0.64}$
M9-VLA49	17:19:07.989	–18:30:23.30	0.04	0.05	9.0	1.7	< 5.2	0.5	···	1.07	···	< 0.8
M9-VLA50	17:19:11.417	–18:30:16.22	0.04	0.05	8.8	1.7	< 5.1	0.8	···	0.71	r_h	< 0.8
M9-VLA51	17:19:22.160	–18:33:15.35	···	···	< 11.0	14.5	28.1	4.9	ext.	3.35	···	···
M9-VLA52	17:18:59.574	–18:28:54.10	0.03	0.03	< 7.2	0.3	24.7	4.2	···	3.56	···	> -1.4
M9-VLA53	17:19:26.889	–18:30:45.66	0.03	0.03	< 8.0	5.1	23.9	4.7	···	3.59	···	> -2.9
M9-VLA54	17:19:22.736	–18:28:29.57	0.03	0.03	< 7.7	-0.6	23.1	4.6	···	3.59	···	> -3.0
M9-VLA55	17:19:14.253	–18:27:53.55	0.03	0.03	< 6.9	2.4	17.7	3.3	···	3.14	···	> -2.1
M9-VLA56	17:18:59.476	–18:30:46.04	0.03	0.03	< 6.3	4.9	17.0	2.8	···	2.92	···	> -1.1
M9-VLA57	17:19:00.493	–18:31:03.32	0.03	0.03	< 6.1	-0.4	16.6	2.7	···	2.68	···	> -1.0
M9-VLA58	17:19:02.698	–18:28:40.10	0.03	0.03	< 6.6	1.9	16.3	3.1	···	3.16	···	> -2.4
M9-VLA59	17:18:58.753	–18:30:55.65	0.03	0.03	< 6.5	0.0	14.7	2.9	···	3.09	···	> -2.6
M9-VLA60	17:19:00.704	–18:31:26.16	0.03	0.03	< 5.9	-2.6	14.7	2.7	···	2.67	···	> -1.9
M9-VLA61	17:19:19.782	–18:32:30.87	0.03	0.03	< 6.1	-0.2	14.3	2.7	···	2.44	···	> -2.1
M9-VLA62	17:19:05.618	–18:32:28.24	0.03	0.03	< 5.7	1.0	12.8	2.2	···	2.09	···	> -1.5
M9-VLA63	17:19:17.991	–18:29:40.06	0.03	0.03	< 5.7	-0.2	12.6	2.2	···	1.97	···	> -1.6
M9-VLA64	17:19:18.729	–18:31:56.05	0.03	0.03	< 5.6	-0.2	11.8	2.3	···	1.91	···	> -2.5
M9-VLA65	17:19:11.628	–18:29:38.56	0.03	0.03	< 5.3	0.7	10.3	1.8	···	1.33	···	> -1.7

Table 3.3 (cont'd)

ID	R.A.[a] (h:m:s)	Dec.[a] (°:′:″)	R.A. unc. (″)	Dec. unc. (″)	S_5[b] (μJy)	S_5 unc. (μJy)	S_7[c] (μJy)	S_7 unc. (μJy)	note[d]	radius[e] (′)	loc.[f]	α[g]
M9-VLA66	17:19:08.710	–18:30:16.39	0.03	0.03	< 5.1	-0.1	9.2	1.7	···	1.01	···	> -2.1
M10-VLA2	16:57:07.591	–04:08:03.14	···	···	862.2	5.2	384.5	3.5	ext.	2.11	···	$-2.06^{+0.03}_{-0.03}$
M10-VLA3	16:57:16.462	–04:08:42.55	0.04	0.04	235.2	3.6	94.7	4.5	···	3.33	···	$-2.33^{+0.13}_{-0.13}$
M10-VLA4	16:57:12.945	–04:08:22.12	0.04	0.04	144.0	3.1	109.1	3.2	···	2.60	···	$-0.71^{+0.09}_{-0.09}$
M10-VLA5	16:57:13.966	–04:07:24.13	0.04	0.04	98.4	2.8	63.4	2.4	···	1.91	r_h	$-1.12^{+0.12}_{-0.12}$
M10-VLA6	16:57:10.762	–04:07:12.17	0.04	0.04	97.7	2.6	114.7	2.3	···	1.32	r_h	$+0.41^{+0.09}_{-0.08}$
M10-VLA7	16:57:04.104	–04:05:28.56	0.04	0.04	74.6	2.6	58.9	2.0	···	1.30	r_h	$-0.60^{+0.12}_{-0.12}$
M10-VLA8	16:57:07.789	–04:08:44.82	0.04	0.04	71.8	5.7	39.1	4.7	ext.?	2.79	···	$-1.57^{+0.37}_{-0.39}$
M10-VLA9	16:57:22.822	–04:05:03.81	0.04	0.04	66.4	3.5	37.8	4.9	···	3.58	···	$-1.48^{+0.35}_{-0.39}$
M10-VLA10	16:57:07.724	–04:08:23.71	0.04	0.04	43.3	5.1	46.3	3.6	···	2.45	···	$+0.19^{+0.38}_{-0.36}$
M10-VLA11	16:57:02.521	–04:07:33.21	0.04	0.04	42.5	3.0	27.4	2.8	···	2.25	···	$-1.13^{+0.32}_{-0.33}$
M10-VLA12	16:57:17.619	–04:04:39.63	0.04	0.04	40.3	2.8	23.8	2.8	···	2.53	···	$-1.37^{+0.34}_{-0.37}$
M10-VLA13	16:57:06.839	–04:08:27.92	0.04	0.04	28.8	3.7	20.4	3.1	···	2.55	···	$-0.90^{+0.52}_{-0.54}$
M10-VLA14	16:56:59.504	–04:07:46.05	0.04	0.04	28.2	3.3	30.7	3.6	···	2.96	···	$+0.22^{+0.43}_{-0.43}$
M10-VLA15	16:57:10.655	–04:03:11.77	0.06	0.06	27.1	3.0	15.4	3.1	···	2.80	···	$-1.52^{+0.58}_{-0.66}$
M10-VLA16	16:57:18.367	–04:06:07.76	0.06	0.06	23.7	2.8	12.5	2.6	···	2.36	···	$-1.71^{+0.61}_{-0.69}$
M10-VLA17	16:57:09.140	–04:07:43.51	0.04	0.04	21.8	2.8	17.8	2.4	···	1.76	r_h	$-0.52^{+0.49}_{-0.49}$
M10-VLA18	16:57:13.967	–04:06:34.89	0.06	0.06	19.6	2.6	10.1	2.2	···	1.40	r_h	$-1.76^{+0.65}_{-0.71}$

Table 3.3 (cont'd)

ID	R.A.[a] (h:m:s)	Dec.[a] (°:′:″)	R.A. unc. (″)	Dec. unc. (″)	S_5[b] (μJy)	S_5 unc. (μJy)	S_7[c] (μJy)	S_7 unc. (μJy)	note[d]	radius[e] (′)	loc.[f]	α[g]
M10-VLA19	16:57:17.463	–04:03:13.81	0.06	0.06	18.2	3.3	< 12.4	-0.8	···	3.47	···	< 0.1
M10-VLA20	16:57:18.872	–04:04:25.92	0.06	0.06	18.0	3.0	< 9.7	3.4	···	2.92	···	< 0.5
M10-VLA21	16:57:05.175	–04:05:52.67	0.04	0.04	17.9	2.7	11.1	2.0	···	0.94	r_h	$-1.25^{+0.62}_{-0.64}$
M10-VLA22	16:57:01.613	–04:03:30.25	0.06	0.06	17.5	3.2	12.9	3.7	···	3.06	···	$-0.90^{+0.88}_{-1.04}$
M10-VLA23	16:56:57.935	–04:04:54.65	0.06	0.06	15.8	3.1	< 10.5	-4.0	···	2.94	···	< 1.0
M10-VLA24	16:57:10.846	–04:07:06.68	0.06	0.06	15.6	2.6	8.4	2.1	···	1.24	r_h	$-1.65^{+0.77}_{-0.83}$
M10-VLA25	16:57:04.920	–04:03:32.26	0.06	0.06	15.1	2.9	< 8.3	-1.4	···	2.63	···	< 0.8
M10-VLA26	16:57:04.929	–04:08:30.27	0.06	0.06	14.9	3.0	< 9.9	-2.2	···	2.73	···	< 1.0
M10-VLA27	16:57:15.314	–04:06:01.81	0.06	0.06	14.8	2.7	< 6.2	2.6	···	1.60	r_h	< 0.2
M10-VLA28	16:57:17.299	–04:07:27.73	0.06	0.06	14.8	3.0	< 9.0	2.4	···	2.57	···	< 0.9
M10-VLA29	16:57:07.932	–04:04:59.56	0.06	0.06	14.8	2.5	< 6.0	-3.2	···	1.00	r_h	< -0.1
M10-VLA30	16:57:16.088	–04:04:28.41	0.06	0.06	14.1	2.7	< 7.8	0.0	···	2.33	···	< 0.8
M10-VLA31	16:57:14.929	–04:07:10.09	0.06	0.06	13.7	2.7	< 7.4	-1.6	···	1.92	r_h	< 0.8
M10-VLA32	16:57:11.398	–04:07:17.68	0.06	0.06	13.2	2.6	8.1	2.2	···	1.46	r_h	$-1.32^{+0.88}_{-0.96}$
M10-VLA33	16:57:07.857	–04:06:56.27	0.04	0.04	12.3	2.6	16.2	2.0	···	1.01	r_h	$+0.63^{+0.48}_{-0.55}$
M10-VLA34	16:57:18.789	–04:08:33.37	0.04	0.04	< 11.6	3.4	25.2	5.0	···	3.57	···	> -2.0
M10-VLA35	16:57:23.149	–04:05:40.93	0.04	0.04	< 10.2	4.7	24.3	4.5	···	3.56	···	> -1.3
M10-VLA36	16:57:01.008	–04:08:34.19	0.04	0.04	< 10.1	4.5	22.6	4.3	···	3.27	···	> -1.6

Table 3.3 (cont'd)

ID	R.A.[a] (h:m:s)	Dec.[a] (°:′:″)	R.A. unc. (″)	Dec. unc. (″)	S_5[b] (μJy)	S_5 unc. (μJy)	S_7[c] (μJy)	S_7 unc. (μJy)	note[d]	radius[e] (′)	loc.[f]	α[g]
M10-VLA37	16:57:07.679	–04:09:04.53	0.04	0.04	< 11.1	0.2	22.0	4.0	···	3.12	···	> -1.3
M10-VLA38	16:57:10.717	–04:08:37.58	0.04	0.04	< 9.4	6.1	20.1	3.3	···	2.70	···	> -0.8
M10-VLA39	16:57:13.101	–04:03:08.21	0.04	0.04	< 9.2	2.0	17.6	3.3	···	3.02	···	> -1.6
M10-VLA40	16:57:15.784	–04:04:03.46	0.04	0.04	< 8.2	5.4	14.8	2.9	···	2.56	···	> -2.0
M10-VLA41	16:57:00.704	–04:05:50.65	0.04	0.04	< 8.0	1.7	14.1	2.5	···	2.05	···	> -1.5
M10-VLA42	16:57:00.799	–04:06:51.38	0.04	0.04	< 8.2	-1.4	13.6	2.6	···	2.21	···	> -1.9
M10-VLA43	16:57:10.871	–04:03:44.22	0.04	0.04	< 8.0	-5.4	13.4	2.7	···	2.28	···	> -2.2
M10-VLA44	16:57:07.819	–04:03:49.06	0.04	0.04	< 8.6	-4.1	12.9	2.5	···	2.17	···	> -2.1
M10-VLA45	16:57:06.831	–04:04:50.08	0.04	0.04	< 7.9	3.1	12.4	2.0	···	1.25	r_h	> -1.3
M10-VLA46	16:57:10.328	–04:04:32.97	0.04	0.04	< 7.6	5.8	11.6	2.0	···	1.46	r_h	> -1.6
M10-VLA47	16:57:05.520	–04:04:59.07	0.04	0.04	< 7.9	-3.7	11.5	2.1	···	1.30	r_h	> -1.9
M10-VLA48	16:57:10.488	–04:06:35.37	0.04	0.04	< 7.7	0.7	11.4	1.9	···	0.74	r_c	> -1.5
M10-VLA49	16:57:14.506	–04:05:33.20	0.04	0.04	< 7.3	-1.3	11.0	2.1	···	1.45	r_h	> -2.0
M10-VLA50	16:57:05.347	–04:06:28.41	0.04	0.04	< 7.6	4.4	10.4	1.9	···	1.03	r_h	> -2.0
M10-VLA51	16:57:08.351	–04:06:07.67	0.04	0.04	< 7.4	1.3	9.4	1.8	···	0.21	r_c	> -2.2
M12-VLA1	16:47:13.231	–01:54:17.52	0.03	0.04	145.3	2.5	109.0	2.9	···	2.63	···	$-0.89^{+0.10}_{-0.10}$
M12-VLA2	16:47:00.195	–01:56:52.59	0.03	0.04	110.1	2.9	68.0	4.1	···	3.49	···	$-1.49^{+0.20}_{-0.21}$
M12-VLA3	16:47:15.744	–01:54:43.18	0.03	0.04	72.1	2.4	86.8	2.6	···	2.23	···	$+0.57^{+0.14}_{-0.14}$

Table 3.3 (cont'd)

ID	R.A.[a] (h:m:s)	Dec.[a] (°:′:″)	R.A. unc. (″)	Dec. unc. (″)	S_5[b] (μJy)	S_5 unc. (μJy)	S_7[c] (μJy)	S_7 unc. (μJy)	note[d]	radius[e] (′)	loc.[f]	α[g]
M12-VLA4	16:47:02.012	–01:57:36.58	0.03	0.04	64.1	2.6	39.0	3.4	···	3.12	···	$-1.55^{+0.29}_{-0.31}$
M12-VLA5	16:47:15.941	–01:55:15.70	0.03	0.04	49.1	2.1	43.2	2.1	···	1.71	r_h	$-0.39^{+0.20}_{-0.20}$
M12-VLA6	16:47:21.700	–01:58:28.31	0.03	0.04	48.9	2.4	34.1	2.8	···	2.44	···	$-1.12^{+0.29}_{-0.30}$
M12-VLA7	16:47:04.776	–01:57:15.33	0.03	0.04	33.9	2.3	22.1	2.6	···	2.38	···	$-1.34^{+0.41}_{-0.44}$
M12-VLA8	16:47:04.734	–01:56:43.79	0.03	0.04	33.7	2.3	19.3	2.6	···	2.37	···	$-1.75^{+0.45}_{-0.50}$
M12-VLA9	16:47:26.040	–01:55:20.09	0.03	0.04	33.0	2.9	19.1	3.7	···	3.36	···	$-1.77^{+0.63}_{-0.71}$
M12-VLA10	16:47:23.635	–01:58:30.16	···	···	31.9	2.7	22.0	3.0	ext.	2.85	···	$-1.18^{+0.49}_{-0.53}$
M12-VLA11	16:47:12.968	–01:55:30.77	0.03	0.04	24.9	2.0	19.8	2.0	···	1.43	r_h	$-0.72^{+0.40}_{-0.41}$
M12-VLA12	16:47:23.078	–01:54:37.64	0.04	0.05	24.8	2.8	15.1	3.5	···	3.19	···	$-1.62^{+0.76}_{-0.85}$
M12-VLA13	16:47:06.558	–01:55:02.64	0.03	0.04	24.0	2.5	14.8	2.8	···	2.67	···	$-1.56^{+0.65}_{-0.73}$
M12-VLA14	16:47:22.809	–01:56:36.20	0.03	0.04	23.4	2.3	16.9	2.4	···	2.18	···	$-1.04^{+0.53}_{-0.57}$
M12-VLA15	16:47:28.080	–01:57:20.99	0.04	0.05	21.5	2.9	< 12.1	6.2	···	3.50	···	< 0.5
M12-VLA16	16:47:28.496	–01:57:03.27	0.04	0.05	19.8	3.0	< 13.3	2.9	···	3.58	···	< 1.0
M12-VLA17	16:47:23.521	–01:58:34.40	0.03	0.04	18.7	2.8	14.0	3.2	ext.?	2.86	···	$-0.98^{+0.85}_{-0.95}$
M12-VLA18	16:47:26.080	–01:58:56.90	0.04	0.05	17.1	3.0	< 12.8	-2.4	···	3.60	···	< 1.3
M12-VLA19	16:47:10.458	–01:54:14.80	0.04	0.05	16.8	2.5	< 9.2	6.7	···	2.82	···	< 0.6
M12-VLA20	16:47:23.423	–01:59:22.52	0.04	0.05	16.4	2.8	< 11.5	-4.1	···	3.38	···	< 1.2
M12-VLA21	16:47:21.644	–01:57:03.41	0.03	0.04	16.1	2.2	12.8	2.2	···	1.87	···	$-0.74^{+0.69}_{-0.73}$

Table 3.3 (cont'd)

ID	R.A.[a] (h:m:s)	Dec.[a] (°:′:″)	R.A. unc. (″)	Dec. unc. (″)	S_5[b] (μJy)	S_5 unc. (μJy)	S_7[c] (μJy)	S_7 unc. (μJy)	note[d]	radius[e] (′)	loc.[f]	α[g]
M12-VLA22	16:47:20.500	–01:57:36.50	0.03	0.04	15.8	2.2	10.4	2.1	···	1.73	r_h	$-1.35^{+0.77}_{-0.83}$
M12-VLA23	16:47:00.400	–01:58:06.30	0.04	0.05	15.7	3.1	< 13.2	-4.7	···	3.64	···	< 1.3
M12-VLA24	16:47:10.117	-02:00:16.56	0.04	0.05	15.3	3.0	< 12.7	-0.5	···	3.51	···	< 1.3
M12-VLA25	16:47:24.497	–01:54:51.37	0.04	0.05	14.7	2.7	< 10.8	1.2	···	3.30	···	< 1.2
M12-VLA26	16:47:01.593	–01:57:50.21	0.04	0.05	14.4	2.7	< 10.8	1.5	···	3.28	···	< 1.2
M12-VLA27	16:47:13.180	–01:59:32.80	0.04	0.05	14.0	2.5	< 8.3	0.1	···	2.65	···	< 0.9
M12-VLA28	16:47:21.278	–01:54:31.44	0.04	0.05	13.7	2.5	< 9.3	1.8	···	2.97	···	< 1.1
M12-VLA29	16:47:26.433	–01:55:56.00	0.04	0.05	13.6	2.7	< 10.2	-2.3	···	3.21	···	< 1.2
M12-VLA30	16:47:14.110	–01:55:34.80	0.04	0.05	13.4	2.1	10.4	2.0	···	1.33	r_h	$-0.82^{+0.78}_{-0.83}$
M12-VLA31	16:47:12.758	–01:53:59.76	0.04	0.05	13.0	2.5	< 9.4	2.2	···	2.94	···	< 1.1
M12-VLA32	16:47:04.535	–01:56:10.49	0.04	0.05	12.7	2.4	< 8.0	4.1	···	2.52	···	< 1.0
M12-VLA33	16:47:23.097	–01:57:15.56	0.04	0.05	12.6	2.3	8.5	2.4	···	2.25	···	$-1.30^{+1.02}_{-1.10}$
M12-VLA34	16:47:07.065	–01:58:24.41	0.04	0.05	12.5	2.4	< 7.4	-0.4	···	2.32	···	< 0.9
M12-VLA35	16:47:17.801	–01:57:23.10	0.04	0.05	12.4	2.0	9.0	1.9	···	1.02	r_h	$-1.04^{+0.83}_{-0.90}$
M12-VLA36	16:47:14.053	–01:57:36.09	0.04	0.05	12.3	2.0	6.2	1.8	···	0.69	r_c	$-2.07^{+0.92}_{-0.85}$
M12-VLA37	16:47:21.597	–01:55:32.20	0.03	0.04	12.2	2.4	12.5	2.4	···	2.31	···	$-0.03^{+0.77}_{-0.87}$
M12-VLA38	16:47:15.401	–01:55:28.14	0.03	0.04	12.2	2.2	13.8	2.1	···	1.47	r_h	$+0.30^{+0.62}_{-0.70}$
M12-VLA39	16:47:19.860	–01:56:19.15	0.04	0.05	11.7	2.1	< 6.1	1.8	···	1.54	r_h	< 0.7

Table 3.3 (cont'd)

ID	R.A.[a] (h:m:s)	Dec.[a] (°:′:″)	R.A. unc. (″)	Dec. unc. (″)	S_5[b] (μJy)	S_5 unc. (μJy)	S_7[c] (μJy)	S_7 unc. (μJy)	note[d]	radius[e] (′)	loc.[f]	α[g]
M12-VLA40	16:47:18.779	–01:55:37.60	0.04	0.05	11.6	2.1	8.0	2.1	···	1.72	r_h	$-1.24^{+0.98}_{-1.06}$
M12-VLA41	16:47:08.166	–01:55:44.53	0.03	0.04	11.5	2.2	11.7	2.2	···	1.90	···	$-0.04^{+0.75}_{-0.85}$
M12-VLA42	16:47:07.466	–01:57:46.63	0.04	0.05	11.2	2.1	< 6.9	-3.3	···	1.89	···	< 0.9
M12-VLA43	16:47:28.412	–01:57:34.40	0.03	0.04	< 8.9	-1.1	22.1	4.4	···	3.62	···	> -2.7
M12-VLA44	16:47:12.328	–01:53:36.23	0.03	0.04	< 8.2	-1.0	21.9	3.6	···	3.34	···	> -1.1
M12-VLA45	16:47:00.933	–01:55:37.53	0.03	0.04	< 8.7	-3.0	21.7	4.3	···	3.55	···	> -2.7
M12-VLA46	16:47:09.567	-02:00:11.23	0.03	0.04	< 8.5	2.9	20.7	4.0	···	3.47	···	> -2.4
M12-VLA47	16:47:00.868	–01:56:53.35	0.03	0.04	< 8.4	-1.0	20.5	3.9	···	3.33	···	> -2.2
M12-VLA48	16:47:03.502	–01:54:57.25	0.03	0.04	< 8.5	-3.1	20.4	3.7	···	3.31	···	> -1.8
M12-VLA49	16:47:08.504	–01:53:44.92	0.03	0.04	< 8.7	-1.0	20.2	4.0	···	3.47	···	> -2.7
M12-VLA50	16:47:06.241	–01:59:07.58	0.03	0.04	< 7.8	4.6	20.1	3.2	···	2.97	···	> -0.9
M12-VLA51	16:47:11.699	-02:00:08.08	0.03	0.04	< 8.2	4.2	19.7	3.8	···	3.28	···	> -2.4
M12-VLA52	16:47:01.913	–01:58:08.40	0.03	0.04	< 8.1	-1.7	18.6	3.7	···	3.30	···	> -2.6
M12-VLA53	16:47:05.247	–01:58:20.97	0.03	0.04	< 7.4	-3.1	17.2	2.8	···	2.65	···	> -1.2
M12-VLA54	16:47:03.314	–01:55:40.24	0.03	0.04	< 7.7	-3.5	17.0	3.3	···	2.99	···	> -2.4
M12-VLA55	16:47:04.694	–01:56:19.69	0.03	0.04	< 6.8	4.1	15.4	2.6	···	2.44	···	> -1.4
M12-VLA56	16:47:19.201	–01:54:23.42	0.03	0.04	< 7.6	-0.1	14.9	2.9	···	2.82	···	> -2.4
M12-VLA57	16:47:23.312	–01:56:41.47	0.03	0.04	< 6.8	1.3	14.6	2.5	···	2.29	···	> -1.5

Table 3.3 (cont'd)

ID	R.A.[a] (h:m:s)	Dec.[a] (°:′:″)	R.A. unc. (″)	Dec. unc. (″)	S_5[b] (μJy)	S_5 unc. (μJy)	S_7[c] (μJy)	S_7 unc. (μJy)	note[d]	radius[e] (′)	loc.[f]	α[g]
M12-VLA58	16:47:07.157	–01:55:07.23	0.03	0.04	< 7.2	-0.1	13.8	2.8	···	2.51	···	> -2.8
M12-VLA59	16:47:19.946	–01:58:45.93	0.03	0.04	< 7.0	-1.1	13.4	2.6	···	2.35	···	> -2.5
M12-VLA60	16:47:17.778	–01:59:07.02	0.03	0.04	< 7.1	-2.7	13.2	2.5	···	2.38	···	> -2.2
M12-VLA61	16:47:21.741	–01:57:53.94	0.03	0.04	< 6.6	2.7	12.7	2.4	···	2.13	···	> -2.3
M12-VLA62	16:47:17.564	–01:58:45.29	0.03	0.04	< 6.7	1.5	12.6	2.4	···	2.03	···	> -2.3
M12-VLA63	16:47:08.818	–01:55:44.03	0.03	0.04	< 6.4	2.8	12.0	2.1	···	1.78	···	> -1.8
M12-VLA64	16:47:16.014	–01:55:22.99	0.03	0.04	< 6.4	1.0	11.5	2.0	···	1.60	r_h	> -1.8
M12-VLA65	16:47:10.951	–01:56:01.43	0.03	0.04	< 6.2	5.9	11.0	1.9	···	1.20	r_h	> -1.8
M12-VLA66	16:47:20.346	–01:57:49.40	0.03	0.04	< 6.5	-2.0	10.4	2.0	···	1.79	···	> -2.5
M12-VLA67	16:47:09.302	–01:57:48.79	0.03	0.04	< 6.2	1.4	10.4	2.0	···	1.52	r_h	> -2.5
M12-VLA68	16:47:08.690	–01:56:39.28	0.03	0.04	< 6.2	-0.2	9.9	2.0	···	1.40	r_h	> -2.8
M12-VLA69	16:47:11.506	–01:57:21.39	0.03	0.04	< 5.9	2.6	9.5	1.8	···	0.80	r_h	> -2.4
M13-VLA1	16:41:46.710	+36:24:23.86	0.04	0.03	101.4	2.5	83.3	4.3	···	3.38	···	$-0.55^{+0.15}_{-0.16}$
M13-VLA2	16:41:49.662	+36:30:43.31	0.04	0.03	87.4	2.8	67.0	5.8	···	3.56	···	$-0.75^{+0.25}_{-0.26}$
M13-VLA3	16:41:45.938	+36:25:32.45	0.04	0.03	63.8	2.1	62.5	2.9	···	2.26	···	$-0.06^{+0.16}_{-0.16}$
M13-VLA4	16:41:37.133	+36:26:33.60	0.04	0.03	34.0	1.9	24.3	2.3	···	1.32	r_h	$-0.94^{+0.30}_{-0.31}$
M13-VLA5	16:41:39.132	+36:29:14.13	0.04	0.03	32.9	2.1	26.2	2.5	···	1.69	r_h	$-0.64^{+0.31}_{-0.33}$
M13-VLA6	16:41:28.611	+36:25:14.89	0.05	0.05	28.8	2.5	< 13.7	13.9	···	3.45	···	< -0.3

Table 3.3 (cont'd)

ID	R.A.[a] (h:m:s)	Dec.[a] (°:′:″)	R.A. unc. (″)	Dec. unc. (″)	S_5[b] (μJy)	S_5 unc. (μJy)	S_7[c] (μJy)	S_7 unc. (μJy)	note[d]	radius[e] (′)	loc.[f]	α[g]
M13-VLA7	16:41:32.595	+36:30:37.64	0.04	0.03	28.7	2.8	< 16.1	10.2	ext.?	3.49	···	< 0.2
M13-VLA8	16:41:55.248	+36:25:40.09	0.04	0.03	22.2	2.7	40.5	4.5	···	3.42	···	$+1.24^{+0.19}_{-0.31}$
M13-VLA9	16:41:46.288	+36:28:01.58	0.04	0.03	20.9	2.1	18.5	2.2	···	1.11	r_h	$-0.34^{+0.43}_{-0.44}$
M13-VLA10	16:41:48.586	+36:29:23.27	0.04	0.03	20.9	2.3	16.5	3.0	···	2.33	···	$-0.72^{+0.58}_{-0.66}$
M13-VLA11	16:41:31.947	+36:28:38.27	0.04	0.03	20.7	2.2	19.8	2.8	···	2.14	···	$-0.15^{+0.49}_{-0.52}$
M13-VLA12	16:41:45.949	+36:24:22.16	0.04	0.03	19.9	2.5	22.9	4.1	···	3.36	···	$+0.31^{+0.58}_{-0.65}$
M13-VLA13	16:41:31.561	+36:30:32.58	0.05	0.05	19.7	2.7	< 16.8	12.3	···	3.53	···	< 1.3
M13-VLA14	16:41:32.833	+36:30:39.00	0.04	0.03	19.3	2.8	21.5	5.4	ext.?	3.49	···	$+0.10^{+0.75}_{-0.97}$
M13-VLA15	16:41:34.443	+36:26:36.54	0.05	0.05	17.7	2.0	10.7	2.4	···	1.68	r_h	$-1.48^{+0.68}_{-0.79}$
M13-VLA16	16:41:38.371	+36:29:54.55	0.04	0.03	17.5	2.2	18.5	3.2	···	2.39	···	$+0.10^{+0.58}_{-0.64}$
M13-VLA17	16:41:23.644	+36:27:56.48	0.05	0.05	17.3	2.6	< 16.1	-0.6	···	3.55	···	< 1.4
M13-VLA18	16:41:37.597	+36:25:16.58	0.05	0.05	16.6	2.3	12.2	2.8	···	2.43	···	$-0.95^{+0.74}_{-0.85}$
M13-VLA19	16:41:37.338	+36:30:42.48	0.05	0.05	14.8	2.6	18.3	4.6	···	3.21	···	$+0.33^{+0.71}_{-0.97}$
M13-VLA20	16:41:51.957	+36:30:01.42	0.05	0.05	14.7	2.8	< 13.3	3.6	···	3.25	···	< 1.3
M13-VLA21	16:41:40.878	+36:27:15.02	0.05	0.05	14.5	2.0	9.2	2.1	···	0.35	r_c	$-1.34^{+0.73}_{-0.83}$
M13-VLA22	16:41:35.020	+36:25:33.44	0.05	0.05	13.8	2.3	8.9	2.9	···	2.39	···	$-1.35^{+0.97}_{-1.09}$
M13-VLA23	16:41:34.986	+36:30:07.98	0.05	0.05	13.6	2.4	< 11.5	5.1	···	2.83	···	< 1.3
M13-VLA24	16:41:48.396	+36:31:01.81	0.04	0.03	13.0	2.8	38.2	6.2	···	3.73	···	$+1.27^{+0.17}_{-0.36}$

Table 3.3 (cont'd)

ID	R.A.[a] (h:m:s)	Dec.[a] (°:′:″)	R.A. unc. (″)	Dec. unc. (″)	S_5[b] (μJy)	S_5 unc. (μJy)	S_7[c] (μJy)	S_7 unc. (μJy)	note[d]	radius[e] (′)	loc.[f]	α[g]
M13-VLA25	16:41:36.558	+36:26:17.04	0.05	0.05	12.8	2.1	10.8	2.3	···	1.61	r_h	$-0.54^{+0.75}_{-0.83}$
M13-VLA26	16:41:46.851	+36:27:31.03	0.04	0.03	12.5	2.0	12.9	2.1	ext.?	1.14	r_h	$+0.05^{+0.62}_{-0.65}$
M13-VLA27	16:41:48.729	+36:27:54.74	0.05	0.05	10.5	2.1	< 6.8	-2.7	···	1.55	r_h	< 0.9
M13-VLA28	16:41:41.895	+36:28:11.71	0.05	0.05	10.2	2.0	< 6.0	1.8	···	0.62	r_c	< 0.8
M13-VLA29	16:41:39.842	+36:31:01.95	0.04	0.03	< 8.1	-1.3	42.3	5.7	···	3.45	···	> 0.0
M13-VLA30	16:41:49.693	+36:30:41.57	0.04	0.03	< 8.4	-1.1	37.5	5.7	···	3.54	···	> -0.5
M13-VLA31	16:41:45.419	+36:31:09.55	0.04	0.03	< 8.3	-2.3	36.8	6.6	···	3.66	···	> -3.0
M13-VLA32	16:41:48.159	+36:30:42.87	0.04	0.03	< 8.0	-2.6	31.1	5.3	···	3.42	···	> -1.4
M13-VLA33	16:41:24.055	+36:26:39.67	0.04	0.03	< 8.0	0.0	30.8	5.0	···	3.57	···	> -0.8
M13-VLA34	16:41:59.197	+36:27:50.74	0.04	0.03	< 8.3	1.7	30.7	5.6	···	3.63	···	> -2.4
M13-VLA35	16:41:54.471	+36:25:27.16	0.04	0.03	< 7.7	4.0	30.3	4.7	···	3.42	···	> -0.5
M13-VLA36	16:41:26.301	+36:29:23.36	0.04	0.03	< 8.2	0.3	29.6	5.2	···	3.49	···	> -1.7
M13-VLA37	16:41:47.562	+36:30:22.77	0.04	0.03	< 7.6	-3.9	26.9	4.2	···	3.06	···	> -0.5
M13-VLA38	16:41:57.924	+36:28:16.26	0.04	0.03	< 8.0	1.8	26.8	5.0	···	3.43	···	> -2.5
M13-VLA39	16:41:24.375	+36:28:11.92	0.04	0.03	< 8.0	0.9	26.1	4.9	···	3.44	···	> -2.4
M13-VLA40	16:41:55.244	+36:29:04.16	0.04	0.03	< 7.8	-6.0	25.6	4.4	···	3.18	···	> -1.1
M13-VLA41	16:41:28.671	+36:26:04.08	0.04	0.03	< 7.3	-3.5	23.6	3.5	···	2.95	···	> -0.3
M13-VLA42	16:41:26.794	+36:25:48.39	0.04	0.03	< 7.8	3.1	22.9	4.5	···	3.41	···	> -2.7

Table 3.3 (cont'd)

ID	R.A.[a] (h:m:s)	Dec.[a] (°:′:″)	R.A. unc. (″)	Dec. unc. (″)	S_5[b] (μJy)	S_5 unc. (μJy)	S_7[c] (μJy)	S_7 unc. (μJy)	note[d]	radius[e] (′)	loc.[f]	α[g]
M13-VLA43	16:41:47.259	+36:30:11.01	0.04	0.03	< 7.1	-0.8	22.5	4.1	···	2.86	···	> -1.9
M13-VLA44	16:41:55.927	+36:28:31.63	0.04	0.03	< 7.5	-1.7	21.9	4.1	···	3.10	···	> -2.1
M13-VLA45	16:41:48.951	+36:24:52.71	0.04	0.03	< 7.4	-0.5	21.9	3.6	···	3.13	···	> -0.8
M13-VLA46	16:41:38.164	+36:30:24.39	0.04	0.03	< 7.3	-2.7	21.7	3.9	···	2.88	···	> -1.6
M13-VLA47	16:41:27.789	+36:26:52.00	0.04	0.03	< 7.0	0.7	19.8	3.3	···	2.80	···	> -0.9
M13-VLA48	16:41:39.834	+36:24:40.52	0.04	0.03	< 7.1	1.2	19.1	3.3	···	2.93	···	> -1.2
M13-VLA49	16:41:53.711	+36:28:55.22	0.04	0.03	< 7.3	-1.9	18.5	3.7	···	2.84	···	> -2.7
M13-VLA50	16:41:53.708	+36:27:50.59	0.04	0.03	< 6.7	-1.8	18.0	3.1	···	2.53	···	> -1.1
M13-VLA51	16:41:35.520	+36:25:04.37	0.04	0.03	< 6.9	0.2	17.9	3.1	···	2.77	···	> -1.2
M13-VLA52	16:41:51.031	+36:25:30.42	0.04	0.03	< 6.9	0.7	17.4	3.4	···	2.87	···	> -2.4
M13-VLA53	16:41:48.539	+36:29:36.76	0.04	0.03	< 6.9	-2.5	17.2	3.2	···	2.50	···	> -1.8
M13-VLA54	16:41:48.269	+36:25:07.40	0.04	0.03	< 7.0	-1.7	16.8	3.4	···	2.85	···	> -2.7
M13-VLA55	16:41:52.287	+36:27:15.59	0.04	0.03	< 6.6	-0.4	15.3	2.8	···	2.25	···	> -1.6
M13-VLA56	16:41:50.332	+36:28:41.92	0.04	0.03	< 6.7	-3.2	14.5	2.8	···	2.14	···	> -2.1
M13-VLA57	16:41:50.439	+36:27:32.48	0.04	0.03	< 6.3	-1.8	14.5	2.5	···	1.86	···	> -1.3
M13-VLA58	16:41:44.713	+36:29:28.95	0.04	0.03	< 6.5	1.7	14.0	2.6	···	2.02	···	> -1.8
M13-VLA59	16:41:32.104	+36:28:08.58	0.04	0.03	< 6.4	2.7	13.8	2.7	···	1.91	···	> -2.3
M13-VLA60	16:41:32.976	+36:28:39.63	0.04	0.03	< 6.5	3.0	13.4	2.6	···	1.97	···	> -2.2

Table 3.3 (cont'd)

ID	R.A.[a] (h:m:s)	Dec.[a] (°:′:″)	R.A. unc. (″)	Dec. unc. (″)	S_5[b] (μJy)	S_5 unc. (μJy)	S_7[c] (μJy)	S_7 unc. (μJy)	note[d]	radius[e] (′)	loc.[f]	α[g]
M13-VLA61	16:41:42.941	+36:25:25.26	0.04	0.03	< 6.4	-0.2	13.3	2.5	···	2.20	···	> -1.9
M13-VLA62	16:41:37.853	+36:26:08.23	0.04	0.03	< 6.2	1.9	11.4	2.3	···	1.61	r_h	> -2.5
M13-VLA63	16:41:41.047	+36:27:43.99	0.04	0.03	< 5.9	-1.8	11.0	2.0	···	0.14	r_c	> -1.7
M13-VLA64	16:41:44.698	+36:27:19.56	0.04	0.03	< 6.0	0.3	10.2	2.0	···	0.75	r_h	> -2.3
M14-VLA1	17:37:41.709	–03:16:59.87	0.03	0.03	278.7	2.4	209.9	2.9	···	2.64	···	$-0.93^{+0.05}_{-0.05}$
M14-VLA2	17:37:40.355	–03:13:21.61	0.03	0.03	193.4	2.0	176.4	2.1	···	1.75	···	$-0.30^{+0.05}_{-0.05}$
M14-VLA3	17:37:38.570	–03:12:54.02	0.03	0.03	138.5	2.1	78.3	2.2	···	1.95	···	$-1.86^{+0.10}_{-0.11}$
M14-VLA4	17:37:35.292	–03:13:52.57	0.03	0.03	100.1	1.9	56.5	1.8	···	0.90	r_h	$-1.87^{+0.12}_{-0.12}$
M14-VLA5	17:37:38.537	–03:18:02.15	0.03	0.03	90.0	2.8	52.9	3.8	···	3.34	···	$-1.75^{+0.25}_{-0.26}$
M14-VLA6	17:37:34.272	–03:17:35.40	0.03	0.03	73.1	2.4	47.8	3.0	···	2.87	···	$-1.39^{+0.23}_{-0.24}$
M14-VLA7	17:37:34.121	–03:13:15.81	0.03	0.03	53.8	2.0	35.8	2.0	···	1.57	···	$-1.34^{+0.22}_{-0.22}$
M14-VLA8	17:37:34.327	–03:14:42.22	0.03	0.03	46.9	1.9	26.6	1.8	···	0.45	r_c	$-1.86^{+0.25}_{-0.26}$
M14-VLA9	17:37:45.118	–03:12:34.44	0.03	0.03	45.0	2.6	29.1	3.5	···	3.13	···	$-1.46^{+0.43}_{-0.46}$
M14-VLA10	17:37:30.096	–03:13:42.31	0.03	0.03	42.3	2.1	20.1	2.1	···	1.83	···	$-2.45^{+0.37}_{-0.39}$
M14-VLA11	17:37:37.139	–03:14:47.04	0.03	0.03	38.6	1.9	26.5	1.7	···	0.26	r_c	$-1.23^{+0.26}_{-0.27}$
M14-VLA12	17:37:44.914	–03:17:38.19	0.03	0.03	38.0	3.0	36.2	4.5	···	3.63	···	$-0.19^{+0.48}_{-0.51}$
M14-VLA13	17:37:26.534	–03:12:49.67	0.03	0.03	36.9	2.6	23.7	3.3	···	3.07	···	$-1.49^{+0.50}_{-0.55}$
M14-VLA14	17:37:44.864	–03:13:25.08	0.03	0.03	36.3	2.3	23.0	2.6	···	2.56	···	$-1.52^{+0.41}_{-0.45}$

Table 3.3 (cont'd)

ID	R.A.[a] (h:m:s)	Dec.[a] (°:′:″)	R.A. unc. (″)	Dec. unc. (″)	S_5[b] (μJy)	S_5 unc. (μJy)	S_7[c] (μJy)	S_7 unc. (μJy)	note[d]	radius[e] (′)	loc.[f]	α[g]
M14-VLA15	17:37:37.567	–03:15:11.85	0.03	0.03	36.0	1.9	34.0	1.7	···	0.57	r_c	$-0.19^{+0.24}_{-0.24}$
M14-VLA16	17:37:31.431	–03:12:20.00	0.03	0.03	34.1	2.3	23.5	2.8	···	2.69	···	$-1.25^{+0.44}_{-0.48}$
M14-VLA17	17:37:44.727	–03:14:55.20	0.03	0.03	30.4	2.1	31.2	2.4	···	2.16	···	$+0.08^{+0.34}_{-0.34}$
M14-VLA18	17:37:45.314	–03:12:45.87	0.04	0.05	29.1	2.6	17.2	3.2	···	3.04	···	$-1.80^{+0.66}_{-0.72}$
M14-VLA19	17:37:32.461	–03:11:56.15	0.04	0.05	26.1	2.5	14.3	3.1	···	2.96	···	$-2.02^{+0.72}_{-0.76}$
M14-VLA20	17:37:27.167	–03:15:57.80	0.03	0.03	23.8	2.3	16.8	2.6	···	2.54	···	$-1.19^{+0.59}_{-0.65}$
M14-VLA21	17:37:25.184	–03:14:12.67	0.03	0.03	22.2	2.4	20.7	2.9	···	2.78	···	$-0.26^{+0.58}_{-0.61}$
M14-VLA22	17:37:37.810	–03:13:37.75	0.04	0.05	21.2	2.0	8.6	1.9	···	1.20	r_h	$-2.76^{+0.61}_{-0.49}$
M14-VLA23	17:37:24.650	–03:16:18.22	0.04	0.05	21.0	2.8	< 10.5	6.2	···	3.25	···	< 0.3
M14-VLA24	17:37:31.548	–03:11:39.99	0.04	0.05	20.5	2.7	< 11.0	5.9	···	3.29	···	< 0.4
M14-VLA25	17:37:40.898	–03:13:04.62	0.04	0.05	20.4	2.1	11.2	2.4	···	2.06	···	$-2.01^{+0.73}_{-0.76}$
M14-VLA26	17:37:41.520	–03:13:20.16	0.03	0.03	19.4	2.1	21.6	2.2	···	1.96	···	$+0.35^{+0.48}_{-0.49}$
M14-VLA27	17:37:35.825	–03:12:14.52	0.04	0.05	19.1	2.2	11.6	2.7	···	2.51	···	$-1.72^{+0.81}_{-0.88}$
M14-VLA28	17:37:36.384	–03:15:50.75	0.03	0.03	18.8	2.0	21.3	1.8	···	1.09	r_h	$+0.41^{+0.45}_{-0.44}$
M14-VLA29	17:37:42.537	–03:17:33.45	0.04	0.05	18.8	2.7	12.2	3.6	···	3.23	···	$-1.52^{+1.00}_{-1.07}$
M14-VLA30	17:37:37.839	–03:13:36.75	0.03	0.03	17.6	2.1	12.5	1.9	···	1.22	r_h	$-1.15^{+0.64}_{-0.67}$
M14-VLA31	17:37:32.014	–03:16:55.59	0.04	0.05	16.7	2.3	11.1	2.6	···	2.40	···	$-1.42^{+0.87}_{-0.95}$
M14-VLA32	17:37:43.581	–03:11:56.20	0.04	0.05	16.3	2.8	< 11.5	5.1	···	3.38	···	< 1.2

Table 3.3 (cont'd)

ID	R.A.[a] (h:m:s)	Dec.[a] (°:′:″)	R.A. unc. (″)	Dec. unc. (″)	S_5[b] (μJy)	S_5 unc. (μJy)	S_7[c] (μJy)	S_7 unc. (μJy)	note[d]	radius[e] (′)	loc.[f]	α[g]
M14-VLA33	17:37:31.896	–03:14:45.36	0.03	0.03	15.8	1.9	10.1	1.9	···	1.05	r_h	$-1.53^{+0.73}_{-0.79}$
M14-VLA34	17:37:22.072	–03:14:17.27	0.04	0.05	15.7	2.9	< 12.3	6.0	···	3.53	···	< 1.3
M14-VLA35	17:37:41.649	–03:16:48.44	0.04	0.05	15.3	2.3	10.7	2.6	···	2.48	···	$-1.27^{+0.93}_{-1.01}$
M14-VLA36	17:37:32.187	–03:13:13.98	0.04	0.05	15.2	2.0	6.8	2.1	···	1.81	···	$-2.41^{+0.85}_{-0.71}$
M14-VLA37	17:37:38.698	–03:12:41.72	0.04	0.05	14.8	2.2	7.0	2.3	···	2.16	···	$-2.26^{+0.94}_{-0.80}$
M14-VLA38	17:37:26.251	–03:12:36.06	0.04	0.05	14.7	2.6	< 11.0	-1.6	···	3.27	···	< 1.2
M14-VLA39	17:37:29.837	–03:13:41.91	0.04	0.05	14.4	2.0	7.7	2.1	···	1.89	···	$-2.03^{+0.90}_{-0.86}$
M14-VLA40	17:37:37.253	–03:13:08.33	0.03	0.03	14.0	2.0	10.8	2.0	···	1.64	···	$-0.90^{+0.78}_{-0.83}$
M14-VLA41	17:37:36.208	–03:17:52.43	0.04	0.05	12.8	2.5	< 10.0	4.3	···	3.12	···	< 1.2
M14-VLA42	17:37:28.358	–03:16:32.25	0.04	0.05	12.7	2.2	< 8.2	0.7	···	2.63	···	< 1.0
M14-VLA43	17:37:38.014	–03:13:55.47	0.04	0.05	12.5	2.0	9.2	1.8	···	0.96	r_h	$-1.04^{+0.84}_{-0.89}$
M14-VLA44	17:37:24.972	–03:15:28.56	0.04	0.05	12.5	2.4	< 8.7	-4.8	···	2.87	···	< 1.1
M14-VLA45	17:37:35.890	–03:14:34.70	0.04	0.05	12.3	1.9	< 5.1	4.6	···	0.18	r_c	< 0.0
M14-VLA46	17:37:31.535	–03:12:17.39	0.04	0.05	12.0	2.4	< 8.4	4.1	···	2.72	···	< 1.1
M14-VLA47	17:37:40.029	–03:13:55.25	0.04	0.05	11.9	1.9	< 5.6	-2.3	···	1.29	r_h	< 0.4
M14-VLA48	17:37:38.470	–03:12:46.99	0.04	0.05	11.9	2.1	< 6.8	-0.3	···	2.06	···	< 0.9
M14-VLA49	17:37:43.495	–03:15:11.79	0.04	0.05	11.7	2.1	< 6.7	3.7	···	1.90	···	< 0.9
M14-VLA50	17:37:37.380	–03:13:52.38	0.04	0.05	11.6	2.0	< 5.4	1.5	···	0.94	r_h	< 0.5

Table 3.3 (cont'd)

ID	R.A.[a] (h:m:s)	Dec.[a] (°:′:″)	R.A. unc. (″)	Dec. unc. (″)	S_5[b] (μJy)	S_5 unc. (μJy)	S_7[c] (μJy)	S_7 unc. (μJy)	note[d]	radius[e] (′)	loc.[f]	α[g]
M14-VLA51	17:37:39.144	–03:14:26.13	0.04	0.05	10.9	1.9	7.8	1.8	···	0.82	r_h	$-1.16^{+0.95}_{-1.02}$
M14-VLA52	17:37:40.089	–03:13:55.18	0.04	0.05	10.9	1.9	< 5.7	5.1	···	1.30	r_h	< 0.7
M14-VLA53	17:37:28.487	–03:11:52.67	0.03	0.03	< 8.2	-4.6	23.8	3.9	···	3.45	···	> -1.2
M14-VLA54	17:37:47.987	–03:13:26.71	0.03	0.03	< 8.1	-3.2	21.1	3.5	···	3.24	···	> -1.3
M14-VLA55	17:37:49.132	–03:14:39.59	0.03	0.03	< 8.0	0.5	21.0	3.6	···	3.25	···	> -1.5
M14-VLA56	17:37:31.174	–03:11:50.03	0.03	0.03	< 7.8	-1.3	18.9	3.5	···	3.17	···	> -2.2
M14-VLA57	17:37:25.994	–03:13:03.10	0.03	0.03	< 7.7	1.6	17.1	3.2	···	3.04	···	> -2.3
M14-VLA58	17:37:28.072	–03:16:05.66	0.03	0.03	< 6.6	-1.4	13.7	2.5	···	2.41	···	> -2.1
M14-VLA59	17:37:26.735	–03:15:22.00	0.03	0.03	< 6.5	-0.8	13.6	2.5	···	2.42	···	> -2.1
M14-VLA60	17:37:27.873	–03:13:58.08	0.03	0.03	< 6.4	2.6	12.8	2.3	···	2.20	···	> -2.1
M14-VLA61	17:37:35.998	–03:13:18.23	0.03	0.03	< 5.9	0.7	11.6	1.9	···	1.45	···	> -1.6
M14-VLA62	17:37:41.547	–03:15:17.97	0.03	0.03	< 5.9	-1.5	9.7	1.9	···	1.46	···	> -2.7
M19-VLA1	17:02:45.415	–26:18:21.17	0.09	0.08	466.5	3.7	323.8	3.6	ext.?	2.84	···	$-1.19^{+0.04}_{-0.04}$
M19-VLA2	17:02:44.142	–26:17:48.95	0.09	0.08	290.5	3.0	219.4	2.9	···	2.24	···	$-0.91^{+0.05}_{-0.05}$
M19-VLA3	17:02:34.663	–26:14:47.97	0.09	0.08	77.8	3.1	41.0	2.4	···	1.46	···	$-2.09^{+0.23}_{-0.23}$
M19-VLA4	17:02:29.270	–26:14:35.45	0.09	0.08	76.2	3.1	51.6	2.7	···	2.42	···	$-1.27^{+0.21}_{-0.22}$
M19-VLA5	17:02:32.249	–26:18:14.03	0.09	0.08	57.2	2.8	46.6	2.8	···	2.49	···	$-0.67^{+0.25}_{-0.25}$
M19-VLA6	17:02:31.522	–26:16:11.57	0.09	0.08	53.7	2.8	45.4	2.1	···	1.41	···	$-0.54^{+0.23}_{-0.23}$

Table 3.3 (cont'd)

ID	R.A.[a] (h:m:s)	Dec.[a] (°:′:″)	R.A. unc. (″)	Dec. unc. (″)	S_5[b] (μJy)	S_5 unc. (μJy)	S_7[c] (μJy)	S_7 unc. (μJy)	note[d]	radius[e] (′)	loc.[f]	α[g]
M19-VLA7	17:02:41.068	–26:13:06.56	0.09	0.08	52.8	3.3	35.8	3.7	···	3.06	···	$-1.29^{+0.39}_{-0.41}$
M19-VLA8	17:02:25.886	–26:13:52.98	0.09	0.08	41.3	3.9	28.2	4.6	···	3.46	···	$-1.30^{+0.61}_{-0.67}$
M19-VLA9	17:02:49.463	–26:15:45.12	0.09	0.08	39.4	2.7	30.0	2.9	···	2.63	···	$-0.90^{+0.38}_{-0.40}$
M19-VLA10	17:02:36.248	–26:19:43.85	0.09	0.08	34.6	3.9	35.6	4.4	···	3.67	···	$+0.08^{+0.55}_{-0.56}$
M19-VLA11	17:02:41.405	–26:14:21.17	0.09	0.08	33.4	2.5	23.3	2.4	···	1.90	···	$-1.19^{+0.41}_{-0.43}$
M19-VLA12	17:02:44.906	–26:18:22.14	0.09	0.08	30.0	3.2	39.5	3.2	···	2.79	···	$+0.86^{+0.37}_{-0.41}$
M19-VLA13	17:02:36.840	–26:16:56.20	0.09	0.08	28.6	2.5	23.5	2.1	···	0.88	r_h	$-0.64^{+0.41}_{-0.42}$
M19-VLA14	17:02:44.407	–26:14:19.92	0.12	0.10	21.7	2.9	17.4	2.8	···	2.29	···	$-0.75^{+0.70}_{-0.72}$
M19-VLA15	17:02:53.947	–26:15:46.24	0.12	0.10	21.7	3.7	< 14.5	4.6	···	3.63	···	< 1.2
M19-VLA16	17:02:42.760	–26:17:20.54	0.12	0.10	21.6	2.3	14.4	2.0	···	1.68	···	$-1.35^{+0.57}_{-0.60}$
M19-VLA17	17:02:43.882	–26:15:03.62	0.12	0.10	21.6	2.7	9.9	2.5	···	1.70	···	$-2.42^{+0.77}_{-0.67}$
M19-VLA18	17:02:30.999	–26:12:48.02	0.12	0.10	20.6	4.0	13.7	4.5	···	3.62	···	$-1.38^{+1.16}_{-1.19}$
M19-VLA19	17:02:48.166	–26:17:02.80	0.09	0.08	20.1	2.9	15.5	2.9	ext.?	2.52	···	$-0.90^{+0.78}_{-0.83}$
M19-VLA20	17:02:48.800	–26:15:07.12	0.09	0.08	20.0	3.0	16.8	3.0	···	2.65	···	$-0.61^{+0.78}_{-0.82}$
M19-VLA21	17:02:37.230	–26:13:09.58	0.12	0.10	18.6	3.2	11.9	3.5	···	2.92	···	$-1.52^{+1.06}_{-1.08}$
M19-VLA22	17:02:30.649	–26:17:07.00	0.12	0.10	18.5	2.6	15.2	2.4	···	1.91	···	$-0.66^{+0.70}_{-0.72}$
M19-VLA23	17:02:36.357	–26:14:57.10	0.09	0.08	18.5	2.5	12.6	2.2	···	1.17	r_h	$-1.29^{+0.73}_{-0.77}$
M19-VLA24	17:02:25.914	–26:16:50.42	0.12	0.10	18.3	3.0	< 9.4	5.1	···	2.77	···	< 0.6

Table 3.3 (cont'd)

ID	R.A.[a] (h:m:s)	Dec.[a] (°:′:″)	R.A. unc. (″)	Dec. unc. (″)	S_5[b] (μJy)	S_5 unc. (μJy)	S_7[c] (μJy)	S_7 unc. (μJy)	note[d]	radius[e] (′)	loc.[f]	α[g]
M19-VLA25	17:02:45.942	–26:15:39.39	0.12	0.10	18.0	2.5	< 7.3	4.5	···	1.87	···	< -0.3
M19-VLA26	17:02:28.860	–26:15:25.23	0.12	0.10	17.1	2.8	< 8.1	5.5	···	2.11	···	< 0.4
M19-VLA27	17:02:47.823	–26:18:15.25	0.12	0.10	17.0	3.3	14.5	3.2	···	3.13	···	$-0.59^{+0.96}_{-1.03}$
M19-VLA28	17:02:31.439	–26:14:24.43	0.09	0.08	16.7	2.9	16.3	2.7	···	2.20	···	$-0.11^{+0.77}_{-0.81}$
M19-VLA29	17:02:45.311	–26:16:22.09	0.09	0.08	16.2	2.5	11.8	2.3	ext.?	1.71	···	$-1.08^{+0.83}_{-0.87}$
M19-VLA30	17:02:33.093	–26:18:02.57	0.12	0.10	15.7	2.8	10.5	2.8	···	2.23	···	$-1.38^{+1.03}_{-1.07}$
M19-VLA31	17:02:31.528	–26:14:34.73	0.12	0.10	14.7	2.9	< 8.2	8.9	···	2.06	···	< 1.0
M19-VLA32	17:02:35.341	–26:17:48.43	0.12	0.10	14.2	2.5	11.9	2.4	···	1.81	···	$-0.63^{+0.88}_{-0.95}$
M19-VLA33	17:02:29.925	–26:17:22.85	0.09	0.08	13.8	2.7	19.6	2.6	···	2.19	···	$+0.83^{+0.44}_{-0.61}$
M19-VLA34	17:02:37.488	–26:15:58.37	0.12	0.10	12.7	2.3	< 5.8	3.7	···	0.13	r_c	< 0.6
M19-VLA35	17:02:32.410	–26:14:46.33	0.09	0.08	12.5	2.8	14.2	2.6	···	1.78	···	$+0.23^{+0.73}_{-0.89}$
M19-VLA36	17:02:39.947	–26:16:04.75	0.09	0.08	12.0	2.4	10.6	2.0	···	0.48	r_h	$-0.44^{+0.87}_{-0.93}$
M19-VLA37	17:02:38.008	–26:15:16.24	0.12	0.10	11.9	2.3	< 6.7	4.4	···	0.81	r_h	< 0.9
M19-VLA38	17:02:33.296	–26:17:27.58	0.09	0.08	< 7.2	1.7	11.0	2.1	···	1.71	···	> -2.6
M22-VLA1	18:36:25.825	–23:54:13.74	0.10	0.09	59.2	2.2	59.2	2.0	···	0.43	r_c	$+0.00^{+0.16}_{-0.16}$
M22-VLA2	18:36:23.824	–23:54:33.51	0.10	0.09	54.3	2.4	53.2	2.0	···	0.27	r_c	$-0.06^{+0.19}_{-0.19}$
M22-VLA3	18:36:24.518	–23:50:41.68	···	···	1130.8	3.9	895.0	4.1	ext.	3.59	···	$-0.76^{+0.02}_{-0.02}$
M22-VLA4	18:36:20.669	–23:51:19.92	···	···	741.0	3.2	557.9	3.6	ext.	3.05	r_h	$-0.92^{+0.03}_{-0.03}$

Table 3.3 (cont'd)

ID	R.A.[a] (h:m:s)	Dec.[a] (°:′:″)	R.A. unc. (″)	Dec. unc. (″)	S_5[b] (μJy)	S_5 unc. (μJy)	S_7[c] (μJy)	S_7 unc. (μJy)	note[d]	radius[e] (′)	loc.[f]	α[g]
M22-VLA5	18:36:32.652	–23:52:39.87	0.10	0.09	110.8	3.1	78.7	2.9	···	2.57	r_h	$-1.11^{+0.15}_{-0.15}$
M22-VLA6	18:36:34.884	–23:55:40.01	0.10	0.09	77.2	3.1	50.9	3.1	···	2.86	r_h	$-1.36^{+0.24}_{-0.24}$
M22-VLA7	18:36:08.773	–23:54:14.54	0.10	0.09	70.0	3.7	47.1	4.2	···	3.47	···	$-1.31^{+0.33}_{-0.35}$
M22-VLA8	18:36:18.458	–23:57:18.07	0.10	0.09	69.9	3.6	46.0	4.3	···	3.27	r_h	$-1.38^{+0.34}_{-0.36}$
M22-VLA9	18:36:25.318	–23:55:31.12	0.10	0.09	63.0	2.5	34.3	2.3	···	1.28	r_c	$-1.99^{+0.25}_{-0.26}$
M22-VLA10	18:36:36.471	–23:55:01.07	0.10	0.09	52.5	2.8	40.4	3.6	···	2.96	r_h	$-0.87^{+0.33}_{-0.35}$
M22-VLA11	18:36:23.374	–23:50:54.69	0.10	0.09	43.8	3.4	38.0	3.7	···	3.38	···	$-0.47^{+0.40}_{-0.41}$
M22-VLA12	18:36:35.261	–23:54:56.75	0.10	0.09	43.6	3.1	32.3	3.0	···	2.67	r_h	$-0.99^{+0.38}_{-0.39}$
M22-VLA13	18:36:12.859	–23:53:31.10	0.10	0.09	36.5	3.3	23.1	3.0	···	2.65	r_h	$-1.52^{+0.52}_{-0.55}$
M22-VLA14	18:36:38.363	–23:54:24.28	0.10	0.09	35.4	3.3	20.7	3.8	···	3.30	r_h	$-1.81^{+0.65}_{-0.72}$
M22-VLA15	18:36:13.846	–23:52:50.77	0.10	0.09	34.2	3.0	31.8	2.9	···	2.72	r_h	$-0.24^{+0.41}_{-0.42}$
M22-VLA16	18:36:18.314	–23:57:36.42	0.10	0.09	31.4	3.9	30.9	5.3	···	3.56	···	$-0.11^{+0.68}_{-0.74}$
M22-VLA17	18:36:29.852	–23:53:07.27	0.10	0.09	30.1	2.7	23.5	2.2	···	1.78	r_h	$-0.80^{+0.43}_{-0.43}$
M22-VLA18	18:36:22.728	–23:51:17.07	0.13	0.11	27.4	3.1	< 10.1	3.5	···	3.01	r_h	< -0.7
M22-VLA19	18:36:32.551	–23:55:28.63	0.10	0.09	26.0	2.6	33.3	2.5	···	2.30	r_h	$+0.79^{+0.37}_{-0.39}$
M22-VLA20	18:36:28.205	–23:54:05.30	0.10	0.09	25.9	2.6	16.5	2.0	···	1.00	r_c	$-1.48^{+0.52}_{-0.53}$
M22-VLA21	18:36:35.316	–23:56:21.10	0.13	0.11	25.4	3.5	< 13.3	6.9	···	3.32	r_h	< 0.4
M22-VLA22	18:36:24.859	–23:55:14.95	0.10	0.09	25.0	2.7	19.5	2.1	···	0.99	r_c	$-0.81^{+0.51}_{-0.51}$

Table 3.3 (cont'd)

ID	R.A.[a] (h:m:s)	Dec.[a] (°:′:″)	R.A. unc. (″)	Dec. unc. (″)	S_5[b] (μJy)	S_5 unc. (μJy)	S_7[c] (μJy)	S_7 unc. (μJy)	note[d]	radius[e] (′)	loc.[f]	α[g]
M22-VLA23	18:36:33.174	–23:55:45.83	0.10	0.09	24.9	3.1	17.5	2.9	···	2.58	r_h	$-1.18^{+0.68}_{-0.72}$
M22-VLA24	18:36:32.368	–23:52:46.70	0.13	0.11	24.9	2.7	14.8	3.0	···	2.45	r_h	$-1.77^{+0.72}_{-0.79}$
M22-VLA25	18:36:09.529	–23:53:21.18	0.13	0.11	24.1	3.4	14.6	3.9	···	3.42	···	$-1.69^{+0.93}_{-0.97}$
M22-VLA26	18:36:10.950	–23:56:07.93	0.13	0.11	23.9	4.0	22.2	5.0	···	3.50	···	$-0.36^{+0.89}_{-1.02}$
M22-VLA27	18:36:15.556	–23:53:07.00	0.10	0.09	23.8	2.8	18.1	2.8	···	2.25	r_h	$-0.93^{+0.64}_{-0.67}$
M22-VLA28	18:36:31.471	–23:52:54.68	0.10	0.09	23.3	2.5	16.2	2.6	···	2.20	r_h	$-1.23^{+0.63}_{-0.67}$
M22-VLA29	18:36:34.254	–23:52:02.19	0.13	0.11	23.3	3.4	< 12.4	7.6	···	3.26	r_h	< 0.5
M22-VLA30	18:36:16.704	–23:54:59.38	0.10	0.09	22.7	2.7	17.9	2.5	···	1.80	r_h	$-0.80^{+0.61}_{-0.63}$
M22-VLA31	18:36:12.108	–23:55:21.54	0.13	0.11	19.0	3.6	< 10.9	11.3	···	2.91	r_h	< 1.0
M22-VLA32	18:36:34.556	–23:55:02.33	0.13	0.11	18.8	3.0	12.4	3.0	···	2.54	r_h	$-1.42^{+0.93}_{-1.00}$
M22-VLA33	18:36:32.917	–23:51:39.76	0.13	0.11	18.3	3.4	< 11.9	11.0	···	3.33	r_h	< 1.2
M22-VLA34	18:36:25.447	–23:54:51.74	0.10	0.09	17.5	2.8	11.9	2.0	···	0.67	r_c	$-1.27^{+0.78}_{-0.80}$
M22-VLA35	18:36:36.963	–23:53:53.00	0.13	0.11	16.5	3.1	< 11.4	5.7	···	3.00	r_h	< 1.2
M22-VLA36	18:36:23.400	–23:55:20.15	0.13	0.11	16.4	2.6	8.7	2.2	···	1.06	r_c	$-2.03^{+0.91}_{-0.85}$
M22-VLA37	18:36:30.021	–23:56:27.54	0.13	0.11	16.0	3.1	< 9.0	0.4	···	2.58	r_h	< 1.0
M22-VLA38	18:36:35.162	–23:54:32.72	0.13	0.11	15.6	2.9	< 8.4	2.4	···	2.58	r_h	< 0.9
M22-VLA39	18:36:22.860	–23:55:13.08	0.13	0.11	14.7	2.6	9.9	2.2	···	0.97	r_c	$-1.32^{+0.94}_{-0.98}$
M22-VLA40	18:36:20.486	–23:53:37.10	0.13	0.11	14.7	2.6	< 6.4	2.4	···	1.03	r_c	< 0.4

Table 3.3 (cont'd)

ID	R.A.[a] (h:m:s)	Dec.[a] (°:′:″)	R.A. unc. (″)	Dec. unc. (″)	S_5[b] (μJy)	S_5 unc. (μJy)	S_7[c] (μJy)	S_7 unc. (μJy)	note[d]	radius[e] (′)	loc.[f]	α[g]
M22-VLA41	18:36:24.299	–23:55:35.45	0.13	0.11	14.4	2.7	< 7.4	6.0	···	1.31	r_c	< 0.8
M22-VLA42	18:36:25.165	–23:55:18.21	0.13	0.11	13.8	2.3	10.8	2.2	···	1.06	r_c	$-0.85^{+0.88}_{-0.94}$
M22-VLA43	18:36:22.421	–23:55:58.74	0.13	0.11	13.7	2.7	< 7.9	5.8	···	1.73	r_h	< 1.0
M22-VLA44	18:36:29.404	–23:55:41.58	0.13	0.11	13.4	2.6	< 8.1	4.8	···	1.88	r_h	< 1.0
M22-VLA45	18:36:27.704	–23:53:56.62	0.10	0.09	13.2	2.6	11.7	2.1	···	0.93	r_c	$-0.42^{+0.87}_{-0.90}$
M22-VLA46	18:36:24.478	–23:53:24.63	0.10	0.09	12.8	2.4	11.9	2.3	···	0.88	r_c	$-0.30^{+0.85}_{-0.92}$
M22-VLA47	18:36:27.975	–23:52:59.22	0.10	0.09	< 7.3	-0.9	12.1	2.2	···	1.59	r_h	> -2.6
M28-VLA1	18:24:43.216	–24:53:09.88	0.04	0.06	341.2	2.9	278.2	3.6	···	2.56	···	$-0.52^{+0.04}_{-0.04}$
M28-VLA2	18:24:17.270	–24:52:44.53	0.04	0.06	184.7	3.7	112.7	6.1	···	3.55	···	$-1.27^{+0.14}_{-0.15}$
M28-VLA3	18:24:32.008	–24:52:10.90	0.04	0.06	134.2	2.6	57.9	2.1	···	0.17	r_c	$-2.15^{+0.10}_{-0.11}$
M28-VLA4	18:24:31.821	–24:48:49.81	0.04	0.06	54.2	3.5	34.0	4.4	···	3.39	···	$-1.22^{+0.36}_{-0.40}$
M28-VLA5	18:24:34.068	–24:53:04.48	0.04	0.06	46.7	2.5	25.9	2.2	···	0.91	r_h	$-1.51^{+0.25}_{-0.27}$
M28-VLA6	18:24:36.364	–24:53:45.15	0.04	0.06	43.5	2.8	26.7	2.8	···	1.74	r_h	$-1.26^{+0.31}_{-0.33}$
M28-VLA7	18:24:47.423	–24:52:23.43	0.06	0.09	40.2	3.6	< 14.2	8.5	···	3.34	···	< -1.0
M28-VLA8	18:24:29.573	–24:49:36.33	0.04	0.06	40.1	3.0	23.9	3.2	···	2.71	···	$-1.36^{+0.38}_{-0.42}$
M28-VLA9	18:24:44.682	–24:51:17.97	0.06	0.09	35.1	3.5	11.0	3.5	···	2.86	···	$-2.76^{+0.60}_{-0.49}$
M28-VLA10	18:24:36.231	–24:52:26.08	0.04	0.06	31.9	2.5	19.4	2.1	···	0.82	r_h	$-1.28^{+0.34}_{-0.35}$
M28-VLA11	18:24:16.918	–24:52:32.46	0.06	0.09	31.1	4.0	19.5	5.7	···	3.60	···	$-1.35^{+0.80}_{-0.96}$

Table 3.3 (cont'd)

ID	R.A.[a] (h:m:s)	Dec.[a] (°:′:″)	R.A. unc. (″)	Dec. unc. (″)	S_5[b] (μJy)	S_5 unc. (μJy)	S_7[c] (μJy)	S_7 unc. (μJy)	note[d]	radius[e] (′)	loc.[f]	α[g]
M28-VLA12	18:24:44.847	–24:53:25.78	0.06	0.09	26.8	3.6	< 12.3	5.0	···	3.00	···	< -0.1
M28-VLA13	18:24:36.287	–24:49:14.26	0.06	0.09	25.7	3.4	17.1	3.9	···	3.09	···	$-1.14^{+0.68}_{-0.79}$
M28-VLA14	18:24:25.481	–24:54:29.26	0.06	0.09	24.3	3.5	16.3	3.9	ext.?	2.80	···	$-1.12^{+0.72}_{-0.83}$
M28-VLA15	18:24:19.790	–24:54:09.15	0.06	0.09	24.0	3.9	20.9	5.9	···	3.52	···	$-0.52^{+0.84}_{-1.04}$
M28-VLA16	18:24:32.338	–24:55:38.33	0.06	0.09	22.7	3.9	< 16.9	7.5	···	3.42	···	< 1.1
M28-VLA17	18:24:33.026	–24:50:52.87	0.04	0.06	21.7	2.7	16.4	2.4	···	1.34	r_h	$-0.73^{+0.50}_{-0.52}$
M28-VLA18	18:24:20.590	–24:51:53.41	0.06	0.09	20.3	3.1	< 10.7	6.5	···	2.77	···	< 0.3
M28-VLA19	18:24:44.044	–24:49:43.12	0.06	0.09	19.4	3.8	< 15.4	-5.7	···	3.58	···	< 1.3
M28-VLA20	18:24:20.538	–24:51:32.79	0.04	0.06	19.1	3.2	18.5	3.7	···	2.85	···	$-0.13^{+0.68}_{-0.74}$
M28-VLA21	18:24:25.554	–24:54:56.29	0.06	0.09	19.1	3.8	< 14.5	-4.3	···	3.17	···	< 1.2
M28-VLA22	18:24:41.940	–24:52:52.06	0.06	0.09	18.5	2.8	14.3	2.9	···	2.19	···	$-0.71^{+0.67}_{-0.73}$
M28-VLA23	18:24:27.106	–24:54:46.92	0.04	0.06	18.0	3.5	24.1	4.4	···	2.86	···	$+0.62^{+0.54}_{-0.67}$
M28-VLA24	18:24:42.810	–24:53:39.72	0.06	0.09	17.8	3.2	< 10.9	1.5	···	2.70	···	< 0.9
M28-VLA25	18:24:31.826	–24:49:24.75	0.06	0.09	17.2	3.2	14.6	3.4	···	2.81	···	$-0.49^{+0.79}_{-0.88}$
M28-VLA26	18:24:28.865	–24:49:42.13	0.06	0.09	17.2	3.1	10.3	3.2	ext.?	2.66	···	$-1.44^{+0.91}_{-1.02}$
M28-VLA27	18:24:46.269	–24:52:08.80	0.06	0.09	17.2	3.2	< 11.9	4.1	···	3.07	···	< 1.1
M28-VLA28	18:24:29.338	–24:50:53.96	0.06	0.09	15.6	2.6	< 6.9	6.3	···	1.53	r_h	< 0.1
M28-VLA29	18:24:35.644	–24:52:53.31	0.06	0.09	15.5	2.6	7.7	2.2	···	0.94	r_h	$-1.85^{+0.82}_{-0.86}$

Table 3.3 (cont'd)

ID	R.A.[a] (h:m:s)	Dec.[a] (°:′:″)	R.A. unc. (″)	Dec. unc. (″)	S_5[b] (μJy)	S_5 unc. (μJy)	S_7[c] (μJy)	S_7 unc. (μJy)	note[d]	radius[e] (′)	loc.[f]	α[g]
M28-VLA30	18:24:42.679	–24:53:18.50	0.06	0.09	15.3	3.0	< 9.9	-2.9	···	2.51	···	< 1.0
M28-VLA31	18:24:32.188	–24:52:14.77	0.06	0.09	14.5	2.6	< 6.3	3.1	···	0.13	r_c	< 0.2
M28-VLA32	18:24:38.855	–24:53:03.79	0.04	0.06	14.4	2.7	14.2	2.5	···	1.63	r_h	$-0.05^{+0.66}_{-0.68}$
M28-VLA33	18:24:26.200	–24:53:13.63	0.04	0.06	11.2	2.9	15.6	2.7	···	1.79	r_h	$+0.61^{+0.51}_{-0.67}$
M28-VLA34	18:24:34.875	–24:53:21.86	0.04	0.06	10.7	2.7	12.0	2.4	···	1.25	r_h	$+0.16^{+0.67}_{-0.80}$
M28-VLA35	18:24:19.254	–24:53:29.65	0.04	0.06	< 10.9	-6.7	25.6	5.0	···	3.31	···	> -1.9
M28-VLA36	18:24:34.696	–24:55:09.75	0.04	0.06	< 10.2	4.1	22.6	4.4	···	2.98	···	> -1.8
M28-VLA37	18:24:22.529	–24:49:58.96	0.04	0.06	< 10.1	4.0	20.8	4.1	···	3.22	···	> -1.9
M28-VLA38	18:24:26.160	–24:54:04.61	0.04	0.06	< 9.5	-1.7	17.5	3.3	···	2.38	···	> -1.7
M28-VLA39	18:24:42.763	–24:53:20.62	0.04	0.06	< 9.2	4.3	16.3	3.2	···	2.54	···	> -2.0
M28-VLA40	18:24:22.378	–24:52:39.74	0.04	0.06	< 8.8	2.5	15.5	3.1	···	2.39	···	> -2.2
M28-VLA41	18:24:40.486	–24:52:34.84	0.04	0.06	< 8.5	-1.9	15.1	2.4	···	1.80	r_h	> -1.1
M28-VLA42	18:24:25.923	–24:50:38.09	0.04	0.06	< 8.2	-0.3	14.3	2.7	···	2.21	···	> -1.8
M28-VLA43	18:24:32.289	–24:50:19.93	0.04	0.06	< 8.3	-3.0	14.1	2.4	···	1.89	r_h	> -1.4
M28-VLA44	18:24:36.764	–24:52:56.14	0.04	0.06	< 7.9	1.1	13.1	2.3	···	1.16	r_h	> -1.5
M28-VLA45	18:24:34.223	–24:52:24.45	0.04	0.06	< 7.5	-0.3	11.3	2.1	···	0.39	r_h	> -1.9
M30-VLA1	21:40:33.245	–23:10:21.53	0.03	0.05	518.5	2.2	481.3	2.7	···	2.59	···	$-0.21^{+0.02}_{-0.02}$
M30-VLA2	21:40:08.296	–23:10:01.28	0.03	0.05	213.3	2.4	150.9	3.0	···	3.27	···	$-0.97^{+0.06}_{-0.06}$

Table 3.3 (cont'd)

ID	R.A.[a] (h:m:s)	Dec.[a] (°:′:″)	R.A. unc. (″)	Dec. unc. (″)	S_5[b] (μJy)	S_5 unc. (μJy)	S_7[c] (μJy)	S_7 unc. (μJy)	note[d]	radius[e] (′)	loc.[f]	α[g]
M30-VLA3	21:40:16.220	–23:08:20.12	0.03	0.05	189.9	2.2	192.6	2.7	···	2.81	···	$+0.04^{+0.05}_{-0.05}$
M30-VLA4	21:40:21.591	–23:11:28.01	0.03	0.05	60.8	1.8	40.8	1.7	···	0.69	r_h	$-1.12^{+0.14}_{-0.14}$
M30-VLA5	21:40:21.361	–23:13:12.65	0.03	0.05	59.7	2.2	38.5	2.3	···	2.43	···	$-1.24^{+0.20}_{-0.20}$
M30-VLA6	21:40:26.572	–23:11:18.82	0.03	0.05	57.1	1.8	34.2	1.7	···	1.15	···	$-1.44^{+0.16}_{-0.17}$
M30-VLA7	21:40:08.801	–23:12:16.57	0.03	0.05	51.5	2.4	32.4	3.3	···	3.40	···	$-1.32^{+0.31}_{-0.33}$
M30-VLA8	21:40:12.875	–23:13:23.15	0.03	0.05	46.4	2.5	30.3	3.5	···	3.35	···	$-1.22^{+0.35}_{-0.38}$
M30-VLA9	21:40:12.571	–23:11:46.96	0.03	0.05	43.9	2.1	26.1	2.2	···	2.41	···	$-1.47^{+0.27}_{-0.28}$
M30-VLA10	21:40:16.085	–23:09:57.75	0.03	0.05	43.8	1.9	24.8	1.8	···	1.62	···	$-1.60^{+0.23}_{-0.25}$
M30-VLA11	21:40:27.767	–23:10:27.54	0.03	0.05	42.1	1.8	29.3	1.7	···	1.34	···	$-1.02^{+0.20}_{-0.21}$
M30-VLA12	21:40:29.259	–23:10:31.65	0.03	0.05	38.7	1.9	32.1	1.8	···	1.66	···	$-0.53^{+0.21}_{-0.21}$
M30-VLA13	21:40:21.085	–23:07:19.96	0.04	0.07	34.9	2.5	15.7	3.4	···	3.47	···	$-2.30^{+0.59}_{-0.63}$
M30-VLA14	21:40:32.126	–23:09:52.49	0.03	0.05	32.7	2.0	22.5	2.3	···	2.48	···	$-1.07^{+0.33}_{-0.35}$
M30-VLA15	21:40:34.656	–23:10:57.23	0.03	0.05	31.6	2.2	24.5	2.6	···	2.89	···	$-0.74^{+0.35}_{-0.37}$
M30-VLA16	21:40:15.055	–23:12:17.84	0.03	0.05	25.3	2.0	12.5	2.2	···	2.21	···	$-2.04^{+0.52}_{-0.58}$
M30-VLA17	21:40:07.029	–23:11:50.64	0.04	0.07	24.7	2.5	17.4	3.7	···	3.62	···	$-1.09^{+0.65}_{-0.77}$
M30-VLA18	21:40:11.603	–23:11:02.33	0.03	0.05	23.6	2.1	14.7	2.4	···	2.43	···	$-1.38^{+0.52}_{-0.58}$
M30-VLA19	21:40:35.586	–23:12:12.97	0.03	0.05	22.8	2.3	24.6	3.3	···	3.41	···	$+0.18^{+0.47}_{-0.50}$
M30-VLA20	21:40:16.400	–23:07:38.18	0.04	0.07	20.8	2.6	14.5	3.2	···	3.42	···	$-1.11^{+0.71}_{-0.81}$

Table 3.3 (cont'd)

ID	R.A.[a] (h:m:s)	Dec.[a] (°:′:″)	R.A. unc. (″)	Dec. unc. (″)	S_5[b] (μJy)	S_5 unc. (μJy)	S_7[c] (μJy)	S_7 unc. (μJy)	note[d]	radius[e] (′)	loc.[f]	α[g]
M30-VLA21	21:40:13.091	–23:09:13.62	0.04	0.07	20.4	2.1	12.2	2.3	···	2.60	···	$-1.51^{+0.59}_{-0.67}$
M30-VLA22	21:40:36.664	–23:12:09.20	0.04	0.07	20.0	2.5	< 11.2	7.5	···	3.61	···	< 0.3
M30-VLA23	21:40:28.178	–23:13:22.28	0.04	0.07	19.6	2.3	9.1	2.9	···	2.93	···	$-2.17^{+0.81}_{-0.79}$
M30-VLA24	21:40:25.701	–23:12:41.87	0.03	0.05	17.7	2.1	15.7	2.2	···	2.08	···	$-0.36^{+0.52}_{-0.54}$
M30-VLA25	21:40:32.054	–23:11:47.25	0.03	0.05	17.4	1.9	15.2	2.2	···	2.49	···	$-0.41^{+0.52}_{-0.54}$
M30-VLA26	21:40:22.641	–23:07:44.00	0.04	0.07	16.9	2.4	< 8.5	3.2	···	3.06	···	< 0.2
M30-VLA27	21:40:14.900	–23:10:28.05	0.03	0.05	15.3	2.0	9.7	1.9	···	1.69	···	$-1.34^{+0.67}_{-0.74}$
M30-VLA28	21:40:21.511	–23:07:12.79	0.04	0.07	14.9	2.6	16.5	3.5	···	3.58	···	$+0.17^{+0.71}_{-0.84}$
M30-VLA29	21:40:26.496	–23:11:20.08	0.04	0.07	14.5	1.8	< 5.1	3.9	···	1.14	···	< -0.7
M30-VLA30	21:40:36.312	–23:09:46.57	0.04	0.07	14.3	2.5	< 9.8	1.6	···	3.42	···	< 1.1
M30-VLA31	21:40:16.416	–23:14:01.39	0.04	0.07	13.4	2.7	< 11.3	-0.4	···	3.49	···	< 1.3
M30-VLA32	21:40:11.539	–23:08:38.22	0.04	0.07	13.4	2.4	< 9.0	-2.9	···	3.25	···	< 1.0
M30-VLA33	21:40:22.928	–23:08:28.66	0.04	0.07	12.9	2.1	< 6.4	1.2	···	2.32	···	< 0.4
M30-VLA34	21:40:24.310	–23:12:33.53	0.04	0.07	12.9	1.9	< 6.0	3.6	···	1.84	···	< 0.1
M30-VLA35	21:40:12.602	–23:09:36.91	0.04	0.07	12.8	2.0	< 6.9	1.5	···	2.48	···	< 0.5
M30-VLA36	21:40:37.136	–23:11:17.23	0.04	0.07	12.7	2.5	11.5	3.3	···	3.49	···	$-0.48^{+0.95}_{-1.16}$
M30-VLA37	21:40:20.073	–23:11:48.98	0.04	0.07	12.2	1.8	8.5	1.7	···	1.13	···	$-1.07^{+0.71}_{-0.77}$
M30-VLA38	21:40:27.378	–23:10:49.25	0.04	0.07	12.1	1.8	< 5.0	2.3	···	1.21	···	< -0.2

Table 3.3 (cont'd)

ID	R.A.[a] (h:m:s)	Dec.[a] (°:′:″)	R.A. unc. (″)	Dec. unc. (″)	S_5[b] (μJy)	S_5 unc. (μJy)	S_7[c] (μJy)	S_7 unc. (μJy)	note[d]	radius[e] (′)	loc.[f]	α[g]
M30-VLA39	21:40:30.748	–23:09:06.97	0.04	0.07	12.1	2.1	< 7.2	2.4	···	2.60	···	< 0.8
M30-VLA40	21:40:16.462	–23:08:43.05	0.04	0.07	11.9	2.1	6.9	2.3	···	2.45	···	$-1.62^{+1.00}_{-1.04}$
M30-VLA41	21:40:11.756	–23:08:46.51	0.04	0.07	11.8	2.3	9.3	2.9	···	3.12	···	$-0.85^{+1.02}_{-1.19}$
M30-VLA42	21:40:28.936	–23:11:58.15	0.04	0.07	11.6	1.9	< 6.0	-1.2	···	1.96	···	< 0.4
M30-VLA43	21:40:31.027	–23:09:08.56	0.04	0.07	11.4	2.1	< 7.2	0.1	···	2.63	···	< 0.9
M30-VLA44	21:40:22.405	–23:10:48.91	0.04	0.07	11.3	1.8	< 4.8	2.6	···	0.07	r_h	< 0.0
M30-VLA45	21:40:18.739	–23:12:34.49	0.04	0.07	11.1	2.0	6.6	2.0	···	1.95	···	$-1.55^{+0.97}_{-1.02}$
M30-VLA46	21:40:31.007	–23:10:19.25	0.04	0.07	10.8	2.0	< 6.2	1.5	···	2.10	···	< 0.8
M30-VLA47	21:40:19.659	–23:13:18.48	0.04	0.07	10.7	2.1	< 7.4	-5.3	···	2.58	···	< 1.0
M30-VLA48	21:40:26.996	–23:13:07.01	0.04	0.07	10.6	2.1	< 7.3	-4.1	···	2.58	···	< 1.0
M30-VLA49	21:40:14.072	–23:12:02.09	0.04	0.07	10.6	2.0	< 6.4	0.6	···	2.23	···	< 0.8
M30-VLA50	21:40:17.394	–23:11:34.39	0.04	0.07	10.4	1.8	6.1	1.9	···	1.34	···	$-1.59^{+0.96}_{-1.01}$
M30-VLA51	21:40:12.302	–23:09:40.05	0.04	0.07	10.4	2.1	< 6.8	2.5	···	2.52	···	< 1.0
M30-VLA52	21:40:25.035	–23:11:49.42	0.04	0.07	10.1	1.7	< 5.2	0.1	···	1.23	···	< 0.5
M30-VLA53	21:40:26.316	–23:09:10.44	0.04	0.07	9.6	1.9	< 6.0	-1.0	···	1.88	···	< 0.9
M30-VLA54	21:40:18.058	–23:09:52.09	0.04	0.07	9.6	1.8	< 5.2	2.3	···	1.31	···	< 0.7
M30-VLA55	21:40:24.453	–23:10:56.10	0.04	0.07	9.2	1.7	< 5.0	-1.4	···	0.55	r_h	< 0.7
M30-VLA56	21:40:31.815	–23:13:43.83	0.03	0.05	< 7.8	0.7	22.2	4.0	···	3.69	···	> -1.6

Table 3.3 (cont'd)

ID	R.A.[a] (h:m:s)	Dec.[a] (°:′:″)	R.A. unc. (″)	Dec. unc. (″)	S_5[b] (μJy)	S_5 unc. (μJy)	S_7[c] (μJy)	S_7 unc. (μJy)	note[d]	radius[e] (′)	loc.[f]	α[g]
M30-VLA57	21:40:07.829	–23:09:31.28	0.03	0.05	< 7.4	-2.6	20.9	3.4	···	3.52	···	> -0.8
M30-VLA58	21:40:21.160	–23:07:15.18	0.03	0.05	< 7.7	2.7	20.7	3.4	···	3.55	···	> -0.9
M30-VLA59	21:40:10.795	–23:08:19.12	0.03	0.05	< 7.4	1.9	17.8	3.5	···	3.59	···	> -2.4
M30-VLA60	21:40:32.774	–23:12:44.82	0.03	0.05	< 6.8	-3.0	15.4	2.9	···	3.13	···	> -1.9
M30-VLA61	21:40:27.210	–23:08:11.27	0.03	0.05	< 6.7	-2.0	13.9	2.6	···	2.85	···	> -1.9
M30-VLA62	21:40:28.394	–23:12:56.42	0.03	0.05	< 6.4	1.2	13.2	2.5	···	2.59	···	> -2.0
M30-VLA63	21:40:24.396	–23:08:11.74	0.03	0.05	< 6.4	-2.2	12.9	2.3	···	2.65	···	> -1.6
M30-VLA64	21:40:32.983	–23:11:43.67	0.03	0.05	< 6.2	-0.5	12.9	2.5	···	2.67	···	> -2.3
M30-VLA65	21:40:13.678	–23:11:43.89	0.03	0.05	< 6.0	0.0	11.7	2.2	···	2.16	···	> -2.0
M30-VLA66	21:40:14.661	–23:11:17.39	0.03	0.05	< 5.8	2.4	9.8	1.8	···	1.79	···	> -2.0
M30-VLA67	21:40:29.064	–23:10:14.73	0.03	0.05	< 5.8	0.7	9.0	1.8	···	1.69	···	> -2.6
M54-VLA1	18:55:10.665	–30:26:51.19	0.04	0.07	2408.4	4.5	2480.9	8.8	···	2.50	···	$+0.09^{+0.01}_{-0.01}$
M54-VLA2	18:55:00.122	–30:30:49.71	0.04	0.07	1636.0	4.1	1590.2	6.1	···	2.15	···	$-0.09^{+0.01}_{-0.01}$
M54-VLA3	18:55:11.777	–30:25:57.91	0.04	0.07	68.0	4.8	64.3	7.3	···	3.36	···	$-0.19^{+0.40}_{-0.43}$
M54-VLA4	18:54:58.440	–30:29:32.40	0.04	0.07	65.2	3.6	48.8	3.1	···	1.29	···	$-0.88^{+0.25}_{-0.26}$
M54-VLA5	18:54:52.911	–30:29:09.82	0.04	0.07	44.7	3.8	28.1	3.9	···	2.27	···	$-1.44^{+0.49}_{-0.53}$
M54-VLA6	18:54:59.421	–30:27:25.60	0.04	0.07	37.5	3.5	44.4	3.4	···	1.60	···	$+0.52^{+0.37}_{-0.37}$
M54-VLA7	18:55:06.593	–30:25:29.20	0.04	0.07	36.2	4.7	36.0	6.9	···	3.38	···	$-0.10^{+0.69}_{-0.78}$

Table 3.3 (cont'd)

ID	R.A.[a] (h:m:s)	Dec.[a] (°:′:″)	R.A. unc. (″)	Dec. unc. (″)	S_5[b] (μJy)	S_5 unc. (μJy)	S_7[c] (μJy)	S_7 unc. (μJy)	note[d]	radius[e] (′)	loc.[f]	α[g]
M54-VLA8	18:55:15.648	–30:28:05.51	0.06	0.10	31.6	4.1	< 14.6	12.1	···	2.74	···	< -0.1
M54-VLA9	18:55:14.398	–30:28:57.11	0.06	0.10	30.1	3.9	18.9	4.6	···	2.39	···	$-1.51^{+0.82}_{-0.91}$
M54-VLA10	18:55:03.671	–30:29:11.76	0.04	0.07	27.8	3.3	21.7	2.9	···	0.41	r_h	$-0.76^{+0.55}_{-0.57}$
M54-VLA11	18:55:08.652	–30:27:26.11	0.06	0.10	26.1	3.7	15.3	3.6	···	1.78	···	$-1.68^{+0.81}_{-0.87}$
M54-VLA12	18:54:52.250	–30:30:57.41	0.06	0.10	24.0	4.8	24.0	6.4	···	3.22	···	$-0.20^{+0.94}_{-1.16}$
M54-VLA13	18:54:56.654	–30:27:13.97	0.06	0.10	23.5	3.8	15.7	4.0	···	2.12	···	$-1.30^{+0.91}_{-1.00}$
M54-VLA14	18:55:14.580	–30:27:49.34	0.06	0.10	23.3	4.1	< 13.8	9.5	···	2.61	···	< 1.0
M54-VLA15	18:55:18.510	–30:29:18.63	0.06	0.10	23.3	4.7	< 18.9	-5.7	···	3.31	···	< 1.4
M54-VLA16	18:55:01.573	–30:27:33.74	0.04	0.07	23.2	3.5	23.4	3.2	···	1.29	···	$+0.03^{+0.62}_{-0.63}$
M54-VLA17	18:54:58.990	–30:26:18.13	0.06	0.10	22.6	3.9	< 13.9	8.7	···	2.66	···	< 1.0
M54-VLA18	18:55:15.482	–30:28:09.23	0.06	0.10	21.6	4.1	21.3	4.8	···	2.70	···	$-0.16^{+0.86}_{-0.99}$
M54-VLA19	18:54:54.979	–30:27:09.12	0.06	0.10	19.0	3.6	< 12.4	5.5	···	2.43	···	< 1.1
M54-VLA20	18:55:09.718	–30:26:10.28	0.04	0.07	< 13.2	-4.0	34.5	6.5	···	2.96	···	> -2.1
M54-VLA21	18:54:51.100	–30:30:38.91	0.04	0.07	< 13.2	-4.1	33.3	6.4	···	3.22	···	> -2.3
M54-VLA22	18:54:59.927	–30:26:04.15	0.04	0.07	< 12.6	-6.6	26.4	5.0	···	2.82	···	> -2.0
M54-VLA23	18:55:15.685	–30:27:55.04	0.04	0.07	< 12.5	-1.0	24.6	4.9	···	2.80	···	> -2.5
M54-VLA24	18:55:02.192	–30:26:35.36	0.04	0.07	< 11.3	1.0	22.7	4.4	···	2.22	···	> -2.2
M54-VLA25	18:55:10.562	–30:28:05.33	0.04	0.07	< 11.3	5.2	18.8	3.4	···	1.71	···	> -1.9

Table 3.3 (cont'd)

ID	R.A.[a] (h:m:s)	Dec.[a] (°:′:″)	R.A. unc. (″)	Dec. unc. (″)	S_5[b] (μJy)	S_5 unc. (μJy)	S_7[c] (μJy)	S_7 unc. (μJy)	note[d]	radius[e] (′)	loc.[f]	α[g]
M54-VLA26	18:55:00.806	–30:28:07.20	0.04	0.07	< 10.4	2.0	15.3	3.0	···	0.86	···	> -2.5
M55-VLA1	19:39:55.243	–30:55:10.72	0.07	0.08	1096.1	3.4	913.6	5.1	···	2.87	···	$-0.55^{+0.02}_{-0.02}$
M55-VLA2	19:40:03.043	–30:54:44.08	···	···	355.3	3.5	226.4	5.8	ext.	3.23	···	$-1.36^{+0.08}_{-0.08}$
M55-VLA3	19:39:53.260	–30:55:38.12	···	···	159.6	3.5	90.2	4.0	ext.	2.64	r_h	$-1.73^{+0.15}_{-0.15}$
M55-VLA4	19:39:59.826	–30:55:25.53	0.07	0.08	112.8	2.7	70.9	3.4	···	2.46	r_h	$-1.41^{+0.16}_{-0.17}$
M55-VLA5	19:39:59.553	–31:00:56.38	0.07	0.08	46.3	3.0	36.2	4.5	···	3.06	···	$-0.78^{+0.41}_{-0.45}$
M55-VLA6	19:39:54.915	–30:57:18.24	0.07	0.08	45.0	2.1	30.1	2.4	···	1.18	r_c	$-1.23^{+0.28}_{-0.29}$
M55-VLA7	19:40:05.538	–30:54:48.39	0.07	0.08	42.6	3.5	51.4	5.6	···	3.32	···	$+0.55^{+0.40}_{-0.42}$
M55-VLA8	19:39:52.182	–30:54:50.41	0.08	0.11	42.4	4.1	24.3	5.8	···	3.45	···	$-1.78^{+0.74}_{-0.82}$
M55-VLA9	19:39:43.679	–30:58:28.84	0.07	0.08	40.5	3.1	38.9	5.9	···	3.49	···	$-0.18^{+0.51}_{-0.57}$
M55-VLA10	19:40:05.848	–31:01:20.63	0.08	0.11	39.4	3.4	25.2	6.4	···	3.70	···	$-1.50^{+0.78}_{-0.91}$
M55-VLA11	19:39:49.274	–31:00:08.66	0.07	0.08	37.6	3.5	33.6	4.7	···	3.18	···	$-0.37^{+0.50}_{-0.55}$
M55-VLA12	19:40:05.241	–30:59:27.16	0.07	0.08	31.7	2.8	17.1	3.0	···	1.96	r_h	$-1.92^{+0.58}_{-0.64}$
M55-VLA13	19:40:01.217	–31:01:02.76	0.08	0.11	29.0	3.4	18.6	5.2	···	3.18	···	$-1.47^{+0.87}_{-1.00}$
M55-VLA14	19:39:51.145	–30:58:31.82	0.07	0.08	28.8	2.8	15.6	2.9	···	1.95	r_h	$-1.92^{+0.62}_{-0.67}$
M55-VLA15	19:40:06.200	–30:57:21.91	0.08	0.11	26.0	2.5	12.4	2.6	···	1.49	r_c	$-2.27^{+0.65}_{-0.66}$
M55-VLA16	19:39:55.397	–30:56:50.52	0.08	0.11	22.4	2.6	9.5	2.7	···	1.39	r_c	$-2.47^{+0.75}_{-0.65}$
M55-VLA17	19:39:59.605	–30:54:52.76	0.08	0.11	21.6	3.4	20.1	4.5	ext.?	3.01	···	$-0.32^{+0.82}_{-0.95}$

Table 3.3 (cont'd)

ID	R.A.[a] (h:m:s)	Dec.[a] (°:′:″)	R.A. unc. (″)	Dec. unc. (″)	S_5[b] (μJy)	S_5 unc. (μJy)	S_7[c] (μJy)	S_7 unc. (μJy)	note[d]	radius[e] (′)	loc.[f]	α[g]
M55-VLA18	19:40:04.915	–30:59:37.54	0.07	0.08	18.8	2.6	21.4	3.2	···	2.07	r_h	$+0.35^{+0.58}_{-0.64}$
M55-VLA19	19:40:05.727	–30:58:43.97	0.08	0.11	18.6	2.5	8.1	2.5	···	1.54	r_c	$-2.39^{+0.82}_{-0.71}$
M55-VLA20	19:39:47.368	–30:56:57.12	0.08	0.11	18.3	2.7	17.0	4.3	···	2.81	r_h	$-0.39^{+0.88}_{-1.05}$
M55-VLA21	19:40:06.339	–30:55:34.64	0.08	0.11	18.1	3.1	< 11.5	6.4	···	2.71	r_h	< 1.0
M55-VLA22	19:40:14.082	–30:58:35.20	0.08	0.11	17.2	3.0	20.0	4.1	···	3.16	···	$+0.30^{+0.70}_{-0.86}$
M55-VLA23	19:40:15.149	–30:57:14.37	0.08	0.11	16.6	3.1	< 17.0	2.5	···	3.37	···	< 1.4
M55-VLA24	19:39:55.861	–31:00:48.73	0.08	0.11	15.7	3.1	< 12.8	9.7	···	3.04	···	< 1.3
M55-VLA25	19:40:07.832	–30:56:29.67	0.08	0.11	15.1	2.7	13.3	3.2	ext.?	2.23	r_h	$-0.49^{+0.90}_{-1.03}$
M55-VLA26	19:40:06.195	–30:58:58.77	0.08	0.11	15.1	2.3	11.4	2.9	···	1.77	r_c	$-0.97^{+0.89}_{-1.03}$
M55-VLA27	19:39:58.894	–30:57:30.11	0.08	0.11	14.0	2.4	8.8	2.3	···	0.42	r_c	$-1.47^{+0.94}_{-1.00}$
M55-VLA28	19:39:55.081	–30:56:42.56	0.08	0.11	13.9	2.4	10.6	2.7	···	1.54	r_c	$-0.93^{+0.93}_{-1.05}$
M55-VLA29	19:40:04.119	–30:56:35.59	0.08	0.11	13.8	2.5	< 7.7	-1.1	···	1.60	r_c	< 0.8
M55-VLA30	19:39:53.701	–30:59:13.89	0.08	0.11	13.0	2.5	< 8.4	1.3	···	1.86	r_h	< 1.0
M55-VLA31	19:40:03.626	–30:56:38.63	0.08	0.11	12.5	2.5	< 7.9	6.4	···	1.50	r_c	< 1.0
M55-VLA32	19:39:59.574	–30:57:30.98	0.08	0.11	12.4	2.4	< 6.8	1.6	···	0.37	r_c	< 0.9
M55-VLA33	19:40:04.097	–30:58:00.57	0.07	0.08	12.3	2.2	11.6	2.2	ext.?	0.95	r_c	$-0.23^{+0.77}_{-0.83}$
M55-VLA34	19:40:00.222	–30:57:39.94	0.07	0.08	11.7	2.4	13.0	2.2	···	0.25	r_c	$+0.21^{+0.67}_{-0.78}$
M55-VLA35	19:40:14.647	–30:57:31.91	0.07	0.08	< 9.1	-1.6	26.7	4.7	···	3.22	···	> -1.5

Table 3.3 (cont'd)

ID	R.A.[a] (h:m:s)	Dec.[a] (°:′:″)	R.A. unc. (″)	Dec. unc. (″)	S_5[b] (μJy)	S_5 unc. (μJy)	S_7[c] (μJy)	S_7 unc. (μJy)	note[d]	radius[e] (′)	loc.[f]	α[g]
M55-VLA36	19:39:46.628	–30:58:18.60	0.07	0.08	< 9.0	-0.9	21.3	4.1	···	2.84	···	> -2.3
M55-VLA37	19:40:08.276	–30:56:57.26	0.07	0.08	< 7.5	0.7	17.3	3.1	···	2.06	r_h	> -1.7
M55-VLA38	19:40:07.112	–30:58:06.37	0.07	0.08	< 7.4	-1.4	16.6	2.6	···	1.60	r_c	> -1.0
M55-VLA39	19:39:54.013	–30:56:17.84	0.07	0.08	< 7.5	-5.3	15.5	2.9	···	2.00	r_h	> -2.0
M62-VLA1	17:01:13.215	–30:06:50.63	0.09	0.08	22.4	3.7	18.9	2.3	···	0.06	r_c	$-0.40^{+0.57}_{-0.53}$
M62-VLA2	17:01:15.541	–30:07:50.06	0.09	0.08	78.9	3.4	39.0	2.6	···	1.16	···	$-1.81^{+0.20}_{-0.21}$
M62-VLA3	17:01:22.221	–30:08:32.65	0.09	0.08	77.3	3.7	63.4	4.3	···	2.64	···	$-0.51^{+0.21}_{-0.22}$
M62-VLA4	17:01:12.789	–30:08:05.62	0.09	0.08	49.5	3.1	25.5	2.4	···	1.28	···	$-1.71^{+0.29}_{-0.30}$
M62-VLA5	17:01:11.053	–30:07:45.64	0.09	0.08	39.9	3.2	20.9	2.4	···	1.03	···	$-1.67^{+0.36}_{-0.37}$
M62-VLA6	17:01:05.540	–30:04:14.76	0.14	0.13	39.1	5.2	15.8	4.1	ext.?	3.03	···	$-2.32^{+0.68}_{-0.67}$
M62-VLA7	17:01:16.806	–30:05:22.64	0.09	0.08	35.0	3.2	21.0	2.6	···	1.66	···	$-1.32^{+0.39}_{-0.41}$
M62-VLA8	17:01:09.710	–30:06:09.20	0.14	0.13	30.0	3.5	8.4	2.2	···	0.97	···	$-2.95^{+0.51}_{-0.37}$
M62-VLA9	17:01:22.141	–30:07:56.54	0.09	0.08	29.5	4.4	18.9	3.4	···	2.28	···	$-1.16^{+0.62}_{-0.64}$
M62-VLA10	17:01:06.278	–30:07:26.00	0.09	0.08	27.6	3.7	20.3	2.5	···	1.57	···	$-0.77^{+0.49}_{-0.48}$
M62-VLA11	17:01:05.552	–30:04:13.64	0.14	0.13	27.4	5.2	17.8	4.2	ext.?	3.05	···	$-1.15^{+0.82}_{-0.87}$
M62-VLA12	17:01:12.508	–30:06:30.27	0.14	0.13	26.3	2.9	< 6.4	5.2	···	0.33	r_h	< -1.6
M62-VLA13	17:01:21.650	–30:06:30.78	0.14	0.13	25.0	4.2	12.4	2.9	···	1.90	···	$-1.82^{+0.75}_{-0.78}$
M62-VLA14	17:01:16.382	–30:07:15.78	0.14	0.13	24.9	3.2	< 7.4	4.2	···	0.86	r_h	< -1.1

Table 3.3 (cont'd)

ID	R.A.[a] (h:m:s)	Dec.[a] (°:′:″)	R.A. unc. (″)	Dec. unc. (″)	S_5[b] (μJy)	S_5 unc. (μJy)	S_7[c] (μJy)	S_7 unc. (μJy)	note[d]	radius[e] (′)	loc.[f]	α[g]
M62-VLA15	17:01:07.809	–30:10:04.45	0.14	0.13	24.9	4.8	< 16.2	2.0	···	3.44	···	< 1.1
M62-VLA16	17:01:06.457	–30:07:41.13	0.14	0.13	24.0	3.7	< 8.4	7.7	···	1.66	···	< -0.5
M62-VLA17	17:01:23.938	–30:08:12.91	0.14	0.13	23.5	4.3	< 12.4	3.2	···	2.75	···	< 0.7
M62-VLA18	17:01:15.562	–30:04:30.14	0.14	0.13	21.9	3.9	< 8.5	3.5	···	2.38	···	< 0.0
M62-VLA19	17:01:12.845	–30:08:11.26	0.14	0.13	21.7	3.3	< 8.3	2.3	ext.?	1.37	···	< -0.3
M62-VLA20	17:01:19.565	–30:08:15.17	0.14	0.13	21.1	3.9	< 9.5	7.3	···	2.02	···	< 0.4
M62-VLA21	17:01:10.826	–30:04:01.56	0.14	0.13	19.2	3.5	< 10.7	-2.6	···	2.83	···	< 0.7
M62-VLA22	17:01:17.728	–30:05:41.26	0.14	0.13	19.0	3.3	8.7	2.6	···	1.53	···	$-2.02^{+0.84}_{-0.83}$
M62-VLA23	17:01:10.596	–30:05:42.92	0.14	0.13	17.4	3.4	< 7.6	8.0	ext.?	1.22	···	< 0.5
M62-VLA24	17:01:15.590	–30:06:43.94	0.14	0.13	17.3	3.3	< 6.8	2.1	···	0.57	r_h	< 0.2
M62-VLA25	17:01:02.447	–30:08:14.84	0.09	0.08	< 12.3	0.4	20.2	4.0	···	2.69	···	> -2.1
M62-VLA26	17:01:11.204	–30:09:20.32	0.09	0.08	< 11.5	-0.2	18.6	3.4	···	2.55	···	> -1.7
M62-VLA27	17:01:16.495	–30:08:22.70	0.09	0.08	< 10.7	2.2	14.1	2.8	···	1.74	···	> -2.3
M92-VLA1	17:17:05.724	+43:08:56.87	···	···	184.4	2.0	112.9	2.0	ext.	0.85	r_h	$-1.40^{+0.06}_{-0.06}$
M92-VLA2	17:17:01.263	+43:10:42.52	0.03	0.03	130.0	2.1	82.7	2.9	ext.?	2.79	···	$-1.29^{+0.11}_{-0.11}$
M92-VLA3	17:17:15.920	+43:06:08.82	0.03	0.03	69.0	2.0	36.1	2.4	···	2.54	···	$-1.86^{+0.20}_{-0.21}$
M92-VLA4	17:16:58.103	+43:11:05.53	0.03	0.03	65.9	2.5	24.0	3.9	···	3.39	···	$-2.87^{+0.41}_{-0.38}$
M92-VLA5	17:17:27.200	+43:07:29.06	0.03	0.03	61.6	2.6	25.6	4.2	···	3.67	···	$-2.54^{+0.45}_{-0.47}$

Table 3.3 (cont'd)

ID	R.A.[a] (h:m:s)	Dec.[a] (°:′:″)	R.A. unc. (″)	Dec. unc. (″)	S_5[b] (μJy)	S_5 unc. (μJy)	S_7[c] (μJy)	S_7 unc. (μJy)	note[d]	radius[e] (′)	loc.[f]	α[g]
M92-VLA6	17:17:02.993	+43:09:28.09	0.03	0.03	57.1	1.8	29.3	1.8	···	1.54	···	$-1.91^{+0.19}_{-0.20}$
M92-VLA7	17:17:23.781	+43:06:23.31	0.03	0.03	49.4	2.4	21.0	3.7	···	3.47	···	$-2.49^{+0.48}_{-0.51}$
M92-VLA8	17:16:49.300	+43:08:00.42	0.03	0.03	43.4	2.3	27.7	3.4	···	3.31	···	$-1.32^{+0.37}_{-0.42}$
M92-VLA9	17:17:07.403	+43:11:35.79	0.04	0.04	35.8	2.4	16.2	3.8	···	3.44	···	$-2.31^{+0.62}_{-0.65}$
M92-VLA10	17:17:06.677	+43:05:46.14	0.03	0.03	33.5	1.9	15.5	2.3	···	2.39	···	$-2.24^{+0.44}_{-0.49}$
M92-VLA11	17:16:59.096	+43:06:53.20	0.03	0.03	33.0	1.9	16.3	2.0	···	1.98	···	$-2.04^{+0.38}_{-0.41}$
M92-VLA12	17:17:02.917	+43:08:02.86	0.04	0.04	25.7	1.7	9.8	1.7	···	0.83	r_h	$-2.74^{+0.47}_{-0.44}$
M92-VLA13	17:17:19.867	+43:05:56.51	0.03	0.03	22.8	2.3	20.3	3.1	ext.?	3.17	···	$-0.37^{+0.52}_{-0.56}$
M92-VLA14	17:17:05.357	+43:06:10.12	0.03	0.03	21.6	1.8	16.0	2.0	···	2.02	···	$-0.88^{+0.43}_{-0.45}$
M92-VLA15	17:16:56.810	+43:10:04.33	0.04	0.04	19.5	2.1	12.1	2.8	···	2.73	···	$-1.47^{+0.71}_{-0.83}$
M92-VLA16	17:16:56.929	+43:06:10.03	0.04	0.04	19.2	2.1	10.1	2.6	···	2.76	···	$-1.92^{+0.75}_{-0.81}$
M92-VLA17	17:17:24.284	+43:06:36.02	0.04	0.04	18.7	2.4	< 11.0	1.1	···	3.45	···	< 0.5
M92-VLA18	17:16:57.685	+43:06:05.18	0.04	0.04	18.4	2.0	< 7.7	4.1	···	2.73	···	< -0.5
M92-VLA19	17:17:08.762	+43:05:43.62	0.04	0.04	17.2	1.9	< 6.9	3.8	···	2.44	···	< -0.6
M92-VLA20	17:16:53.690	+43:09:37.65	0.04	0.04	16.5	2.2	11.2	2.9	···	2.91	···	$-1.24^{+0.83}_{-0.96}$
M92-VLA21	17:17:19.884	+43:05:55.80	0.04	0.04	16.1	2.3	< 9.4	0.1	ext.?	3.18	···	< 0.6
M92-VLA22	17:17:01.037	+43:10:27.24	0.04	0.04	15.8	2.1	< 7.6	7.7	···	2.58	···	< 0.0
M92-VLA23	17:17:06.696	+43:09:30.53	0.03	0.03	15.6	1.8	9.9	1.9	···	1.36	···	$-1.37^{+0.63}_{-0.71}$

Table 3.3 (cont'd)

ID	R.A.[a] (h:m:s)	Dec.[a] (°:′:″)	R.A. unc. (″)	Dec. unc. (″)	S_5[b] (μJy)	S_5 unc. (μJy)	S_7[c] (μJy)	S_7 unc. (μJy)	note[d]	radius[e] (′)	loc.[f]	α[g]
M92-VLA24	17:17:10.005	+43:11:14.40	0.04	0.04	15.6	2.2	< 9.8	4.7	···	3.12	···	< 0.8
M92-VLA25	17:16:59.415	+43:07:22.10	0.04	0.04	15.1	1.9	9.9	1.9	···	1.66	···	$-1.27^{+0.66}_{-0.72}$
M92-VLA26	17:17:23.192	+43:08:16.67	0.04	0.04	14.9	2.1	9.3	2.8	···	2.88	···	$-1.48^{+0.91}_{-1.02}$
M92-VLA27	17:17:19.850	+43:05:57.53	0.04	0.04	14.5	2.3	< 9.4	-0.6	ext.?	3.16	···	< 0.9
M92-VLA28	17:17:01.773	+43:05:07.56	0.04	0.04	14.4	2.2	< 9.3	5.7	···	3.20	···	< 0.9
M92-VLA29	17:17:06.587	+43:05:48.81	0.04	0.04	14.3	1.9	11.6	2.2	ext.?	2.35	···	$-0.66^{+0.67}_{-0.74}$
M92-VLA30	17:17:06.358	+43:08:26.51	0.04	0.04	13.7	1.7	< 4.9	3.9	···	0.35	r_h	< -0.8
M92-VLA31	17:17:05.035	+43:08:41.55	0.04	0.04	13.7	1.8	< 5.0	2.6	···	0.69	r_h	< -0.6
M92-VLA32	17:16:53.974	+43:07:14.77	0.04	0.04	12.8	2.0	< 7.4	5.1	···	2.62	···	< 0.7
M92-VLA33	17:17:01.612	+43:06:04.10	0.04	0.04	12.7	1.9	< 6.7	4.0	···	2.34	···	< 0.4
M92-VLA34	17:17:10.937	+43:06:57.57	0.04	0.04	12.4	1.8	7.6	1.7	···	1.36	···	$-1.48^{+0.77}_{-0.84}$
M92-VLA35	17:16:57.783	+43:07:56.00	0.04	0.04	11.5	1.8	< 5.9	1.1	···	1.77	···	< 0.4
M92-VLA36	17:16:53.049	+43:06:17.47	0.04	0.04	11.4	2.3	< 9.3	-3.5	···	3.22	···	< 1.2
M92-VLA37	17:17:04.379	+43:05:05.16	0.04	0.04	11.3	2.2	< 9.0	2.0	···	3.12	···	< 1.2
M92-VLA38	17:17:15.116	+43:05:28.00	0.04	0.04	10.8	2.1	< 8.7	3.0	···	3.03	···	< 1.2
M92-VLA39	17:17:17.642	+43:06:24.86	0.04	0.04	10.6	2.0	< 7.1	0.1	···	2.55	···	< 1.0
M92-VLA40	17:17:01.007	+43:05:33.35	0.04	0.04	10.4	2.0	< 8.2	1.4	···	2.85	···	< 1.1
M92-VLA41	17:16:55.903	+43:08:33.44	0.04	0.04	10.2	1.9	< 6.5	3.8	···	2.14	···	< 0.9

Table 3.3 (cont'd)

ID	R.A.[a] (h:m:s)	Dec.[a] (°:′:″)	R.A. unc. (″)	Dec. unc. (″)	S_5[b] (μJy)	S_5 unc. (μJy)	S_7[c] (μJy)	S_7 unc. (μJy)	note[d]	radius[e] (′)	loc.[f]	α[g]
M92-VLA42	17:16:58.758	+43:09:54.39	0.04	0.04	10.1	1.9	< 7.0	2.9	···	2.36	···	< 1.0
M92-VLA43	17:17:01.674	+43:06:36.61	0.04	0.04	10.0	1.8	7.0	2.0	···	1.87	···	$-1.15^{+0.96}_{-1.08}$
M92-VLA44	17:17:10.208	+43:06:58.14	0.04	0.04	9.9	1.8	8.2	1.7	···	1.29	···	$-0.59^{+0.80}_{-0.86}$
M92-VLA45	17:17:12.042	+43:09:47.98	0.04	0.04	9.4	1.8	7.6	1.9	···	1.85	···	$-0.72^{+0.89}_{-1.02}$
M92-VLA46	17:17:03.132	+43:06:26.20	0.04	0.04	9.3	1.8	< 5.9	0.3	···	1.89	···	< 0.9
M92-VLA47	17:17:13.908	+43:07:24.37	0.04	0.04	9.1	1.8	< 5.4	-0.5	···	1.40	···	< 0.8
M92-VLA48	17:17:09.818	+43:05:48.51	0.03	0.03	6.8	1.8	11.7	2.3	···	2.38	···	$+0.68^{+0.39}_{-0.66}$
M92-VLA49	17:17:00.450	+43:10:56.96	0.03	0.03	< 6.7	-2.9	17.6	3.1	···	3.07	···	> -1.4
M92-VLA50	17:17:03.106	+43:11:16.05	0.03	0.03	< 6.8	1.7	17.0	3.4	···	3.21	···	> -2.8
M92-VLA51	17:17:13.886	+43:05:06.05	0.03	0.03	< 6.7	-1.2	16.6	3.3	···	3.27	···	> -2.7
M92-VLA52	17:17:20.125	+43:09:52.70	0.03	0.03	< 6.4	-0.3	14.8	2.9	···	2.89	···	> -2.5
M92-VLA53	17:17:07.422	+43:05:43.82	0.03	0.03	< 5.8	-1.4	12.4	2.2	···	2.42	···	> -1.6
M92-VLA54	17:16:57.695	+43:07:14.89	0.03	0.03	< 5.5	-0.1	12.1	2.0	···	1.99	···	> -1.2
M92-VLA55	17:16:55.457	+43:08:40.42	0.03	0.03	< 5.7	2.8	11.8	2.2	···	2.24	···	> -2.0
M92-VLA56	17:16:58.536	+43:08:27.16	0.03	0.03	< 5.4	0.2	10.6	1.9	···	1.65	···	> -1.8
M92-VLA57	17:17:11.826	+43:09:31.64	0.03	0.03	< 5.3	-1.0	9.6	1.9	···	1.59	···	> -2.6
M107-VLA1	16:32:24.751	–13:01:19.02	···	···	5059.0	10.6	3613.9	12.4	ext.	2.58	···	$-1.00^{+0.01}_{-0.01}$
M107-VLA2	16:32:23.274	–13:04:53.52	0.03	0.04	443.4	2.9	402.6	3.4	···	2.67	···	$-0.29^{+0.03}_{-0.03}$

Table 3.3 (cont'd)

ID	R.A.[a] (h:m:s)	Dec.[a] (°:′:″)	R.A. unc. (″)	Dec. unc. (″)	S_5[b] (μJy)	S_5 unc. (μJy)	S_7[c] (μJy)	S_7 unc. (μJy)	note[d]	radius[e] (′)	loc.[f]	α[g]
M107-VLA3	16:32:26.211	-12:59:55.74	0.03	0.04	331.1	4.0	222.7	6.0	···	3.57	···	$-1.18^{+0.09}_{-0.09}$
M107-VLA4	16:32:28.699	–13:03:18.01	0.03	0.04	149.3	2.7	110.0	2.6	···	0.77	r_h	$-0.91^{+0.09}_{-0.09}$
M107-VLA5	16:32:25.109	–13:04:48.54	0.03	0.04	60.0	2.8	29.9	2.8	···	2.28	···	$-2.09^{+0.30}_{-0.33}$
M107-VLA6	16:32:41.539	–13:01:55.59	0.03	0.04	59.1	2.8	41.6	3.2	···	2.69	···	$-1.05^{+0.27}_{-0.28}$
M107-VLA7	16:32:36.244	–13:04:55.19	0.03	0.04	47.3	2.5	20.7	2.5	···	2.00	···	$-2.49^{+0.38}_{-0.41}$
M107-VLA8	16:32:17.882	–13:02:37.40	0.03	0.04	35.2	3.4	33.8	4.7	···	3.46	···	$-0.15^{+0.50}_{-0.54}$
M107-VLA9	16:32:41.877	–13:04:01.03	0.03	0.04	31.4	2.8	21.3	3.1	···	2.56	···	$-1.19^{+0.50}_{-0.55}$
M107-VLA10	16:32:37.562	–13:04:54.33	0.04	0.06	28.3	2.5	9.5	2.6	···	2.18	···	$-2.90^{+0.56}_{-0.41}$
M107-VLA11	16:32:29.792	–13:06:28.64	0.04	0.06	27.6	3.4	13.0	4.3	···	3.29	···	$-2.20^{+0.86}_{-0.80}$
M107-VLA12	16:32:45.124	–13:02:59.91	0.04	0.06	26.9	3.3	< 12.0	7.8	···	3.24	···	< -0.2
M107-VLA13	16:32:37.312	–13:03:44.39	0.03	0.04	26.0	2.4	15.0	2.2	ext.?	1.42	r_h	$-1.68^{+0.51}_{-0.56}$
M107-VLA14	16:32:20.557	–13:05:40.62	0.04	0.06	22.9	3.5	< 15.6	6.4	···	3.68	···	< 1.0
M107-VLA15	16:32:25.348	–13:00:24.43	0.04	0.06	22.3	3.8	< 15.5	-8.7	···	3.24	···	< 1.2
M107-VLA16	16:32:20.076	–13:03:11.78	0.04	0.06	20.9	2.7	19.2	3.4	···	2.87	···	$-0.31^{+0.65}_{-0.71}$
M107-VLA17	16:32:30.402	–13:00:40.78	0.04	0.06	20.4	3.1	< 9.5	6.5	···	2.57	···	< 0.2
M107-VLA18	16:32:28.577	–13:06:16.98	0.04	0.06	20.3	3.0	< 11.4	0.3	···	3.16	···	< 0.6
M107-VLA19	16:32:30.758	–13:03:42.03	0.03	0.04	20.1	2.4	13.8	2.1	···	0.54	r_c	$-1.14^{+0.58}_{-0.61}$
M107-VLA20	16:32:19.881	–13:01:41.40	0.04	0.06	20.1	3.3	< 13.4	5.4	···	3.30	···	< 1.1

Table 3.3 (cont'd)

ID	R.A.[a] (h:m:s)	Dec.[a] (°:′:″)	R.A. unc. (″)	Dec. unc. (″)	S_5[b] (μJy)	S_5 unc. (μJy)	S_7[c] (μJy)	S_7 unc. (μJy)	note[d]	radius[e] (′)	loc.[f]	α[g]
M107-VLA21	16:32:36.639	–13:00:04.65	0.04	0.06	19.8	3.2	< 12.5	2.5	···	3.36	···	< 0.9
M107-VLA22	16:32:28.680	–13:02:04.99	0.04	0.06	19.0	2.5	< 7.7	-0.6	···	1.38	r_h	< -0.3
M107-VLA23	16:32:21.888	–13:05:33.26	0.04	0.06	18.0	3.2	< 12.9	-3.9	···	3.36	···	< 1.2
M107-VLA24	16:32:18.958	–13:04:47.20	0.04	0.06	17.9	3.3	< 13.9	3.6	···	3.51	···	< 1.3
M107-VLA25	16:32:43.366	–13:02:08.67	0.04	0.06	17.7	3.1	< 10.9	-3.2	···	3.00	···	< 1.0
M107-VLA26	16:32:40.561	–13:05:27.14	0.04	0.06	17.5	3.2	< 11.1	-4.3	···	3.07	···	< 1.1
M107-VLA27	16:32:31.361	–13:01:51.58	0.04	0.06	16.9	2.8	< 7.4	3.8	···	1.37	r_h	< 0.2
M107-VLA28	16:32:32.012	–13:05:02.72	0.04	0.06	16.7	2.6	< 7.7	1.7	···	1.82	···	< 0.2
M107-VLA29	16:32:44.242	–13:02:13.01	0.04	0.06	16.7	3.0	< 11.6	-4.8	···	3.18	···	< 1.2
M107-VLA30	16:32:20.760	–13:04:19.15	0.04	0.06	16.7	3.2	< 10.7	-3.3	···	2.92	···	< 1.1
M107-VLA31	16:32:41.219	–13:01:30.51	0.04	0.06	16.6	2.8	< 10.2	1.2	···	2.85	···	< 0.9
M107-VLA32	16:32:40.832	–13:00:40.09	0.04	0.06	16.5	3.2	< 12.9	-2.1	···	3.36	···	< 1.3
M107-VLA33	16:32:30.480	–13:01:14.06	0.04	0.06	16.3	3.0	< 9.0	5.2	···	2.02	···	< 0.8
M107-VLA34	16:32:37.141	–13:00:18.30	0.04	0.06	16.2	3.1	< 12.1	-1.5	···	3.19	···	< 1.3
M107-VLA35	16:32:35.368	–13:02:05.47	0.04	0.06	16.1	2.7	< 6.9	3.1	···	1.42	r_h	< 0.2
M107-VLA36	16:32:44.473	–13:03:38.64	0.04	0.06	15.8	3.0	< 11.0	-0.1	···	3.10	···	< 1.2
M107-VLA37	16:32:23.465	–13:03:50.37	0.04	0.06	15.4	2.5	< 8.0	3.2	···	2.13	···	< 0.6
M107-VLA38	16:32:32.131	–13:02:37.49	0.04	0.06	15.3	2.4	< 6.7	6.0	···	0.61	r_h	< 0.0

Table 3.3 (cont'd)

ID	R.A.[a] (h:m:s)	Dec.[a] (°:′:″)	R.A. unc. (″)	Dec. unc. (″)	S_5[b] (μJy)	S_5 unc. (μJy)	S_7[c] (μJy)	S_7 unc. (μJy)	note[d]	radius[e] (′)	loc.[f]	α[g]
M107-VLA39	16:32:30.876	–13:05:49.82	0.04	0.06	15.3	2.7	< 9.7	-1.0	···	2.61	···	< 1.0
M107-VLA40	16:32:27.868	–13:04:10.08	0.04	0.06	14.9	2.5	11.4	2.4	···	1.35	r_h	$-0.85^{+0.82}_{-0.89}$
M107-VLA41	16:32:38.751	–13:01:29.48	0.04	0.06	14.5	2.7	< 8.7	0.2	···	2.41	···	< 1.0
M107-VLA42	16:32:37.429	–13:03:38.80	0.04	0.06	14.2	2.4	< 6.9	-0.3	···	1.42	r_h	< 0.5
M107-VLA43	16:32:38.335	–13:02:05.66	0.04	0.06	14.0	2.6	< 7.5	0.7	···	1.94	···	< 0.8
M107-VLA44	16:32:37.279	–13:03:46.10	0.04	0.06	12.8	2.3	< 6.8	3.3	ext.?	1.43	r_h	< 0.7
M107-VLA45	16:32:23.634	–13:04:14.85	0.04	0.06	12.8	2.5	< 8.2	-1.8	···	2.25	···	< 1.0
M107-VLA46	16:32:36.867	–13:02:46.93	0.04	0.06	12.7	2.2	< 6.5	-2.7	···	1.30	r_h	< 0.6
M107-VLA47	16:32:31.958	–13:03:59.21	0.04	0.06	12.7	2.4	< 6.4	-1.5	···	0.76	r_h	< 0.7
M107-VLA48	16:32:30.024	–13:03:23.00	0.04	0.06	12.4	2.3	< 6.4	-0.2	···	0.47	r_c	< 0.7
M107-VLA49	16:32:42.090	–13:05:44.31	0.03	0.04	< 10.2	-5.0	29.9	4.7	···	3.54	···	> -0.7
M107-VLA50	16:32:46.369	–13:03:59.80	0.03	0.04	< 10.0	2.0	26.4	5.0	···	3.62	···	> -2.1
M107-VLA51	16:32:43.332	–13:00:48.80	0.03	0.04	< 10.6	-1.0	25.8	5.0	···	3.69	···	> -2.2
M107-VLA52	16:32:20.783	–13:05:25.96	0.03	0.04	< 9.5	-2.4	23.5	4.6	···	3.48	···	> -2.5
M107-VLA53	16:32:24.457	–13:05:57.80	0.03	0.04	< 9.4	-2.3	23.2	4.2	···	3.28	···	> -1.6
M107-VLA54	16:32:19.005	–13:04:43.65	0.03	0.04	< 9.7	0.0	22.6	4.2	···	3.47	···	> -1.8
M107-VLA55	16:32:23.459	–13:02:16.58	0.03	0.04	< 10.4	0.1	20.5	3.6	···	2.26	···	> -1.5
M107-VLA56	16:32:33.582	–13:00:08.37	0.03	0.04	< 9.2	-5.9	20.4	4.0	···	3.12	···	> -2.4

Table 3.3 (cont'd)

ID	R.A.[a] (h:m:s)	Dec.[a] (°:′:″)	R.A. unc. (″)	Dec. unc. (″)	S_5[b] (μJy)	S_5 unc. (μJy)	S_7[c] (μJy)	S_7 unc. (μJy)	note[d]	radius[e] (′)	loc.[f]	α[g]
M107-VLA57	16:32:24.412	–13:02:39.62	0.03	0.04	< 8.6	-3.8	18.0	2.8	···	1.90	···	> -1.0
M107-VLA58	16:32:37.288	–13:05:57.30	0.03	0.04	< 9.1	0.1	17.8	3.5	···	3.03	···	> -2.3
M107-VLA59	16:32:24.234	–13:02:54.46	0.03	0.04	< 7.8	2.3	17.0	2.7	···	1.88	···	> -1.0
M107-VLA60	16:32:34.494	–13:05:56.33	0.03	0.04	< 8.8	-1.3	16.9	3.2	···	2.79	···	> -2.0
M107-VLA61	16:32:40.440	–13:02:36.10	0.03	0.04	< 8.3	0.7	16.7	2.7	···	2.18	···	> -1.2
M107-VLA62	16:32:42.059	–13:02:18.13	0.03	0.04	< 8.2	-1.0	16.5	3.0	···	2.65	···	> -1.8
M107-VLA63	16:32:32.863	–13:05:38.60	0.03	0.04	< 8.2	-5.3	15.3	2.9	···	2.43	···	> -2.2
M107-VLA64	16:32:23.810	–13:02:51.07	0.03	0.04	< 7.8	-0.3	15.2	2.9	···	2.00	···	> -2.2
M107-VLA65	16:32:40.945	–13:03:13.02	0.03	0.04	< 7.4	-0.9	14.9	2.7	···	2.21	···	> -1.8
M107-VLA66	16:32:32.951	–13:03:09.72	0.03	0.04	< 6.8	-0.8	14.1	2.3	···	0.27	r_c	> -1.2
M107-VLA67	16:32:34.347	–13:00:59.36	0.03	0.04	< 8.1	1.8	14.0	2.7	···	2.32	···	> -2.3
M107-VLA68	16:32:32.791	–13:04:52.60	0.03	0.04	< 7.3	-1.8	13.6	2.4	···	1.67	r_h	> -1.7
M107-VLA69	16:32:39.088	–13:01:56.98	0.03	0.04	< 7.5	5.5	13.3	2.5	···	2.17	···	> -2.1
M107-VLA70	16:32:28.984	–13:02:11.34	0.03	0.04	< 7.6	-0.8	12.9	2.5	···	1.25	r_h	> -2.4
M107-VLA71	16:32:30.069	–13:03:36.10	0.03	0.04	< 6.9	-3.6	12.2	2.2	···	0.58	r_h	> -1.9
M107-VLA72	16:32:29.922	–13:03:32.20	0.03	0.04	< 7.0	0.3	12.0	2.2	···	0.56	r_c	> -2.0
M107-VLA73	16:32:29.265	–13:03:58.49	0.03	0.04	< 7.0	0.0	11.5	2.3	···	0.98	r_h	> -2.6
M107-VLA74	16:32:31.100	–13:03:45.53	0.03	0.04	< 7.2	4.1	11.2	2.1	···	0.56	r_c	> -2.3

Table 3.3 (cont'd)

ID	R.A.[a] (h:m:s)	Dec.[a] (°:′:″)	R.A. unc. (″)	Dec. unc. (″)	S_5[b] (μJy)	S_5 unc. (μJy)	S_7[c] (μJy)	S_7 unc. (μJy)	note[d]	radius[e] (′)	loc.[f]	α[g]
N6304-VLA1	17:14:25.311	–29:25:28.31	0.05	0.06	124.0	5.4	102.7	7.1	···	2.84	···	$-0.55^{+0.23}_{-0.24}$
N6304-VLA2	17:14:43.462	–29:25:10.64	0.05	0.06	98.8	5.6	75.9	9.8	···	3.78	···	$-0.79^{+0.40}_{-0.44}$
N6304-VLA3	17:14:33.106	–29:26:34.48	0.05	0.06	97.1	4.6	58.8	4.3	···	1.17	r_h	$-1.44^{+0.25}_{-0.25}$
N6304-VLA4	17:14:27.393	–29:24:39.28	0.05	0.06	77.4	5.3	50.9	8.9	···	3.30	···	$-1.27^{+0.52}_{-0.61}$
N6304-VLA5	17:14:20.295	–29:28:17.42	0.06	0.09	37.1	4.6	< 18.7	12.3	···	3.04	···	< 0.1
N6304-VLA6	17:14:38.598	–29:28:59.60	0.06	0.09	32.9	4.1	< 14.0	15.2	···	2.03	···	< -0.3
N6304-VLA7	17:14:38.622	–29:25:35.05	0.06	0.09	31.0	4.7	25.7	5.8	···	2.67	···	$-0.63^{+0.79}_{-0.90}$
N6304-VLA8	17:14:20.988	–29:25:47.40	0.06	0.09	29.4	5.2	< 23.8	7.1	···	3.41	···	< 1.4
N6304-VLA9	17:14:20.662	–29:25:17.35	0.06	0.09	28.8	5.6	< 29.9	2.3	···	3.78	···	< 1.5
N6304-VLA10	17:14:44.970	–29:26:48.19	0.06	0.09	28.3	5.0	< 21.5	7.2	···	3.31	···	< 1.3
N6304-VLA11	17:14:23.835	–29:27:11.29	0.06	0.09	27.6	4.1	19.1	4.6	···	2.17	···	$-1.15^{+0.81}_{-0.92}$
N6304-VLA12	17:14:25.511	–29:30:47.93	0.06	0.09	26.8	5.4	< 26.5	2.6	···	3.51	···	< 1.5
N6304-VLA13	17:14:43.906	–29:29:29.03	0.06	0.09	26.2	5.2	< 23.5	2.5	···	3.40	···	< 1.4
N6304-VLA14	17:14:34.327	–29:30:07.31	0.06	0.09	23.8	4.5	< 18.1	-3.5	···	2.45	···	< 1.3
N6304-VLA15	17:14:27.102	–29:29:49.56	0.06	0.09	22.0	4.4	< 16.6	-8.0	···	2.46	···	< 1.3
N6304-VLA16	17:14:23.615	–29:28:48.37	0.06	0.09	21.3	4.2	< 15.2	14.7	···	2.41	···	< 1.3
N6304-VLA17	17:14:21.129	–29:25:21.31	0.05	0.06	< 17.3	-8.0	54.3	9.3	···	3.65	···	> -1.1
N6304-VLA18	17:14:27.337	–29:24:45.87	0.05	0.06	< 15.9	11.1	39.6	7.7	···	3.20	···	> -2.2

Table 3.3 (cont'd)

ID	R.A.[a] (h:m:s)	Dec.[a] (°:′:″)	R.A. unc. (″)	Dec. unc. (″)	S_5[b] (μJy)	S_5 unc. (μJy)	S_7[c] (μJy)	S_7 unc. (μJy)	note[d]	radius[e] (′)	loc.[f]	α[g]
N6304-VLA19	17:14:29.997	–29:30:31.17	0.05	0.06	< 14.5	-3.3	35.0	6.9	···	2.85	···	> -2.3
N6304-VLA20	17:14:20.952	–29:29:00.23	0.05	0.06	< 14.0	-1.9	32.5	6.3	···	3.10	···	> -2.1
N6304-VLA21	17:14:41.042	–29:27:52.30	0.05	0.06	< 12.3	0.6	25.5	4.9	···	2.20	···	> -1.9
N6304-VLA22	17:14:40.216	–29:28:41.12	0.05	0.06	< 13.2	3.9	24.9	5.0	···	2.21	···	> -2.3
N6304-VLA23	17:14:24.420	–29:27:53.24	0.05	0.06	< 11.7	4.8	22.7	4.3	···	1.96	···	> -1.9
N6304-VLA24	17:14:30.180	–29:28:38.83	0.05	0.06	< 11.2	2.3	18.8	3.7	···	1.06	r_h	> -2.2
N6325-VLA1	17:17:47.595	–23:47:59.92	0.03	0.05	141.9	2.8	85.8	5.3	···	3.35	···	$-1.44^{+0.18}_{-0.19}$
N6325-VLA2	17:17:56.665	–23:44:13.66	0.03	0.05	112.6	2.1	102.4	2.5	···	1.83	···	$-0.27^{+0.09}_{-0.09}$
N6325-VLA3	17:17:59.955	–23:49:30.88	0.03	0.05	82.8	3.0	103	6.3	···	3.56	···	$+0.62^{+0.20}_{-0.21}$
N6325-VLA4	17:18:00.997	–23:47:46.46	0.03	0.05	63.4	2.2	40.2	2.7	···	1.86	···	$-1.31^{+0.21}_{-0.22}$
N6325-VLA5	17:18:13.864	–23:46:27.51	0.03	0.05	56.0	2.8	45.7	5.2	···	3.39	···	$-0.61^{+0.35}_{-0.38}$
N6325-VLA6	17:17:48.327	–23:46:55.53	0.03	0.05	40.5	2.4	23.9	3.5	···	2.67	···	$-1.56^{+0.44}_{-0.49}$
N6325-VLA7	17:17:51.400	–23:47:32.68	0.03	0.05	38.5	2.4	18.3	3.2	···	2.39	···	$-2.18^{+0.50}_{-0.56}$
N6325-VLA8	17:18:00.934	–23:44:13.58	0.03	0.05	36.6	2.1	20.8	2.5	···	1.78	···	$-1.64^{+0.37}_{-0.40}$
N6325-VLA9	17:18:06.491	–23:45:31.83	0.03	0.05	36.1	2.2	18.1	2.6	···	1.72	···	$-2.02^{+0.44}_{-0.48}$
N6325-VLA10	17:17:50.592	–23:47:46.57	0.04	0.07	35.8	2.4	16.0	3.7	···	2.68	···	$-2.33^{+0.61}_{-0.64}$
N6325-VLA11	17:18:08.647	–23:44:43.96	0.03	0.05	33.9	2.1	28.6	3.1	···	2.48	···	$-0.51^{+0.35}_{-0.37}$
N6325-VLA12	17:17:45.418	–23:47:44.67	0.04	0.07	30.3	3.0	< 18.0	0.7	···	3.62	···	< 0.3

Table 3.3 (cont'd)

ID	R.A.[a] (h:m:s)	Dec.[a] (°:′:″)	R.A. unc. (″)	Dec. unc. (″)	S_5[b] (μJy)	S_5 unc. (μJy)	S_7[c] (μJy)	S_7 unc. (μJy)	note[d]	radius[e] (′)	loc.[f]	α[g]
N6325-VLA13	17:17:55.729	–23:46:40.10	0.03	0.05	26.8	2.0	15.3	2.3	···	1.07	···	$-1.66^{+0.47}_{-0.52}$
N6325-VLA14	17:18:02.386	–23:43:07.03	0.03	0.05	24.7	2.4	22.8	3.7	···	2.94	···	$-0.28^{+0.53}_{-0.59}$
N6325-VLA15	17:17:56.169	–23:46:13.70	0.03	0.05	24.4	2.0	15.4	2.1	···	0.75	···	$-1.34^{+0.45}_{-0.49}$
N6325-VLA16	17:17:46.156	–23:47:08.22	0.04	0.07	23.8	2.7	16.0	4.5	···	3.21	···	$-1.31^{+0.84}_{-1.00}$
N6325-VLA17	17:17:54.608	–23:46:36.83	0.03	0.05	22.9	2.0	13.8	2.4	···	1.24	···	$-1.51^{+0.54}_{-0.62}$
N6325-VLA18	17:18:04.171	–23:44:21.07	0.03	0.05	22.6	2.2	16.5	2.6	···	1.97	···	$-0.94^{+0.53}_{-0.57}$
N6325-VLA19	17:17:59.420	–23:45:06.91	0.03	0.05	22.2	1.9	13.3	2.2	···	0.85	···	$-1.52^{+0.52}_{-0.59}$
N6325-VLA20	17:17:55.643	–23:45:28.79	0.03	0.05	20.9	1.9	14.3	2.2	···	0.95	···	$-1.13^{+0.50}_{-0.55}$
N6325-VLA21	17:18:02.176	–23:44:41.28	0.04	0.07	20.8	2.0	7.0	2.3	···	1.44	···	$-2.78^{+0.64}_{-0.49}$
N6325-VLA22	17:17:47.718	–23:44:27.27	0.04	0.07	19.1	2.6	< 12.2	9.0	ext.?	3.03	···	< 0.7
N6325-VLA23	17:18:10.104	–23:43:48.92	0.04	0.07	18.8	2.7	< 13.7	3.6	···	3.29	···	< 1.1
N6325-VLA24	17:18:11.358	–23:45:43.38	0.04	0.07	18.4	2.4	12.0	3.7	···	2.79	···	$-1.39^{+0.92}_{-1.06}$
N6325-VLA25	17:17:45.200	–23:47:48.08	0.04	0.07	18.2	3.0	< 18.9	-0.8	···	3.70	···	< 1.4
N6325-VLA26	17:17:49.168	–23:43:29.11	0.04	0.07	17.0	2.8	20.0	4.9	···	3.38	···	$+0.24^{+0.74}_{-0.97}$
N6325-VLA27	17:18:08.197	–23:42:54.29	0.04	0.07	17.0	2.9	< 17.2	-1.2	···	3.68	···	< 1.4
N6325-VLA28	17:17:55.113	–23:47:30.28	0.04	0.07	16.7	2.1	< 8.1	9.7	···	1.81	···	< 0.0
N6325-VLA29	17:17:56.943	–23:48:00.23	0.04	0.07	16.6	2.3	< 8.7	0.7	···	2.11	···	< 0.3
N6325-VLA30	17:17:54.957	–23:44:46.58	0.04	0.07	15.8	2.1	10.0	2.4	···	1.53	···	$-1.40^{+0.78}_{-0.88}$

Table 3.3 (cont'd)

ID	R.A.[a] (h:m:s)	Dec.[a] (°:′:″)	R.A. unc. (″)	Dec. unc. (″)	S_5[b] (μJy)	S_5 unc. (μJy)	S_7[c] (μJy)	S_7 unc. (μJy)	note[d]	radius[e] (′)	loc.[f]	α[g]
N6325-VLA31	17:17:58.208	–23:44:46.04	0.04	0.07	15.6	2.0	10.0	2.2	···	1.21	···	$-1.35^{+0.72}_{-0.82}$
N6325-VLA32	17:18:09.221	–23:47:02.03	0.04	0.07	14.9	2.3	11.0	3.3	···	2.53	···	$-1.04^{+0.95}_{-1.11}$
N6325-VLA33	17:17:49.177	–23:44:16.09	0.04	0.07	14.4	2.4	< 11.0	4.7	···	2.85	···	< 1.2
N6325-VLA34	17:17:47.714	–23:44:28.37	0.04	0.07	13.8	2.5	< 12.3	5.4	ext.?	3.02	···	< 1.3
N6325-VLA35	17:18:08.448	–23:46:31.86	0.04	0.07	13.7	2.1	12.0	2.9	···	2.19	···	$-0.50^{+0.81}_{-0.96}$
N6325-VLA36	17:17:57.547	–23:43:09.38	0.04	0.07	13.5	2.5	< 10.6	5.4	···	2.83	···	< 1.2
N6325-VLA37	17:17:49.298	–23:45:14.59	0.04	0.07	13.4	2.2	< 9.3	6.3	···	2.38	···	< 1.0
N6325-VLA38	17:18:06.778	–23:46:31.61	0.04	0.07	13.4	2.1	< 7.9	1.7	···	1.82	···	< 0.7
N6325-VLA39	17:17:51.497	–23:47:38.56	0.04	0.07	13.1	2.3	13.0	3.1	···	2.44	···	$-0.16^{+0.81}_{-0.96}$
N6325-VLA40	17:18:05.863	–23:43:10.14	0.04	0.07	13.1	2.5	< 12.3	4.0	···	3.18	···	< 1.3
N6325-VLA41	17:17:51.527	–23:44:32.91	0.04	0.07	12.5	2.2	< 8.5	3.3	···	2.25	···	< 1.0
N6325-VLA42	17:18:00.338	–23:48:15.25	0.04	0.07	12.5	2.3	< 9.4	4.9	···	2.31	···	< 1.1
N6325-VLA43	17:18:01.534	–23:44:15.44	0.04	0.07	11.9	2.1	< 7.4	3.4	···	1.78	···	< 0.9
N6325-VLA44	17:17:50.228	–23:47:36.53	0.04	0.07	11.8	2.4	< 10.4	-0.2	···	2.63	···	< 1.3
N6325-VLA45	17:17:55.475	–23:47:38.37	0.04	0.07	11.6	2.1	< 8.3	4.9	···	1.88	···	< 1.1
N6325-VLA46	17:17:59.782	–23:48:09.17	0.04	0.07	11.5	2.3	< 9.2	-8.5	···	2.20	···	< 1.2
N6325-VLA47	17:17:57.310	–23:43:52.39	0.04	0.07	11.4	2.2	< 8.5	1.6	···	2.13	···	< 1.1
N6325-VLA48	17:18:02.080	–23:44:37.46	0.04	0.07	11.3	2.0	< 7.0	2.3	···	1.49	···	< 0.9

Table 3.3 (cont'd)

ID	R.A.[a] (h:m:s)	Dec.[a] (°:′:″)	R.A. unc. (″)	Dec. unc. (″)	S_5[b] (μJy)	S_5 unc. (μJy)	S_7[c] (μJy)	S_7 unc. (μJy)	note[d]	radius[e] (′)	loc.[f]	α[g]
N6325-VLA49	17:17:58.269	–23:43:43.54	0.04	0.07	10.6	2.1	< 8.1	-1.2	···	2.24	···	< 1.1
N6325-VLA50	17:17:56.747	–23:46:12.39	0.04	0.07	10.0	1.9	< 6.4	1.8	···	0.62	r_h	< 0.9
N6325-VLA51	17:18:03.588	–23:46:30.09	0.04	0.07	9.9	2.0	11.0	2.3	···	1.14	···	$+0.13^{+0.69}_{-0.85}$
N6325-VLA52	17:18:03.333	–23:45:21.74	0.04	0.07	9.5	1.9	< 6.4	1.7	···	1.12	···	< 0.9
N6325-VLA53	17:17:53.239	–23:49:14.14	0.03	0.05	< 8.8	-3.7	33.6	6.0	···	3.55	···	> -2.4
N6325-VLA54	17:17:43.692	–23:46:27.28	0.03	0.05	< 8.6	-0.2	32.0	5.7	···	3.58	···	> -2.2
N6325-VLA55	17:18:12.738	–23:47:53.47	0.03	0.05	< 9.0	1.2	31.9	6.2	···	3.65	···	> -3.1
N6325-VLA56	17:18:14.479	–23:46:01.94	0.03	0.05	< 8.2	-2.7	29.1	5.4	···	3.49	···	> -2.7
N6325-VLA57	17:17:45.165	–23:44:52.35	0.03	0.05	< 8.1	5.4	26.5	5.1	···	3.39	···	> -2.9
N6325-VLA58	17:17:46.295	–23:45:02.16	0.03	0.05	< 7.5	5.1	25.1	4.2	···	3.10	···	> -1.0
N6325-VLA59	17:18:09.276	–23:46:49.82	0.03	0.05	< 7.0	1.5	16.7	3.2	···	2.46	···	> -2.2
N6325-VLA60	17:18:10.047	–23:45:25.69	0.03	0.05	< 6.9	0.3	16.3	3.2	···	2.54	···	> -2.5
N6325-VLA61	17:17:56.429	–23:44:36.66	0.03	0.05	< 6.0	-2.3	12.9	2.3	···	1.49	···	> -1.6
N6325-VLA62	17:18:01.890	–23:46:53.21	0.03	0.05	< 6.0	3.0	11.6	2.2	···	1.11	···	> -2.1
N6325-VLA63	17:18:00.505	–23:45:49.44	0.03	0.05	< 5.6	-2.7	11.0	2.0	···	0.33	r_h	> -1.8
N6440-VLA1	17:48:47.962	–20:19:59.11	0.05	0.06	5072.3	3.7	3260.9	3.9	···	1.97	···	$-1.26^{+0.01}_{-0.01}$
N6440-VLA2	17:48:46.319	–20:21:36.35	0.07	0.08	2206.0	3.2	1316.1	3.3	···	1.50	···	$-1.47^{+0.01}_{-0.01}$
N6440-VLA3	17:48:52.046	–20:21:53.21	0.07	0.08	289.3	2.8	219.4	2.6	···	0.31	r_h	$-0.79^{+0.04}_{-0.04}$

Table 3.3 (cont'd)

ID	R.A.[a] (h:m:s)	Dec.[a] (°:′:″)	R.A. unc. (″)	Dec. unc. (″)	S_5[b] (μJy)	S_5 unc. (μJy)	S_7[c] (μJy)	S_7 unc. (μJy)	note[d]	radius[e] (′)	loc.[f]	α[g]
N6440-VLA4	17:48:55.325	–20:19:11.82	0.05	0.06	114.1	3.7	80.8	4.0	···	2.50	···	$-0.99^{+0.17}_{-0.17}$
N6440-VLA5	17:48:49.000	–20:22:59.61	0.05	0.06	104.8	3.2	90.7	3.8	···	1.63	···	$-0.42^{+0.15}_{-0.15}$
N6440-VLA6	17:48:52.685	–20:21:39.62	0.05	0.06	76.8	2.9	37.8	2.8	···	0.04	r_c	$-2.03^{+0.23}_{-0.24}$
N6440-VLA7	17:48:42.207	–20:22:33.91	0.05	0.06	53.8	3.4	32.5	4.7	···	2.64	···	$-1.49^{+0.44}_{-0.49}$
N6440-VLA8	17:48:42.641	–20:20:24.84	0.05	0.06	46.8	3.4	33.9	4.5	···	2.65	···	$-0.96^{+0.42}_{-0.47}$
N6440-VLA9	17:48:51.274	–20:18:34.28	0.07	0.08	41.6	3.5	24.4	5.7	···	3.06	···	$-1.64^{+0.68}_{-0.80}$
N6440-VLA10	17:48:38.060	–20:21:42.56	0.07	0.08	33.1	3.9	< 22.2	13.8	···	3.43	···	< 0.7
N6440-VLA11	17:49:00.993	–20:22:16.31	0.05	0.06	26.9	2.9	29.3	3.8	···	2.05	···	$+0.22^{+0.48}_{-0.50}$
N6440-VLA12	17:49:04.055	–20:24:06.04	0.07	0.08	25.7	4.2	< 26.5	16.6	···	3.64	···	< 1.4
N6440-VLA13	17:48:45.592	–20:24:06.63	0.07	0.08	24.5	3.8	< 17.5	-5.9	···	3.00	···	< 1.1
N6440-VLA14	17:48:41.580	–20:22:56.32	0.07	0.08	23.9	3.9	< 16.6	3.3	···	2.92	···	< 1.1
N6440-VLA15	17:49:00.459	–20:22:53.77	0.07	0.08	21.3	3.3	< 11.8	2.0	···	2.22	···	< 0.5
N6440-VLA16	17:49:04.564	–20:21:24.98	0.07	0.08	20.9	3.5	< 14.9	7.2	···	2.79	···	< 1.2
N6440-VLA17	17:48:37.562	–20:21:51.25	0.07	0.08	20.3	3.8	< 22.1	-4.6	···	3.56	···	< 1.5
N6440-VLA18	17:48:45.347	–20:18:26.79	0.07	0.08	19.8	3.9	< 21.7	5.4	···	3.61	···	< 1.5
N6440-VLA19	17:48:57.901	–20:19:29.34	0.07	0.08	19.8	3.2	< 11.9	-5.8	···	2.45	···	< 0.8
N6440-VLA20	17:48:47.562	–20:20:13.34	0.07	0.08	18.8	3.2	< 10.1	-0.2	···	1.84	···	< 0.7
N6440-VLA21	17:49:02.089	–20:21:38.44	0.07	0.08	18.3	3.3	13.5	3.9	···	2.20	···	$-1.00^{+0.98}_{-1.10}$

Table 3.3 (cont'd)

ID	R.A.[a] (h:m:s)	Dec.[a] (°:′:″)	R.A. unc. (″)	Dec. unc. (″)	S_5[b] (μJy)	S_5 unc. (μJy)	S_7[c] (μJy)	S_7 unc. (μJy)	note[d]	radius[e] (′)	loc.[f]	α[g]
N6440-VLA22	17:48:52.032	–20:18:56.94	0.07	0.08	16.7	3.3	< 13.6	-4.5	···	2.67	···	< 1.3
N6440-VLA23	17:48:48.906	–20:21:31.26	0.07	0.08	16.1	2.9	< 8.3	1.8	···	0.89	···	< 0.7
N6440-VLA24	17:48:50.024	–20:19:50.78	0.07	0.08	15.4	3.1	< 10.5	3.0	···	1.88	···	< 1.1
N6440-VLA25	17:48:51.659	–20:21:07.54	0.07	0.08	15.4	2.9	< 7.8	4.3	···	0.55	···	< 0.7
N6440-VLA26	17:48:52.660	–20:21:06.28	0.07	0.08	13.9	2.7	< 7.7	-2.2	···	0.51	···	< 0.9
N6440-VLA27	17:48:51.483	–20:25:09.19	0.05	0.06	< 12.3	1.5	50.8	8.4	···	3.55	···	> -1.3
N6440-VLA28	17:49:03.646	–20:19:04.76	0.05	0.06	< 12.4	2.7	45.3	7.6	···	3.61	···	> -1.1
N6440-VLA29	17:48:44.850	–20:18:33.96	0.05	0.06	< 11.3	3.3	40.7	7.1	···	3.56	···	> -1.6
N6440-VLA30	17:49:06.542	–20:22:04.06	0.05	0.06	< 11.4	-3.7	35.9	6.7	···	3.28	···	> -2.2
N6440-VLA31	17:48:57.669	–20:24:23.00	0.05	0.06	< 10.7	-0.9	32.5	5.7	···	3.00	···	> -1.3
N6440-VLA32	17:48:50.030	–20:24:28.87	0.05	0.06	< 11.9	-7.3	30.4	5.7	···	2.93	···	> -1.8
N6440-VLA33	17:48:56.797	–20:18:58.51	0.05	0.06	< 10.4	4.3	30.3	4.8	···	2.81	···	> -0.6
N6440-VLA34	17:49:04.978	–20:20:28.65	0.05	0.06	< 10.9	-1.8	28.2	5.6	···	3.09	···	> -2.6
N6440-VLA35	17:48:51.024	–20:24:06.01	0.05	0.06	< 10.6	0.2	26.6	4.7	···	2.52	···	> -1.2
N6440-VLA36	17:48:45.283	–20:20:39.55	0.05	0.06	< 9.0	2.7	23.2	3.5	···	1.98	···	> -0.6
N6440-VLA37	17:49:01.526	–20:20:07.75	0.05	0.06	< 9.4	-6.1	21.8	3.9	···	2.55	···	> -1.4
N6440-VLA38	17:48:54.065	–20:23:51.06	0.05	0.06	< 9.6	3.5	20.1	4.0	···	2.26	···	> -2.3
N6440-VLA39	17:48:57.570	–20:23:28.60	0.05	0.06	< 9.7	3.6	19.8	3.8	···	2.18	···	> -1.9

Table 3.3 (cont'd)

ID	R.A.[a] (h:m:s)	Dec.[a] (°:′:″)	R.A. unc. (″)	Dec. unc. (″)	S_5[b] (μJy)	S_5 unc. (μJy)	S_7[c] (μJy)	S_7 unc. (μJy)	note[d]	radius[e] (′)	loc.[f]	α[g]
N6440-VLA40	17:48:56.136	–20:23:19.11	0.05	0.06	< 8.9	3.5	19.7	3.4	···	1.88	···	> -1.2
N6440-VLA41	17:48:52.734	–20:23:16.68	0.05	0.06	< 8.9	2.0	17.8	3.4	···	1.66	···	> -2.0
N6440-VLA42	17:48:56.285	–20:23:26.49	0.05	0.06	< 9.0	-6.2	17.7	3.5	···	2.01	···	> -2.3
N6440-VLA43	17:48:48.272	–20:20:19.61	0.05	0.06	< 9.2	-2.1	17.5	3.4	···	1.65	···	> -2.1
N6440-VLA44	17:48:55.270	–20:20:04.36	0.05	0.06	< 9.2	2.2	16.7	3.1	···	1.66	···	> -1.8
N6440-VLA45	17:48:56.283	–20:22:26.29	0.05	0.06	< 8.2	-0.6	14.7	2.9	···	1.18	···	> -2.3
N6440-VLA46	17:48:57.721	–20:21:22.98	0.05	0.06	< 8.8	0.1	14.1	2.8	···	1.20	···	> -2.5
N6539-VLA1	18:04:52.367	–07:35:21.03	0.03	0.04	248.4	1.9	168.0	2.3	···	0.69	r_h	$-1.20^{+0.05}_{-0.05}$
N6539-VLA2	18:04:52.805	–07:36:01.81	0.03	0.04	150.8	1.8	163.6	2.6	···	1.17	r_h	$+0.25^{+0.06}_{-0.06}$
N6539-VLA3	18:04:46.339	–07:32:07.33	0.03	0.04	40.8	2.3	33.1	5.0	···	3.15	···	$-0.70^{+0.48}_{-0.55}$
N6539-VLA4	18:05:00.232	–07:34:53.29	0.03	0.04	36.4	2.1	43.1	3.9	···	2.63	···	$+0.51^{+0.32}_{-0.34}$
N6539-VLA5	18:04:48.442	–07:32:22.54	0.04	0.05	33.2	2.1	20.2	4.1	···	2.80	···	$-1.63^{+0.63}_{-0.74}$
N6539-VLA6	18:04:39.204	–07:35:50.45	0.04	0.05	29.0	2.1	16.4	3.9	···	2.68	···	$-1.86^{+0.71}_{-0.80}$
N6539-VLA7	18:04:51.579	–07:38:06.88	0.04	0.05	28.8	2.3	15.5	4.6	···	2.99	···	$-1.99^{+0.83}_{-0.86}$
N6539-VLA8	18:04:39.754	–07:33:57.37	0.03	0.04	25.3	2.2	30.1	3.8	···	2.74	···	$+0.50^{+0.46}_{-0.50}$
N6539-VLA9	18:04:57.321	–07:34:49.12	0.03	0.04	19.8	1.9	14.6	2.8	···	1.92	···	$-1.03^{+0.66}_{-0.75}$
N6539-VLA10	18:05:03.300	–07:33:52.38	0.04	0.05	16.5	2.7	< 19.7	-8.9	···	3.61	···	< 1.5
N6539-VLA11	18:04:49.887	–07:35:24.84	0.03	0.04	15.9	1.9	13.0	2.4	···	0.26	r_c	$-0.68^{+0.68}_{-0.75}$

Table 3.3 (cont'd)

ID	R.A.[a] (h:m:s)	Dec.[a] (°:′:″)	R.A. unc. (″)	Dec. unc. (″)	S_5[b] (μJy)	S_5 unc. (μJy)	S_7[c] (μJy)	S_7 unc. (μJy)	note[d]	radius[e] (′)	loc.[f]	α[g]
N6539-VLA12	18:04:50.648	–07:35:26.64	0.03	0.04	14.4	1.7	13.0	2.3	···	0.37	r_c	$-0.38^{+0.66}_{-0.72}$
N6539-VLA13	18:04:44.401	–07:34:12.74	0.04	0.05	13.8	1.8	< 7.8	8.8	···	1.61	r_h	< 0.5
N6539-VLA14	18:04:41.181	–07:32:08.10	0.04	0.05	13.5	2.6	< 21.9	5.1	···	3.69	···	< 1.5
N6539-VLA15	18:04:49.385	–07:36:40.01	0.04	0.05	13.2	1.8	9.8	2.6	···	1.51	r_h	$-1.07^{+0.90}_{-1.05}$
N6539-VLA16	18:04:58.761	–07:37:27.85	0.04	0.05	13.1	2.4	< 15.5	0.6	···	3.22	···	< 1.4
N6539-VLA17	18:04:49.289	–07:38:39.09	0.04	0.05	12.7	2.5	< 18.6	5.8	···	3.49	···	< 1.5
N6539-VLA18	18:04:56.241	–07:37:40.70	0.04	0.05	12.6	2.2	< 13.6	0.1	···	3.00	···	< 1.4
N6539-VLA19	18:04:54.705	–07:36:53.01	0.03	0.04	12.4	1.9	17.1	3.0	···	2.13	···	$+0.72^{+0.49}_{-0.67}$
N6539-VLA20	18:04:50.458	–07:35:06.26	0.04	0.05	11.3	1.8	< 6.9	4.1	···	0.20	r_c	< 0.8
N6539-VLA21	18:04:47.760	–07:33:07.43	0.04	0.05	10.8	1.9	< 9.1	-0.6	···	2.09	···	< 1.2
N6539-VLA22	18:04:48.671	–07:33:19.38	0.04	0.05	10.8	1.8	< 8.3	1.1	···	1.85	···	< 1.1
N6539-VLA23	18:04:35.991	–07:36:38.52	0.03	0.04	10.6	2.7	35.9	7.1	···	3.70	···	$+1.13^{+0.27}_{-0.60}$
N6539-VLA24	18:04:49.723	–07:35:26.74	0.03	0.04	9.6	1.9	12.7	2.4	···	0.29	r_c	$+0.51^{+0.53}_{-0.76}$
N6539-VLA25	18:04:56.234	–07:34:03.24	0.04	0.05	9.3	1.9	< 8.7	1.7	···	1.96	···	< 1.2
N6539-VLA26	18:04:52.248	–07:35:53.15	0.04	0.05	9.2	1.8	< 7.1	-0.9	···	0.97	r_h	< 1.1
N6539-VLA27	18:04:49.133	–07:38:26.64	0.03	0.04	7.7	2.4	31.2	5.0	···	3.29	···	$+1.23^{+0.19}_{-0.38}$
N6539-VLA28	18:04:50.488	–07:38:48.49	0.03	0.04	< 7.9	1.8	38.2	6.9	···	3.65	···	> -3.3
N6539-VLA29	18:04:54.850	–07:38:28.51	0.03	0.04	< 7.8	3.0	37.8	6.3	···	3.56	···	> -2.8

Table 3.3 (cont'd)

ID	R.A.[a] (h:m:s)	Dec.[a] (°:′:″)	R.A. unc. (″)	Dec. unc. (″)	S_5[b] (μJy)	S_5 unc. (μJy)	S_7[c] (μJy)	S_7 unc. (μJy)	note[d]	radius[e] (′)	loc.[f]	α[g]
N6539-VLA30	18:04:44.441	–07:38:26.38	0.03	0.04	< 7.7	-0.1	37.1	6.4	···	3.53	···	> -3.1
N6539-VLA31	18:04:37.493	–07:36:57.21	0.03	0.04	< 7.7	1.0	36.3	6.2	···	3.51	···	> -2.9
N6539-VLA32	18:04:57.726	–07:38:12.37	0.03	0.04	< 7.8	-0.9	35.8	7.1	···	3.64	···	> -3.4
N6539-VLA33	18:04:35.543	–07:34:48.35	0.03	0.04	< 7.5	-0.9	33.9	6.3	···	3.52	···	> -3.3
N6539-VLA34	18:05:00.191	–07:37:12.78	0.03	0.04	< 7.2	-4.1	32.8	5.7	···	3.32	···	> -3.0
N6539-VLA35	18:04:57.590	–07:37:55.34	0.03	0.04	< 7.2	-2.7	31.9	5.6	···	3.39	···	> -3.0
N6539-VLA36	18:04:56.486	–07:32:10.19	0.03	0.04	< 7.4	-0.4	29.9	5.9	···	3.43	···	> -3.4
N6539-VLA37	18:04:53.829	–07:38:16.69	0.03	0.04	< 7.1	-2.7	28.8	5.5	···	3.28	···	> -3.3
N6539-VLA38	18:04:36.388	–07:35:54.06	0.03	0.04	< 7.4	-0.2	28.8	5.7	···	3.38	···	> -3.4
N6539-VLA39	18:05:01.757	–07:36:15.17	0.03	0.04	< 7.3	-1.4	26.4	5.0	···	3.19	···	> -3.1
N6539-VLA40	18:04:59.236	–07:36:47.68	0.03	0.04	< 6.4	0.0	26.2	4.3	···	2.88	···	> -1.8
N6539-VLA41	18:04:53.590	–07:32:17.07	0.03	0.04	< 6.8	0.9	24.2	4.7	···	3.03	···	> -3.2
N6539-VLA42	18:04:42.768	–07:33:16.43	0.03	0.04	< 6.2	0.2	23.1	3.7	···	2.55	···	> -1.1
N6539-VLA43	18:04:50.217	–07:32:14.71	0.03	0.04	< 6.6	3.2	22.9	4.3	···	2.92	···	> -3.0
N6539-VLA44	18:05:00.848	–07:36:00.61	0.03	0.04	< 6.6	1.0	21.4	4.3	···	2.90	···	> -3.3
N6539-VLA45	18:04:57.971	–07:33:15.59	0.03	0.04	< 6.1	-0.7	21.2	4.1	···	2.80	···	> -3.3
N6539-VLA46	18:04:42.294	–07:37:15.35	0.03	0.04	< 6.3	-1.9	20.5	3.9	···	2.78	···	> -3.0
N6539-VLA47	18:04:53.660	–07:37:35.19	0.03	0.04	< 6.1	3.2	19.6	3.8	···	2.62	···	> -3.2

Table 3.3 (cont'd)

ID	R.A.[a] (h:m:s)	Dec.[a] (°:′:″)	R.A. unc. (″)	Dec. unc. (″)	S_5[b] (μJy)	S_5 unc. (μJy)	S_7[c] (μJy)	S_7 unc. (μJy)	note[d]	radius[e] (′)	loc.[f]	α[g]
N6539-VLA48	18:04:58.121	–07:36:23.07	0.03	0.04	< 6.0	-2.1	19.2	3.6	···	2.42	···	> -2.9
N6539-VLA49	18:04:55.662	–07:33:12.99	0.03	0.04	< 5.9	0.2	18.1	3.5	···	2.44	···	> -3.0
N6539-VLA50	18:04:45.863	–07:32:58.63	0.03	0.04	< 5.8	0.0	17.7	3.3	···	2.38	···	> -2.8
N6539-VLA51	18:04:46.215	–07:33:01.68	0.03	0.04	< 5.7	-1.7	16.4	3.3	···	2.30	···	> -3.2
N6539-VLA52	18:04:42.722	–07:34:52.17	0.03	0.04	< 5.6	-1.8	16.1	2.8	···	1.75	···	> -1.7
N6539-VLA53	18:04:44.004	–07:35:19.68	0.03	0.04	< 5.2	1.3	15.9	2.5	···	1.42	r_h	> -1.0
N6539-VLA54	18:04:44.494	–07:34:31.27	0.03	0.04	< 5.2	-0.5	14.1	2.5	···	1.43	r_h	> -2.0
N6539-VLA55	18:04:56.217	–07:35:37.29	0.03	0.04	< 5.4	0.7	13.8	2.7	···	1.68	r_h	> -2.9
N6539-VLA56	18:04:52.596	–07:35:21.76	0.03	0.04	< 5.5	-0.4	13.5	2.3	···	0.75	r_h	> -1.5
N6539-VLA57	18:04:56.384	–07:35:26.23	0.03	0.04	< 5.3	-1.5	13.3	2.7	···	1.68	r_h	> -3.1
N6539-VLA58	18:04:52.684	–07:35:27.75	0.03	0.04	< 5.4	-0.2	13.2	2.2	···	0.80	r_h	> -1.3
N6539-VLA59	18:04:52.936	–07:35:51.23	0.03	0.04	< 5.4	2.3	13.1	2.4	···	1.07	r_h	> -2.1
N6539-VLA60	18:04:49.220	–07:35:21.58	0.03	0.04	< 5.6	-1.6	12.9	2.4	···	0.23	r_c	> -2.2
N6539-VLA61	18:04:47.046	–07:34:46.35	0.03	0.04	< 5.1	0.4	12.1	2.3	···	0.76	r_h	> -2.5
N6544-VLA1	18:07:25.015	–24:58:35.73	0.04	0.06	224.8	3.0	164.5	2.7	···	1.71	···	$-0.80^{+0.05}_{-0.05}$
N6544-VLA2	18:07:09.189	–24:58:09.76	0.04	0.06	206.7	3.5	136.8	4.1	···	3.02	···	$-1.05^{+0.09}_{-0.09}$
N6544-VLA3	18:07:17.734	–25:03:20.91	0.04	0.06	132.9	4.1	65.5	6.5	···	3.50	···	$-1.83^{+0.26}_{-0.28}$
N6544-VLA4	18:07:33.024	–25:01:34.73	0.04	0.06	84.6	3.7	63.0	4.8	···	3.37	···	$-0.76^{+0.22}_{-0.23}$

Table 3.3 (cont'd)

ID	R.A.[a] (h:m:s)	Dec.[a] (°:′:″)	R.A. unc. (″)	Dec. unc. (″)	S_5[b] (μJy)	S_5 unc. (μJy)	S_7[c] (μJy)	S_7 unc. (μJy)	note[d]	radius[e] (′)	loc.[f]	α[g]
N6544-VLA5	18:07:10.138	–24:58:10.56	0.04	0.06	84.1	3.1	44.2	3.7	···	2.84	···	$-1.65^{+0.23}_{-0.24}$
N6544-VLA6	18:07:20.355	–24:59:52.96	0.04	0.06	79.6	2.5	17.0	2.1	···	0.05	r_h	$-3.41^{+0.12}_{-0.07}$
N6544-VLA7	18:07:23.271	–25:01:42.90	0.04	0.06	74.6	2.9	48.9	2.8	···	1.96	···	$-1.08^{+0.17}_{-0.18}$
N6544-VLA8	18:07:32.983	–25:01:03.67	0.04	0.06	42.2	3.3	30.3	4.1	···	3.14	···	$-0.88^{+0.40}_{-0.43}$
N6544-VLA9	18:07:22.893	–25:01:33.52	0.04	0.06	41.1	2.9	42.5	2.7	···	1.78	···	$+0.09^{+0.25}_{-0.24}$
N6544-VLA10	18:07:33.842	–24:59:07.28	0.06	0.09	29.4	3.5	16.1	4.0	···	3.20	···	$-1.65^{+0.68}_{-0.79}$
N6544-VLA11	18:07:34.441	–24:59:44.03	0.06	0.09	28.6	3.1	14.3	4.3	···	3.25	···	$-1.89^{+0.76}_{-0.84}$
N6544-VLA12	18:07:36.503	–25:00:20.13	0.06	0.09	28.0	4.0	< 17.1	8.5	···	3.74	···	< 0.6
N6544-VLA13	18:07:12.576	–24:59:11.16	0.04	0.06	27.9	3.0	18.2	2.7	···	1.85	···	$-1.12^{+0.47}_{-0.50}$
N6544-VLA14	18:07:22.866	–24:56:11.84	0.06	0.09	27.4	3.9	23.6	5.5	···	3.75	···	$-0.49^{+0.71}_{-0.83}$
N6544-VLA15	18:07:16.367	–25:00:37.86	0.04	0.06	24.6	2.7	14.9	2.3	···	1.12	r_h	$-1.32^{+0.49}_{-0.52}$
N6544-VLA16	18:07:09.897	–25:02:10.74	0.06	0.09	24.1	3.9	< 15.8	-0.9	···	3.25	···	< 0.9
N6544-VLA17	18:07:08.795	–24:59:03.75	0.04	0.06	22.9	3.3	20.7	3.4	···	2.70	···	$-0.28^{+0.57}_{-0.60}$
N6544-VLA18	18:07:21.096	–25:02:29.12	0.04	0.06	22.2	3.4	19.9	3.8	···	2.60	···	$-0.31^{+0.64}_{-0.68}$
N6544-VLA19	18:07:07.696	–24:57:42.73	0.06	0.09	22.0	3.6	< 16.5	-2.9	···	3.56	···	< 1.1
N6544-VLA20	18:07:18.337	–25:03:27.88	0.06	0.09	22.0	4.2	< 20.1	2.9	···	3.59	···	< 1.4
N6544-VLA21	18:07:05.829	–24:58:46.05	0.06	0.09	21.3	3.6	19.2	4.8	···	3.43	···	$-0.38^{+0.79}_{-0.93}$
N6544-VLA22	18:07:27.492	–24:56:37.60	0.06	0.09	21.2	3.5	< 15.6	7.9	···	3.67	···	< 1.1

Table 3.3 (cont'd)

ID	R.A.[a] (h:m:s)	Dec.[a] (°:′:″)	R.A. unc. (″)	Dec. unc. (″)	S_5[b] (μJy)	S_5 unc. (μJy)	S_7[c] (μJy)	S_7 unc. (μJy)	note[d]	radius[e] (′)	loc.[f]	α[g]
N6544-VLA23	18:07:28.998	–24:59:39.95	0.06	0.09	21.1	2.8	< 7.7	2.7	···	2.02	···	< -0.6
N6544-VLA24	18:07:20.875	–25:00:01.90	0.06	0.09	20.6	2.6	9.2	2.2	···	0.22	r_h	$-2.11^{+0.66}_{-0.70}$
N6544-VLA25	18:07:22.732	–24:59:17.87	0.04	0.06	20.4	2.6	19.9	2.2	···	0.84	r_h	$-0.05^{+0.45}_{-0.44}$
N6544-VLA26	18:07:10.208	–24:59:05.96	0.04	0.06	19.8	3.0	16.3	3.2	···	2.38	···	$-0.54^{+0.65}_{-0.70}$
N6544-VLA27	18:07:06.910	–24:58:20.79	0.06	0.09	18.5	3.3	< 14.3	1.5	···	3.37	···	< 1.2
N6544-VLA28	18:07:19.341	–24:56:25.82	0.06	0.09	18.2	3.5	< 13.8	6.4	···	3.47	···	< 1.2
N6544-VLA29	18:07:17.301	–25:01:50.31	0.06	0.09	18.1	3.0	< 9.0	-2.2	···	2.05	···	< 0.4
N6544-VLA30	18:07:28.387	–25:02:24.42	0.06	0.09	17.8	3.4	< 14.2	-1.6	···	3.13	···	< 1.3
N6544-VLA31	18:07:28.239	–25:00:32.38	0.06	0.09	17.8	2.7	< 7.9	8.1	···	1.95	···	< 0.0
N6544-VLA32	18:07:16.684	–25:01:52.60	0.06	0.09	17.1	3.1	< 9.5	2.0	···	2.13	···	< 0.7
N6544-VLA33	18:07:09.000	–24:59:15.70	0.06	0.09	17.0	3.0	< 9.8	-1.8	···	2.60	···	< 0.7
N6544-VLA34	18:07:24.165	–25:01:47.04	0.06	0.09	14.5	2.8	< 8.8	-0.5	···	2.10	···	< 0.9
N6544-VLA35	18:07:18.288	–25:00:48.04	0.06	0.09	14.0	2.7	< 6.8	1.5	···	1.00	r_h	< 0.6
N6544-VLA36	18:07:19.679	–25:00:33.32	0.06	0.09	13.9	2.6	< 6.5	-1.8	···	0.67	r_h	< 0.4
N6544-VLA37	18:07:22.870	–24:58:53.55	0.06	0.09	13.1	2.6	< 6.6	1.3	···	1.18	r_h	< 0.6
N6544-VLA38	18:07:17.798	–24:59:30.46	0.06	0.09	12.3	2.4	< 6.1	-1.9	···	0.65	r_h	< 0.6
N6544-VLA39	18:07:18.723	–24:58:42.71	0.04	0.06	8.2	2.7	11.5	2.3	···	1.22	···	$+0.42^{+0.54}_{-0.76}$
N6544-VLA40	18:07:21.707	–25:03:23.92	0.04	0.06	< 11.9	-3.6	35.0	6.0	···	3.52	···	> -0.8

Table 3.3 (cont'd)

ID	R.A.[a] (h:m:s)	Dec.[a] (°:′:″)	R.A. unc. (″)	Dec. unc. (″)	S_5[b] (μJy)	S_5 unc. (μJy)	S_7[c] (μJy)	S_7 unc. (μJy)	note[d]	radius[e] (′)	loc.[f]	α[g]
N6544-VLA41	18:07:27.970	–25:03:03.02	0.04	0.06	< 12.2	-6.0	34.7	6.4	···	3.62	···	> -1.4
N6544-VLA42	18:07:06.865	–24:58:25.08	0.04	0.06	< 10.1	3.2	24.4	4.5	···	3.35	···	> -1.3
N6544-VLA43	18:07:28.588	–25:01:21.88	0.04	0.06	< 8.8	5.3	17.3	3.2	···	2.42	···	> -1.5
N6544-VLA44	18:07:09.882	–25:00:25.61	0.04	0.06	< 9.1	-0.1	16.9	3.3	···	2.38	···	> -1.9
N6544-VLA45	18:07:29.466	–24:59:31.98	0.04	0.06	< 8.6	-2.2	15.6	2.9	···	2.15	···	> -1.6
N6544-VLA46	18:07:29.531	–24:59:25.49	0.04	0.06	< 8.6	1.5	15.0	2.7	···	2.18	···	> -1.5
N6544-VLA47	18:07:14.992	–24:59:53.11	0.04	0.06	< 7.9	4.7	13.7	2.3	···	1.16	r_h	> -1.3
N6544-VLA48	18:07:14.607	–24:58:01.07	0.04	0.06	< 8.5	2.3	13.7	2.7	···	2.25	···	> -2.1
N6712-VLA1	18:53:01.057	–08:45:30.05	0.03	0.04	422.3	3.4	243.9	5.0	···	3.24	···	$-1.40^{+0.06}_{-0.06}$
N6712-VLA2	18:52:56.172	–08:45:25.43	0.03	0.04	238.7	3.9	144.9	6.5	···	3.66	···	$-1.28^{+0.12}_{-0.12}$
N6712-VLA3	18:52:51.677	–08:43:26.25	0.03	0.04	178.9	3.2	116.0	4.8	···	3.30	···	$-1.11^{+0.11}_{-0.12}$
N6712-VLA4	18:53:11.018	–08:39:33.66	0.03	0.04	138.7	3.1	113.9	4.3	···	3.26	···	$-0.50^{+0.11}_{-0.11}$
N6712-VLA5	18:52:58.922	–08:45:17.45	0.03	0.04	138.6	3.3	129.8	5.0	ext.?	3.21	···	$-0.17^{+0.11}_{-0.12}$
N6712-VLA6	18:53:00.667	–08:45:41.13	0.03	0.04	125.8	3.5	96.4	5.7	···	3.44	···	$-0.69^{+0.16}_{-0.17}$
N6712-VLA7	18:53:04.866	–08:42:20.34	0.03	0.04	88.4	2.3	92.8	2.1	···	0.14	r_c	$+0.12^{+0.09}_{-0.09}$
N6712-VLA8	18:53:13.330	–08:43:06.79	0.03	0.04	67.7	2.7	42.6	3.0	···	2.35	···	$-1.19^{+0.20}_{-0.21}$
N6712-VLA9	18:53:02.401	–08:42:19.01	0.03	0.04	65.2	2.3	51.6	2.0	···	0.47	r_c	$-0.60^{+0.13}_{-0.13}$
N6712-VLA10	18:53:09.175	–08:44:27.37	0.03	0.04	59.6	2.8	39.3	3.1	···	2.41	···	$-1.07^{+0.23}_{-0.24}$

Table 3.3 (cont'd)

ID	R.A.[a] (h:m:s)	Dec.[a] (°:′:″)	R.A. unc. (″)	Dec. unc. (″)	S_5[b] (μJy)	S_5 unc. (μJy)	S_7[c] (μJy)	S_7 unc. (μJy)	note[d]	radius[e] (′)	loc.[f]	α[g]
N6712-VLA11	18:53:10.207	–08:43:08.26	0.03	0.04	53.2	2.4	27.1	2.4	···	1.65	···	$-1.74^{+0.25}_{-0.27}$
N6712-VLA12	18:52:58.506	–08:40:05.45	0.03	0.04	46.8	2.5	37.4	3.2	···	2.69	···	$-0.59^{+0.26}_{-0.27}$
N6712-VLA13	18:52:50.785	–08:41:32.33	0.03	0.04	40.9	3.1	26.4	4.9	···	3.44	···	$-1.20^{+0.50}_{-0.59}$
N6712-VLA14	18:53:03.395	–08:40:58.87	0.03	0.04	39.3	2.3	31.0	2.3	···	1.40	···	$-0.61^{+0.24}_{-0.25}$
N6712-VLA15	18:52:54.683	–08:41:54.27	0.03	0.04	31.5	2.6	18.6	3.1	···	2.42	···	$-1.40^{+0.47}_{-0.53}$
N6712-VLA16	18:52:53.008	–08:40:44.80	0.03	0.04	31.1	3.0	27.1	4.2	···	3.23	···	$-0.39^{+0.46}_{-0.50}$
N6712-VLA17	18:53:15.854	–08:41:48.44	0.05	0.06	30.7	2.9	< 10.9	8.6	···	2.91	···	< -0.9
N6712-VLA18	18:53:08.443	–08:44:03.13	0.05	0.06	22.6	2.6	9.4	2.8	···	1.97	···	$-2.27^{+0.72}_{-0.71}$
N6712-VLA19	18:53:07.821	–08:45:21.92	0.05	0.06	21.8	3.3	16.5	4.4	···	3.12	···	$-0.85^{+0.79}_{-0.96}$
N6712-VLA20	18:52:56.889	–08:44:03.51	0.03	0.04	21.5	2.8	33.2	3.4	···	2.49	···	$+1.02^{+0.31}_{-0.38}$
N6712-VLA21	18:53:16.293	–08:41:34.79	0.05	0.06	20.5	3.0	< 12.0	1.1	···	3.07	···	< 0.5
N6712-VLA22	18:53:00.924	–08:45:44.18	0.05	0.06	20.1	3.4	25.9	5.8	···	3.47	···	$+0.47^{+0.61}_{-0.79}$
N6712-VLA23	18:53:12.818	–08:44:38.27	0.05	0.06	18.9	3.2	< 13.2	10.6	···	3.10	···	< 1.0
N6712-VLA24	18:53:18.823	–08:43:17.31	0.05	0.06	18.8	3.5	< 18.3	-11.8	···	3.71	···	< 1.4
N6712-VLA25	18:53:09.690	–08:43:43.56	0.03	0.04	17.9	2.4	21.3	2.7	···	1.90	···	$+0.44^{+0.47}_{-0.48}$
N6712-VLA26	18:52:56.463	–08:43:35.96	0.05	0.06	16.6	2.8	< 9.0	6.3	···	2.30	···	< 0.6
N6712-VLA27	18:53:14.627	–08:44:10.04	0.05	0.06	15.9	3.1	< 13.1	4.8	···	3.12	···	< 1.3
N6712-VLA28	18:53:05.218	–08:44:00.03	0.05	0.06	15.8	2.5	< 7.5	1.2	···	1.65	···	< 0.2

Table 3.3 (cont'd)

ID	R.A.[a] (h:m:s)	Dec.[a] (°:′:″)	R.A. unc. (″)	Dec. unc. (″)	S_5[b] (μJy)	S_5 unc. (μJy)	S_7[c] (μJy)	S_7 unc. (μJy)	note[d]	radius[e] (′)	loc.[f]	α[g]
N6712-VLA29	18:53:10.364	–08:40:55.63	0.05	0.06	15.7	2.6	< 8.2	3.2	···	2.08	···	< 0.4
N6712-VLA30	18:52:56.157	–08:40:26.42	0.05	0.06	15.5	2.9	< 10.0	0.4	···	2.79	···	< 1.0
N6712-VLA31	18:53:00.122	–08:44:12.41	0.05	0.06	13.8	2.8	10.9	3.0	···	2.11	···	$-0.72^{+0.89}_{-1.02}$
N6712-VLA32	18:53:00.934	–08:40:38.51	0.05	0.06	13.5	2.4	< 7.6	2.0	···	1.91	···	< 0.7
N6712-VLA33	18:53:07.852	–08:43:49.64	0.05	0.06	13.1	2.3	9.6	2.4	···	1.70	···	$-0.89^{+0.80}_{-0.91}$
N6712-VLA34	18:52:56.993	–08:41:04.02	0.05	0.06	12.9	2.5	< 8.1	-0.6	···	2.22	···	< 0.9
N6712-VLA35	18:52:57.580	–08:42:10.39	0.05	0.06	12.8	2.4	< 7.5	-1.8	···	1.67	···	< 0.8
N6712-VLA36	18:52:58.975	–08:41:33.08	0.05	0.06	12.2	2.4	9.5	2.4	···	1.55	···	$-0.74^{+0.85}_{-0.95}$
N6712-VLA37	18:53:11.200	–08:44:11.22	0.03	0.04	10.9	2.7	17.6	3.3	···	2.49	···	$+0.80^{+0.43}_{-0.64}$
N6712-VLA38	18:53:17.598	–08:42:07.81	0.03	0.04	< 9.5	0.8	24.6	4.6	···	3.29	···	> -1.5
N6712-VLA39	18:53:05.337	–08:45:36.28	0.03	0.04	< 9.4	0.3	24.3	4.8	···	3.25	···	> -2.2
N6712-VLA40	18:53:02.591	–08:45:22.45	0.03	0.04	< 9.4	-2.3	21.7	4.3	···	3.04	···	> -2.1
N6712-VLA41	18:53:10.415	–08:44:48.46	0.03	0.04	< 8.9	0.1	21.0	4.0	···	2.87	···	> -1.7
N6712-VLA42	18:52:57.097	–08:44:16.37	0.03	0.04	< 8.4	-2.9	20.1	3.6	···	2.61	···	> -1.2
N6712-VLA43	18:52:59.185	–08:44:13.63	0.03	0.04	< 8.2	-4.7	17.3	3.1	···	2.25	···	> -1.3
N6712-VLA44	18:53:08.580	–08:40:05.21	0.03	0.04	< 8.1	-1.1	16.4	3.1	···	2.51	···	> -1.7
N6712-VLA45	18:53:11.516	–08:44:03.44	0.03	0.04	< 7.8	2.6	15.7	3.1	···	2.46	···	> -2.1
N6712-VLA46	18:53:14.000	–08:42:02.79	0.03	0.04	< 7.7	0.6	15.6	3.1	···	2.42	···	> -2.1

Table 3.3 (cont'd)

ID	R.A.[a] (h:m:s)	Dec.[a] (°:′:″)	R.A. unc. (″)	Dec. unc. (″)	S_5[b] (μJy)	S_5 unc. (μJy)	S_7[c] (μJy)	S_7 unc. (μJy)	note[d]	radius[e] (′)	loc.[f]	α[g]
N6712-VLA47	18:53:05.136	–08:40:06.16	0.03	0.04	< 7.9	-0.2	15.4	2.8	···	2.27	···	> -1.4
N6712-VLA48	18:52:58.448	–08:41:57.26	0.03	0.04	< 7.4	2.7	13.3	2.3	···	1.50	···	> -1.3
N6712-VLA49	18:53:02.796	–08:43:53.17	0.03	0.04	< 7.2	-0.9	12.5	2.4	···	1.56	···	> -1.9
N6712-VLA50	18:53:02.794	–08:42:03.45	0.03	0.04	< 7.0	-0.6	11.0	2.1	···	0.48	r_c	> -2.0
N6760-VLA1	19:11:10.421	+01:04:34.17	0.03	0.03	2223.6	3.1	1278.6	4.1	···	2.77	···	$-1.60^{+0.01}_{-0.01}$
N6760-VLA2	19:11:15.631	+00:58:18.26	0.03	0.03	927.7	3.7	660.8	7.3	···	3.64	···	$-0.98^{+0.03}_{-0.03}$
N6760-VLA3	19:11:17.529	+01:05:15.90	0.03	0.03	87.3	3.5	59.0	6.1	···	3.70	···	$-1.17^{+0.32}_{-0.34}$
N6760-VLA4	19:11:12.231	+00:58:50.51	0.03	0.03	82.9	2.9	52.2	4.0	···	2.99	···	$-1.35^{+0.24}_{-0.25}$
N6760-VLA5	19:11:16.058	+01:00:20.33	0.03	0.03	63.3	2.4	49.8	2.7	···	1.80	···	$-0.70^{+0.19}_{-0.19}$
N6760-VLA6	19:10:59.637	+01:02:25.18	0.03	0.03	43.6	3.3	44.1	4.6	···	3.15	···	$+0.02^{+0.38}_{-0.39}$
N6760-VLA7	19:11:01.662	+01:03:13.08	0.03	0.03	27.0	3.0	31.5	3.9	···	2.94	···	$+0.43^{+0.47}_{-0.50}$
N6760-VLA8	19:11:17.481	+01:01:00.54	0.03	0.03	24.5	2.4	25.4	2.5	···	1.59	···	$+0.10^{+0.41}_{-0.41}$
N6760-VLA9	19:11:03.945	+00:59:15.76	0.05	0.05	24.1	3.2	19.8	4.9	···	3.26	···	$-0.72^{+0.81}_{-0.97}$
N6760-VLA10	19:11:17.565	+01:05:00.10	0.03	0.03	23.7	3.3	32.6	5.4	···	3.46	···	$+0.75^{+0.48}_{-0.62}$
N6760-VLA11	19:11:07.132	+01:00:47.28	0.03	0.03	22.8	2.3	18.0	2.4	···	1.60	···	$-0.71^{+0.49}_{-0.51}$
N6760-VLA12	19:11:22.430	+01:02:37.26	0.05	0.05	22.6	2.8	16.4	3.6	···	2.72	···	$-1.03^{+0.73}_{-0.83}$
N6760-VLA13	19:11:22.918	+01:00:09.11	0.05	0.05	21.1	3.1	< 13.5	3.7	···	3.20	···	< 0.9
N6760-VLA14	19:11:16.893	+00:58:30.73	0.05	0.05	20.4	3.4	< 17.0	4.0	···	3.53	···	< 1.4

Table 3.3 (cont'd)

ID	R.A.[a] (h:m:s)	Dec.[a] (°:′:″)	R.A. unc. (″)	Dec. unc. (″)	S_5[b] (μJy)	S_5 unc. (μJy)	S_7[c] (μJy)	S_7 unc. (μJy)	note[d]	radius[e] (′)	loc.[f]	α[g]
N6760-VLA15	19:11:19.250	+00:59:40.41	0.05	0.05	20.3	2.9	< 11.1	3.5	ext.?	2.81	···	< 0.4
N6760-VLA16	19:10:58.516	+01:01:37.88	0.05	0.05	20.3	3.3	< 15.2	-1.9	···	3.38	···	< 1.2
N6760-VLA17	19:11:05.043	+01:04:15.36	0.05	0.05	19.9	2.9	< 12.7	10.1	···	2.99	···	< 0.8
N6760-VLA18	19:11:13.010	+01:04:21.44	0.05	0.05	18.7	2.7	12.3	3.2	···	2.54	···	$-1.33^{+0.85}_{-0.96}$
N6760-VLA19	19:11:04.059	+00:58:57.98	0.05	0.05	18.1	3.5	< 16.8	-5.0	···	3.48	···	< 1.4
N6760-VLA20	19:11:03.927	+01:00:50.55	0.05	0.05	17.9	2.6	9.7	2.9	···	2.25	···	$-1.83^{+0.89}_{-0.92}$
N6760-VLA21	19:11:17.834	+00:58:56.18	0.05	0.05	17.6	3.2	< 14.1	9.1	···	3.24	···	< 1.3
N6760-VLA22	19:11:23.882	+01:02:07.56	0.05	0.05	17.5	3.0	< 11.9	11.6	···	2.98	···	< 1.1
N6760-VLA23	19:11:12.305	+00:58:13.75	0.05	0.05	17.1	3.4	< 18.3	-7.3	···	3.60	···	< 1.4
N6760-VLA24	19:11:06.791	+01:00:41.68	0.05	0.05	16.8	2.4	9.4	2.4	···	1.73	···	$-1.76^{+0.82}_{-0.88}$
N6760-VLA25	19:11:09.932	+01:01:37.18	0.05	0.05	15.7	2.3	< 6.4	6.7	···	0.56	r_h	< -0.2
N6760-VLA26	19:11:19.348	+01:04:29.95	0.05	0.05	15.4	3.1	< 13.9	5.5	···	3.24	···	< 1.4
N6760-VLA27	19:11:14.592	+01:01:15.08	0.05	0.05	14.9	2.4	9.0	2.1	···	0.87	r_h	$-1.52^{+0.83}_{-0.88}$
N6760-VLA28	19:11:08.392	+01:02:40.36	0.05	0.05	14.8	2.3	9.9	2.2	···	1.24	r_h	$-1.23^{+0.80}_{-0.88}$
N6760-VLA29	19:11:16.634	+01:02:05.94	0.05	0.05	14.6	2.4	< 6.8	5.7	···	1.19	r_h	< 0.3
N6760-VLA30	19:10:59.876	+01:01:48.99	0.05	0.05	14.5	2.8	< 12.7	0.4	···	3.03	···	< 1.3
N6760-VLA31	19:11:19.591	+01:03:57.10	0.05	0.05	14.3	2.8	< 11.4	1.8	···	2.85	···	< 1.3
N6760-VLA32	19:11:05.218	+01:00:47.91	0.05	0.05	14.0	2.6	11.9	2.7	···	1.99	···	$-0.55^{+0.86}_{-0.95}$

Table 3.3 (cont'd)

ID	R.A.[a] (h:m:s)	Dec.[a] (°:′:″)	R.A. unc. (″)	Dec. unc. (″)	S_5[b] (μJy)	S_5 unc. (μJy)	S_7[c] (μJy)	S_7 unc. (μJy)	note[d]	radius[e] (′)	loc.[f]	α[g]
N6760-VLA33	19:11:03.550	+00:59:45.06	0.05	0.05	14.0	2.8	< 12.1	2.9	···	2.96	···	< 1.3
N6760-VLA34	19:11:11.084	+01:02:09.73	0.05	0.05	13.9	2.3	< 6.0	6.6	···	0.41	r_h	< 0.1
N6760-VLA35	19:11:12.156	+01:03:20.76	0.05	0.05	13.3	2.4	< 7.0	0.7	···	1.52	···	< 0.7
N6760-VLA36	19:11:11.908	+01:03:31.03	0.05	0.05	13.0	2.3	< 7.4	2.1	···	1.69	···	< 0.8
N6760-VLA37	19:11:16.097	+01:01:27.26	0.03	0.03	12.3	2.4	14.0	2.2	···	1.09	r_h	$+0.30^{+0.63}_{-0.70}$
N6760-VLA38	19:11:10.190	+01:00:10.99	0.05	0.05	12.1	2.4	< 7.4	-0.3	···	1.71	···	< 0.9
N6760-VLA39	19:11:16.463	+01:03:19.82	0.05	0.05	11.8	2.4	< 7.8	-0.4	···	1.87	···	< 1.0
N6760-VLA40	19:11:04.771	+01:04:58.93	0.03	0.03	< 10.9	-2.7	35.5	6.1	···	3.64	···	> -1.2
N6760-VLA41	19:11:15.505	+00:58:31.68	0.03	0.03	< 10.2	-3.6	28.4	5.3	ext.?	3.41	···	> -1.9
N6760-VLA42	19:11:25.625	+01:02:15.28	0.03	0.03	< 9.8	-1.2	27.7	5.4	···	3.43	···	> -2.6
N6760-VLA43	19:11:18.365	+01:04:41.89	0.03	0.03	< 9.5	0.9	24.7	4.7	···	3.28	···	> -2.1
N6760-VLA44	19:10:59.603	+01:02:47.88	0.03	0.03	< 9.7	3.6	24.0	4.7	···	3.25	···	> -2.4
N6760-VLA45	19:11:01.318	+01:02:08.34	0.03	0.03	< 8.4	5.1	23.8	3.5	···	2.69	···	> -0.4
N6760-VLA46	19:11:10.806	+01:04:47.83	0.03	0.03	< 9.0	0.4	23.0	4.3	···	2.98	···	> -1.9
N6760-VLA47	19:11:21.622	+01:03:18.61	0.03	0.03	< 8.6	-1.2	21.5	3.7	···	2.82	···	> -1.2
N6760-VLA48	19:11:00.691	+01:00:54.28	0.03	0.03	< 8.7	-3.5	21.4	4.0	···	2.98	···	> -1.9
N6760-VLA49	19:11:03.846	+01:00:17.40	0.03	0.03	< 8.2	-3.3	17.7	3.3	···	2.56	···	> -1.8
N6760-VLA50	19:11:03.200	+01:00:30.34	0.03	0.03	< 8.3	-0.6	17.1	3.3	···	2.57	···	> -2.2

Table 3.3 (cont'd)

ID	R.A.[a] (h:m:s)	Dec.[a] (°:′:″)	R.A. unc. (″)	Dec. unc. (″)	S_5[b] (μJy)	S_5 unc. (μJy)	S_7[c] (μJy)	S_7 unc. (μJy)	note[d]	radius[e] (′)	loc.[f]	α[g]
N6760-VLA51	19:11:06.896	+00:59:45.68	0.03	0.03	< 8.2	-2.3	16.9	3.0	···	2.43	···	> -1.5
N6760-VLA52	19:11:19.142	+01:03:12.40	0.03	0.03	< 7.9	0.5	14.8	2.9	···	2.25	···	> -2.3
N6760-VLA53	19:11:18.856	+01:00:58.76	0.03	0.03	< 7.3	-2.4	13.7	2.6	···	1.91	···	> -2.1
N6760-VLA54	19:11:17.819	+01:01:02.35	0.03	0.03	< 7.3	-0.8	13.0	2.5	···	1.65	···	> -2.2
N6760-VLA55	19:11:05.644	+01:02:10.84	0.03	0.03	< 7.2	-1.6	12.5	2.4	···	1.63	···	> -2.2
N6760-VLA56	19:11:08.467	+01:03:04.17	0.03	0.03	< 7.2	-5.3	12.3	2.4	···	1.52	···	> -2.4
N6760-VLA57	19:11:16.815	+01:01:23.71	0.03	0.03	< 6.9	2.8	12.1	2.3	···	1.28	···	> -2.2

[a]ICRS position at epoch of observation.

[b]Flux density in the lower subband.

[c]Flux density in the higher subband.

[d]Whether the source is extended or a possible imaging artifact.

[e]Projected radius from the cluster center.

[f]Whether the source is within the core (r_c) or half-light (r_h) radius.

[g]Spectral index α of source, for $S \propto \nu^{\alpha}$

Table 3.4. Source Counts at 5.0 and 7.2 GHz.

S_ν[a] (μJy)	lim. (low)[b] (μJy)	lim. (high)[c] (μJy)	$N_{5.0}$[d]	$N_{7.2}$[e]	$S_\nu^{2.5}\,dN_{5.0}/dS$[f] (Jy$^{1.5}$ sr^{-1})	$S_\nu^{2.5}\,dN_{7.2}/dS$[g] (Jy$^{1.5}$ sr^{-1})
9.15	7.90	10.61	35	32	$0.41^{+0.08}_{-0.07}$	$0.52^{+0.11}_{-0.09}$
12.3	10.61	14.25	162	127	$0.67^{+0.06}_{-0.05}$	$0.80^{+0.08}_{-0.07}$
16.5	14.25	19.14	211	159	$0.66^{+0.05}_{-0.05}$	$0.74^{+0.06}_{-0.06}$
22.2	19.14	25.72	157	149	$0.62^{+0.05}_{-0.05}$	$0.74^{+0.07}_{-0.06}$
29.8	25.72	34.55	96	94	$0.58^{+0.07}_{-0.06}$	$0.60^{+0.07}_{-0.06}$
40	34.55	46.42	67	56	$0.63^{+0.09}_{-0.08}$	$0.53^{+0.08}_{-0.07}$
53.8	46.42	62.36	33	28	$0.48^{+0.10}_{-0.08}$	$0.41^{+0.09}_{-0.08}$
72.3	62.36	83.77	33	18	$0.75^{+0.16}_{-0.13}$	$0.41^{+0.12}_{-0.10}$
97.1	83.77	112.53	21	18	$0.74^{+0.20}_{-0.16}$	$0.64^{+0.19}_{-0.15}$
130	112.53	151.18	19	13	$1.04^{+0.30}_{-0.24}$	$0.71^{+0.26}_{-0.20}$
175	151.18	203.09	10	6	$0.86^{+0.37}_{-0.27}$	$0.51^{+0.31}_{-0.20}$
235	203.09	272.83	6	8	$0.80^{+0.48}_{-0.32}$	$1.07^{+0.53}_{-0.37}$
316	272.83	366.52	8	3	$1.67^{+0.82}_{-0.58}$	$0.62^{+0.61}_{-0.34}$
425	366.52	492.39	4	3	$1.30^{+1.02}_{-0.62}$	$0.97^{+0.94}_{-0.53}$
571	492.39	661.47	3	4	$1.52^{+1.47}_{-0.82}$	$2.03^{+1.60}_{-0.97}$
767	661.47	888.62	2	0	$1.58^{+2.07}_{-1.02}$	—
1030	888.62	1193.8	3	3	$3.68^{+3.57}_{-2.00}$	$3.68^{+3.57}_{-2.00}$
1380	1193.8	1603.7	1	3	$1.90^{+4.34}_{-1.57}$	$5.69^{+5.52}_{-3.09}$

Table 3.4 (cont'd)

S_ν[a] (μJy)	lim. (low)[b] (μJy)	lim. (high)[c] (μJy)	$N_{5.0}$[d]	$N_{7.2}$[e]	$S_\nu^{2.5}\,dN_{5.0}/dS$[f] (Jy$^{1.5}$ sr^{-1})	$S_\nu^{2.5}\,dN_{7.2}/dS$[g] (Jy$^{1.5}$ sr^{-1})
1860	1603.7	2154.4	1	0	$2.98^{+6.81}_{-2.47}$	—
2500	2154.4	2894.3	3	1	$13.92^{+13.50}_{-7.55}$	$4.64^{+10.62}_{-3.85}$
3350	2894.3	3888.2	0	2	—	$14.37^{+18.87}_{-9.25}$
4510	3888.2	5223.4	2	0	$22.40^{+29.43}_{-14.43}$	—
6050	5223.4	7017.0	0	0	—	—
8130	7017.0	9426.7	0	0	—	—
10900	9426.7	12663.8	0	0	—	—
14700	12663.8	17012.5	0	1	—	$66.21^{+151.44}_{-54.85}$
19700	17012.5	22854.6	1	0	$102.50^{+234.44}_{-84.92}$	—

[a]Characteristic flux value of the bin (geometric mean).

[b]Lower limit of bin.

[c]Upper limit of bin.

[d]Raw 5.0 GHz counts.

[e]Raw 7.2 GHz counts.

[f]Euclidian-normalized 5.0 GHz differential source counts.

[g]Euclidian-normalized 7.2 GHz differential source counts.

Table 3.5. 5.0 GHz Radio Source Excesses

ID	Excess ($r < r_c$)	Excess ($r < r_h$)
M2	-0.27 ± 0.07	2.77 ± 2.60
M3	-0.24 ± 0.06	2.73 ± 4.26
M4	5.37 ± 2.57	29.47 ± 10.16
M5	-0.53 ± 0.12	-4.29 ± 3.04
M9	-0.09 ± 1.02	-2.69 ± 1.87
M10	-1.34 ± 0.36	2.28 ± 4.25
M12	-1.38 ± 1.14	-2.36 ± 3.87
M13	1.31 ± 1.38	3.54 ± 3.22
M14	1.48 ± 2.03	7.34 ± 3.86
M19	0.64 ± 0.97	2.95 ± 2.81
M22	6.05 ± 3.65	-0.97 ± 6.92
M28	1.73 ± 1.40	-7.99 ± 5.09
M30	-0.016 ± 0.003	-1.96 ± 2.09
M54	-0.011 ± 0.003	-0.03 ± 1.02
M55	4.50 ± 3.96	6.20 ± 6.36
M62	0.89 ± 0.95	2.09 ± 2.12
M92	-0.29 ± 0.05	-0.61 ± 2.19
M107	0.68 ± 1.47	1.27 ± 4.48
NGC 6304	-0.05 ± 0.02	-1.62 ± 1.25

Table 3.5 (cont'd)

ID	Excess ($r < r_c$)	Excess ($r < r_h$)
NGC 6325	-0.002 ± 0.001	-0.20 ± 1.07
NGC 6440	0.94 ± 1.02	1.31 ± 1.43
NGC 6539	3.78 ± 1.96	4.36 ± 3.28
NGC 6544	-0.007 ± 0.001	20.14 ± 10.22
NGC 6712	0.49 ± 1.42	-2.47 ± 1.71
NGC 6760	-0.46 ± 0.10	-0.46 ± 2.96

Note. — These are the sensitivity-corrected "excesses" of 5.0 GHz radio sources within the core or half-light radius of the GC compared to the scaled local density of background sources.

Chapter 4

The MAVERIC Survey: Multi-wavelength Classification of Radio-Selected Black Hole Candidates in Globular Clusters

4.1 Introduction

Following the source counts analysis, which provided statistical evidence for an excess of radio sources in some clusters, we will attempt to find individual black hole candidates by examining select sources from the MAVERIC radio source catalog. Despite the few known black holes discovered in globular clusters, the abundance of NS LMXBs and radio MSPs in GCs suggest that some accreting black holes could exist in GCs at the present day. While previously thought to mostly be expelled from the cluster over time due to strong gravitational encounters with other massive objects, recent observations and dynamic analyses question that conclusion.

The MAVERIC radio source catalog provides an opportunity to discover BH candidates in GCs by selecting sources by the characteristics of their radio emission. The LMXBs

discovered in GCs were first noticed due to their X-ray emission, and the X-ray sources in GCs have been analyzed many times in the past 3 decades. Selecting potential candidates by their radio emission could allow for the discovery of new BH candidates, particularly those with little or no persistent X-ray emission, which are believed to represent the majority of BH LMXB systems.

This chapter is outlined as follows: Section 2 lists our selection criteria for narrowing the catalog sources into the most likely BH candidates, Section 3 goes over the observed properties of each source, and Section 4 summarizes our findings.

4.2 Selection Criteria

The main selection criteria of the black hole candidate sample are: sources located in the core of their host cluster, sources with a flat (>-1.0) radio spectral index (α), and radio sources with a match (<1″away) in the MAVERIC X-ray source catalog (Bahramian et al., 2020). We justify these choices in the following text.

Because of mass segregation, the most massive stars in the globular cluster system migrate towards the center of the cluster over time (Verbunt & Meylan, 1988). Therefore we expect to find compact objects, in particular BH candidates, in the cores of globular clusters, because they are much heavier than the typical $\sim 0.5 M_{\odot}$ stars in the cluster.

The choice of constraining the sample to sources with a radio spectral index α >-1.0 is two-fold. Known stellar-mass BH binaries in quiescence typically have a flat $\alpha \approx 0$ radio spectral index due to partially self-absorbed synchrotron radiation emanating from the radio jets of the BH (Blandford & Königl, 1979; Hjellming & Johnston, 1988). This constraint would also keep many millisecond pulsars (MSPs) from being included the BH candidate

sample. MSPs are abundant in GCs (Camilo & Rasio, 2005; Ransom, 2008) but on average have a steeper negative spectral index ($\alpha \approx -1.4$ to -2; Bates et al. (2013)).

The final criteria of a radio/X-ray source match is implemented due to the importance of observed X-ray emission in accreting BH binary systems, via the complementary MAVERIC Chandra catalog of faint X-ray sources in 38 Galactic GCs (Bahramian et al., 2020). Bahramian et al. (2020) details the construction of the X-ray catalog, which includes spectral analysis of each source, probability of being a foreground/background source, and characterization of variability where possible. The absolute astrometric accuracy of Chandra is rarely better than about $1''$except for when clear matches can be made at radio or optical wavelengths. Hence an X-ray match to within $1''$of a radio source is typically good enough to be a likely true astrometric match, except in the densest few clusters with the highest number of X-ray and/or radio sources, in which case more care needs to be taken. In addition, while we recognize the possibility that some true accreting BHs might only have faint radio emission and no detected X-ray emission, it is hard to separate these sources from background active galactic nuclei, so we focus on objects with detections in both wavelengths here.

4.3 Candidate sources

There are 9 radio sources in total from the overall survey that meet our selection criteria: 7 of these come from the VLA survey which has been the main focus of my thesis (4.1). Another two were originally observed in the southern component of the MAVERIC survey that uses the Australia Telescope Compact Array (ATCA), as described in Tudor et al. (2022), but were characterized using VLA data from MAVERIC. An overview of their observed properties

is given below.

Table 4.1: List of MAVERIC selected candidates. We include the position of each source detection as well as their radio flux densities at 5.0 GHz & 7.2 GHz. Note that the two Terzan 5 sources were also observed at 2.6GHz, 3.4GHz, 9.0GHz, and 11.0GHz (see section 4.3.8), and their fluxes measured by Urquhart et al. (2020).

ID	R.A.	Dec.	S_5	S_7	$S_{9.0}$
α					
	(h:m:s)	($^\circ$:$'$:$''$)	(μJy)	(μJy)	
M4-VLA31	16:23:31.44	–26:30:57.90	9.7±2.7	12.2±2.2	$0.37^{+0.59}_{-0.77}$
M22-VLA22	18:36:24.85	–23:55:14.95	25.0±2.7	19.5±2.1	$-0.81^{+0.51}_{-0.51}$
M28-VLA31	18:24:32.18	–24:52:14.77	14.5±2.6	<6.3±3.1	< 0.2
M55-VLA32	19:39:59.57	–30:57:30.98	12.4±2.4	<6.8±1.6	< 0.9
M55-VLA34	19:40:00.22	–30:57:39.94	11.7±2.4	13.0±2.2	$0.21^{+0.67}_{-0.78}$
M62-VLA1	17:01:13.21	–30:06:50.63	22.4±3.7	18.9±2.3	$-0.40^{+0.57}_{-0.53}$
N6539-VLA24	18:04:49.72	–07:35:26.32	9.6±1.9	12.7±2.4	$0.51^{+0.53}_{-0.76}$
Ter5-VLA31	17:48:05.02	-24:46:43.87	32±3	14±4	−0.2±0.02
Ter5-VLA42	17:48:05.23	-24:46:47.66	–	–	–

4.3.1 M4-VLA31

M4-VLA31 was detected by the MAVERIC source finding algorithm above the 5σ significance threshold at 7.0 GHz, and subsequently detected at lower significance at the same position in the 5.0 GHz radio image (Figure 4.2). M4-VLA31 is located at the coordinates 16:23:31.448 $\pm 0.08''$, -26:30:57.90 $\pm 0.07''$. It is near the edge of the cluster core, $1'$ from the center of M4. The radio flux density was measured as S_5=9.7$\pm$2.7μJy at 5.0 GHz and S_7=12.2$\pm$2.2μJy at 7.0 GHz, which correspond to a slightly inverted radio spectral index of α=$0.37^{+0.59}_{-0.77}$ (4.1). We calculate the radio luminosity at 5.0 GHz to be $L_R = 2.81 \times 10^{26}$ erg s^{-1}.

The MAVERIC GOOSE catalog contains a Chandra X-ray source $0.405''$away from the radio position of M4-VLA31, which is a high-probability astrometric match to the radio source. The GOOSE coordinates of source CXOU 162331.46-263057.9 are 245.881159°, -26.516087°$\pm 0.0530''$(16:23:478, -26:30:57.91). Its X-ray spectrum is best fit using using a power-law, with the resultant 1-10keV unabsorbed flux given as $F_{1-10} = 7.943 \times 10^{-15}$ erg s^{-1} cm^{-2}. From this flux we derive the 1-10keV X-ray luminosity: $L_X = 4.6 \times 10^{30}$ erg s^{-1}. The power-law fit photon index is given in the GOOSE catalog as $\Gamma = 2.52 \pm 0.43$. On the radio-X-ray correlation for accreting compact objects (4.1) M4-VLA31 lies toward the lower-luminosity end of the figure, but almost directly on the black hole correlation line.

This X-ray source was first designated as CX8 in a Chandra X-ray survey of M4 and matched to a known variable optical counterpart and classified as an active binary (Kaluzny et al., 1997; Mochejska et al., 2002; Bassa et al., 2004). Kaluzny et al. (2013) finds that the optical source is 0.1 magnitudes redder and 1 magnitudes brighter than the M4 main sequence, and classifies it as a red straggler. They find the luminosity varies with modulated period of P=0.7785087, but note that the average luminosity also varies by season (Kaluzny

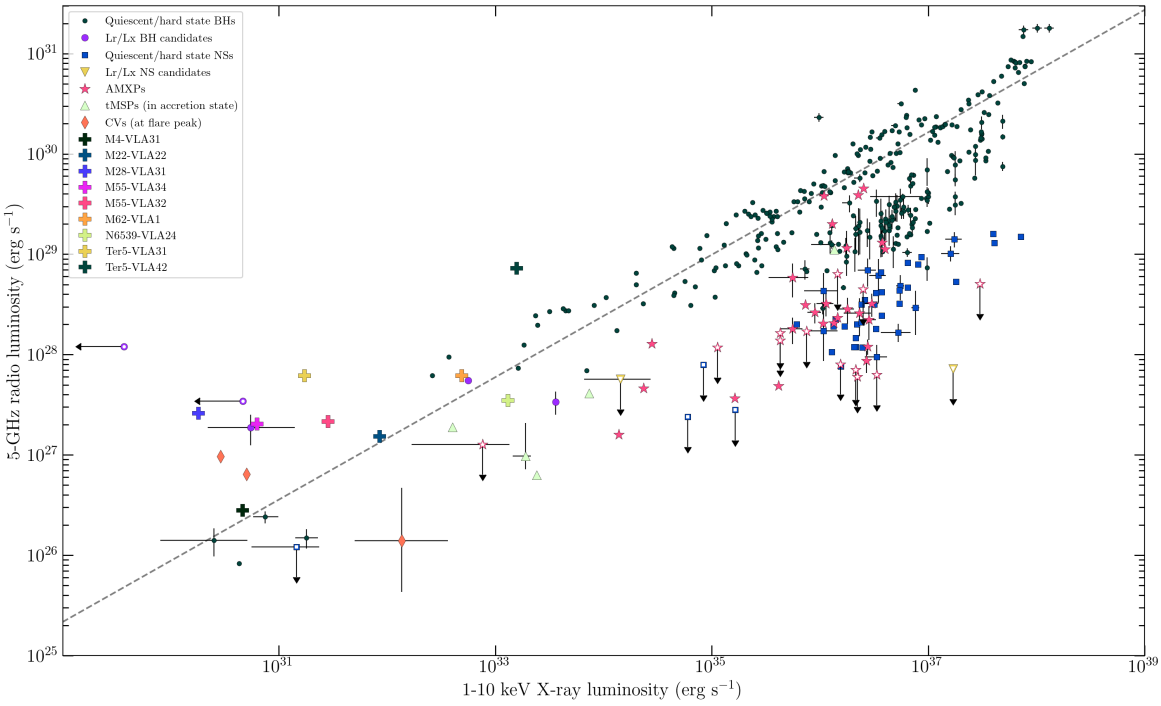

Figure 4.1 The radio/X-ray correlation for accreting compact objects, showing the 10 black hole candidates with filled cross sign from MAVERIC survey using VLA and ATCA radio data and *Chandra* X-ray. The dark green circles show known quiescent black holes in the field (Miller-Jones et al., 2011; Gallo et al., 2012; Ratti et al., 2012; Corbel et al., 2013; Rushton et al., 2016; Plotkin et al., 2017). The dotted black line shows the best-fitting L_R–L_X correlation for black holes from Gallo et al. (2014). Purple circles are radio-selected black hole candidates, (Strader et al., 2012; Chomiuk et al., 2013; Miller-Jones et al., 2015; Tetarenko et al., 2016a; Bahramian et al., 2017). The light green triangles are transitional millisecond pulsars (Hill et al., 2011; Papitto et al., 2013; Deller et al., 2015; Bogdanov et al., 2018a). Blue squares are NSs in the hard state, and pink stars are accretion-powered millisecond X-ray pulsars (Migliari & Fender, 2006; Tudor et al., 2017). The orange diamonds are the bright CVs AE Aqr ($L_X = 5.0 \times 10^{30}$ erg s^{-1}), SS Cyg (in outburst; $L_X = 1.4 \times 10^{32}$ erg s^{-1}; Russell et al. (2016)), and white dwarf "pulsar" AR Sco ($L_X = 2.9 \times 10^{30}$ erg s^{-1}; Marsh et al. (2016)). Figure adapted from Bahramian et al. (2018)).

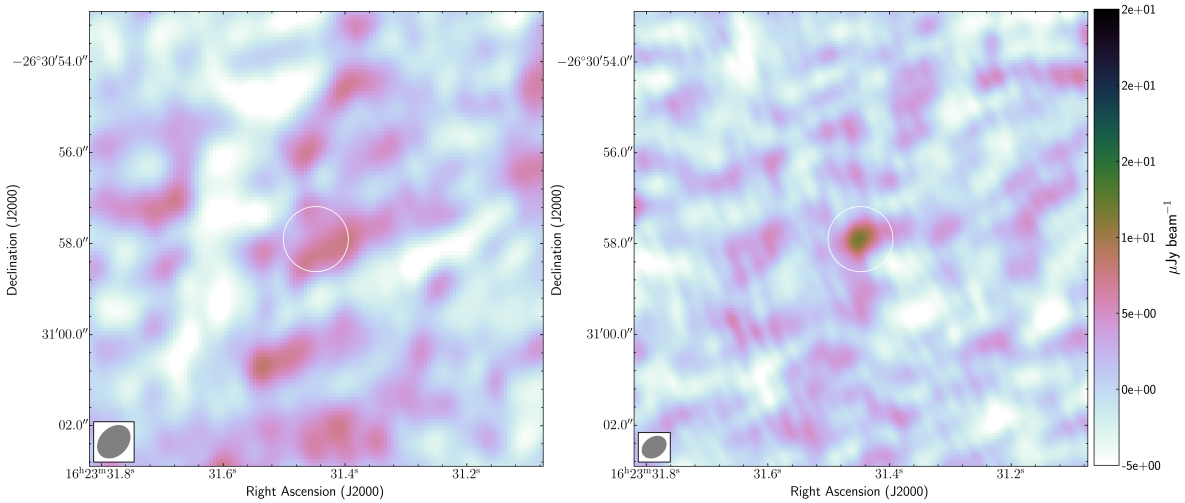

Figure 4.2 VLA images of 5.0 GHz (left) and 7.4 GHz (right) show a 10″x 10″field of view centered at M4-VLA31 (white circle). The flux density is 9.7±2.7μJy at 5.0 GHz and 12.2±2.2μJy at 7.0 GHz. The synthesized beam is plotted on the left corner of each radio map with grey color.

et al., 2013). A light curve of the source shows optical flaring, leading to their classification of the source as a chromospherically active binary (Kaluzny et al., 2013). In this interpretation, the radio emission would result from a chromospheric process, and would not indicate accretion. Preliminary optical spectroscopy of this source shows a low semi-amplitude (J. Strader, private communication) and hence supports the interpretation of this source as an active binary rather than a black hole binary.

4.3.2 M22-VLA22

M22-VLA22 was detected at $>5\sigma$ significance in both the 5.0GHz and 7.0GHz radio images of M22 (4.3). Its position was measured at 18:36:24.859 ±0.10″, -23:55:14.95 ±0.09″, 0.99′ from the center of M22. The radio flux density is S_5=25.0±2.7μJy at 5.0 GHz and S_7=19.5±2.1μJy at 7.0 GHz (4.1). The calculated radio spectral index is $\alpha=-0.81^{+0.51}_{-0.51}$. The 5.0GHz radio luminosity is $L_R = 1.53 \times 10^{27}$ erg s^{-1}.

There is a CHANDRA X-ray source coincident with M22-VLA22 in the MAVERIC GOOSE catalog, CXOU 183624.84-235514.4. The GOOSE coordinates of this source are 279.103536°, -23.920675°±0.024″(18:36:24.849, -23:55:14.43), 0.539″away from the radio position of M22-VLA22, and consistent with an astrometric match. The 1-10keV unabsorbed X-ray Flux is $F_{1-10} = 6.9 \times 10^{-14}$ erg s^{-1} cm^{-2} when the spectrum is fit by a power-law. The X-ray luminosity over 1-10keV is calculated as $L_X = 8.5 \times 10^{31}$ erg s^{-1}, and the photon index is given to be $\Gamma = 1.23^{+0.19}_{-0.18}$. In 4.1 M22-VLA22 sits almost directly on the radio-X-ray black hole correlation.

The X-ray counterpart to M22-VLA22 has been included in earlier Chandra catalogs as well as X-ray source catalogs created by observations done with XMM-Newton (Wang et al., 2016; Tranin et al., 2022; Evans et al., 2010). However, there have been no published attempts to characterize the nature of the X-ray source thus far. At optical wavelengths, M22-VLA22 has a close counterpart in the Hubble Space Telescope photometric catalogs of the HST UV Globular Cluster Survey (HUGS) (Sarajedini et al., 2007; Piotto et al., 2015; Nardiello et al., 2018). The optical source is 0.13″from the radio position of M22-VLA22 (4.4), and has measured magnitudes in the following filters: F275W=19.6, F336W=18.6, F438W=18.6, F606W=17.5, F814W=16.7. A color-magnitude diagram using the HUGS catalog for M22 is shown in 4.5, with the M22-VLA22 optical counterpart shown in blue. It is clearly on the main sequence of M55, right at or just below the turn-off to the sub-giant branch. This confirms that the optical counterpart is a member of the cluster, and of spectral type often found in LMXBs. It does not clearly have a UV excess, so there is no evidence for a bright accretion disk, though one would not necessarily be visible at this X-ray luminosity. Optical spectroscopy is needed to further clarify the nature of this candidate.

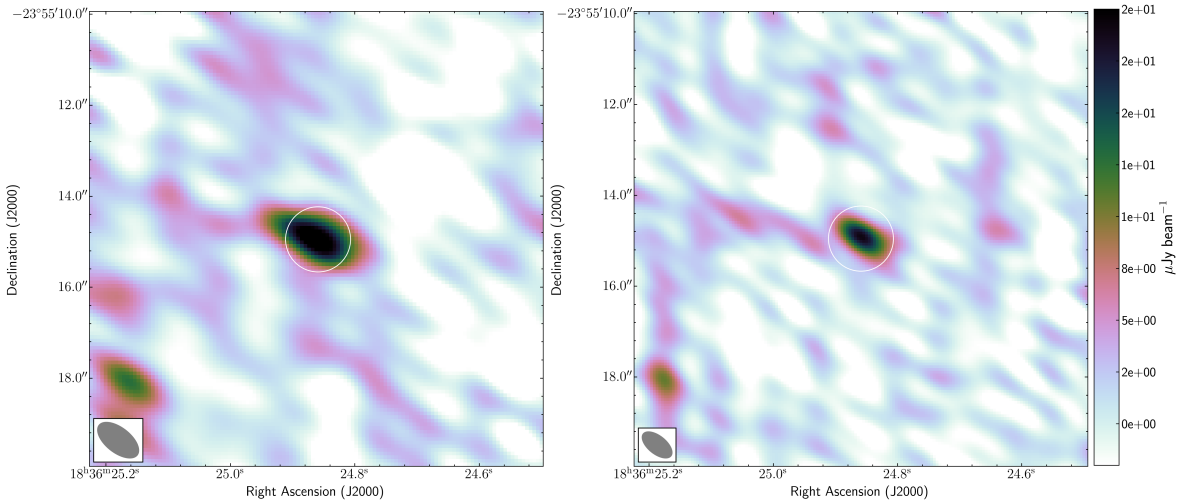

Figure 4.3 VLA images of 5.0 GHz (left) and 7.4 GHz (right) show a 10″x 10″field of view centered at M22-VLA22 (white circle). The flux density is 25±2.7μJy at 5.0 GHz and an upper limit of 19.5±2.1μJy at 7.4 GHz. The synthesized beam is plotted on the left corner of each radio map with grey color

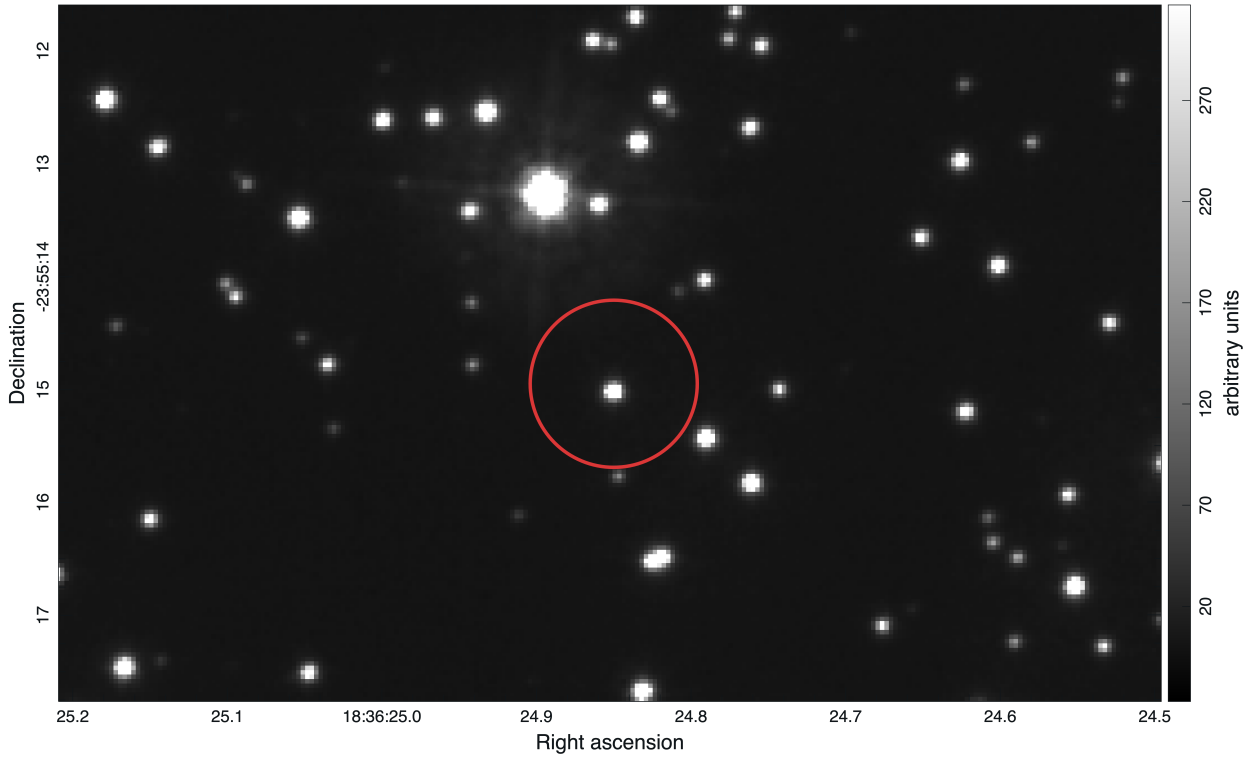

Figure 4.4 Hubble Space Telescope image of M22 in the F275W filter. The radio position of M22-VLA22 is denoted by the red circle, and its optical counterpart can be clearly seen at the same position.

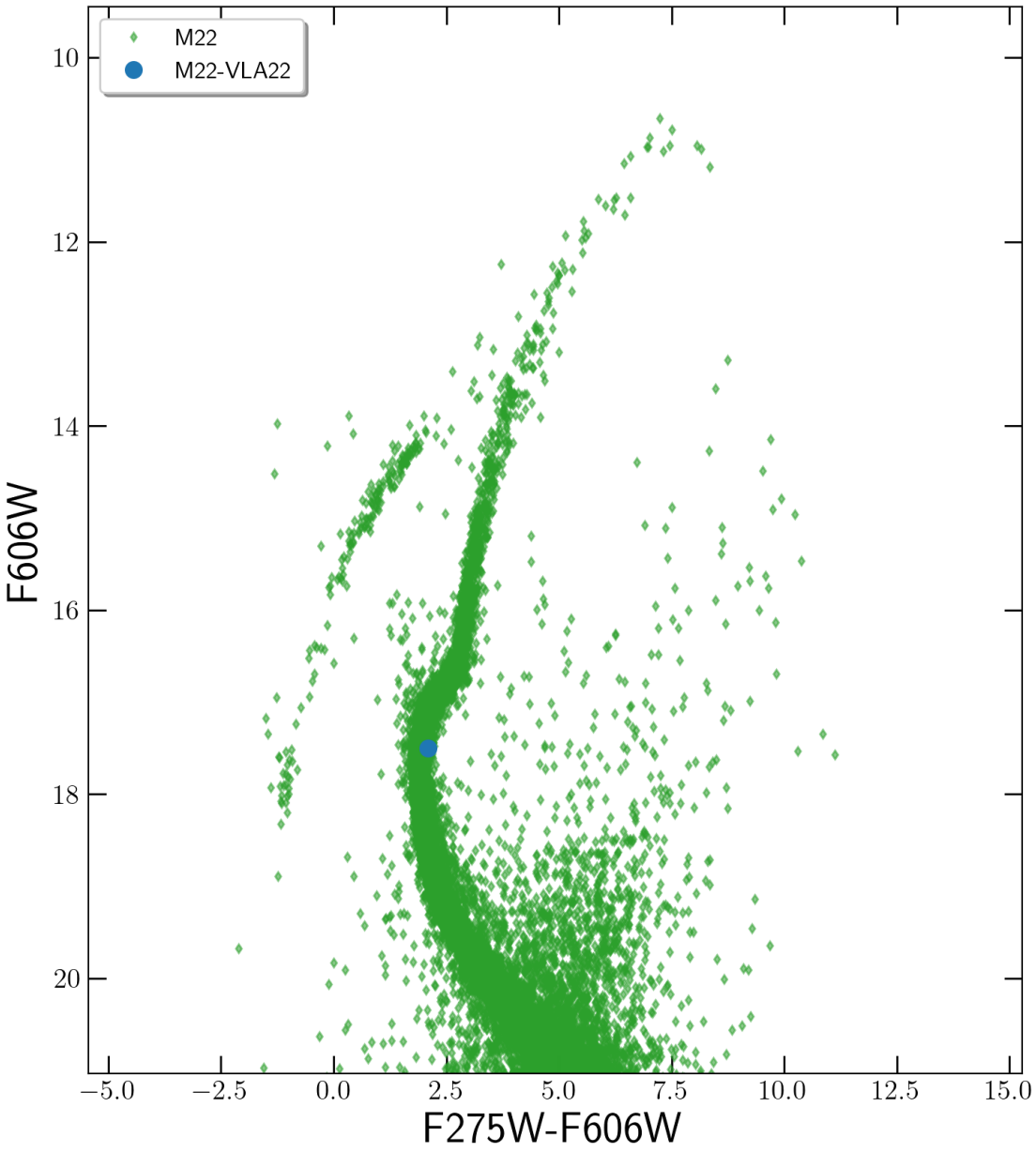

Figure 4.5 A F606W vs. F275W-F606W color-magnitude diagram of the stars in M22 from the HUGS catalog. The optical counterpart is shown by the blue circle, and the other stars in the M22 field are the green diamonds.

4.3.3 M28-VLA31

M28-VLA31 was detected at $>5\sigma$ significance in the 5.0 GHz radio image of M28 (Fig. 4.6), but not detected at all at 7.0 GHz. Its position was measured as 18:24:32.188 $\pm 0.06''$, -24:52:14.77 $\pm 0.09''$, $0.13'$ from the center of M28, within the cluster core. The radio flux density is S_5=14.5$\pm$2.6μJy at 5.0 GHz with an upper limit of $S_7 < 6.3\pm3.1\mu$Jy at 7.0 GHz (Table 4.1). These data constrained the radio spectral index to $\alpha < 0.2$. The 5.0 GHz radio luminosity is $L_R = 2.62 \times 10^{27}$ erg s^{-1}.

M28-VLA31 is close match (separation = $0.05''$) with a CHANDRA X-ray source in the MAVERIC GOOSE catalog, CXOU 182432.18-245214.8. The GOOSE coordinates of this source are 276.134119°, -24.870783°$\pm 0.102''$(18:24:32.189, -24:52:14.82). The 1-10 keV unabsorbed X-ray Flux is $F_{1-10} = 5.0 \times 10^{-16}$ erg s^{-1} cm^{-2} when the spectrum is fit by a power-law. The calculated X-ray luminosity over 1-10 keV is $L_X = 1.8 \times 10^{30}$ erg s^{-1}, and the photon index is given as $\Gamma = 3.15^{+0.71}_{-1.12}$.

M28-VLA31 is a known X-ray source and has been previously identified as radio pulsar binary J1824-2452C (Bégin, 2006; Bogdanov et al., 2011). The system pulsar has a measured spin period of P=4.16 ms, and orbital period of P=8.1 days. Its systemic mass is estimated to be $\approx 1.6 M_\odot$. Our calculated radio and X-ray luminosities are not at odds with the pulsar interpretation given that we could only constrain the radio spectral index to $\alpha < 0.2$. Therefore we are satisfied with classifying this source as a radio pulsar. This source is also an example of how a pulsar can look like an accreting black hole if only has an upper limit on the spectral index vs. a measurement.

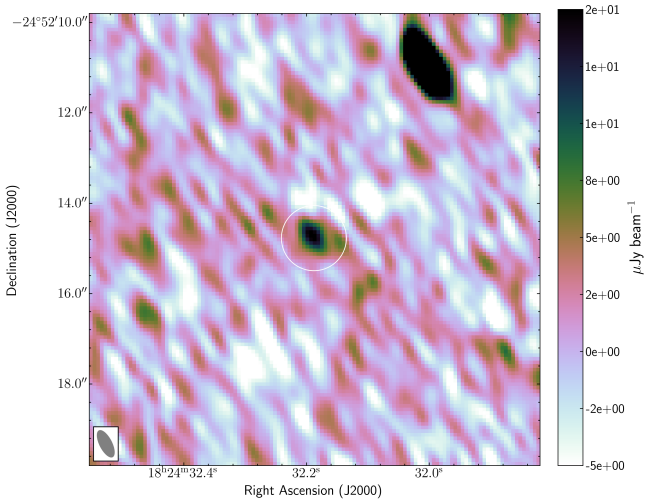

Figure 4.6 VLA radio map of 5.0 GHz show a 10″x 10″field of view centered at M28-VLA31 (white circle). The flux density is 14.5 ±2.6μJy. The synthesized beam is plotted on the left corner with grey color

4.3.4 M55-VLA32

M55-VLA32 was detected with a flux density of 12.4 ± 2.4μJy at 5.0 GHz and an upper limit of <6.8 ± 1.6μJy at 7.0 GHz (see Figure 4.7; Table 4.1). It is located at the coordinates 19:39:59.574 ±0.08″, -30:57:30.98 ±0.11″, 0.37′ from the center of M55. The radio flux density measurements constrain the radio spectral index as $\alpha < 0.9$. The 5.0 GHz radio luminosity is $L_R = 2.16 \times 10^{27}$ erg s^{-1}.

The GOOSE X-ray source closest to M55-VLA32 is identified as CXOU 193959.59-305730.2. It is 0.51″away from the position of M55-VLA32, with coordinates given by 294.998280°, -30.958471° ±0.1280″, consistent with an astrometric match. The unabsorbed X-ray flux over 1-10 keV is $F_{1-10} = 8.2 \times 10^{-15}$ erg s^{-1} cm^{-2}, assuming the spectrum follows a power-law. The subsequent X-ray luminosity in the 1-10 keV range is $L_X = 2.8 \times 10^{31}$ erg s^{-1}. The photon index is listed as $\Gamma = 0.11^{+2.29}_{-0.94}$, although the spectral analysis is flagged as "not reliable" owing to the low number of source photon counts ($N = 6$). It is

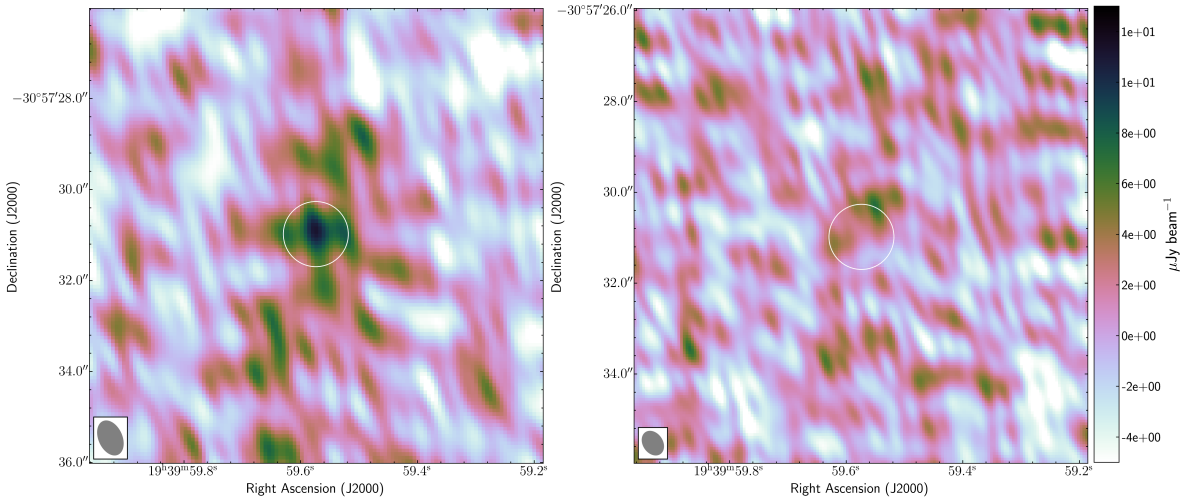

Figure 4.7 VLA images of 5.0 GHz (left) and 7.4 GHz (right) show a 10″x 10″field of view centered at M55-VLA32 (white circle). The flux density is 12.4 ± 2.4μJy at 5.0 GHz and an upper limit of <6.8 ± 1.6μJy at 7.4 GHz. The synthesized beam is plotted on the left corner of each radio map with grey color

also worth noting that the probability of the source being a background AGN is substantial, estimated to be P=0.362. On the radio-X-ray correlation (4.1) M55-VLA32 sits near the BH correlation line, about a half-magnitude brighter in radio luminosity.

M55-VLA32 is not associated with any previously characterised sources. It has an optical counterpart in the HUGS catalog for M55, 0.16″away from the radio position. 4.10 shows an optical image from ACS Survey of Globular Clusters with the radio position of M55-VLA32 overlaid. The measured photometry from the HUGS catalogs in each filter is listed as: F275W=21.2, F336W=20.2, F438W=20.5, F606W=19.6, F814W=18.9. A color-magnitude diagram of the M55 field is shown in 4.8, with the optical counterpart to M55-VLA32 overlaid in a blue circle. The counterparts position in the color-magnitude diagram is distinctly redder than the main sequence of the cluster in the figure. This suggests that the optical counterpart is most likely not a member of the cluster, and likely a background source.

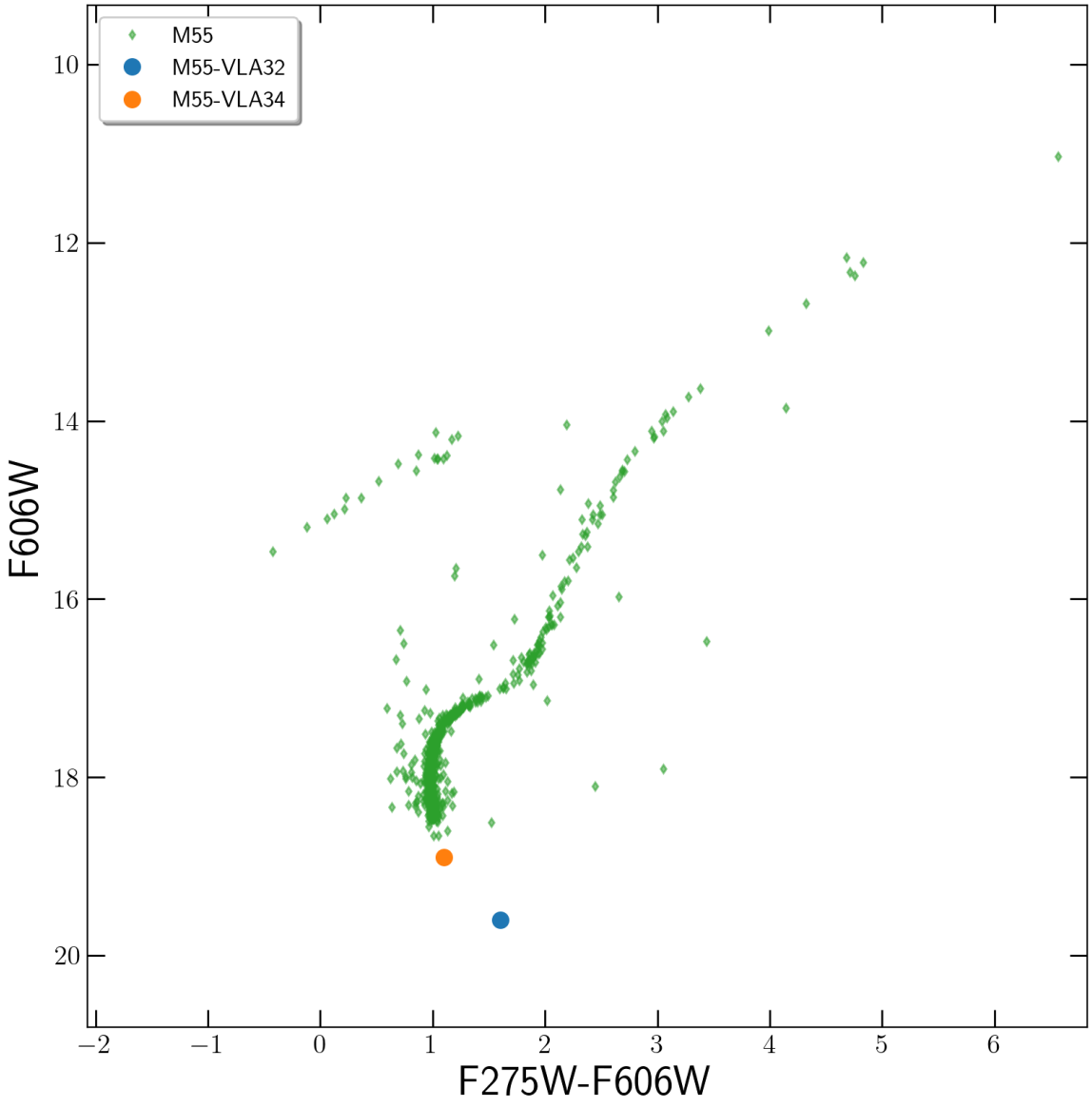

Figure 4.8 A F606W vs. F275W-F606W color-magnitude diagram of the stars in M55 from the HUGS catalog. The optical counterparts to M55-VLA32 and M55-VLA34 are shown by the blue and orange circles respectively. The other stars in the M55 field are shown by the green diamonds.

4.3.5 M55-VLA34

M55-VLA34 is located within the core of M55, at position 19:40:00.222±0.07″, -30:57:39.94±0.08″, 15″from the cluster center (4.9). It was detected in both 5.0 GHz and 7.0 GHz radio images with a flux density of 11.7±2.4 μJy and 13.0±2.2 μJy, respectively (4.1). The radio flux density measurements correspond to a radio spectral index of α=$0.21^{+0.67}_{-0.78}$. The 5.0 GHz radio luminosity is $L_R = 2.04 \times 10^{27}$ erg s^{-1}.

An X-ray counterpart to M55-VLA34 (separation=0.4226″) was found in the GOOSE catalog. The source, with Chandra identifier: CXOU 194000.25-305739.8, has the coordinates 295.001060°, -30.961075°±0.1840″(19:40:00.254, -30:57:39.87). Like M55-VLA32, this source has a decent probability of being an AGN (P=0.322), and an unreliable spectral fit due to a low number of photon counts (N=6 from 1-10keV). The photon index is listed as $\Gamma = 2.52^{+1.16}_{-1.25}$. The X-ray flux in the 1-10keV energy band is $F_{1-10} = 1.8 \times 10^{-15}$ erg s^{-1} cm^{-2}, which corresponds to an X-ray luminosity of $L_X = 6.3 \times 10^{30}$ erg s^{-1}. On the radio-X-ray plane (4.1), M55-VLA34 lies about one magnitude in radio luminosity above the BH LMXB correlation.

The X-ray source corresponding the M55-VLA34 has been observed in the past, but no classification has been made based on its X-ray properties (Evans et al., 2010; Chen et al., 2019). The VISTA Hemisphere Survey catalog (VHS; McMahon et al. (2013, 2021)) shows a near-infrared counterpart 0.371″away from M22-VLA22 and classifies it as a galaxy, with a probability of P=0.9 of being a background galaxy. Like M55-VLA32, M55-VLA34 has an optical counterpart in the HUGS catalog (Piotto et al., 2015; Sarajedini et al., 2007). It is 0.268″away, and can be seen in the optical F814W image of the radio position of M55-VLA34 (4.10; Sarajedini et al. (2007)). The position of the HUGS counterpart on a color-magnitude

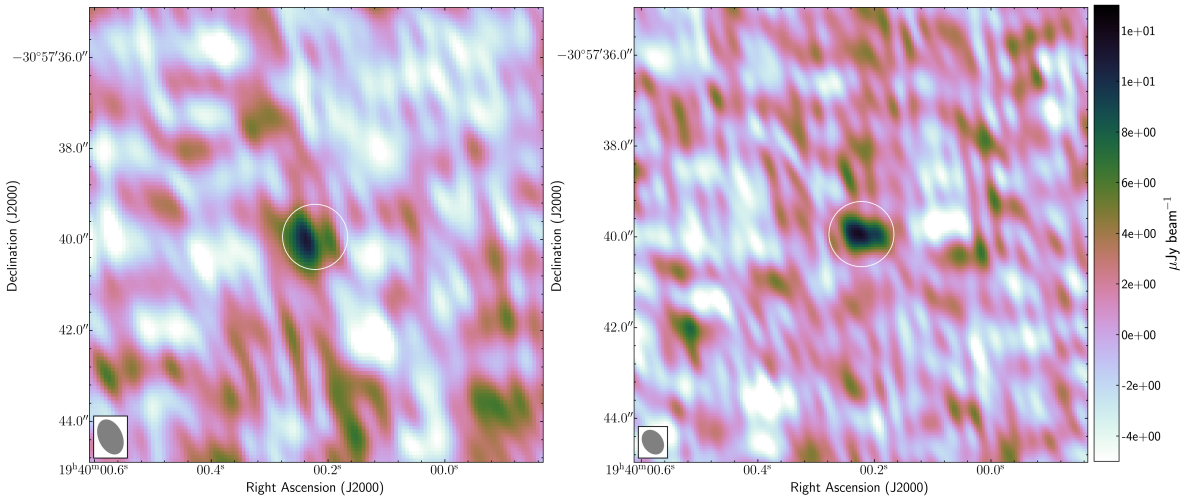

Figure 4.9 VLA images of 5.0 GHz (left) and 7.4 GHz (right) show a 10″x 10″field of view centered at M55-VLA34 (white circle). The flux density is 10.5 ± 2.3μJy at 5.0 GHz and 11.4 ± 2.3μJy at 7.4 GHz. The synthesized beam is plotted on the left corner of each radio map with grey color.

diagram of the stars in M55 can be seen in Fig. 4.8. The optical counterpart looks like it could be consistent with a main sequence star in M55, but the plotted data are not deep enough to assess this one way or the other. We tentatively suggest this source is a background AGN, but additional photometry and/or an optical spectrum would be valuable to aid in classification.

4.3.6 M62-VLA1

M62-VLA1 is located 3.7″(0.12 pc) from the center of M62, at the position 17:01:13.214±0.07″, -30:06:50.63±0.08″(Figure 4.11). Its radio catalog values are 22.4±3.7 μJy and 18.9±2.3 μJy at 5.0 and 7.2 GHz respectively, and it has a radio spectral index of α=$-0.4^{+0.50}_{-0.53}$ (Table 4.1). This source was discovered at the very beginning of the MAVERIC project, and classified in detail by Chomiuk et al. (2013) as a LMXB. I will summarize that discussion below.

M62-VLA1 shows variations in C-band radio flux within ∼1 week and has a flat radio

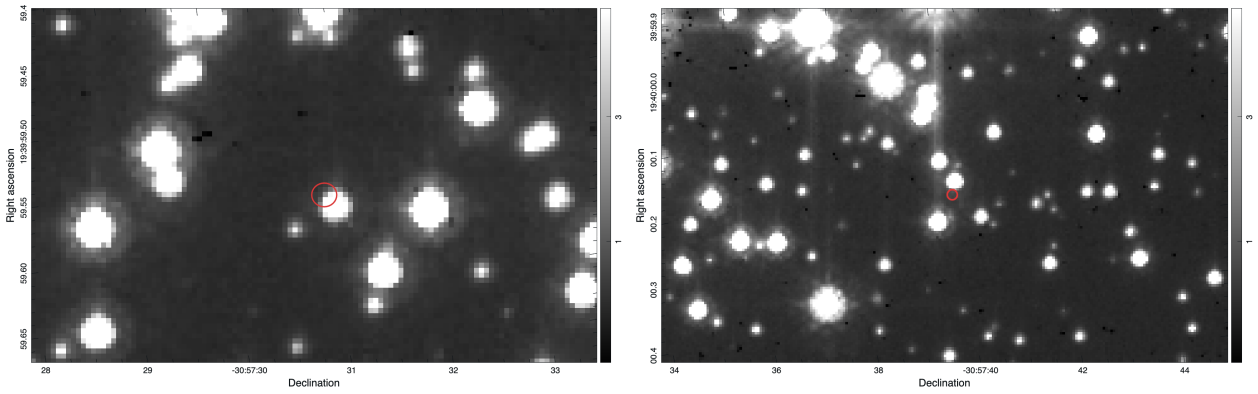

Figure 4.10 Optical image of the M55 globular cluster centered at the M55-VLA32 source (red region, left) and M55-VLA34 source (red region, right). The data were taken with HSTACS WFC instrument in the F814W (I) filter.

spectral index similar to previously discovered LMXB black hole systems. CHANDRA observations revealed an unabsorbed X-ray luminosity of $L_X = 4.8 \times 10^{32}$ erg s^{-1} and a photon index $\Gamma = 2.5 \pm 0.1$. On the radio-X-ray correlation (Fig. 4.1), M62-VLA1 lies almost directly on the black hole correlation line. A combined power-law and black-body model fits best its X-ray spectrum, however, accreting neutron stars show similar X-ray spectra in the low-hard accretion state.

Archival Hubble Space Telescope (HST)/Advanced Camera for Surveys (ACS) images show that M62-VLA1 is accompanied by a star on the lower red-giant branch. Narrow band data from F658N show a slight evidence of Hα excess while a variability of 0.05-0.07 mag, and consistent with a 3-4 day period.

There is newer high resolution data of M62-VLA1, taken from the panoramic integral-field spectrograph at the Very Large Telescope (MUSE; Bacon et al. (2010)). The data were taken as part of a survey of Galactic globular clusters, and the multiple spectra taken between 2015 and 2018 are presented by Göttgens et al. (2019) (Figure 4.12). There is clear broad Hα emission, consistent with an accreting compact objects, and evidence for radial velocity variations from the absorption lines. Additional MUSE data have been obtained

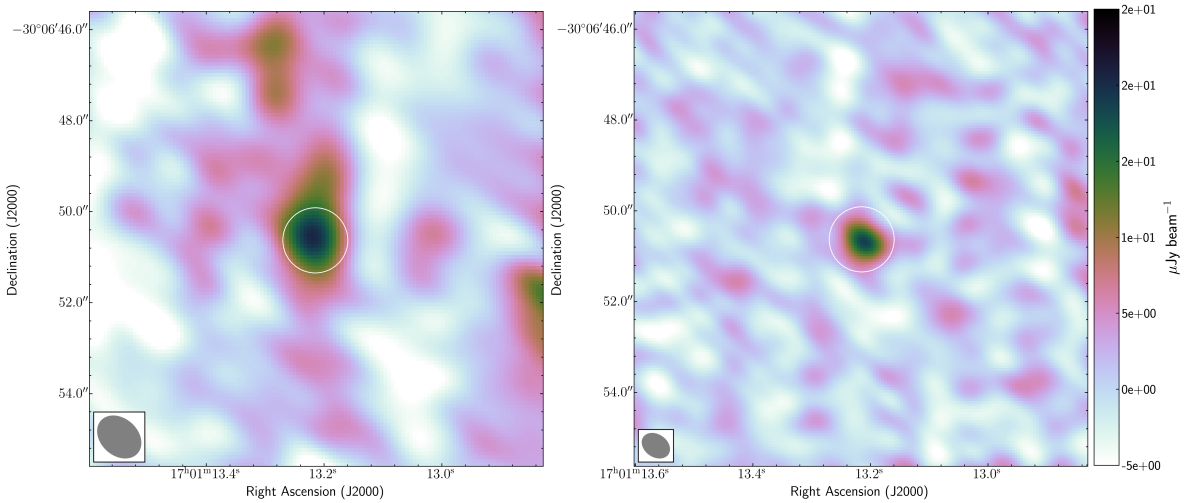

Figure 4.11 VLA images of 5.0 GHz (left) and 7.2 GHz (right) show a 10″x 10″field of view centered at M62-VLA1 (white circle). The flux density is 22.4 ± 3.7μJy at 5.0 GHz and 18.9 ± 2.3μJy at 7.2 GHz. The synthesized beam is plotted on the left corner of each radio map with grey color.

that should allow the determination of the period and semi-amplitude for this source to assess whether it is an accreting black hole or else an unusually accreting neutron star.

4.3.7 NGC6539-VLA24

NGC6539-VLA24 (R.A 18:04:49.723±0.03″, DEC -07:35:26.32±0.04″) is within the core of NGC6539, 17″from the cluster center (Fig. 4.13). It has measured flux densities of 9.6 ± 1.9 and 12.7 ±2.4 μJy at 5.0 and 7.2 GHz, respectively (Table 4.1). These values imply a spectral index of $\alpha = 0.51^{+0.53}_{-0.76}$, consistent with a flat or inverted radio spectrum. The corresponding radio luminosity is $L_R = 3.5 \times 10^{27}$ erg $\frac{}{s}^{-1}$.

X-ray observations of the NGC6539 globular cluster show a counterpart 0.5″from N6539-VLA24, CXOU J180449.72–073526.7. This source is the brightest X-ray source in the cluster at $L_X \approx 2 \times 10^{33}$ erg s^{-1}, and is described in detail in Bahramian et al. (2020). The source

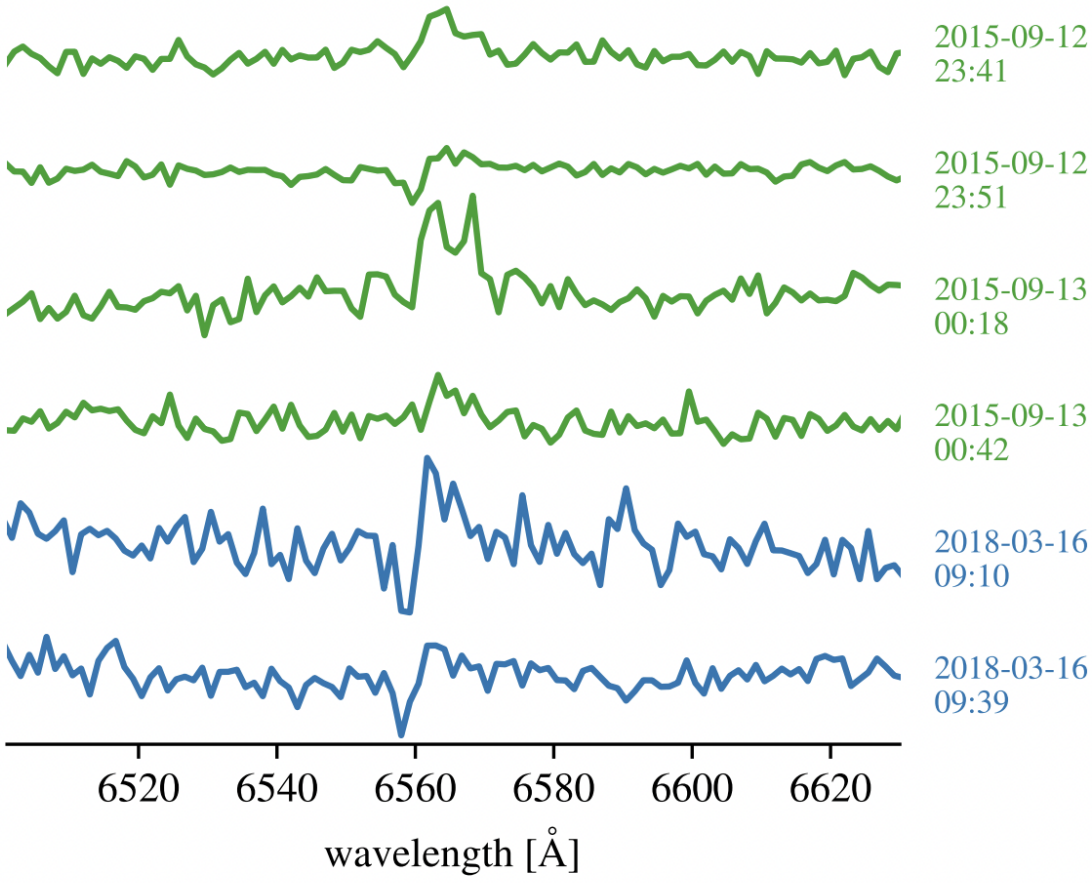

Figure 4.12 M62-VLA1 Hα spectra of the black-hole candidate M62-VLA1. This part of the spectrum varies on the timescale of minutes. Adapted from Göttgens et al. (2019)

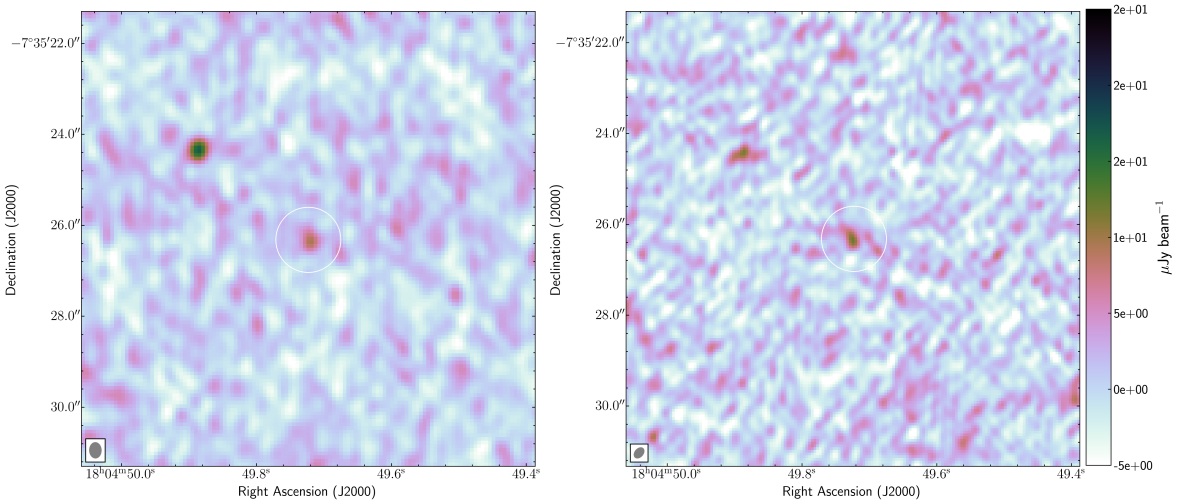

Figure 4.13 VLA images of 5.0 GHz (left) and 7.4 GHz (right) show a 10″x 10″field of view centered at NGC6539-VLA24 (white circle). The flux density is 19.6 ± 1.9 μJy at 5.0 GHz and 12.7 ±2.4 μJy at 7.2 GHz. The synthesized beam is plotted on the left corner of each radio map with grey color.

shows evidence of strong variability while it has a hard X-ray spectrum, which is best fit by an absorbed power law or an absorbed APEC (Figure 4.14). The X-ray photon index is $\Gamma = 1.64 \pm 0.28$, and the source has a very low probability of being a background AGN ($P = 0.001$). Using the radio and the X-ray data, in Figure 4.1 we plot the source on the radio-X-ray correlation and it is located in the region occupied both by black holes and by transitional millisecond pulsars in the sub-luminous disk state.

In the absence of radio pulsations, this source can only be differentiated between a black hole and neutron star binary with constraints on the accretor's mass. Initial optical spectroscopy has shown strong Hα emission consistent with an accreting compact object, and additional follow-up is needed to obtain the period and semi-amplitude.

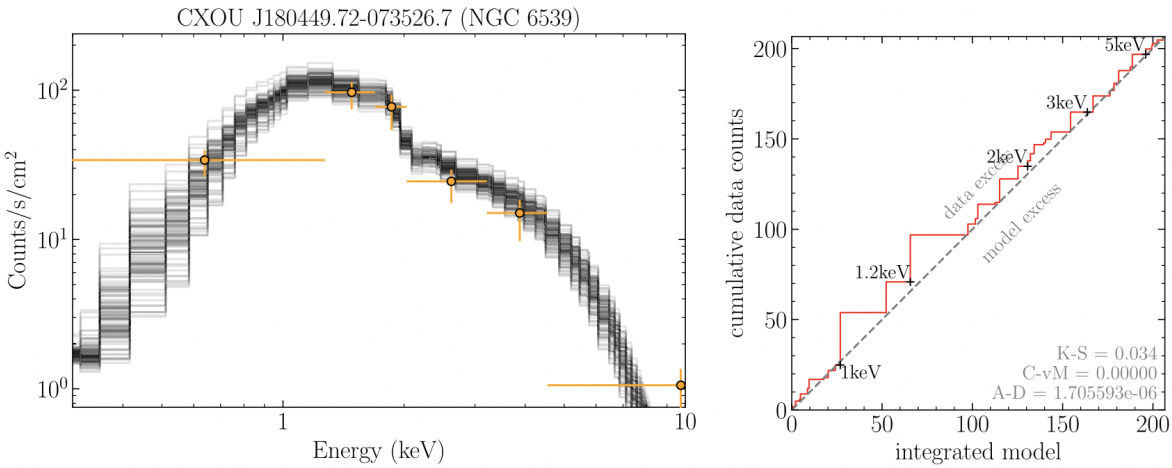

Figure 4.14 CXOU J185503.47–302847.6 X-ray spectra (left) and quantile–quantile (qq) plot for the NGC6539-VLA24 source. The black curves represent a random sample from the posterior for the best-fit model. For the purpose of plotting, the data in the spectral plots have been binned adaptively with at least 5 counts. Adapted from Bahramian et al. (2020)

4.3.8 Terzan 5

Terzan 5 is an exceptionally interesting globular cluster due to its high stellar density and stellar interaction rate (Bahramian et al., 2013). It has a large population of X-ray sources (Heinke et al., 2006) and many confirmed MSPs (Prager et al., 2017). Due to its known pulsar population, Terzan 5 was observed between 2012 and 2015 with the VLA radio telescope array at multi frequency bands covering $\sim$ 2.5 to $\sim$ 11 GHz. Unfortunately the Terzan 5 VLA data were not included in the initial MAVERIC source count catalog (Shishkovsky et al., 2020) due to calibration issues. These were later fixed with the results published by Urquhart et al. (2020).

4.3.8.1 Ter5-VLA31

An extensive analysis of VLA radio data is presented in Urquhart et al. (2020) for Ter5-VLA31 in Urquhart et al. (2020)). The fluxes at 5.0 and 7.4 GHz are listed in Table 4.1. It

is shown to have a flat radio spectral index of α = -0.2 $\pm$ 0.2 in the VLA data (the only radio source with a well constrained flat spectral index within the cluster's half-light radius). The source was fairly persistent, being detected in most of the 2012 and 2014 VLA observations, except at 2.6 GHz (see Figure 4.15). The 5.0 GHz radio luminosity is calculated to be $L_R = 6.2 \times 10^{27}$ erg $_s^{-1}$.

An X-ray source was detected at the radio position of Ter5-VLA31 (Bahramian et al., 2020), which was best fit with a soft power law spectrum, yielding a photon index of $\Gamma = 2.1 \pm 0.5$. The unabsorbed 1–10 keV luminosity is $L_X = 1.57 \times 10^{33}$ erg s^{-1}. In Figure 4.1, we plot the X-ray and radio luminosities of Ter5-ATCA2. Compared to the space occupied by with other compact objects, Ter5-ATCA2 is closest to the region corresponding to the black hole systems, with the caveat that the radio-X-ray correlation is less populated at the lower X-ray luminosities.

Alternative scenarios (e.g., radio flare from accreting white dwarfs, accreting neutron star) for the nature of the accretor are discussed in Urquhart et al. (2020). These are ultimately deemed unlikely due to the lack of X-ray variability and the magnitude of X-ray and radio luminosity. The overall properties of Ter5-ATCA2 are most consistent with that of quiescent stellar-mass black hole, but a confirmation of the accretors mass is required to definitively give Ter5-ATCA2 a black hole designation.

4.3.8.2 Ter5-VLA42

Ter5-VLA42 was included in this sample despite its non-detections at 5.0 and 7.4 GHz because Urquhart et al. (2020) detects the source at 9.0 and 11.0 GHz: S_9=99$\pm$4μJy & S_{11}=95$\pm$4μJy (see Tab. 4.1). And although the spectral index is unconstrained, it is located in the core of Terzan 5, and has an X-ray counterpart. Ter5-VLA42 is a known neutron star

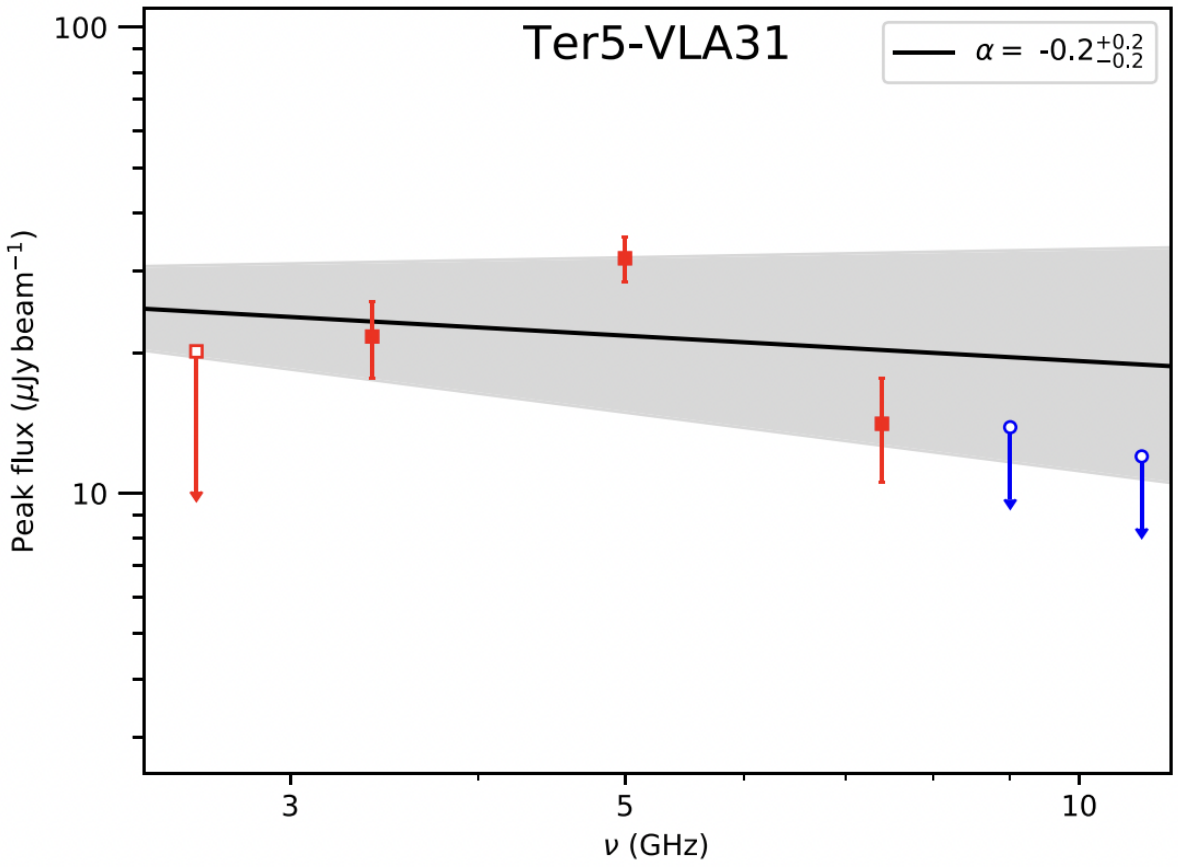

Figure 4.15 Adapted from Urquhart et al. (2020). Radio spectrum of the candidate stellar-mass black hole candidate Ter5-ATCA2. Red squares indicate the quasi-simultaneous 2012 VLA observations at frequencies 2.6, 3.2, 5.0, and 7.4 GHz. Blue circles represent the 9.0 and 11.0 GHz VLA observations from 2014. Open data points indicate 3σ upper limits. The best fitting spectral index (black solid line) is calculated using only the quasi simultaneous 2012 observations (red) points. The shaded regions indicate the 1σ uncertainties on the spectral index.

low mass X-ray binary, alternately identified as EXO 1745–248.

In the X-ray catalog of Bahramian et al. (2020), a corresponding X-ray source is located at the position of Ter5-VLA42. It has a photon index of Γ=1.5 and $L_X = 1.6 \times 10^{33}$ erg s^{-1} cm^{-2}. Figure 4.1 shows Ter5-VLA424 lying in much more radio bright region compared to other neutron stars. The source has a very steep radio-X-ray relationship relative to other neutron stars, and lies closer to the black hole region of the plot, despite being a confirmed neutron star system (Figure 4.1).

A detailed analysis of its 2015 outburst combining MAVERIC radio data and Swift/XRT data have been presented in Tetarenko et al. (2016b), which focuses on the characteristic of the disc/jet coupling. They find that the radio spectral index of the source varies from being inverted, flat, and somewhat steep over timescales of weeks. They use 10 GHz radio luminosity to examine the radio/X-ray correlation for black holes and neutrons stars and find that Ter5-VLA42 is approximately a magnitude below the black hole correlation, in the region occupied by tMSPs and AMXPs.

This is an interesting system that does not exhibit the typical infow/outflow seen in quiescent neutron star LMXBs, and may turn out to be an AMXP or rare tMSP system. Nonetheless, it has been firmly established to have a neutron star accretor through characteristic X-ray bursts, and can be ruled out as a black hole candidate.

4.4 Conclusions

Of the nine sources analyzed, two already considered identified. M28-VLA31 is a known pulsar, and Ter5-VLA42 is a known accreting neutron star binary. Two sources are potentially background galaxies: M55-VLA32 is likely to be one, while the evidence for M55-VLA34 is

more equivocal. The identification of M4-VLA31 is not final, but the best explanation that explains its observed properties is as an "active binary" without a compact object.

Three of the sources have already been identified by the MAVERIC collaboration as possible black hole candidates: M62-VLA1, NGC6359-VLA24, and Ter5-VLA31. For the first two of these, ongoing optical spectroscopy programs can help classify them and will give a definitive answer to their nature. Ter5-VLA31 is more difficult to assess due to the high extinction toward this object, though future spectroscopy with the James Webb Space Telescope is a potential avenue to discovering its nature.

The source represents a new black hole candidate: M22-VLA22. This candidate is sufficiently bright that ground-based optical spectroscopy is a viable means to determine its identity in the future.

For all of these objects whose nature is as yet unconfirmed, the the MAVERIC radio and X-ray data would be vital to providing scientific justification in order to be granted the necessary telescope time.

Chapter 5

Summary and Conclusions

This work describes our efforts to use radio continuum imaging to study radio sources in globular clusters, in particular those that have the characteristics of accreting black hole binaries. Here we give an overview of our results, and outline the next steps for this projects in the future.

5.1 Summary of Results

In chapter 2, we focused on the discovery and classification of the radio selected black hole binary M10-VLA1. This source was first discovered at significance in a 7.4 GHz image of the Milky Way globular cluster M10. It has a flat to inverted radio spectrum as well as an X-ray counterpart shown in Chandra X-ray observations. Its radio and X-ray properties together put it close to the black hole binary correlation. It has an unusual red straggler optical companion that has been observed to have an orbital period of ≈3.3 days. SOAR telescope observations show double-peaked Hα emission, that could be interpreted as evidence of an accretion disk. However, spectroscopy shows that the system has a low velocity semi-amplitude, which would require an almost face-on orientation to be indicative of a black hole accretor. We conclude that at present, the most likely explanations for this system are either a face-on accreting black hole binary, or a bright RS CVn active binary.

Chapter 3 details the compilation of our GC radio source catalog, as well as the properties

of that source population. We performed the first deep radio imaging survey of 25 Milky Way globular clusters, for an average of 10 hrs each, in the VLA C-band with central frequencies at 5.0 and 7.2 GHz. A radio source-finding procedure was used to catalog almost 1300 radio sources to 5σ significance. Comparing our source-density to the estimated background density at 5.0 GHz we find strong evidence for an excess of radio sources in certain clusters. We examined the distribution of radio spectral indices of our sample, and observed a bimodal distribution. It showed a flat-spectrum and steep-spectrum source population which we interpret as possible compact binaries and millisecond pulsars.

In chapter 4, we examine a selection of the MAVERIC radio catalog sources in an attempt to identify quality black hole binary candidates. We first selected cataloged radio sources that were confined to the cores of their host clusters, as well as those with flat radio spectral indices. Those remaining sources were then matched to the X-ray catalogs in another MAVERIC group study cataloging the faint X-ray sources in galactic globular clusters. There were 9 sources that met the required criteria, 7 from the VLA catalog, and 2 from the ATCA catalog that also had VLA data. This method was effective in picking out three previously identified black hole candidates, as well as a new black hole candidates to be further investigated in the future of this project.

5.2 Implications and Future Work

Overall, the discovery of candidate accreting black holes in globular clusters has already had a significant impact on the field. Early papers in this field by the MAVERIC collaboration was a factor in prompting theorists to revisit their models of black holes in dense stellar clusters, which previously predicted that black holes should be rare or absent. Now, using

the most recent simulations, several groups now argue that significant numbers of black holes can be retained to the present day, consistent with our findings.

These results have wide implications: perhaps the most important is that dynamical interactions in globular clusters can lead to the formation of black hole–black hole binaries observable as gravitational wave sources, and that some of the black hole–black hole binaries detected in the last several years by the Advanced LIGO/Virgo project may have formed in globular clusters.

Unfortunately, the dynamical confirmation of a stellar-mass black hole in a candidate discovered in the radio has been more challenging than initially anticipated. While there is little doubt that some black holes exist in clusters, the theoretical models need to be confronted with details that can only be obtained by observations: what masses of black holes exist in clusters today? Do these vary with cluster properties to the extent predicted from models? We have made progress on these questions, but still need to confirm candidates using optical or near-infrared observations to continue to progress. I also should emphasize that owing to the restrictive nature of my search, other black hole candidates likely remain in the MAVERIC radio catalogs, and need follow-up as well.

BIBLIOGRAPHY

Abada-Simon M., Lecacheux A., Bastian T. S., Bookbinder J. A., Dulk G. A., 1993, , 406, 692

Abbott B. P., et al., 2016, Physical Review X, 6, 041015

Bacon R., et al., 2010, in McLean I. S., Ramsay S. K., Takami H., eds, Society of Photo-Optical Instrumentation Engineers (SPIE) Conference Series Vol. 7735, Ground-based and Airborne Instrumentation for Astronomy III. p. 773508, doi:10.1117/12.856027

Bahramian A., Heinke C. O., Sivakoff G. R., Gladstone J. C., 2013, , 766, 136

Bahramian A., et al., 2017, , 467, 2199

Bahramian A., et al., 2018, , 864, 28

Bahramian A., et al., 2020, , 901, 57

Bailyn C. D., Grindlay J. E., 1990, , 353, 159

Bassa C., et al., 2004, , 609, 755

Bates S. D., Lorimer D. R., Verbiest J. P. W., 2013, , 431, 1352

Baumgardt H., Hilker M., 2018, , p. 1027

Becker R. H., White R. L., McLean B. J., Helfand D. J., Zoonematkermani S., 1990, , 358, 485

Bégin S., 2006, Master's thesis, University of British Columbia, Canada

Birkinshaw M., Downes A. J. B., 1982, , 258, 154

Blandford R. D., Königl A., 1979, , 232, 34

Bogdanov S., et al., 2011, , 730, 81

Bogdanov S., et al., 2018a, , 856, 54

Bogdanov S., et al., 2018b, , 856, 54

Breen P. G., Heggie D. C., 2013, , 432, 2779

Camilo F., Rasio F. A., 2005, in Rasio F. A., Stairs I. H., eds, Astronomical Society of the Pacific Conference Series Vol. 328, Binary Radio Pulsars. p. 147 (arXiv:astro-ph/0501226)

Chatterjee S., Rodriguez C. L., Rasio F. A., 2017, , 834, 68

Chen J. C., et al., 2019, VizieR Online Data Catalog, p. IX/57

Chomiuk L., Strader J., Maccarone T. J., Miller-Jones J. C. A., Heinke C., Noyola E., Seth A. C., Ransom S., 2013, , 777, 69

Clark G. W., 1975, , 199, L143

Clark G. W., Markert T. H., Li F. K., 1975, , 199, L93

Condon J. J., 1984, , 287, 461

Condon J. J., 1992, , 30, 575

Condon J. J., 1997, , 109, 166

Coppejans D. L., Körding E. G., Miller-Jones J. C. A., Rupen M. P., Knigge C., Sivakoff G. R., Groot P. J., 2015, , 451, 3801

Corbel S., Fender R. P., Tzioumis A. K., Nowak M., McIntyre V., Durouchoux P., Sood R., 2000, , 359, 251

Corbel S., Nowak M. A., Fender R. P., Tzioumis A. K., Markoff S., 2003, , 400, 1007

Corbel S., Coriat M., Brocksopp C., Tzioumis A. K., Fender R. P., Tomsick J. A., Buxton M. M., Bailyn C. D., 2013, , 428, 2500

Davies M. B., Hansen B. M. S., 1998, , 301, 15

Deller A. T., et al., 2015, , 809, 13

Drake S. A., Simon T., Linsky J. L., 1992, , 82, 311

Evans I. N., et al., 2010, , 189, 37

Fabian A. C., Pringle J. E., Rees M. J., 1975, , 172, 15

Fender R. P., 2001, , 322, 31

Fomalont E. B., Windhorst R. A., Kristian J. A., Kellerman K. I., 1991, , 102, 1258

Gallo E., Miller B. P., Fender R., 2012, , 423, 590

Gallo E., et al., 2014, , 445, 290

Gallo E., Degenaar N., van den Eijnden J., 2018, , 478, L132

Giesers B., et al., 2018, , 475, L15

Giveon U., Becker R. H., Helfand D. J., White R. L., 2005, , 129, 348

Gopal-Krishna Steppe H., 1980, , 88, 354

Göttgens F., et al., 2019, , 631, A118

Greisen E. W., 2003, in Information Handling in Astronomy - Historical Vistas. Edited by Andr© Heck, Strasbourg Astronomical Observatory, France. Astrophysics and Space Science Library, Vol. 285. Dordrecht: Kluwer Academic Publishers, 2003., p.109. p. 109, doi:10.1007/0-306-48080-8˙7

Griffith M. R., Wright A. E., 1993, , 105, 1666

Grindlay J. E., Hertz P., Steiner J. E., Murray S. S., Lightman A. P., 1984, , 282, L13

Grindlay J. E., Camilo F., Heinke C. O., Edmonds P. D., Cohn H., Lugger P., 2002, , 581, 470

Hancock P. J., Murphy T., Gaensler B. M., Hopkins A., Curran J. R., 2012, , 422, 1812

Hancock P. J., Trott C. M., Hurley-Walker N., 2018, Publications of the Astronomical Society of Australia, 35, e011

Harris W. E., 2010, preprint, p. arXiv:1012.3224 (arXiv:1012.3224)

Heggie D. C., Giersz M., 2014, , 439, 2459

Heinke C. O., Grindlay J. E., Lugger P. M., Cohn H. N., Edmonds P. D., Lloyd D. A., Cool A. M., 2003, , 598, 501

Heinke C. O., Wijnands R., Cohn H. N., Lugger P. M., Grindlay J. E., Pooley D., Lewin W. H. G., 2006, , 651, 1098

Heywood I., Bielby R. M., Hill M. D., Metcalfe N., Rawlings S., Shanks T., Smirnov O. M., 2013, , 428, 935

Hill A. B., et al., 2011, , 415, 235

Hills J. G., 1976, , 175, 1P

Hjellming R. M., Johnston K. J., 1988, , 328, 600

Hoare M. G., et al., 2012, , 124, 939

Huynh M. T., Jackson C. A., Norris R. P., Fernand ez-Soto A., 2008, , 135, 2470

Huynh M. T., Bell M. E., Hopkins A. M., Norris R. P., Seymour N., 2015, , 454, 952

Huynh M. T., Seymour N., Norris R. P., Galvin T., 2020, , 491, 3395

Irwin J. A., Brink T. G., Bregman J. N., Roberts T. P., 2010, , 712, L1

Ivanova N., Heinke C. O., Rasio F. A., Belczynski K., Fregeau J. M., 2008, , 386, 553

Ivanova N., Chaichenets S., Fregeau J., Heinke C. O., Lombardi J. C. J., Woods T. E., 2010, , 717, 948

Johnson H. M., 1976, , 208, 706

Johnson H. M., Catura R. C., Charles P. A., Sanford P. W., 1977, , 212, 112

Kaluzny J., Thompson I. B., Krzeminski W., 1997, , 113, 2219

Kaluzny J., Thompson I. B., Rozyczka M., Krzeminski W., 2013, , 63, 181

Kremer K., Ye C. S., Chatterjee S., Rodriguez C. L., Rasio F. A., 2018, , 855, L15

Kulkarni S. R., Hut P., McMillan S., 1993, , 364, 421

Lewin W. H. G., van Paradijs J., van den Heuvel E. P. J., 1997, Cambridge Astrophysics Series, 26

Maccarone T. J., 2004, , 351, 1049

Maccarone T. J., Kundu A., Zepf S. E., Rhode K. L., 2007, , 445, 183

Maccarone T. J., et al., 2012, , 426, 3057

Mackey A. D., Wilkinson M. I., Davies M. B., Gilmore G. F., 2008, , 386, 65

Marsh T. R., et al., 2016, , 537, 374

McMahon R. G., Banerji M., Gonzalez E., Koposov S. E., Bejar V. J., Lodieu N., Rebolo R., VHS Collaboration 2013, The Messenger, 154, 35

McMahon R. G., Banerji M., Gonzalez E., Koposov S. E., Bejar V. J., Lodieu N., Rebolo R., VHS Collaboration 2021, VizieR Online Data Catalog, p. II/367

McMullin J. P., Waters B., Schiebel D., Young W., Golap K., 2007, in Astronomical Data Analysis Software and Systems XVI ASP Conference Series, Vol. 376, proceedings of the conference held 15-18 October 2006 in Tucson, Arizona, USA. Edited by Richard A. Shaw, Frank Hill and David J. Bell., p.127. p. 127

Migliari S., Fender R. P., 2006, , 366, 79

Miller-Jones J. C. A., Jonker P. G., Maccarone T. J., Nelemans G., Calvelo D. E., 2011, , 739, L18

Miller-Jones J. C. A., et al., 2015, , 453, 3918

Misner C. W., Thorne K. S., Wheeler J. A., 1973, Gravitation

Mochejska B. J., Kaluzny J., Thompson I., Pych W., 2002, , 124, 1486

Moody K., Sigurdsson S., 2009, , 690, 1370

Morscher M., Umbreit S., Farr W. M., Rasio F. A., 2013, , 763, L15

Morscher M., Pattabiraman B., Rodriguez C., Rasio F. A., Umbreit S., 2015a, , 800, 9

Morscher M., Pattabiraman B., Rodriguez C., Rasio F. A., Umbreit S., 2015b, , 800, 9

Nardiello D., et al., 2018, , 481, 3382

Padovani P., Giommi P., Landt H., Perlman E. S., 2007, , 662, 182

Papitto A., et al., 2013, , 501, 517

Peacock M. B., et al., 2012, , 759, 126

Piotto G., et al., 2015, , 149, 91

Plotkin R. M., et al., 2017, , 834, 104

Poutanen J., Veledina A., 2014, , 183, 61

Prager B. J., Ransom S. M., Freire P. C. C., Hessels J. W. T., Stairs I. H., Arras P., Cadelano M., 2017, , 845, 148

Purcell C. R., et al., 2013, , 205, 1

Ransom S. M., 2008, in Vesperini E., Giersz M., Sills A., eds, IAU Symposium Vol. 246, Dynamical Evolution of Dense Stellar Systems. pp 291–300, doi:10.1017/S1743921308015810

Ratti E. M., et al., 2012, , 423, 2656

Rodriguez C. L., Chatterjee S., Rasio F. A., 2016, , 93, 084029

Rood R. T., Turner K. C., Goldstein S. J., 1978, , 225, 804

Rushton A. P., et al., 2016, , 463, 628

Russell T. D., et al., 2016, , 460, 3720

Ryle M., Neville A. C., 1962, , 125, 39

Ryle M., Scheuer P. A. G., 1955, Proceedings of the Royal Society of London Series A, 230, 448

Sarajedini A., et al., 2007, , 133, 1658

Sarazin C. L., Irwin J. A., Bregman J. N., 2001, , 556, 533

Scheuer P. A. G., 1957, Proceedings of the Cambridge Philosophical Society, 53, 764

Shishkovsky L., et al., 2018, , 855, 55

Shishkovsky L., et al., 2020, , 903, 73

Sigurdsson S., Hernquist L., 1993, , 364, 423

Sippel A. C., Hurley J. R., 2013, , 430, L30

Smolčić V., et al., 2008, , 177, 14

Smolčić V., et al., 2017, , 602, A1

Steiner J. F., McClintock J. E., Remillard R. A., Gou L., Yamada S., Narayan R., 2010, , 718, L117

Strader J., Chomiuk L., Maccarone T. J., Miller-Jones J. C. A., Seth A. C., 2012, , 490, 71

Sutantyo W., 1975, , 44, 227

Tanaka Y., Shibazaki N., 1996, , 34, 607

Tetarenko B. E., et al., 2016a, , 825, 10

Tetarenko A., Sivakoff G. R., Bahramian A., Heinke C. O., Miller-Jones J. C. A., Maccarone T., Degenaar N., Wijnands R., 2016b, The Astronomer's Telegram, 8744, 1

Tisanić K., et al., 2019, , 621, A139

Tranin H., Godet O., Webb N., Primorac D., 2022, , 657, A138

Tremou E., et al., 2018, , 862, 16

Tudor V., et al., 2017, , 470, 324

Tudor V., et al., 2022, , 513, 3818

Urquhart R., et al., 2020, , 904, 147

Verbunt F., Hut P., 1983, , 127, 161

Verbunt F., Hut P., 1987, in Helfand D. J., Huang J. H., eds, IAU Symposium Vol. 125, The Origin and Evolution of Neutron Stars. p. 187

Verbunt F., Lewin W. H. G., 2006, Globular cluster X-ray sources. pp 341–379

Verbunt F., Meylan G., 1988, , 203, 297

Wang S., Liu J., Qiu Y., Bai Y., Yang H., Guo J., Zhang P., 2016, , 224, 40

Weatherford N. C., Chatterjee S., Rodriguez C. L., Rasio F. A., 2018, , 864, 13

Weatherford N. C., Chatterjee S., Kremer K., Rasio F. A., 2019, arXiv e-prints, p. arXiv:1911.09125

Wilman R. J., et al., 2008, , 388, 1335

Windhorst R. A., van Heerde G. M., Katgert P., 1984, , 58, 1

Windhorst R., Mathis D., Neuschaefer L., 1990, The evolution of weak radio galaxies at radio and optical wavelengths.. pp 389–403

Windhorst R. A., Fomalont E. B., Partridge R. B., Lowenthal J. D., 1993, , 405, 498

Zdziarski A. A., Gierliński M., 2004, Progress of Theoretical Physics Supplement, 155, 99

Zepf S. E., et al.,,

Zhao Y., et al., 2020, , 493, 6033

de Zotti G., Massardi M., Negrello M., Wall J., 2010, , 18, 1